

# **Studies of Quantum Dots using Machine Learning**

by

Even Marius Nordhagen

THESIS

for the degree of

MASTER OF SCIENCE



Faculty of Mathematics and Natural Sciences  
University of Oslo

November 2019

All illustrations in this thesis are created using the TikZ package<sup>1</sup> if nothing else is specified. The plots are produced using a controversial combination of Matplotlib<sup>2</sup> and PGFPlots<sup>1</sup>.

The L<sup>A</sup>T<sub>E</sub>X document preparation system was applied for typesetting.

## Abstract

With the ability to solve the many-body Schrödinger equation accurately, in principle all physics and chemistry could be derived from first principles. However, exact wave functions of realistic and interesting systems are in general unavailable because they are non-deterministic polynomial-hard to compute<sup>3</sup>. This implies that we need to rely on approximations. The variational Monte Carlo (VMC) method is widely used for ground state studies, but requires a trial wave function ansatz which must trade off between efficiency and accuracy. The method also has many common features with machine learning algorithms, and as neural networks have shown impressive power as function approximators, the idea is to use a neural network as the trial wave function guess. For fermionic systems, like electronic structure systems, the wave function needs to obey Fermi-Dirac statistics, which typically is achieved using a Slater determinant. As a neural network hardly can model this feature, our approach is to replace the single-particle functions in the Slater determinant with restricted Boltzmann machines (RBM). In addition, we add further correlations via so-called Jastrow factors<sup>4</sup>.

Our primary focus is on closed-shell circular quantum dots, where we compute the ground state energy and electron density of two-dimensional systems with up to  $N = 90$  electrons and three-dimensional systems with up to  $N = 70$  electrons. The energy obtained by the RBM was reasonably close to experimental results, and it gradually became closer as we added more complex correlation factors. For our most complicated Jastrow factor, the energy was found to be lower than the VMC-energy for small dots, but for larger dots it was slightly higher. However, the one-body density profile reveals that the RBM gives more distinctly located electrons compared to the VMC method, which can be explained by the way the RBM models the correlations. From the two-body density profile, we also observe that the repulsive interactions get more significant as we add a Jastrow factor. Based on the electron densities and the energy distribution between kinetic and potential energy, it is certain that the various methods provide different electron configurations. For low-frequency dots, the electron density becomes more localized with an additional radial peak compared to high-frequency dots. This is reminiscent of what is known as Wigner localization<sup>5</sup>.

The computational time consumption was found to be favorable for the RBM for small systems and VMC for large systems, which can be explained by the exploding number of variational parameters in the RBM as the system sizes increase. RBMs with Jastrow factors were notably more computationally intensive than the other methods, and evidently, there is no reason to use the simplest Jastrow factor when more complicated Jastrow factors are available.



## Acknowledgements

After five exciting years at Blindern, I would sincerely like to acknowledge some people who have been important throughout my studies. First, I would like to thank my excellent supervisor, Morten Hjorth-Jensen, whom I luckily got to know three years ago. From day one, you took me under your wing and enthralled me with your eager, work ethic and massive knowledge. Few things make me more motivated than a conversation with you, be it in real-life at Blindern or through video conversations from whatever place you happen to be at.

I also very much appreciate the support from mum, dad and my sister. Even though the schedule has been full and I have not spent as much time with you as I wanted, you were always understanding. Thanks to my friends (you know who you are), who are always ready for a beer (or ten) whenever I need to disconnect from the studies. These moments, filled with lively discussions and dark humor, make me able to focus on the studies when needed.

The computational physics group is a funny composition of different people with a shared predilection for physics and programming. There are so many talented guys in the group, and I really enjoy spending early mornings and late nights with you. I would also like to thank my high school teacher, Jens Otto Opaker, who with his enthusiasm and dedication got me hooked on science in the first place.

Last, but not least, thanks to Sebastian Gregorius Winther-Larsen, Robert Solli, Marius Jonsson and Kaitlin Rose Preusser for proofreading and constructive feedback.

A handwritten signature in black ink that reads "Even M. Nordhagen". The signature is fluid and cursive, with "Even" on the top line, "M." in a smaller circle on the middle line, and "Nordhagen" on the bottom line.

Even Marius Nordhagen



# Contents

<b>1</b>	<b>Introduction</b>	<b>1</b>
1.1	The many-body problem . . . . .	1
1.2	Machine learning . . . . .	2
1.3	Quantum dots . . . . .	2
1.4	Computer experiments . . . . .	3
1.5	Ethics in science . . . . .	4
1.6	Goals and contributions . . . . .	4
1.7	The developed code . . . . .	5
1.8	Structure of the thesis . . . . .	5
<b>I</b>	<b>Quantum Theory</b>	<b>7</b>
<b>2</b>	<b>Preliminary Quantum Mechanics</b>	<b>9</b>
2.1	The postulates of quantum mechanics . . . . .	11
2.2	The Schrödinger equation . . . . .	11
2.2.1	The hydrogen atom . . . . .	13
2.3	The variational principle . . . . .	13
2.4	Quantum numbers . . . . .	14
2.5	The virial theorem . . . . .	14
<b>3</b>	<b>Many-body Quantum Mechanics</b>	<b>17</b>
3.1	The electronic Hamiltonian . . . . .	18
3.2	The many-body wave function . . . . .	18
3.2.1	Anti-symmetry and the Pauli principle . . . . .	19
3.2.2	The Slater determinant . . . . .	19
3.2.3	Basis set . . . . .	20
3.2.4	Modeling the cusp . . . . .	21
3.3	Electron density . . . . .	21
3.3.1	Wigner crystals . . . . .	23
<b>4</b>	<b>Systems</b>	<b>25</b>
4.1	Quantum dots . . . . .	26
4.2	Quantum double dots . . . . .	27
4.3	Atoms . . . . .	27

<b>II Machine Learning Theory</b>	<b>31</b>
<b>5 Supervised Learning</b>	<b>33</b>
5.1 Polynomial regression . . . . .	35
5.1.1 An example on polynomial regression . . . . .	36
5.2 Bias-variance tradeoff . . . . .	38
5.3 Linear regression . . . . .	39
5.3.1 Singular value decomposition . . . . .	39
5.3.2 Ridge regression . . . . .	40
5.3.3 LASSO regression . . . . .	40
5.4 Logistic regression . . . . .	41
5.5 Neural networks . . . . .	43
5.5.1 Forward phase . . . . .	44
5.5.2 Activation function . . . . .	44
5.5.3 Backward propagation . . . . .	45
5.6 Optimization algorithms . . . . .	47
5.6.1 Gradient descent . . . . .	47
5.6.2 Stochastic gradient descent . . . . .	48
5.6.3 Adding momentum . . . . .	48
5.6.4 ADAM . . . . .	49
<b>6 Boltzmann Machines</b>	<b>51</b>
6.1 Statistical foundation . . . . .	52
6.1.1 Marginal distributions . . . . .	53
6.1.2 Conditional distributions . . . . .	53
6.1.3 Maximum log-likelihood estimate . . . . .	54
6.2 Unrestricted Boltzmann machines . . . . .	54
6.3 Restricted Boltzmann machines . . . . .	55
6.3.1 Gaussian-binary units . . . . .	56
6.4 Partly restricted Boltzmann machines . . . . .	58
6.5 Deep Boltzmann machines . . . . .	59
<b>III Methods</b>	<b>61</b>
<b>7 Quantum Monte Carlo Methods</b>	<b>63</b>
7.1 Variational Monte Carlo . . . . .	64
7.1.1 The trial wave function . . . . .	64
7.1.2 The Jastrow factor . . . . .	66
7.1.3 The local energy . . . . .	67
7.1.4 Parameter update . . . . .	68
7.1.5 The electron density . . . . .	69
7.1.6 Common extensions . . . . .	69
7.2 Unifying Quantum Mechanics and Machine Learning . . . . .	69
7.2.1 Restricted Boltzmann machine without Jastrow factor (RBM) . . . . .	70
7.2.2 RBM with a simple Jastrow factor (RBM+SJ) . . . . .	70
7.2.3 RBM with a Padé-Jastrow factor (RBM+PJ) . . . . .	70
7.3 The Metropolis Algorithm . . . . .	71
7.3.1 Brute-force sampling . . . . .	71
7.3.2 Importance sampling . . . . .	72

7.3.3	Gibbs sampling . . . . .	73
7.4	Diffusion Monte Carlo . . . . .	74
7.5	Error estimation . . . . .	75
7.5.1	Central concepts of statistics . . . . .	76
7.5.2	Blocking . . . . .	77
<b>IV</b>	<b>Implementation</b>	<b>79</b>
<b>8</b>	<b>Scientific Programming</b>	<b>81</b>
8.1	Object-oriented programming in Python . . . . .	82
8.1.1	An example based on Monte Carlo simulations . . . . .	84
8.2	Low-level programming with C++ . . . . .	85
8.2.1	Built-in data types . . . . .	85
8.2.2	Access modifiers . . . . .	86
8.2.3	Virtual functions . . . . .	86
8.2.4	Constructors and destructors . . . . .	87
8.2.5	Pointers . . . . .	87
8.2.6	Back to the Monte Carlo example . . . . .	87
<b>9</b>	<b>Implementation: Variational Monte Carlo</b>	<b>89</b>
9.1	Flexibility and readability . . . . .	89
9.2	Decomposing the trial wave function . . . . .	90
9.2.1	Local energy computations . . . . .	91
9.2.2	Parameter gradients . . . . .	92
9.2.3	Probability ratio . . . . .	92
9.3	Slater determinant . . . . .	93
9.3.1	Factorizing out elements . . . . .	94
9.3.2	The Gaussian . . . . .	95
9.3.3	The determinant . . . . .	96
9.3.4	Efficient calculation of the determinant . . . . .	97
9.4	Jastrow factor . . . . .	100
9.4.1	The Simple Jastrow factor . . . . .	100
9.4.2	The Padé-Jastrow factor . . . . .	101
9.4.3	Updating the distance matrix . . . . .	102
9.5	Sampling . . . . .	103
9.5.1	Brute force sampling . . . . .	103
9.5.2	Importance sampling . . . . .	104
9.6	Update of parameters . . . . .	105
9.6.1	Gradient descent . . . . .	105
9.6.2	ADAM optimizer . . . . .	105
9.7	Parallel processing . . . . .	106
9.8	Electron density . . . . .	107
9.9	Random number generator . . . . .	109
<b>10</b>	<b>Implementation: Restricted Boltzmann Machines</b>	<b>111</b>
10.1	RBM-Gaussian . . . . .	112
10.2	RBM-product . . . . .	113
10.3	Partly restricted Boltzmann machine . . . . .	115

<b>V Results and Discussion</b>	<b>117</b>
<b>11 Selected Results</b>	<b>119</b>
11.1 Computational cost . . . . .	120
11.2 Energy convergence . . . . .	122
11.3 No repulsive interaction . . . . .	123
11.3.1 Quantum dots . . . . .	123
11.3.2 Atoms . . . . .	126
11.4 Quantum dots . . . . .	127
11.4.1 Ground state energy . . . . .	127
11.4.2 One-body density . . . . .	131
11.4.3 Two-body density . . . . .	137
11.4.4 Energy distribution . . . . .	140
11.4.5 Low frequency dots . . . . .	143
11.4.6 Large dots . . . . .	146
11.5 Atoms . . . . .	146
<b>VI Conclusion</b>	<b>151</b>
<b>12 Conclusions and Future Work</b>	<b>153</b>
<b>A Natural Units</b>	<b>157</b>
A.1 Quantum dots . . . . .	157
A.2 Atoms . . . . .	158
<b>B Distributions of Gaussian-binary restricted Boltzmann machines</b>	<b>159</b>
B.1 Distributions of visible units . . . . .	159
B.1.1 Marginal distribution . . . . .	160
B.1.2 Conditional distribution . . . . .	160
B.2 Distributions of hidden units . . . . .	160
B.2.1 Marginal distribution . . . . .	161
B.2.2 Conditional distribution . . . . .	161
<b>C Collection of Results</b>	<b>163</b>
C.1 CPU time . . . . .	163
C.2 Ground state energy . . . . .	164
C.2.1 Two dimensions . . . . .	165
C.2.2 Three dimensions . . . . .	169
C.3 One-body density . . . . .	173
C.4 Two-body density plots . . . . .	181

## CHAPTER 1

# Introduction

Quantum mechanical laws determine the properties and behavior of quantum many-body systems, and have been known since the 1930s. The time-dependent Schrödinger equation describes the binding energy of atoms and molecules, as well as the interaction between particles in a gas. Moreover, it has been used to determine the energy of artificial structures like quantum dots<sup>6</sup>, nanowires<sup>7</sup> and ultracold condensates<sup>8</sup>. Since quantum mechanics is one of the most precisely tested theories in the history of science<sup>9</sup>, computer experiments are in principle capable of obtaining the energy as precisely as laboratory experiments, and can in that sense replace laboratory experiments.

Although we know the laws of quantum mechanics, we encounter many challenges when calculating real-world problems. Firstly, interesting systems often involve a large number of particles. This causes expensive calculations. Secondly, the correct wave functions are seldom known for complex systems. Together, they contribute to the many-body problem.

## 1.1 The many-body problem

In quantum mechanics, a many-body system contains three or more interacting particles. These interactions create so-called quantum correlations, which make the wave function of the system a complicated object holding a large amount of information. As a consequence, exact or analytical calculations become impractical or even impossible. This is known as the many-body problem. Indeed, Paul Dirac recognized these problems already in 1929:

“ The general theory of quantum mechanics is now almost complete... ...The underlying physical laws necessary for the mathematical theory of a large part of physics and the whole of chemistry are thus completely known, and the difficulty is only that the exact application of these laws leads to equations much too complicated to be soluble.

Paul M. Dirac, *Quantum Mechanics of Many-electron Systems*<sup>10</sup>

”

There are numerous approaches to overcome this problem, where approximative methods often are used to reduce the, sometimes extreme, computational cost. Popular methods include the Hartree-Fock method, which replaces the interaction by a mean-field<sup>11,12</sup>, and methods like Full Configuration Interaction (FCI) and Coupled Cluster theory, which seek to solve the problem by approximating the total wave function in terms of single-particle basis sets<sup>13</sup>. As an example, an FCI calculation introduces a series of so-called Slater determinants based on such basis sets. Quantum Monte Carlo (QMC) methods use a different approach and attempt to solve the Schrödinger equation directly using a stochastic evaluation of the integrals<sup>14</sup>. What all these methods have in common, is that they require significant amounts of physical intuition in order

to work. In general, prior knowledge of the wave function, covering information about the interactions and potential, is required. This knowledge is often unavailable, especially for complex systems, making accurate estimates of the observable unavailable.

The ultimate goal of this work is to reduce the amount of physical intuition needed by inventing more flexible and sophisticated methods. Machine learning techniques appear as a natural base for these methods, as they can "learn" themselves and thus estimate observables through training processes. The apparent link between machine learning and quantum mechanics are the QMC methods, since they both address to minimize a *cost function* in order to obtain optimal configurations. The connection between machine learning and QMC methods, in particular variational Monte Carlo (VMC), will be discussed thoroughly throughout this work.

## 1.2 Machine learning

Machine learning has recently achieved immense popularity in fields such as economics<sup>15</sup>, autonomy<sup>16</sup> - and science, as we will see later, due to its ability to learn without being explicitly programmed. As a branch of artificial intelligence, machine learning is based on studies of the human brain and attempts to recreate the way neurons in the brain process information.

In particular, the artificial neural networks have experienced significant progress over the past decade, which can be attributed to an array of innovations. Most notably, the convolutional neural network (CNN) AlexNet<sup>17</sup> managed to increase the top-5 test error rate of image recognition with a remarkable 11.1% compared to the second-best back in 2012! Today, the CNNs have been further improved, and they are even able to beat humans in recognizing images<sup>18</sup>. Also, speech recognition algorithms have lately been revolutionized, thanks to recurrent neural networks (RNNs), and especially long short-term memory (LSTM) networks. Their ability to recognize sequential (time-dependent) data has made the technology good enough for entry to millions of people's everyday-life through services such as Google Translate<sup>19</sup>, Apple's Siri<sup>20</sup> and Amazon Alexa<sup>21</sup>. It is also interesting to see how machine learning has made computers eminent tacticians using reinforcement learning. The DeepMind-developed program AlphaGo demonstrated this by beating the 9-dan professional, Sedol, in the board game Go<sup>22</sup>. Thereafter, an improved version beat the highest-rated chess computer at that time, Stockfish, in chess<sup>23</sup>. Both these scenarios were unbelievable just a couple of decades ago.

Admitting that all these branches are both exciting and promising, they will not be discussed further in this work, since they are not relevant to our approach. The reason is that they initially require labeled data in order to be trained, they obey so-called *supervised* learning. For our quantum mechanical systems, we do not have labeled data and therefore need to rely on *unsupervised* learning with the focus on restricted Boltzmann machines (RBMs). Recently, some effort has been put towards this field, known as quantum machine learning. Carleo & Troyer<sup>24</sup> demonstrated the link between RBMs and QMC and named the states *neural-network quantum states* (NQS). They used the technique to study the Ising model and the Heisenberg model. Pfau *et al.*<sup>25</sup> went further and predicted the dissociation curves of the nitrogen molecule using a so-called fermionic neural network, and Flugsrud<sup>26</sup> investigated ground state properties of circular quantum dots, also using RBMs. We will extend the work she did to larger quantum dots.

## 1.3 Quantum dots

Quantum dots are often termed artificial atoms because of their common features in comparison to real atoms, where both are made up of electronic structure systems with electrons confined by an external potential. Quantum dots are interesting both from a theoretical, technological

and experimental point of view, and are therefore covered in different fields of research. Theoretically, quantum dots are interesting as they are relatively simple structures that can model a long range of phenomena. An example on this is the Wigner localization, which has been observed in strongly interacting quantum dots where the potential energy dominates over the kinetic energy<sup>5,27</sup>. As these systems are more strongly correlated than, for instance, atoms, other challenges are encountered which might require other approaches. Research indicate that quantum Monte Carlo methods are the best suited techniques for studies of these systems<sup>5</sup>.

Over the past decade, the popularity of quantum dots has increased, thanks to technological progress in semiconductor research. In particular, they are expected to be the next big thing in display technology due to their ability to emit photons of specific wavelengths, create a smoother transition between different colors and enhance the control of the diodes<sup>28</sup>. The quantum displays have also proven to be 30% more energy efficient than the current generation of LED displays<sup>29</sup>, and Samsung already claim that they use this technology in their displays<sup>28</sup>. Another reason why we are interested in simulating quantum dots is because there exist experiments that can be used as benchmarks. Due to very strong confinement in the z-direction, the experimental dots, made by patterning GaAs/AlGaAs heterostructures, become essentially two-dimensional<sup>30,31</sup>. For that reason, our main focus in this work is on two-dimensional dots, but also dots of three dimensions will be investigated.

## 1.4 Computer experiments

The advent of computer technology has offered a new opportunity for studies of quantum (and many other) problems. In addition to the traditional laboratory experiments and analytical approaches, it serves as a third way of doing science which is based on simulations. By the term simulations, we mean reality-based computational models rooted in physical laws, such as the Schrödinger equation. The value behind these models lies in their ability to provide new information or to make predictions which otherwise is too costly or even impossible to obtain. QMC methods illustrates what is the power and potential of such methodologies.

The use and popularity of QMC methods have increased as personal computers and computer clusters have become more powerful. With today's reliable computers, we see these methods as a natural choice when ground state properties of quantum mechanical systems are investigated. Even the most straightforward method, VMC, typically yields excellent results, and the more complicated diffusion Monte Carlo (DMC) is in principle capable of employing exact results. They both appear to have among the highest performance-to-cost ratios out of all the quantum many-body methods.

Albeit the QMC methods relatively recently have been applied to large-scale calculations, some of the ideas go back to the time before the invention of the electronic computer. Already in the 1940s, Enrico Fermi revealed the similarities between the imaginary time Schrödinger equation and stochastic processes in statistical mechanics<sup>32,33</sup>. The first attempt to use this link on actual calculations was performed by a group of scientists at Los Alamos National Laboratory in the early 1950s when they tried to compute the ground state energy of the hydrogen molecule using a simple version of VMC<sup>14</sup>. At around the same time, Metropolis & Ulam<sup>32</sup> introduced the original Metropolis algorithm, which estimates the energy by moving particles randomly in an ergodic scheme and rejecting inappropriate moves. This method was further improved in the early 1960s when Kalos<sup>34</sup> laid down the statistical and mathematical framework for Green's functions in QMC methods, and Hastings<sup>35</sup> developed an efficient algorithm based on the theory, where the particles are moved after the so-called quantum force. The use of the QMC methods on many-fermion systems was first done by Ceperley & Alder<sup>33</sup> in the 1970-1980s and started a new era of stochastic methods applied to electronic structure problems.

## 1.5 Ethics in science

In science, as an entirety, there are some general guidelines that we all should follow in order to maintain ethical behavior. Firstly, one should always have respect for others work, and the authors should be credited whenever one uses others work, no matter the scope. With work, we mean illustrations, text, code, methods, algorithms *et cetera*, which are protected by the Copyright Act (in Norway, åndsverkloven). Secondly, all the research that one does should always be detailed in a such way that others can reproduce the experiments and results. This means that all the factors which possibly have a significant impact on the experiments should be described, and computer experiments are no exceptions. Lastly, there are unfortunately many examples of misuse of knowledge throughout history, something that has to be avoided.

In our specific work, the ethical aspects are also related to the use of machine learning, which can cause fatal consequences if it is not used correctly and carefully. The fact that machine learning allows the computers to learn things themselves have made two of the greatest minds of our time, Stephen Hawking<sup>36</sup> and Elon Musk<sup>37</sup>, warn us that they can be greatly misused if they are set on learning the wrong things. Every person who develops machine learning algorithms should take this warning seriously, remember that in the end, it is one of us who end up creating the multi-headed monster *Hydra*.

## 1.6 Goals and contributions

The goals of this work are twofold: First, a flexible software for variational Monte Carlo (VMC) simulations has to be developed. To reduce the required physical intuition, it will support trial wave functions created by restricted Boltzmann machines (RBMs). Also traditional trial wave functions will be implemented used as references. Second, we want to use the developed software to study quantum dots. An important part of this is to provide a thorough comparison of the results obtained by the VMC method with a standard and an RBM trial wave function. We can summarize the goals in five points:

- Software development:
  - Develop a flexible VMC code.
  - Implement RBMs as trial wave functions.
- Obtaining and analyzing results:
  - Study ground state properties of quantum dots and atoms using the VMC method with a standard and an RBM trial wave function.
  - Experiment with adding selected Jastrow factors to the trial wave function.
  - Make a critical evaluation of the results obtained when using the various trial wave functions.

We believe that machine learning-based methods are the next big thing in many-body quantum mechanics. This work contributes to the rapid developing field of quantum machine learning, as we have investigated one of the many possible approaches. The results are contributions in the sense that we see how good the methods perform, but also the developed software itself is a contribution as it is open-source and can be reused and rewritten by others.

## 1.7 The developed code

There exists plenty of commercial software programs for solving the quantum many-body problem, and they are often optimized for efficiency. In general, it is wise to use already existing tools and software when doing science. First, this saves time that can be spent on other things. Second, the existing code is usually hard to compete with when it comes to efficiency. However, in our case we will investigate untraditional trial wave functions ansätze which, as far as we know, are not available in existing VMC software. Moreover, we study quantum dots which are not implemented in the most common VMC packages.

Our VMC solver is written in object-oriented C++, inspired by the example implementation developed by Ledium<sup>38</sup>, and our single-particle functions are assumed to be given in Cartesian coordinates. The goal is not to compete with the performance of commercial software, but we will still make significant efforts to develop an efficient code. As far as it is possible, all operations are vectorized using the open-source template library Eigen, which again is based on the highly optimized packages BLAS and LAPACK. We used the profiling tool Valgrind to analyze which functions that require most computer power and thus which parts of the code that should be made more efficient. Additionally, the message passing interface (MPI) lets us parallelize the code and thereby run on computer clusters. For implementation details, see chapter 9 and 10.

The outcome of this work can in its entirety be found on <https://github.com/evenmn/>, where the source code is found in the repository `VMC/src` under the MIT license<sup>39</sup>. Python scripts used for less costly operations like plotting, linear regression and symbolic integration are found in the directory `VMC/scripts`, and all the scripts that we refer to throughout the thesis can be found there. We also provide the raw data, including electron density source files, energy expectation value files, files containing final parameters and the raw slurm output files from the Abel computer cluster in Ref. [40].

## 1.8 Structure of the thesis

This thesis is divided into six parts, where each part again is divided into respective chapters. Part I presents the quantum theory, includes an introduction (chapter 2), discussion of many-body quantum mechanics (chapter 3) and detailed about the systems we have investigated (chapter 4). Thereafter, the machine learning theory is addressed in Part II, where the supervised learning (chapter 5) is used as a motivation for the Boltzmann machines (chapter 6). The method is described in Part III, and the actual implementation, with focus on efficiency, flexibility and readability, is detailed in Part IV. Part V aims the presentation and discussion of the results, and lastly, we summarize the work and observations in Part VI.

Items that are relevant, but do not belong to the main text are moved to the appendix. This includes derivation of natural units (appendix A), derivation of a general restricted Boltzmann machine with Gaussian-binary units (appendix B) and an extended collection of results (appendix C).



**Part I**

**Quantum Theory**



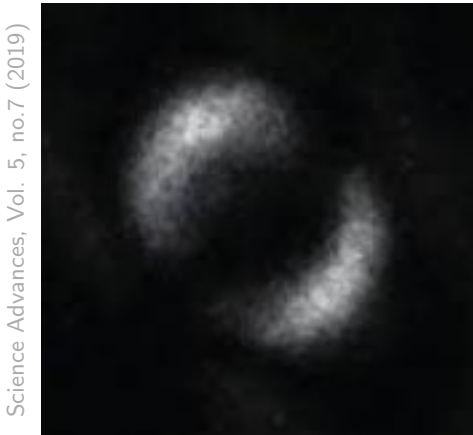
## CHAPTER 2

# Preliminary Quantum Mechanics

I do not like it, and I am sorry I ever had anything to do with it.

---

Erwin Schrödinger,<sup>41</sup>



Science Advances, Vol. 5, no. 7 (2019)

**Figure 2.1:** The first ever image of quantum entanglement, where two groups of particles share the physical state  $\Psi(\mathbf{x})$ , was published by Moreau *et al.*<sup>42</sup> with the title *Imaging Bell-type nonlocal behavior* in 2019.

Quantum theory is a fundamental theory that describes nature at the smallest scales, typically used to explain the behavior of atoms and subatomic particles. Although the theory in principle holds for systems containing a large number of particles as well, the calculations become both comprehensive and expensive as the system size increases, and exact computations are therefore reserved for small systems. When performing calculations of larger systems, we need in practice to rely on approximative estimates. As the size of the system increases, it quickly becomes infeasible to make accurate computations due to rapidly increasing complexity.

In the most general form, the theory is based on the time-dependent Schrödinger equation,

$$i\hbar \frac{\partial}{\partial t} |\Psi(\mathbf{x}, t)\rangle = \hat{\mathcal{H}} |\Psi(\mathbf{x}, t)\rangle, \quad (2.1)$$

which describes the state, or the wave function,  $\Psi(\mathbf{x}, t)$ , of a system with Hamiltonian  $\hat{\mathcal{H}}$ . The coordinate, as a common term for the position and the spin, is specified by  $\mathbf{x} = \{\mathbf{r}, \sigma\}$ ,  $\hbar$  is the

reduced Planck's constant and  $i$  is the solution of the equation  $x^2 = -1$ . As we later will see, the quantum mechanical system is entirely specified by the wave function, so by solving the Schrödinger equation we can find all the information about the system.

Schrödinger<sup>43</sup> introduced the now-called Schrödinger equation, (2.1), in 1926 as one of many contributions to the quantum mechanics at that time. Other contributors include Born<sup>44</sup> who suggested the now-standard interpretation of the probability density function as  $|\Psi(x, t)|^2$  in 1926 and Heisenberg<sup>45</sup>, who formulated the matrix mechanics representation in 1925. However, many physicists were skeptical about the new theory, including Albert Einstein and Schrödinger himself. The theory differed from classical mechanics in the sense that it was based on a statistical interpretation, with some strange consequences. For instance, the theory allowed particles to *go through* a potential wall, known as quantum tunneling. Later, Einstein<sup>46</sup> also pointed out that when pairs or groups of particles are generated in ways such that the wave function of each particle cannot be described independently of the other state, they will be affected by each other even at large distances. He called this "*spooky action at a distance*", and used the observation to argue that the quantum theory had to be incorrect. However, the observation was later proven to be correct and as late as in 2019 the first image of quantum entanglement, as the phenomenon is called, was captured by Moreau *et al.*<sup>42</sup>, presented in figure (2.1).

Today, there is wide agreement in the physics society on the quantum theory. Actually, the theory is the most precisely tested theory in the history of science, where computed observable of atoms agree perfectly with experiments. Most notably, quantum electrodynamical calculations of the fine structure constant  $\alpha$  are, by Odom *et al.*<sup>9</sup>, found to agree with experiments within ten parts in a billion.

In this chapter, we will first state the postulates of quantum mechanics, and thereafter we discuss the time-independent Schrödinger equation and challenges encountered when solving it. As we will see, every observable in quantum mechanics is associated with an operator. Consequently, all obtained values are identified with standard errors which are also important to specify in order to present the accuracy of the value.

Next we discuss the variational principle, which states that the ground state energy is the lowest possible energy calculated, so by minimizing the energy in a variational scheme, a ground state energy estimation can be obtained. We also provide a brief overview of the quantum numbers, which are the values that give acceptable solutions to the Schrödinger equation, and the virial theorem, which relates kinetic and potential energy.

Because quantum mechanics will make up the framework for this work, we will in this chapter only discuss the theory needed for the work, making it unsuitable as an encyclopedia to quantum mechanics. For a complete introduction to the topic, *Introduction to Quantum Mechanics* written by Griffiths<sup>47</sup> serves as an excellent read. Before we get started, we make a few assumptions in order to simplify our problem. The most important assumptions are specified below with an explanation of why they are valid.

- **Point-like particles:** For all practical purposes, our length scales are much larger than the assumed radius of electrons and protons. Treating the electrons and protons as points-like particles is therefore a good approximation.
- **Non-relativistic spacetime:** Second, we operate in the non-relativistic spacetime, which is an excellent approximation as long as we do not approach the speed of light and we do not involve the strong nuclear force. Applying classical physics, we can find that the speed of the electron in a hydrogen atom is about 1% of the speed of light. Even though the electrons achieve higher velocities in heavy atoms, we do not need to worry about it as we will stick to the lighter atoms. In the quantum dots, this assumption holds even for large systems, as the velocity and density will still be sufficiently low.

- For specific systems, we might make new assumptions and approximations. For instance, for atomic systems, we will assume that the nucleus is at rest. These approximations will be discussed consecutively.

## 2.1 The postulates of quantum mechanics

Quantum mechanics is characterized by a set of fundamental axioms that make up the base of the theory. As we assume that they always hold, every statement in quantum mechanics is based on them, and it is natural to list them here in the beginning. The postulates can be formulated in six points:

1. "The state of a quantum mechanical system is completely specified by the wave function  $\Psi(x, t)$ ."
2. "To every observable in classical mechanics, there is a corresponding a linear, Hermitian operator in quantum mechanics."
3. "In any measurement of the observable associated with an operator  $\hat{O}$ , the only values that will ever be observed are the eigenvalues  $o$  which satisfy  $\hat{O}\Psi(x, t) = o\Psi(x, t)$ ."
4. "The expectation value of the observable corresponding to operator  $\hat{O}$  is given by

$$\langle \hat{O} \rangle = \frac{\int dx dt \Psi^*(x, t) \hat{O} \Psi(x, t)}{\int dx dt \Psi^*(x, t) \Psi(x, t)}. "$$

5. "The wave function evolves in time according to the time-dependent Schrödinger equation,

$$\hat{\mathcal{H}}\Psi(x, t) = i\hbar \frac{\partial \Psi(x, t)}{\partial t}. "$$

6. "The total wave function must be anti-symmetric concerning the interchange of all coordinates of one fermion with these of another. Electronic spin must be included in this set of coordinates."

All the postulates will be used in this work, and they will be described in detail when we need them. Even though we will look at stationary states only, even the time-dependent Schrödinger from the fifth postulate will be discussed due to the description of the diffusion Monte Carlo method in section 7.4. The other postulates will be covered in the current and the next chapter. The formulation of the presented postulates are taken from Ref. [48].

## 2.2 The Schrödinger equation

We have already presented the time-dependent Schrödinger equation on several occasions, but as mentioned above, we will in this work study stationary systems only. If we also recall that the particles are assumed to be non-relativistic, the focus will be on solving the time-independent non-relativistic Schrödinger equation. By defining  $\Psi_n(x)$  as the wave function of a state  $n$  with energy  $E_n$ , the equation can be expressed as

$$\hat{\mathcal{H}}\Psi_n(x) = E_n\Psi_n(x), \quad (2.2)$$

where  $\hat{\mathcal{H}}$  is the aforementioned Hamiltonian, the total energy operator. By analogy with the classical mechanics, the total mechanical energy is the kinetic and potential energy summed,

$$\hat{H} = \hat{T} + \hat{V}, \quad (2.3)$$

with  $\hat{T}$  and  $\hat{V}$  as the kinetic and potential energy operators, respectively.

In classical mechanics, the kinetic energy of a moving particle of mass  $m$  is  $T = p^2/2m$  where  $p$  is the (linear) momentum, the quantized kinetic energy operator can be represented as

$$\hat{T} = \frac{\hat{p}^2}{2m}, \quad (2.4)$$

according to Ehrenfest's theorem<sup>49</sup> and the second postulate. The momentum operator is  $\hat{p} = -i\hbar\hat{\nabla}$  with  $\hat{\nabla}$  as the differential operator and the factor  $i\hbar$  arising from the canonical commutator relation between the position operator and the momentum operator,

$$[\hat{x}, \hat{p}] = \hat{x}\hat{p} - \hat{p}\hat{x} = i\hbar, \quad (2.5)$$

which indicates that the momentum and the position do not *commute*, and that the order of the operators in an equation is not arbitrary.

The potential depends on the system we want to study. For atomic systems, the potential as a function of the nucleus-electron distance can be found from Coulomb's law and reads

$$V(r) = \frac{1}{4\pi\epsilon_0} \frac{Ze^2}{r}. \quad (2.6)$$

In this expression, the nucleus is assumed to be at rest at the origin,  $k_e = 1/4\pi\epsilon_0$  is the Coulomb constant,  $Z$  is the atomic number of the nucleus, and  $e$  is the elementary charge. For a general potential, the Hamiltonian can be expressed as

$$\hat{\mathcal{H}} = -\frac{\hbar^2}{2m} \nabla^2 + V(r). \quad (2.7)$$

By setting up equation (2.2) with respect to the energies, we obtain an integral,

$$E_n = \frac{\int d\mathbf{x} \Psi_n^*(\mathbf{x}) \hat{\mathcal{H}} \Psi_n(\mathbf{x})}{\int d\mathbf{x} \Psi_n^*(\mathbf{x}) \Psi_n(\mathbf{x})}, \quad (2.8)$$

which according to the 4th postulate can be difficult to solve. For almost\* all many-electron systems, this becomes analytically infeasible due to a two-body interaction term. This will be covered in chapter 3.

As suggested by Max Born<sup>44</sup>, we get the probability density function if we take the dot product between the complex conjugate wave function and the wave function itself,

$$P(\mathbf{r}) = \Psi_n^*(\mathbf{x}) \Psi_n(\mathbf{x}) = |\Psi_n(\mathbf{x})|^2, \quad (2.9)$$

so the denominator in equation (2.8) is basically the integral over all the probabilities. If the wave function is normalized correctly, this should always give 1. As a very brief example, we will below calculate the binding energy of the hydrogen atom.

---

\*Exceptions include quantum dots of two electrons in two and three dimensions, where Taut has presented semi-analytical energies for a few oscillator frequencies<sup>50,51</sup>.

### 2.2.1 The hydrogen atom

We presented the one-particle Hamiltonian in equation (2.7), and the potential from the nucleus in equation (2.6). By introducing the Bohr radius,

$$a_0 = \frac{4\pi\epsilon_0\hbar^2}{m_e Ze^2}, \quad (2.10)$$

we can set up the total Hamiltonian as

$$\hat{\mathcal{H}} \cdot \frac{(4\pi\epsilon_0)^2\hbar^2}{m_e Z^2 e^4} = -\frac{1}{2}a_0^2 \nabla^2 - \frac{a_0}{r}, \quad (2.11)$$

where we have multiplied all the terms by the factor  $(4\pi\epsilon_0)^2\hbar^2/m_e Z^2 e^4$  in order to make the equation dimensionless. We can further scale the energy as  $E \leftarrow E \cdot (4\pi\epsilon_0)^2\hbar^2/m_e Z^2 e^4$  and the distance as  $r \leftarrow r/a_0$ , which both are dimensionless, and obtain the Hamiltonian

$$\hat{\mathcal{H}} = -\frac{1}{2}\nabla^2 - \frac{1}{r}, \quad (2.12)$$

where all quantities are in Hartree atomic units.

The hydrogen ground state wave function is well-known and reads

$$\Psi(r) = \frac{1}{\sqrt{\pi}}e^{-r} \quad (2.13)$$

in atomic units. The binding energy in Hydrogen is found from the Schrödinger equation in equation (2.2), and gives

$$\hat{\mathcal{H}}\Psi(r) = \left( -\frac{1}{2}\nabla^2 - \frac{1}{r} \right)\Psi(r) = -\frac{1}{2}\Psi(r), \quad (2.14)$$

indicating that  $E_0 = -0.5$ .

## 2.3 The variational principle

In the equations above, the presented wave functions are assumed to be the exact eigenfunctions of the Hamiltonian. However, often we do not know the exact wave functions, and we need to guess what the wave functions might be. In these cases, we apply the variational principle, which states that only the exact ground state wave function can give the ground state energy. All other wave functions that fulfill the required properties (see section 3.2) give higher energies, and mathematically we can express the statement as

$$E_0 \leq \langle \Psi | \hat{\mathcal{H}} | \Psi \rangle, \quad (2.15)$$

where  $\Psi$  is an arbitrary wave function. The variational method is a way of estimating the energy ground state, which is based on the variational principle. Most notably, the variational Monte Carlo method is named after the principle and attempts to solve the integrals directly by varying a trial wave function. The variational principle ensures that the obtained energy never goes below the ground state energy, as further described in chapter 7.

## 2.4 Quantum numbers

Unlike in classical mechanics, all the observable in quantum mechanics are discrete or *quantized*, which means that the energy can only take discrete values. The possible numbers, called quantum numbers, are always associated with the degrees of freedom. The first quantum number,  $n$ , is the principal quantum number and can take positive integers. We also have other quantum numbers identified with the angular momentum and spin as described below.

### Principal

The **principal** quantum number describes the electron shell, and can take all positive integers,  $n \in [1, 2, 3, \dots]$ . As  $n$  increases, the electron excites to a higher shell such that also the energy increases. In general,  $E_1 < E_2 < E_3 \dots$  as long as all other quantum numbers are fixed. The electron shells can again be split up in subshells, requiring more quantum numbers.

### Angular

An electron shell can possibly have more than one subshell, described by the **angular** quantum number  $l$ .  $l$  can take all non-negative integers up to  $n$ ,  $l \in [0, 1, \dots, n - 1]$ , such that the subshell degeneracy in a shell is simply  $n$ . In atoms, the angular quantum number describes the shape of the shell, where  $l = 0$  gives a spherical shape,  $l = 1$  gives a polar shape while  $l = 2$  gives a cloverleaf shape.

### Magnetic

We also have a **magnetic** quantum number,  $m_l$ , which has the range  $-l, -l + 1, \dots, l - 1, l$ . If  $l$  describes the shape of a shell,  $m_l$  specifies its orientation in space. This quantum number was first observed under the presence of a magnetic field, hence the name.

### Spin

The **spin** quantum number,  $s$ , gives the spin of a particle, which can just be seen as a particle's property. Particles are often classified into two groups depending on the spin because of their different behavior: **bosons** have integer spin, while **fermions** have half-integer spin. Electrons and protons have spin  $s = 1/2$ , making them fermions.

### Spin projection

The last number we will discuss is the **spin projection** quantum number  $m_s$ . It has the range  $-s, -s + 1, \dots, s - 1, s$ , and is therefore related to the spin quantum number in the same way as the magnetic number  $m_l$  is related to the angular number  $l$ . Electrons can for that reason take the values  $m_s = +1/2$  or  $m_s = -1/2$ , such that there are two groups of electrons. The consequences will be discussed in the section 3.2.

## 2.5 The virial theorem

The virial theorem relates the kinetic energy to the potential energy, and makes it possible to find the (time) average of the kinetic energy even for complex systems. The classical statement

of the theorem was formulated during the 19th century and named by Clausius<sup>52</sup> in 1870. It is in the most general form given by

$$\langle \hat{T} \rangle = -\frac{1}{2} \sum_{i=1}^N \langle \mathbf{F}_i \cdot \mathbf{r}_i \rangle_t, \quad (2.16)$$

where  $\mathbf{F}_i$  represents the force on particle  $i$  at position  $\mathbf{r}_i$ . The quantum mechanical version was proven by Fock<sup>53</sup> in 1930, where the expectation value of the force is represented with  $d\langle p \rangle / dt$ . For potential sources in the form of  $V_i = ar^{n_i}$ , we can use Ehrenfest's theorem<sup>49</sup> to express the virial theorem in a simpler fashion,

$$2\langle \hat{T} \rangle = \sum_i n_i \langle \hat{V}_i \rangle. \quad (2.17)$$

The same expression can be found in classical physics as well, using the relation  $\mathbf{F} = -\nabla V$ . The virial theorem requires that the system is in a bound state. An example of a system that does not fulfill the requirements, is a comet that has enough kinetic energy to escape a planet's gravitational field.

On the other hand, the hydrogen atom, discussed in section 2.2.1, satisfies the virial theorem as the potential is in the form of  $V(r) \propto r^{-1}$  and the electron is bound. For that particular case, the virial theorem reads  $2\langle \hat{T} \rangle = -\langle \hat{V} \rangle$ , resulting in  $E = \langle \hat{V} \rangle / 2$ .

It is also important to emphasize that the expectation value discussed above is, in principle, the time average of the operator. However, if the ergodic hypothesis holds for the system, i.e. the ensemble average is equal to the time average, an ensemble average can also be taken<sup>54</sup>.



## CHAPTER 3

# Many-body Quantum Mechanics

We have to remember that what we observe is not nature in itself but nature exposed to our method of questioning.

---

Werner Heisenberg,<sup>55</sup>

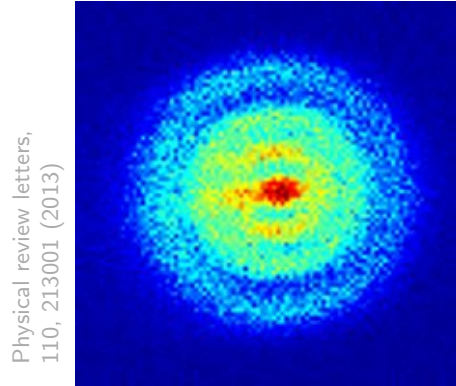


**Figure 3.1:** The first photograph of a hydrogen atom was captured by an ultra sensitive camera in 2013. One can actually see the probability distribution  $|\Psi(x)|^2$  with the naked eye. Published by Stodolna *et al.*<sup>56</sup> with the title *Hydrogen atoms under magnification*.

In the previous chapter, quantum mechanics of single particles was discussed. We presented the time-independent Schrödinger equation, and from that, we obtained a general expression for the energy of a stationary particle. The energy expression of a stationary many-particle system is almost identical and given by

$$E_n = \langle \Psi_n(\mathbf{X}) | \hat{\mathcal{H}} | \Psi_n(\mathbf{X}) \rangle \quad (3.1)$$

where we have used the dirac formalism<sup>112</sup>. However, here we use the many-body wave function  $\Psi_n(\mathbf{X})$  of state  $n$  with  $\mathbf{X} = \{x_1, x_2, \dots, x_N\} = \{\{r_1, \sigma_1\}, \{r_2, \sigma_2\}, \dots, \{r_N, \sigma_N\}\}$  denoting the collective coordinates, again including the positions and spins, of all the  $N$  particles in the system. The Hamiltonian,  $\hat{\mathcal{H}}$ , defines the system and is given explicitly in the next section. As noted before, the wave function of large systems needs to store an immense amount of information and is therefore impractical or even impossible to deal with. In this section, we will first look at how the many-body Hamiltonian is composed, before we have an extensive discussion of how the many-body wave function is constructed.

### 3.1 The electronic Hamiltonian

We have already seen what the one-body Hamiltonian looks like, and the many-body Hamiltonian is not very different. We recall that it can be split in a kinetic and a potential term,

$$\hat{H} = \hat{T} + \hat{V}, \quad (3.2)$$

where  $\hat{T}$  is the kinetic energy and  $\hat{V}$  is the potential energy. Nevertheless, as we study electrons, they are charged and will therefore interact with each other. For that reason, we need to add an interaction term to the Hamiltonian, which in general is included in the potential term  $\hat{V} = \hat{V}_{\text{ext}} + \hat{V}_{\text{int}}$  with  $\hat{V}_{\text{ext}}$  as the external potential and  $\hat{V}_{\text{int}}$  as the interaction potential. In the same way as the nucleus-electron potential, the interaction potential is given by Coulomb's law, for two electrons given by

$$\hat{V}_{\text{int}} = k_e \frac{e^2}{r_{12}}, \quad (3.3)$$

where  $r_{12}$  is the distance between the electrons. For a general system containing  $N$  electrons, the total Hamiltonian can therefore be expressed as

$$\hat{\mathcal{H}} = - \sum_{i=1}^N \frac{\hbar^2}{2m_e} \nabla_i^2 + \sum_{i=1}^N V_{\text{ext}}(x_i) + \sum_{i=1}^N \sum_{j>i}^N k_e \frac{e^2}{r_{ij}}, \quad (3.4)$$

without specifying the external potential,  $V_{\text{ext}}$ . The relative distance between particles  $i$  and  $j$  is defined by  $r_{ij} \equiv |\mathbf{r}_i - \mathbf{r}_j|$ . From now on, we will use atomic units setting  $\hbar = m_e = k_e = e = 1$ , see appendix A for details.

By inserting the Hamiltonian in equation (3.4) into equation (3.1), the integral can be split in three terms,

$$E_n = \sum_{i=1}^N \left[ -\frac{1}{2} \langle \Psi_n(\mathbf{X}) | \nabla_i^2 | \Psi_n(\mathbf{X}) \rangle + \langle \Psi_n(\mathbf{X}) | V_{\text{ext}}(x_i) | \Psi_n(\mathbf{X}) \rangle + \sum_{j>i}^N \langle \Psi_n(\mathbf{X}) | \frac{1}{r_{ij}} | \Psi_n(\mathbf{X}) \rangle \right], \quad (3.5)$$

where the two former terms are the one-body integrals, or *matrix elements*, which in many cases can be solved analytically. However, the last term is often difficult to solve, and in fact there are analytical solutions available for the two-particle case only. In other words, a precise evaluation of this integral can usually only be found using numerical methods, which we will take a closer look at in chapter 7 in conjunction with quantum Monte Carlo methods.

### 3.2 The many-body wave function

By the first postulate of quantum mechanics presented in section 2.1, the wave function contains all the information specifying the state of the system. This means that all observables in classical mechanics can in principle also be estimated from the wave function, implying that finding the wave function is the main goal. As discussed in chapter 2, we can define the wave function for a single particle, known as the *single-particle function* (SPF),  $\psi(\mathbf{r}, \sigma)$ . Can we combine the SPFs of the electrons in a system and obtain the many-body wave function? Possibly, the most straightforward way of doing this is to simply multiply all the SPFs,

$$\Psi(\mathbf{X}) = \psi(\mathbf{r}_1, \sigma_1) \psi(\mathbf{r}_2, \sigma_2) \cdots \psi(\mathbf{r}_N, \sigma_N), \quad (3.6)$$

known as the *Hartree product*. However, this product is generally not correct, as it does not include the required symmetry properties of the many-body wave function. Instead, we can

account for the symmetry by expressing the many-body wave function as a determinant or a permanent, as we will see in section 3.2.2. Together with the symmetry properties, there is an array of requirements the wave function needs to meet in order to be physically correct. Some of them are:

1. **Normalizability:** The wave function needs to be normalizable in order to make physical sense. The total probability should always be 1, and a wave function that cannot be normalized will not have a finite total probability. The consequence is that the wave function goes to zero when the positions get large,  $\Psi(x \rightarrow \pm\infty) \rightarrow 0$ .
2. **Cusp condition:** From electrostatics, we know that identical, charged particles will repulse each other. This means that the probability of finding two particles close together should be low, which needs to be included in the wave function. The reduction of the wave function due to an electron-electron pair is called an electron-electron cusp. Also nucleon-electron pairs and nucleon-nucleon pairs cause wave function cusps, and they are all subject to the cusp condition.
3. **Symmetry and anti-symmetry:** The wave function needs to be either symmetric or anti-symmetric under the exchange of two coordinates, depending on whether the electrons are fermions or bosons. This is the statement of the sixth postulate, which will be further explained in the next section.

### 3.2.1 Anti-symmetry and the Pauli principle

Symmetry and anti-symmetry are central concepts in quantum mechanics, and often one can use symmetry arguments to simplify expressions and calculations. Assume that we have a permutation operator,  $\hat{P}(i \rightarrow j)$ , which exchanges the coordinates of the particles  $i$  and  $j$  in the many-body wave function. With  $M$  particles, the mathematical operation can be described by

$$\hat{P}(i \rightarrow j)\Psi_n(x_1, \dots, x_i, \dots, x_j, \dots, x_M) = p\Psi_n(x_1, \dots, x_j, \dots, x_i, \dots, x_M), \quad (3.7)$$

where  $p$  is the eigenvalue coming from the transformation. If we again apply the  $\hat{P}$  operator, we should switch the same coordinates back, and we expect to end up with the initial wave function. For that reason,  $p$  must be either +1 or -1 \*. The particles that have an anti-symmetric wave function under the exchange of two coordinates are called fermions, named after Enrico Fermi, and as discussed before, they have half-integer spin. On the other hand, the particles that have a symmetric wave function under the exchange of two coordinates are called bosons, named after Satyendra Nath Bose, and have integer spin. A consequence of the anti-symmetric wave function is that two identical fermions cannot occupy the same single-particle state, known as the Pauli principle. This means that identical fermions even in the many-particle ground state (at zero temperature) spread over multiple states, and in the next section, we will see how this principle is included in the wave function through a Slater determinant.

### 3.2.2 The Slater determinant

For a system of many particles, we can define a many-body wave function, which is a composition of all the SPF's and contains all the information about the system as the 1st postulate requires. For fermions, we need to combine the SPF's such that the Pauli principle is fulfilled at all times, which can be accomplished by a determinant.

---

\* Actually, in two-dimensional systems a third possibility is allowed which gives an *anyon*. The theory on this was developed by Leinaas & Myrheim<sup>57</sup> during the 1970s.

Consider a system of two identical fermions with SPF $s \psi_1(\mathbf{r}, \sigma)$  and  $\psi_2(\mathbf{r}, \sigma)$  of coordinates  $\{\mathbf{r}_1, \sigma_1\}$  and  $\{\mathbf{r}_2, \sigma_2\}$ , respectively. The way we define the many-body wave function is then

$$\begin{aligned}\Psi(\mathbf{X}) &= \frac{1}{\sqrt{2}} \begin{vmatrix} \psi_1(\mathbf{r}_1, \sigma_1) & \psi_2(\mathbf{r}_1, \sigma_1) \\ \psi_1(\mathbf{r}_2, \sigma_2) & \psi_2(\mathbf{r}_2, \sigma_2) \end{vmatrix}, \\ &= \frac{1}{\sqrt{2}} [\psi_1(\mathbf{r}_1, \sigma_1)\psi_2(\mathbf{r}_2, \sigma_2) - \psi_2(\mathbf{r}_1, \sigma_1)\psi_1(\mathbf{r}_2, \sigma_2)],\end{aligned}\quad (3.8)$$

which is zero if the particles happen to have the same quantum numbers. If the particles, on the other hand, have different spins, they are allowed to appear at the same spatial state at the same time and the determinant will not equate to zero. For larger systems, the Slater determinant is constructed in the same way as above, and any pair of identical particles located in the same state will make the determinant collapse. A Slater determinant containing  $N$  electrons reads

$$\Psi(\mathbf{X}) = \frac{1}{\sqrt{N!}} \begin{vmatrix} \psi_1(\mathbf{r}_1, \sigma_1) & \psi_2(\mathbf{r}_1, \sigma_1) & \cdots & \psi_N(\mathbf{r}_1, \sigma_1) \\ \psi_1(\mathbf{r}_2, \sigma_2) & \psi_2(\mathbf{r}_2, \sigma_2) & \cdots & \psi_N(\mathbf{r}_2, \sigma_2) \\ \vdots & \vdots & \ddots & \vdots \\ \psi_1(\mathbf{r}_N, \sigma_N) & \psi_2(\mathbf{r}_N, \sigma_N) & \cdots & \psi_N(\mathbf{r}_N, \sigma_N) \end{vmatrix}, \quad (3.9)$$

where the  $\psi(\mathbf{r}, \sigma)$  is the tensor product between the radial part  $\phi(\mathbf{r})$  and the spin part  $\xi(\sigma)$ ,

$$\psi(\mathbf{r}, \sigma) = \phi(\mathbf{r}) \otimes \xi(\sigma). \quad (3.10)$$

In section 9.3.3, we show that the Slater determinant can be split in a spin-up and a spin-down part with the assumption that the Hamiltonian is spin-independent. From this, it follows that the spin-dependency,  $\xi(\sigma)$ , can be omitted. For that reason, we can define a basis set depending on the spatial coordinates only.

As a side note, we will in the rest of this thesis use  $\Psi$  as the many-particle wave function,  $\psi$  are the SPF $s$ , and  $\phi$  is the spatial part of the SPF. We reserve  $\xi$  for the spin part of the SPF $s$ , but it will often be omitted as the spin-part can be factorized out of the wave function. Sometimes it is appropriate to split up the many-particle wave function, and we will, in that case, denote each part by  $\Psi_i$  where  $i$  is an index associated with the particular element. Lastly, the basis functions will be denoted by  $\varphi$ , which we will discuss in the next section.

### 3.2.3 Basis set

In quantum chemistry, a basis set usually refers to a set of one-particle functions used to build the SPF $s$  discussed above. The basis functions depict the eigenstates of atoms, and are therefore often called *atomic orbitals*. On the other hand, the SPF $s$  are linear combinations of the atomic orbitals suited for describing the the wave-like behavior of an electron in a molecule, hence named *molecular orbitals*. Commonly used atomic orbitals are Pople basis sets<sup>58</sup> (in the form of x-yz G), correlation-consistent basis sets<sup>59</sup> (in the form of cc-pVNZ) and Slater-type orbitals<sup>60</sup> (in the form of STO-nG), where all are built on Gaussian functions. Gaussian functions are preferred as they allow efficient implementations of post Hartree-Fock methods, defined as the methods developed to improve on the Hartree-Fock method.

In our work, however, the molecular orbitals correspond to the basis functions, as we in most of the cases do not expand our SPF $s$ ,  $\psi(\mathbf{r}, \sigma)$ , in a basis set. Our SPF $s$  are typically the solution of the non-interacting system, and as the Jastrow factor is supposed to deal with the interaction, we use the same functions for the interacting case as well.

A common notation is to use the Greek letter  $\varphi$  for the atomic orbitals and  $\psi$  for the molecular orbitals, such that single-particle functions can be obtained from an expansion of the  $N$  basis

functions  $\{\varphi_1(\mathbf{r}), \varphi_2(\mathbf{r}), \dots, \varphi_N(\mathbf{r})\}$  in the manner of

$$\psi_i(\mathbf{r}) = \sum_{j=1}^N c_{ji} \varphi_j(\mathbf{r}), \quad (3.11)$$

where  $c_{ij}$  are the coefficients to be found. There are different approaches to obtain these coefficients, where the popular Hartree-Fock algorithm generates  $c_{ij}$ 's in order to find the optimal Slater determinant. For a larger basis, the results will be more accurate, but at an increasing computational cost<sup>13</sup>. The actual functions used in this work are presented in chapter 4 and they are linked to their respective systems.

### 3.2.4 Modeling the cusp

According to Coulomb's law, particles of the same charge repeal each other, and particles of opposite charge attract each other. For an interacting system, this will affect the wave function. An electron-electron pair causes a pit in the wave function, while a electron-nucleon pair causes a peak in the wave function. These interaction-caused shapes of the wave functions are called cusps, and are subject to the cusp condition. In general, it provides a relation between the wave function and the slope of the wave function when we approach the cusp,

$$\left. \frac{\partial \Psi(\mathbf{R})}{\partial r_{\alpha\beta}} \right|_{r_{\alpha\beta}=0} = \Psi(\mathbf{R}) f(r_{\alpha\beta}) \quad (3.12)$$

where  $r_{\alpha\beta}$  is the distance between two particles  $\alpha$  and  $\beta$ , and  $f(r_{\alpha\beta})$  is a function dependent on the particles types<sup>61</sup>.

Different methods address this challenge in different ways. The Hartree-Fock method attempts to construct an optimal single Slater determinant by expanding the molecular orbitals in atomic orbitals, like shown in equation (3.11). These coefficients can be obtained using for example the Hartree-Fock algorithm<sup>11,12</sup>. Then, we only need to deal with a Slater determinant, and as the correlations are not given explicitly, the Hartree-Fock theory is often called a mean-field theory. Further, we have post Hartree-Fock methods, like configuration interaction theory and the coupled cluster method. Both methods utilize the Hartree-Fock basis, but express the wave function as a linear combination of Slater determinants, where the correlations are determined by the coefficients<sup>13</sup>. If a sufficient number of Slater determinants are included in the linear combination, both methods are capable of providing exact results. However, since the methods are computationally intensive, this is possible only for very small systems.

The variational Monte Carlo (VMC) method, which we have implemented in this work, models the electron-electron cusp in a totally different way. We there define a *trial wave function*, which consists of one or more Slater determinants and a Jastrow factor, where the latter is assumed to account for the correlations. The Jastrow factor will be discussed further in section 7.1.2.

## 3.3 Electron density

In quantum many-body computations, the electron density is frequently calculated, and there are several reasons for that. First, the electron density can be found experimentally, such that the calculations can be benchmarked. Second, the electron density is very informative, since information about all particles can be gathered in a plot. In this work we will limit us to the

one-body density denoted by  $\rho_1(\mathbf{r}_i)$  and the two-body density denoted by  $\rho_2(\mathbf{r}_i, \mathbf{r}_j)$ . They are given by

$$\rho_1(\mathbf{r}_i) = N \int_{-\infty}^{\infty} d\mathbf{r}_1 \cdots d\mathbf{r}_{i-1} d\mathbf{r}_{i+1} \cdots d\mathbf{r}_N |\Psi(\mathbf{r}_1, \dots, \mathbf{r}_N)|^2 \quad (3.13)$$

and

$$\rho_2(\mathbf{r}_i, \mathbf{r}_j) = N \int_{-\infty}^{\infty} d\mathbf{r}_1 \cdots d\mathbf{r}_{i-1} d\mathbf{r}_{i+1} \cdots d\mathbf{r}_{j-1} d\mathbf{r}_{j+1} \cdots d\mathbf{r}_N |\Psi(\mathbf{r}_1, \dots, \mathbf{r}_N)|^2, \quad (3.14)$$

respectively. These integrals are in general difficult to solve, and they can be found analytically for just a few realistic systems. For other systems, we need to solve the integral numerically, and we will in chapter 7 describe how this can be done using Monte Carlo integration. As we cannot pinpoint a particle in quantum mechanics, i.e. it is impossible to distinguish two identical particles in any way, the electron density is the same irrespective of which particle we decide to leave out.

The density should not be normalized to unit both when it is calculated analytically and numerically, but to the number of particles, given by

$$\int_{-\infty}^{\infty} d\mathbf{r}_1 \cdots d\mathbf{r}_{i-1} d\mathbf{r}_{i+1} \cdots d\mathbf{r}_N [\rho_P(\mathbf{r}_1, \dots, \mathbf{r}_P)] = N \quad (3.15)$$

for the one-body density.

Which physical information can we read from the electron density? The one-body density, is sometimes simply referred to as the electron density. It gives the probability density of finding an electron throughout the space, and give insight about how the particles are distributed in the system. On the other hand, the two-body density becomes a two-dimensional function and is therefore often expressed as a matrix. It gives the probability density of finding an electron throughout the space, given the coordinates of another particle. It, therefore, contains information about how the particles distribute relative to each other and is essential when we want to study the pairwise interaction. In systems where the strong nucleon force is important, the three-body interactions are essential. Then, calculating the three-body density,  $\rho_3(\mathbf{r}_i, \mathbf{r}_j, \mathbf{r}_k)$ , also gives useful insight about the system. For closed-shell circular quantum dots, the radial electron density profile is often preferred as the density then also is circular and independent of the angle.

For non-interacting systems, the wave function is separable with respect to the different particles. In these cases we can easily find the electron density analytically, since the single-particle functions of the particles that we do not integrate over can be taken out of the integral. Represented by the one-body density,

$$\begin{aligned} \rho_1(\mathbf{r}_i) &= \int_{-\infty}^{\infty} d\mathbf{r}_1 \cdots d\mathbf{r}_{i-1} d\mathbf{r}_{i+1} \cdots d\mathbf{r}_N |\Psi(\mathbf{r}_1, \dots, \mathbf{r}_N)|^2, \\ &= \int_{-\infty}^{\infty} d\mathbf{r}_1 \cdots d\mathbf{r}_{i-1} d\mathbf{r}_{i+1} \cdots d\mathbf{r}_N |\Psi(\mathbf{r}_1)|^2 \cdots |\Psi(\mathbf{r}_N)|^2, \\ &= |\Psi(\mathbf{r}_i)|^2 \underbrace{\int_{-\infty}^{\infty} d\mathbf{r}_1 |\Psi(\mathbf{r}_1)|^2 \cdots}_{=1} \underbrace{\int_{-\infty}^{\infty} d\mathbf{r}_{i-1} |\Psi(\mathbf{r}_{i-1})|^2 \cdots}_{=1} \underbrace{\int_{-\infty}^{\infty} d\mathbf{r}_{i+1} |\Psi(\mathbf{r}_{i+1})|^2 \cdots}_{=1} \underbrace{\int_{-\infty}^{\infty} d\mathbf{r}_N |\Psi(\mathbf{r}_N)|^2}_{=1}, \\ &= |\Psi(\mathbf{r}_i)|^2, \end{aligned} \quad (3.16)$$

where we have assumed that the wave functions are normalized. This result has no scientific importance, but will be used to validate the implementation of the electron density in the code, see section 11.3.

### 3.3.1 Wigner crystals

A Wigner crystal is a solid phase where electrons maximize the distance to each other in order to minimize the potential energy. As Coulomb's law gives the interaction potential, the potential is minimized when the distances between the electrons are maximized. In one-dimensional systems, the electrons are thus found at discrete locations, such that they form an evenly spaced lattice. In two-dimensional systems, the Wigner crystals form triangular lattices which are known to be the configuration that maximizes the distance in a limited space, and in three-dimensional systems, the electrons form so-called body-centered cubics. The phenomenon occurs only when the potential energy dominates the kinetic energy since the electrons then are almost "at rest" and external forces are not strong enough to push the electrons close to each other.



## CHAPTER 4

# Systems

We must be clear that when it comes to atoms, language can be used only as in poetry.

---

Niels Bohr,<sup>62</sup>

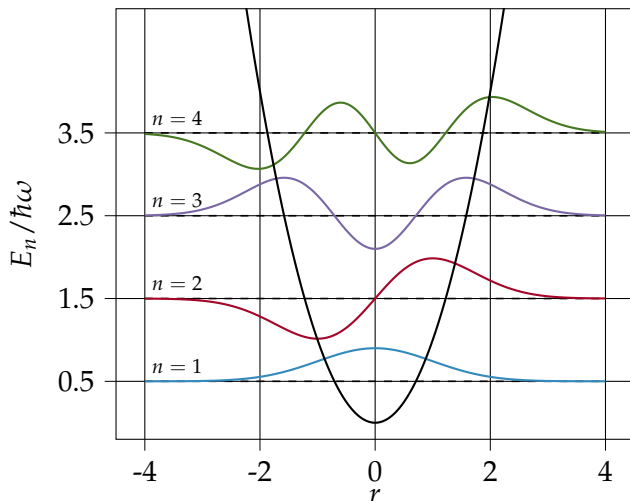


**Figure 4.1:** The harmonic oscillator potential (solid black line), with the exact single-particle wave functions, the Hermite functions, represented up to the 4th order. The quantum harmonic oscillator has many applications, be it first-order approximation of the binding potential in molecules<sup>63</sup>, lattice vibrations (phonons)<sup>64</sup> or any trapped particle.

In quantum physics, as in classical physics, there are many different systems with various complexities. If a system gets very complicated, it is often beneficial to approximate it with a simpler system, which hopefully catches the essential features in the system. Approximations of systems are especially advantageous in quantum mechanics, as just a few systems can be solved analytically. We have already seen that the atomic system can be solved analytically for the non-interacting case, and additionally harmonic systems can be solved analytically. Our circular quantum dots have a confinement represented by the harmonic potential, and for non-interacting quantum dots, we can thus also find analytical expressions.

We will in this chapter set up the explicit expressions of the Hamiltonians for the various systems and single-particle functions for various quantum mechanical systems. Although the quantum dots will be investigated in the first place, it is natural to include a brief discussion of the atomic systems as there are many common features with the quantum dots. Moreover,

double quantum dots will be covered, as one can find analytical solutions by an expansion of single quantum dot functions.

## 4.1 Quantum dots

Quantum dots are tiny systems consisting of fermions or bosons trapped in an external potential which is usually not created by a nucleus, like what we have in atomic systems. However, they have discrete electronic states with a well-defined shell structure like atoms and are therefore often called artificial atoms. In this thesis, we will study circular quantum dots with electrons confined in a harmonic oscillator potential, sometimes called Hooke's atom<sup>65</sup>.

The harmonic oscillator is often the first system that one is introduced to when attending an introductory course to quantum mechanics, for several reasons. First, many systems can be approximated with the harmonic oscillator potential, including molecular vibrations<sup>63</sup> and lattice vibrations<sup>64</sup>. Second, the harmonic oscillator behaves nicely with simple equations, and we only have a minimum, which is the global minimum. For an electron  $i$ , the external potential reads

$$V_{\text{ext}}(r_i) = \frac{1}{2}m\omega^2 r_i^2, \quad (4.1)$$

where  $m$  is the electron mass,  $\omega$  is the oscillator frequency and  $r_i$  is the relative distance from particle  $i$  to the center of the dot. Using natural units as described in Appendix B, we can write the Hamiltonian as

$$\hat{\mathcal{H}} = \sum_{i=1}^N \left( -\frac{1}{2}\nabla_i^2 + \frac{1}{2}\omega^2 r_i^2 \right) + \sum_{i < j} \frac{1}{r_{ij}}, \quad (4.2)$$

where the energy is given in units of  $\hbar$  and the lengths are scaled with respect to  $\sqrt{\hbar/m}$ . The exact solutions of the non-interacting Hamiltonian are the Hermite functions<sup>47</sup>,

$$\phi_n(x) = \frac{1}{\sqrt{2^n n!}} \cdot \left(\frac{\omega}{\hbar}\right)^{1/4} H_n(\sqrt{\omega}x) \exp(-\omega x^2/2), \quad (4.3)$$

where  $H_n(x)$  is the Hermite polynomial of  $n$ 'th degree, and the first four Hermite functions are illustrated in figure (4.1). The energy of an electron with principal quantum number  $n$  in a certain dimension is given by

$$E_n = \omega \left( n + \frac{1}{2} \right) \quad \forall \quad n \in \{0, 1, 2, \dots\}, \quad (4.4)$$

where we in multi-dimensional potentials need to summarize the contribution from all the dimensions.

We will study closed-shell systems only as the Slater determinant in that case is unambiguous, i.e, there is only one possible determinant. In open-shell systems, there are in general multiple possible Slater determinants, and the trial wave function is thus a linear combination of them. The number of particles in closed-shell systems are called magic numbers, which in two dimensions are  $N = 2, 6, 12, \dots$ . In general, the magic numbers are given by the binomial coefficients

$$N = s \binom{n+d}{d} \quad \forall \quad n \in \{0, 1, 2, \dots\}, \quad (4.5)$$

where  $s$  is the number of spin configurations (2 for electrons),  $n$  is the principal quantum number and  $d$  is the number of dimensions. This is a direct consequence of the Pauli principle, where the ground state can take two electrons with spatial single-particle functions  $\phi_{n_x=0, n_y=0}(x, y)$ , the first

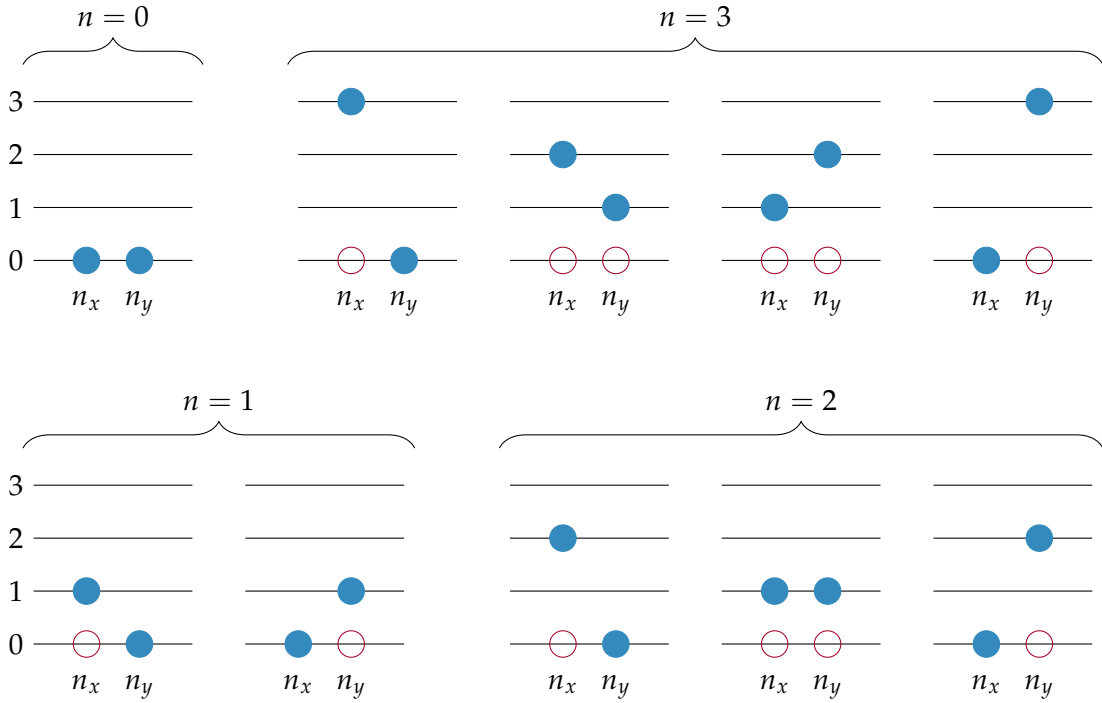


**Figure 4.2:** The possible states of a two-dimensional quantum dot for  $n = n_x + n_y = 0, 1, 2, 3$ . By recalling that an electron can take spins  $+1/2$  and  $-1/2$ , one can use this schematic to determine the maximal number of electrons in each shell and thus reveal the magic numbers.

excited energy level can take four electrons with spatial single-particle functions  $\phi_{n_x=1,n_y=0}(x, y)$  and  $\phi_{n_x=0,n_y=1}(x, y)$  with degeneracy 2 and so on. An illustration of the first few states in a two-dimensional quantum dot can be found in figure (4.2).

## 4.2 Quantum double dots

Another historically important quantum system is the double dot, which similarly to the single dot can be solved analytically. The potential of symmetrical quantum dots can in principle take a variety of different shapes, but the most used one-dimensional symmetrical potentials can be derived from the formula

$$V_i(x) = \frac{1}{2}\omega^2 \left[ |x_i|^a - \left(\frac{b}{2}\right)^a \right]^2, \quad (4.6)$$

with  $b$  as the distance between the lowest points of the wells and  $a$  as an arbitrary integer<sup>66</sup>. Setting  $a = 1$  gives two parabolic wells with a sharp local maximum at  $x = 0$ , while  $a = 2$  gives a smoother but steeper well. In figure (4.3) the potential is plotted for  $a = 1, 2$  and  $3$  and  $b = 2$ .

We have not studied this system, but it can be implemented in the code with a minimum of effort.

## 4.3 Atoms

Although we will focus on quantum dots in this work, atoms are relevant as they behave similarly to quantum dots and can be studied using the same code framework with few modifi-

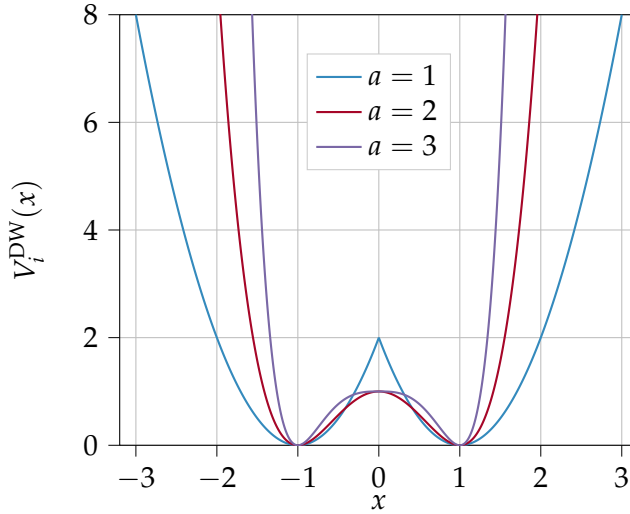


**Figure 4.3:** One-dimensional double-well potentials plotted with  $a = 1, 2$  and  $3$ , and  $b = 2$ . For  $a = 1$  the potential was multiplied with 2 to make it comparable to the others.

cations. When defining the atomic Hamiltonian, one often freezes out the nucleonic degrees of freedom, known as the Born-Oppenheimer approximation. The electrons will affect the nucleus, but due to the mass difference this effect is negligible. The external potential between the atomic nucleus and an electron at distance  $r_i$  from the nucleus is given by

$$V_{\text{ext}}(r_i) = -\frac{1}{2}k_e \frac{Ze^2}{r_i}, \quad (4.7)$$

where  $k_e$  is Coulomb's constant,  $e$  is the elementary charge and  $Z$  is the atomic number (number of protons in the nucleus). The total Hamiltonian,

$$\hat{\mathcal{H}} = \sum_{i=1}^N \left( -\frac{1}{2} \nabla_i^2 - \frac{Z}{r_i} \right) + \sum_{i < j} \frac{1}{r_{ij}}, \quad (4.8)$$

is given in Hartree atomic units which also is discussed in Appendix B. For the non-interacting case, the energy of a particle in shell  $n$  is given by the Bohr formula<sup>47</sup>

$$E_n = -\frac{Z^2}{2n^2}. \quad (4.9)$$

Additionally for this system, we need to specify a basis set to use. For atoms where the electrons do not interact, the wave functions are given by the *hydrogen-like orbitals*, which in spherical coordinates can be split in a radial part and an angular part,

$$\psi_{nlm_l}(r, \theta, \phi) = R_{nl}(r)Y_l^{m_l}(\theta, \phi), \quad (4.10)$$

where  $n$  again is the principal quantum number,  $l$  is the angular quantum number and  $m_l$  is the magnetic quantum number. Henceforth  $m_l$  will be simplified as  $m$  to make the expressions neater. We use the physicist's notation for polar coordinates, with  $\theta$  as the polar angle and  $\phi$  as the azimuthal angle.

The radial part can be presented as a function of the *associated Laguerre polynomials* or *generalized Laguerre polynomials*,  $L_q^p(x)$  and the hydrogen wave function presented in section 2.2.1,

$$R_{nl}(r) = \sqrt{\left(\frac{2Z}{n}\right)^3 \frac{(n-l-1)!}{2n[(n+l)!]}} r^l e^{-Zr/n} \left[ L_{n-l-1}^{2l+1} \left( \frac{2r}{n} Z \right) \right]. \quad (4.11)$$

**Table 4.1:** Degeneracy and naming conventions for  $l = 0, 1, 2, 3, 4$ .

Subshell label	$l$	Max electrons	Name
$s$	0	2	sharp
$p$	1	6	principal
$d$	2	10	diffuse
$f$	3	14	fundamental
$g$	4	18	alphabetic hereafter

The angular part is given by the *spherical harmonics*,

$$Y_l^m(\theta, \phi) = AP_l^m(\cos \theta)e^{im\phi}, \quad (4.12)$$

where  $P_l^m(x)$  are the *associated Legendre polynomials* and  $A$  is a normalization factor. The complex part in the spherical harmonics can be avoided by introducing the real solid harmonics instead,

$$S_l^m(\theta, \phi) \propto P_l^{|m|}(\cos \theta) \begin{cases} \cos(m\phi) & \text{if } m \geq 0 \\ \sin(|m|\phi) & \text{if } m < 0 \end{cases}, \quad (4.13)$$

such that

$$\psi_{nlm}(r, \theta, \phi) = R_{nl}(r)S_l^m(\theta, \phi). \quad (4.14)$$

The real solid harmonics do not alter any physical quantities that are degenerated in the subspace consisting of opposite magnetic quantum numbers. Alternatively, we can use a Hartree-Fock basis based on Gaussian functions, as discussed in section 3.2.3. More or less all electronic structure studies of atoms nowadays use these expansions, as they provide very precise results and high performance due to the evaluation properties of the Gaussian functions. Even though the Gaussian functions do not have the correct shape, an expansion can be fitted pretty well, as demonstrated by Hehre *et al.*<sup>67</sup>.

As for the quantum dot systems, we will study closed shells only, but for atoms, we will introduce subshells as well which are dependent on  $l$  and  $m$  in addition to the principal quantum number  $n$ . Traditionally, the first few subshells are denoted by  $s, p, d$  and  $f$ , and the meaning can be found in table (4.1), together with number of electrons in each subshell. For helium, we have two electrons with  $n = 1$ , which means that both have  $l = 0$  and both electrons are in the  $s$ -subshell, or the so-called  $s$ -wave. We can thus write the electron configuration as  $1s^2$ . Similarly to the principal quantum number  $n$ , we can use the rule of thumb that the lower  $l$ , the lower energy, such that for beryllium all four electrons are still in the  $s$ -subshell. beryllium therefore has electron configuration  $1s^22s^2$  or  $[\text{He}] 2s^2$ . Since both subshells are fully occupied, beryllium can be included in our closed-shell calculations. If we continue with the same rules, we see that the next closed-shell atom has a fully occupied  $p$ -subshell as well, which is neon with 10 electrons. This is a noble gas, and we can write the electron configuration as  $[\text{Be}] 2p^6$ . All noble gases have endings  $Xs^2Xp^6$ , which is the reason why they always have eight valence electrons.

We can now compare this to the periodic table, and observe that the first two rows agree with the theory presented above: The first row has two elements, and the second has eight. However, the third one also has eight elements, which does not fit our theory. It must be something we have overlooked. The reason is that the angular momentum contribution is not taken into account, i.e. we need to include the term,

$$V_L = \frac{l(l+1)}{2r^2}, \quad (4.15)$$

in the Hamiltonian. If we do so, we see that the rule of thumb defined above not always holds. Sometimes a low  $l$  in a higher  $n$  causes lower energy than a high  $l$  in a lower  $n$ .

## **Part II**

# **Machine Learning Theory**



## CHAPTER 5

# Supervised Learning

People worry that computers will get too smart and take over the world, but the real problem is that they're too stupid and they've already taken over the world.

---

Pedro Domingos,<sup>68</sup>

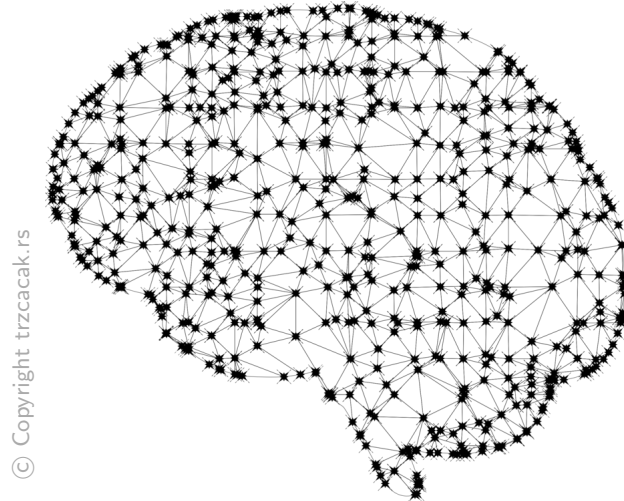


**Figure 5.1:** Artificial neural networks are inspired by neural networks in the brain. The figure is taken from [trzcacak.rs](http://trzcacak.rs).

The use of the term *machine learning* has exploded over the past years, and sometimes it even sounds like it is a new field. However, the truth is that many of the methods are relatively old. For instance, linear regression was known in the early 19th century, when Legendre<sup>69</sup> and Gauss<sup>70</sup> independently developed the concepts of mean square error (MSE). These methods have just recently been taken under the machine learning umbrella, and is one of the reasons why the term is used more frequently than before. Another essential contributor to the booming popularity is the dramatic improvement of a majority of the machine learning algorithms, most notably neural networks, as discussed in the introduction.

Unlike traditional algorithms, machine learning algorithms perform a specific task without using explicit instructions, but they use optimization tools to minimize a *cost function* and fit a model to a certain data set. As a consequence, we often do not know precisely what the

algorithms do and why they behave like they do. Because of this behavior and the fact that artificial neural networks are inspired by the human brain, the processing is often called artificial intelligence. As a definition of the term machine learning, we use the translation by Stanford University<sup>71</sup>:

**“** Machine learning is the science of getting computers to act without being explicitly programmed. **”**

In our search for a technique to solve quantum mechanical problems where less physical intuition is needed, machine learning appears as a natural tool. Firstly, machine learning algorithms are able to provide impressive results, even with absence of rules specifying what the network should do. This was, for instance, demonstrated by Silver *et al.*<sup>23</sup> who developed a chess engine which learned the rules by playing against itself thousands of times. Secondly, the fundamental goal of machine learning is to fit a model in order to minimize a cost function, which is exactly what we do when applying the popular variational Monte Carlo (VMC) method with the wave function as the model and with the energy as the cost function. However, in traditional VMC, the trial wave function is tailored to each particular system, which naturally requires a significant amount of physical intuition. Our goal is to find a trial wave function so flexible that it can approach the true wave function even with lack of physical intuition. For that, we use a restricted Boltzmann machine (RBM), an energy-based neural network. Reducing the need of physical intuition is important because the study of many urgent systems is out of reach for existing methods, due to lack of information about the wave function. Examples include bosonic systems, where expressions for two-body correlations in general are unavailable<sup>72</sup>, and nuclear systems, where three-body correlations are crucial<sup>73</sup>.

We typically classify machine learning methods as being either supervised or unsupervised, based on the way we define the cost function. Supervised models are provided with *targets*, which are outputs that the model should obtain with a certain input data set. We then define the cost function as the error between the output from the model and the targets, and the model is trained until it is able to reproduce the targets. For unsupervised models, we need to find another way to define the cost function, as they are not provided with targets. These kinds of models will be used in this work, as we in general do not have labeled data for our particular problem. In our work, we aim at constructing powerful methods for the study of the ground state of complex systems. As targets for these systems usually are unavailable, we will use unsupervised algorithms. For RBMs, the cost function is traditionally defined by a system energy which we want to minimize.

As there are many common concepts in supervised and unsupervised learning, we will in this chapter adhere to supervised learning and introduce essential concepts like artificial neurons, weights and optimization schemes. The Boltzmann machines, which are the models that we actually use in this work, are discussed in chapter 6.

Supervised learning maps an input to an output based on example input-output pairs. To functionalize this, we need to train the model such that the error between the targets and the outputs is minimized. However, this is in general not sufficient as we also want to make new predictions from the same model. The two points that need to be satisfied in supervised learning are therefore:

1. The model needs to reproduce the targets
2. The model should be able to fit future observations.

In this chapter, we will examine how to find a model that satisfies both the requirements, and challenges and possible mistakes will be covered. Subsequently, we will see that there is no

guaranty that the second point is satisfied even when the first point is satisfied. We begin by introducing the polynomial regression to explain fundamental concepts of machine learning in an intuitive way, and thereafter we generalize the theory in form of linear regression. In the end, we present neural networks which have many common features with the restricted Boltzmann machines discussed in chapter 6.

## 5.1 Polynomial regression

Polynomial regression is perhaps the most intuitive example of supervised learning, as it can be used to solve familiar problems. In general, polynomial regression finds the  $p$ 'th degree polynomial,  $f(x; c) = \sum_{i=0}^p c_i x^i$ , that fits a set of points in the best possible way with  $c$  as the coefficients or *estimators*. In two dimensions, the data set consists of some  $n$  number of  $x$ - and  $y$ -coordinates,

$$\begin{aligned}\mathbf{x} &= (x_1, x_2, \dots, x_n), \\ \mathbf{y} &= (y_1, y_2, \dots, y_n),\end{aligned}$$

henceforth denoted by  $\mathcal{D} = \{\mathbf{x}, \mathbf{y}\}$ . The data set can for instance be fitted to a second-order polynomial,

$$f(x; a, b, c) = ax^2 + bx + c, \quad (5.1)$$

where the parameters  $a$ ,  $b$  and  $c$  are our estimators. The polynomial is now our model, and by evaluating it on all values in the  $x$ -vector we obtain a set of  $n$  equations

$$\begin{aligned}\tilde{y}_1 &= ax_1^2 + bx_1 + c \\ \tilde{y}_2 &= ax_2^2 + bx_2 + c \\ \vdots &\quad \vdots \quad \vdots \quad \vdots \\ \tilde{y}_n &= ax_n^2 + bx_n + c,\end{aligned} \quad (5.2)$$

where  $\tilde{y}_i = f(x_i)$  is the output from the model with  $x_i$  as the input. What we want to do is to determine the estimators,  $a$ ,  $b$  and  $c$ , such that the mean squared error (MSE) of all these equations,

$$\min_{a,b,c} \frac{1}{n} \sum_{i=0}^{n-1} (y_i - f(x_i; a, b, c))^2, \quad (5.3)$$

is minimized. For this problem, we define the cost function,  $\mathcal{C}(\theta)$ , as the MSE, which is always the function that we want to minimize in machine learning. For our choice of model, the cost function reads

$$\mathcal{C}(a, b, c) = \frac{1}{n} \sum_{i=0}^{n-1} (y_i - (ax_i^2 + bx_i + c))^2, \quad (5.4)$$

which can be minimized in several ways. Before we proceed to the minimization, we will introduce a more general notation, where the estimators are collected in a column vector

$$\boldsymbol{\theta} \equiv (a, b, c)^T, \quad (5.5)$$

and the  $x_i^j$ 's are collected in a row vector

$$\mathbf{X}_i \equiv (x_i^2, x_i^1, x_i^0) = (x_i^2, x_i, 1). \quad (5.6)$$

By using this, the cost function can be rewritten as

$$\begin{aligned}\mathcal{C}(\boldsymbol{\theta}) &= \frac{1}{n} \sum_{i=0}^{n-1} \left( y_i - \sum_{j=0}^2 X_{ij} \theta_j \right)^2, \\ &= \frac{1}{n} \sum_{i=0}^{n-1} \left( y_i - \mathbf{X}_i \boldsymbol{\theta} \right)^2, \\ &= \frac{1}{n} (\mathbf{y} - \mathbf{X} \boldsymbol{\theta})^T (\mathbf{y} - \mathbf{X} \boldsymbol{\theta}),\end{aligned}\tag{5.7}$$

where we in the last step have collected all the vectors  $\mathbf{X}_i$  in a matrix  $\mathbf{X} = [\mathbf{X}_1, \mathbf{X}_2, \dots, \mathbf{X}_n]$ . As the minimum of the cost function with respect to an estimator  $\theta_k$  is found when the derivative is zero, we need to solve the equation

$$\begin{aligned}\frac{\partial \mathcal{C}(\boldsymbol{\theta})}{\partial \theta_k} &= \frac{\partial}{\partial \theta_k} \left( \frac{1}{n} \sum_{i=0}^{n-1} \left( y_i - \sum_{j=0}^2 X_{ij} \theta_j \right)^2 \right), \\ &= \frac{2}{n} \sum_{i=0}^{n-1} X_{ik} \left( y_i - \sum_{j=0}^2 X_{ij} \theta_j \right) = 0.\end{aligned}\tag{5.8}$$

We can go further and write it on matrix-vector form as

$$\frac{\partial \mathcal{C}(\boldsymbol{\theta})}{\partial \boldsymbol{\theta}} = \frac{2}{n} \mathbf{X}^T (\mathbf{y} - \mathbf{X} \boldsymbol{\theta}) = 0,\tag{5.9}$$

where the differentiating is done element-wise,  $\partial \mathcal{C}(\boldsymbol{\theta}) / \partial \theta_k$ . This is satisfied if and only if

$$\boldsymbol{\theta} = (\mathbf{X}^T \mathbf{X})^{-1} \mathbf{X}^T \mathbf{y},\tag{5.10}$$

which is the equation we seek to solve to find the best fitting polynomial. Before we proceed to the general case, let us take a quick look at an example.

### 5.1.1 An example on polynomial regression

In this example, we will do the polynomial regression on an actual two-dimensional data set consisting of 10 points,

$$\begin{aligned}\mathbf{x} &= (1, 2, 4, 6, 7, 9, 10, 11, 13, 16), \\ \mathbf{y} &= (15, 30, 50, 60, 65, 63, 60, 55, 40, 0),\end{aligned}\tag{5.11}$$

which is nothing else than a second-order polynomial with some noise. The data points are plotted in figure (5.2 a), and we want to fit a  $p$ 'th degree polynomial to the points. The first thing we need to realize is that in order to validate our models, we cannot use all points for the training. There is no strict rule on how much of the data set that should be used for training and validation, but at least the training data set should be larger than the validation data set. For this particular problem, we decide to leave out  $\{(1, 15), (9, 63), (10, 60)\}$  from the training, which we later will use for validation.

Furthermore, we use equation (5.10) for finding the best fitting first-, second- and sixth-order polynomials, and obtain the functions presented in table (5.1) with the respective training and prediction errors. The polynomials are also plotted in figure (5.2 b) together with the actual data points.

What we immediately observe, is that the more complex model (higher degree polynomial) we use, the lower training error we get. The polynomial of sixth-order fits the points entirely.

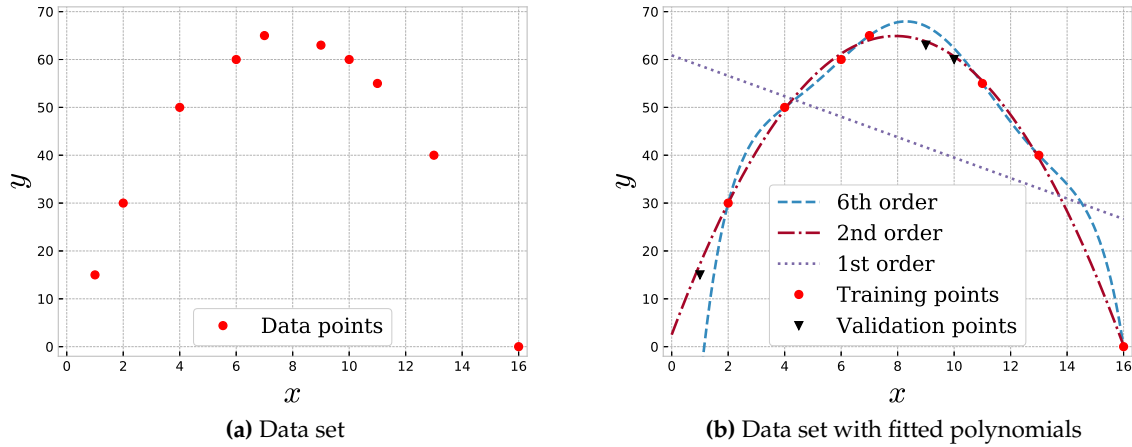


**Figure 5.2:** Figure (a) presents the data points given in equation (5.11), while the figure (b) illustrates how a first-, second- and sixth-order polynomial can be fitted to the training set in the best possible way.

**Table 5.1:** Best fitting polynomials of first-, second- and sixth-order degree to the data set in equation (5.11).  $f(x)$  gives the actual form of the polynomial, the training error is the MSE of the training data set and the prediction error is the MSE of the validation data set.

Order	$f(x)$	Training error	Prediction error
1st	$-2.14x + 60.87$	327.22	927.87
2nd	$-x^2 + 15.74x + 2.51$	0.47	2.04
6th	$-0.001x^6 + 0.04x^5 - 0.90x^4 + 9.04x^3 - 47.52x^2 + 129.74x - 98.67$	2.54E-11	187.53

The first-order polynomial performs poorly, while the second-order polynomial performs intermediately. However, when we want to predict future observations, the prediction error is more crucial than the training error as it shows the ability to reproduce unlabeled data. The prediction error of the output from the sixth-order polynomial is enormous, indicating that the polynomial is a bad fit to the data set. When a model can reproduce the training set very well, but is not able to reproduce the training set, we say that it overfits the data set. This means that the model is too complex considering the problem. On the other hand, we see that the first-order polynomial also has a significant prediction error, which means that it is not able to reproduce the validation set either. We say that it underfits the data set, indicating the need for a more complex model.

Finally, we have the second-order polynomial, which is miles ahead of its competitors when it comes to the prediction error. It turns out that the second-order model has an appropriate complexity, which we could have guessed by looking at the data points. The natural question now is "*How do we find a correct model complexity?*". The answer is that there is no easy way of doing this, which is one reason why machine learning is difficult. The trial and error method is the standard approach, where we examine various complexities and calculate the prediction error for each model. To find the prediction error precisely, one typically uses  $K$  cross-validation resampling, which evaluates  $K$  different choices of validation set to make the most use of the data. More about resampling analysis can be found in section 7.5.2. A deeper understanding of

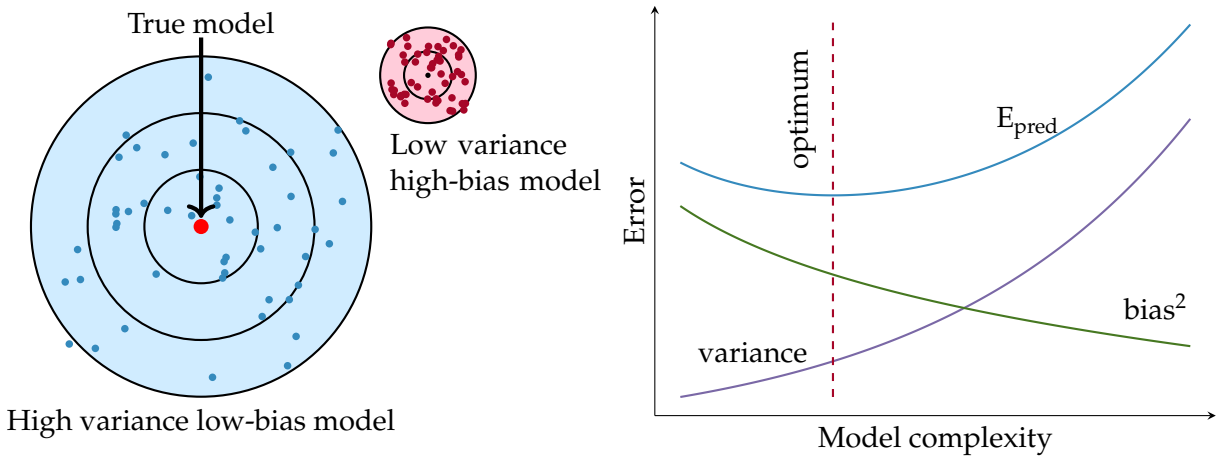


**Figure 5.3:** Illustration of the bias and variance. (Left) the predicted values of a two-dimensional high variance low-bias model (blue) and low variance high bias model (red). (Right) the bias-variance decomposition.

the prediction error and how to reveal whether a model overfits or underfits will hopefully be gained in the next section, on bias-variance tradeoff.

## 5.2 Bias-variance tradeoff

Up to this point, we have skipped some important terms in the statistics behind machine learning. First, we have the *bias*, which describes the best our model could do if we had an infinite amount of training data. We also have the *variance*, which is a measure of the fluctuations occurring due to finite sampling effects. In the left part of figure (5.3), examples of high variance low-bias and low variance high bias models are presented. What we actually want is a low variance low-bias model, but this model is normally not feasible, and we need to find the optimal tradeoff between bias and variance. This is known as the bias-variance tradeoff.

In the right part of figure (5.3), the bias-variance tradeoff is illustrated as a function of the model complexity. We observe that the prediction error is large when the model complexity is too low, which corresponds to a low variance. This substantiates what we discussed in section 5.1.1, where we claimed that a too low model complexity underfits the data set. Therefore, a too low variance is associated with underfitting. On the other side of the plot, we can see that also a too complex model causes a large prediction error, which corresponds to a low bias. As discussed before, a too complex model overfits the model, which is associated with low bias.

Ideally, we should both minimize the bias and the variance. However, since this usually is impossible, we need to find the bias and variance which corresponds to the lowest error. To see how the error is distributed between the bias and variance, we can perform a so-called bias-variance decomposition. This is easiest if we assume that the true data is generated from a noisy model,

$$y = f(x) + \epsilon, \quad (5.12)$$

where the noise,  $\epsilon$ , is normally distributed with mean zero and standard deviation  $\sigma_\epsilon$ . In that case, it can be shown that the prediction error,  $E_{\text{pred}}$ , can be decomposed in a bias part and a

variance part,

$$E_{\text{pred}} \equiv \langle \langle (y_\epsilon - \tilde{y})^2 \rangle \rangle_\epsilon = \underbrace{\sum_i (f(x_i) - \langle \tilde{y} \rangle)^2}_{\text{bias}^2} + \underbrace{\sum_i \langle (\tilde{y} - \langle \tilde{y} \rangle)^2 \rangle}_{\text{variance}} + \underbrace{\sum_i \sigma_\epsilon^2}_{\text{noise}}, \quad (5.13)$$

where the expectation values are over the data set,  $\mathcal{D}$ , if nothing else is specified. This decomposition is discussed in great detail by Mehta *et al.*<sup>74</sup>.

## 5.3 Linear regression

Polynomial regression, discussed in section 5.1, is an instance of linear regression that we introduced to motivate before we study linear regression in general. Instead of fitting a polynomial to a set of points, we can fit a general function in the form of

$$f(x_i) = \sum_{j=0}^p X_{ij}(x_i)\theta_j \quad (5.14)$$

to the points, where we have  $p+1$  estimators  $\theta_j$ . The matrix  $X$  is called the *design matrix*, and the case where  $X_{ij}(x_i) = x_i^j$  corresponds to polynomial regression, but it can in principle be an arbitrary function of  $x_i$ . The cost function for the *ordinary least square regression* (OLS) case is already found in equation (5.7), and we can recall it as

$$\mathcal{C}(\theta) = \sum_{i=1}^n \left( y_i - \sum_{j=0}^p X_{ij}\theta_j \right)^2, \quad \text{OLS} \quad (5.15)$$

which is minimized when

$$\theta = (X^T X)^{-1} X^T y. \quad (5.16)$$

To solve this equation, we need to find the inverse of the matrix  $X^T X$ , which is typically done by *lower-upper* (LU) decomposition or *singular values decomposition* (SVD). Often when dealing with large data sets, the design matrix becomes singular. A singular matrix is defined by a determinant equal to zero, making them non-invertible. Fortunately, SVD always works, and in cases where the matrix is singular, it turns out to be a good idea to perform such a decomposition. In the next section we will see why.

### 5.3.1 Singular value decomposition

Singular value decomposition is a method which decomposes an  $m \times n$  matrix,  $X$ , into a product of three matrices, written as

$$X = U \Sigma V^T, \quad (5.17)$$

where  $U$  is a unitary  $m \times m$  matrix,  $V$  is a unitary  $n \times n$  matrix and  $\Sigma$  is a diagonal  $m \times n$  matrix. This might sounds like a bad idea, but especially for singular matrices this often makes life easier. The reason for this, is that only  $\Sigma$  is singular after the decomposition. For our case, we can thus write the matrix  $X^T X$  as

$$X^T X = V \Sigma^T \Sigma V^T = V D V^T, \quad (5.18)$$

where we exploit that  $U^T U = \mathbb{1}$  and  $\Sigma^T \Sigma = D$  by definition. Further we can multiply by  $V$  on the right-hand side,

$$(X^T X)V = V D, \quad (5.19)$$

to get rid of  $V^T$ . A similar exercise can be performed on  $XX^T$ , and we will obtain

$$(XX^T)\mathbf{U} = \mathbf{U}\mathbf{D}. \quad (5.20)$$

By using the former of the two expressions, one can show that

$$\mathbf{X}\boldsymbol{\theta} = \mathbf{U}\mathbf{U}^T\mathbf{y}, \quad (5.21)$$

which is solvable even when  $\mathbf{X}^T\mathbf{X}$  is singular.

### 5.3.2 Ridge regression

Ridge regression is an extension of ordinary least square regression, introduced for two main reasons. Firstly, it is used to keep the matrix  $\mathbf{X}^T\mathbf{X}$  non-singular, and secondly, it is used to introduce regularization. The most intuitive way of avoiding singular values in the matrix, is to add values to the diagonal as a matrix with values along the diagonal is not singular. The procedure is to add the same value, the penalty  $\lambda$ , to all the diagonal elements to ensure that all the diagonal elements will get a non-zero value. Still using the matrix-vector form, this can be written as

$$\boldsymbol{\theta} = (\mathbf{X}^T\mathbf{X} + \lambda\mathbb{1})^{-1}\mathbf{X}^T\mathbf{y}, \quad (5.22)$$

where  $\mathbb{1}$  is the identity matrix. The penalty,  $\lambda$ , is a so-called *hyper-parameter*, in contrast to the estimators which are variational parameters. What distinguishes hyper-parameters from variational parameters, is that the former are specified before the training and the latter are determined throughout the training. This method is called Ridge regression, and has a cost function given by

$$\mathcal{C}(\boldsymbol{\theta}) = \sum_{i=1}^n \left( y_i - \sum_{j=0}^p X_{ij}\theta_j \right)^2 + \lambda \sum_{j=1}^p |\theta_j|^2, \quad \text{Ridge} \quad (5.23)$$

where we in principle just add the L2-norm of the estimator vector to the OLS cost function. The link between equation (5.22) and (5.23) can be easiest found by going from the latter to the former, similarly to what we did for the polynomial regression in equations (5.7-5.10).

### 5.3.3 LASSO regression

Finally, we introduce the *least absolute shrinkage and selection operator* (LASSO) regression, which in the same way as Ridge regression is based on regularization. Instead of adding the L2-norm of the estimator matrix, we add the the L1-norm,  $|\theta_j|$ , and the cost function expresses

$$\mathcal{C}(\boldsymbol{\theta}) = \sum_{i=1}^n \left( y_i - \sum_{j=0}^p X_{ij}\theta_j \right)^2 + \lambda \sum_{j=1}^p |\theta_j|. \quad \text{Lasso} \quad (5.24)$$

For LASSO regression, we cannot set  $\partial\mathcal{C}(\boldsymbol{\theta})/\partial\theta_k = 0$  and find a closed-form expression of  $\boldsymbol{\theta}$ . This means that we need to use an iterative optimization algorithm in order to obtain the optimal estimators. Such optimization methods are essential in non-linear problems such as deep neural networks and variational Monte Carlo. In section 5.6, we present various optimization methods, but from now on we will stick to one of the most basic methods, *gradient descent*, which can be written as

$$\theta_{k,t} = \theta_{k,t-1} - \eta \frac{\partial\mathcal{C}(\boldsymbol{\theta}_{t-1})}{\partial\theta_k}, \quad (5.25)$$

where  $\theta_{k,t}$  is the parameter  $\theta_k$  at iteration  $t$  and  $\mathcal{C}(\boldsymbol{\theta})$  is an arbitrary cost function. Here we are introduced to a new hyper-parameter,  $\eta$ , known as the *learning rate*, which controls the rate of converge in the estimators. It has to be specified carefully, where a too large  $\eta$  will make the cost function diverge and a too small  $\eta$  will make the training too slow. We experience that an  $\eta \in \{0.01 - 0.0001\}$  is a good choice. For OLS, the vectorized iterative parameter update can be written as

$$\boldsymbol{\theta}_t = \boldsymbol{\theta}_{t-1} - \eta \mathbf{X}^T (\mathbf{y} - \mathbf{X}\boldsymbol{\theta}_{t-1}). \quad (5.26)$$

## 5.4 Logistic regression

So far, we have discussed polynomial regression and linear regression, where both methods includes models giving continuous outputs. However, what if we want discrete outputs, for example, in the form of classification? This is what logistic regression is all about, where the name comes from the logistic function (sigmoid function) which is used to fire or not fire the neurons. As for the linear regression, we also need a cost function in logistic regression. The cost function will be motivated in the following.

Consider a system that can take two possible energies,  $\varepsilon_0$  and  $\varepsilon_1$ . From elementary statistical mechanics, we know that the probability of finding a system in a state of energy  $\varepsilon_0$  is given by the Boltzmann distribution, such that

$$P(y_i = 0) = \frac{\exp(-\varepsilon_0/k_B T)}{\exp(-\varepsilon_0/k_B T) + \exp(-\varepsilon_1/k_B T)}, \quad (5.27)$$

$$= \frac{1}{1 + \exp(-(\varepsilon_1 - \varepsilon_0)/k_B T)}, \quad (5.28)$$

which is the *sigmoid*, in the most general given by

$$f(x) = \frac{1}{1 + \exp(-x)}. \quad (5.29)$$

The first denominator is known as the *partition function*,

$$Z = \sum_{i=0}^1 \exp(-\varepsilon_i/k_B T), \quad (5.30)$$

where  $k_B$  is Boltzmann's constant and  $T$  is the system temperature. The probability of finding the system in the second state is given by

$$P(y_i = 1) = 1 - P(y_i = 0), \quad (5.31)$$

$$= \frac{1}{1 + \exp(-(\varepsilon_0 - \varepsilon_1)/k_B T)}. \quad (5.32)$$

Note that the only thing we need is the energy difference,  $\Delta\varepsilon = \varepsilon_1 - \varepsilon_0$ , between the two states rather than the energy itself. This is often the case in physics, where we for instance have no absolute potential energy. We now assume that the energy difference can be written as the inner product between a row vector,  $\mathbf{X}_i$ , specifying the state  $i$  and a column vector with parameters,  $\mathbf{w}$ . These parameters are known as the *weights*, the difference can be written as

$$\Delta\varepsilon = \mathbf{X}_i \mathbf{w} \equiv \tilde{y}_i. \quad (5.33)$$

giving the conditional probability

$$P(\mathbf{X}_i, y_i | \mathbf{w}) = (f(\mathbf{X}_i \mathbf{w}))^{y_i} (1 - f(\mathbf{X}_i \mathbf{w}))^{1-y_i}. \quad (5.34)$$

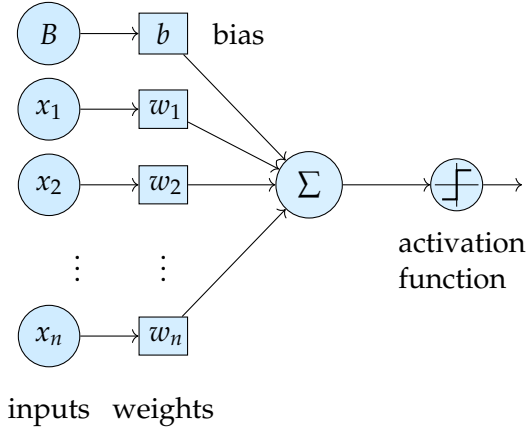


**Figure 5.4:** Logistic regression model with  $n$  inputs. Each input  $x_j$  is multiplied with a weight  $w_j$ , and the contributions from all units are summarized. The output is obtained after the sum is activated by an activation function.

If we have a set of multiple states stored in a  $\mathcal{D} = \{(X_i, y_i)\}$ , the joint probability yields

$$P(\mathcal{D}|\mathbf{w}) = \prod_{i=1}^n (f(X_i\mathbf{w}))^{y_i} (1 - f(X_i\mathbf{w}))^{1-y_i}, \quad (5.35)$$

which is known as the *likelihood*. The *log-likelihood* function is simply the log of the likelihood, and is given by

$$l(\mathbf{w}) = \sum_{i=1}^n [y_i \log f(X_i\mathbf{w}) + (1 - y_i) \log(1 - f(X_i\mathbf{w}))]. \quad (5.36)$$

As in linear regression, we want to find a cost function which we can minimize in order to fit the model to the data set. Since the log-likelihood function has its maximum at the highest probability, a natural choice is to set the cost function to the negative log-likelihood function,

$$\mathcal{C}(\mathbf{w}) = -l(\mathbf{w}) = - \sum_{i=1}^n [y_i \log f(X_i\mathbf{w}) + (1 - y_i) \log(1 - f(X_i\mathbf{w}))], \quad (5.37)$$

which is the *cross entropy*. To clarify things, we will try to illustrate how this works. In figure (5.4), we have an input set  $X_i = \{x_1, x_2, \dots, x_n\}$  where each unit is multiplied with a parameter  $w_j$  and summarized. This corresponds to the inner product  $X_i\mathbf{w}$ . Further, the sum (or the inner product) is *activated* by an *activation function*, which we above have assumed to be the sigmoid. The output is then given by

$$a_i = f(X_i\mathbf{w}), \quad (5.38)$$

where the bias node is included in the  $X_i$ 's and the bias weights are included in the  $\mathbf{w}$ 's. The bias node is added in order to shift the activation function to the left or right, and works in the same way as a constant term in a function.

The output from the activation is then used in the cost function to calculate the prediction error. As for LASSO regression, the cost function is then minimized iteratively, where, for example, the gradient descent method gives the weight update

$$\mathbf{w}_t = \mathbf{w}_{t-1} - \eta \mathbf{X}[\mathbf{y} - f(\mathbf{X}\mathbf{w}_{t-1})], \quad (5.39)$$

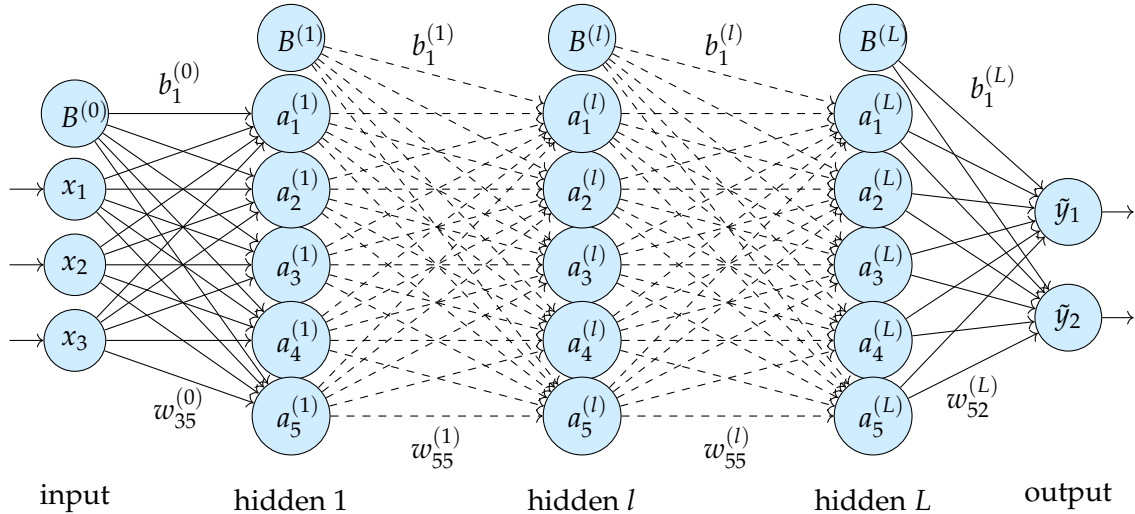


**Figure 5.5:** Neural network with 3 input units,  $L$  hidden layers with 5 hidden units each and two outputs.  $B^{(0)}, B^{(1)}, B^{(l)}$  and  $B^{(L)}$  are the bias units for the respective layers, and the dashed lines indicate that it might be more layers between the two layers. We have labeled a few of the lines to relate them to the weights.

where  $\mathbf{X}$  is a matrix containing all the column vectors  $\mathbf{X}_i$ . This expression is extremely similar, not to say identical, to the estimator update for ordinary least square presented in equation (5.26). The difference is that we now denote the parameters by  $w$  instead of  $\theta$  to prepare for the neural networks, but they are basically the same thing.

## 5.5 Neural networks

Now we know enough to examine the field of artificial neural networks. Neural networks can provide either continuous or discrete outputs and are therefore competitors to both linear and logistic regression. The great strength of neural networks is that one can add multiple *layers*, which makes the model extremely flexible. According to **the universal approximation theorem**, a neural network with only one hidden layer with a finite number of units can approximate any continuous function<sup>75</sup>. However, often, multiple layers are used since these networks are in general known to be easier to train and work better for complex systems. Neural networks of more than one layer are called *deep* networks, and as more layers are added, the network gets *deeper*. Deep networks contain more weights than narrower networks with the same number of units, and are therefore often preferred.

In figure (5.5), we have illustrated a deep neural network with an unspecified number of layers and five hidden units in each layer. It has some similarities with the logistic regression model in figure (5.4), but with multiple hidden layers and multiple outputs, this model is more complex. We decided to drop the representation of the weights (apart from some selected labeled ones), but each line corresponds to a weight.

Without a hidden layer, we have seen that the update of weights is straightforward. For a neural network consisting of multiple layers, the question is: *How do we update the weights when we do not know the values of the hidden units?* This question will be answered in section 5.5.3, where the most popular technique for weight update in neural networks, back propagation, is discussed. Before that, we will generalize the forward phase presented in logistic regression.

### 5.5.1 Forward phase

In the previous section, we saw how the output is found for a single perceptron, i.e. the model presented in figure (5.4). For a neural network, also called a multi-layer perceptron, the net output to the first layer is similar, and given by

$$z_j^{(1)} = \sum_{i=1}^{N_0+1} x_i w_{ij}^{(0)} = \mathbf{X} \mathbf{w}_j^{(0)}.$$

Here,  $N_0$  is the number of units in layer 0 (the input layer),  $\mathbf{X}$  is the input vector which is assumed to be a row vector and  $\mathbf{w}_j^{(1)}$  is the  $i$ 'th column of the  $\mathbf{w}$ -matrix associated with the first layer. We have again assumed that the bias node is included in  $\mathbf{X}$  and the first set of bias weights are included in  $\mathbf{w}^{(0)}$  (therefore  $N_0 + 1$  elements in the sum). The same applies for the other layers as well. If we let the activation function,  $f(x)$ , act on the net output, we get the real output given by

$$a_j^{(1)} = f(z_j^{(1)}) = f\left(\sum_{i=1}^{N_0+1} x_i w_{ij}^{(0)}\right).$$

This is then again the input to the next layer with  $N_1$  units, so the output from the second layer is simply

$$a_j^{(2)} = f\left(\sum_{i=1}^{N_1+1} a_i^{(1)} w_{ij}^{(1)}\right).$$

For a neural network of multiple layers, the same procedure applies for all the layers and we can find a general formula for the output at a layer  $l + 1$ . The net output to a node  $z_j^{(l+1)}$  in layer  $l + 1$  can be found to be

$$z_j^{(l+1)} = \sum_{i=1}^{N_l+1} a_i^{(l)} w_{ij}^{(l)}, \quad (5.40)$$

where layer  $l$  has  $N_l$  units and we need to be aware that  $a_j^{(0)} = x_j$ . After activation, the output is obviously found to be

$$a_j^{(l+1)} = f(z_j^{(l+1)}) = f\left(\sum_{i=1}^{N_l+1} a_i^{(l)} w_{ij}^{(l)}\right), \quad (5.41)$$

which is the only formula needed for the forward phase. In practice, the operation is always implemented in a vectorized fashion, reading  $\mathbf{a}^{(l+1)} = f(\mathbf{a}^{(l)} \mathbf{w}^{(l)})$ . The activation function  $f(x)$  is not explicitly defined, because it is often expedient having the chance to experiment with multiple activation functions.

### 5.5.2 Activation function

The task of the activation function is to define a soft (or hard) threshold for passing the information forward, hence the name "activation". There are multiple reasons to do this, where the most important is to introduce non-linearity into the output of a unit. Without an activation function, all of our layers would simply stack one affine transformation after another resulting in a composition of transformations equal to one layer. In other words, the deep networks would have lost their clout without the activation functions.

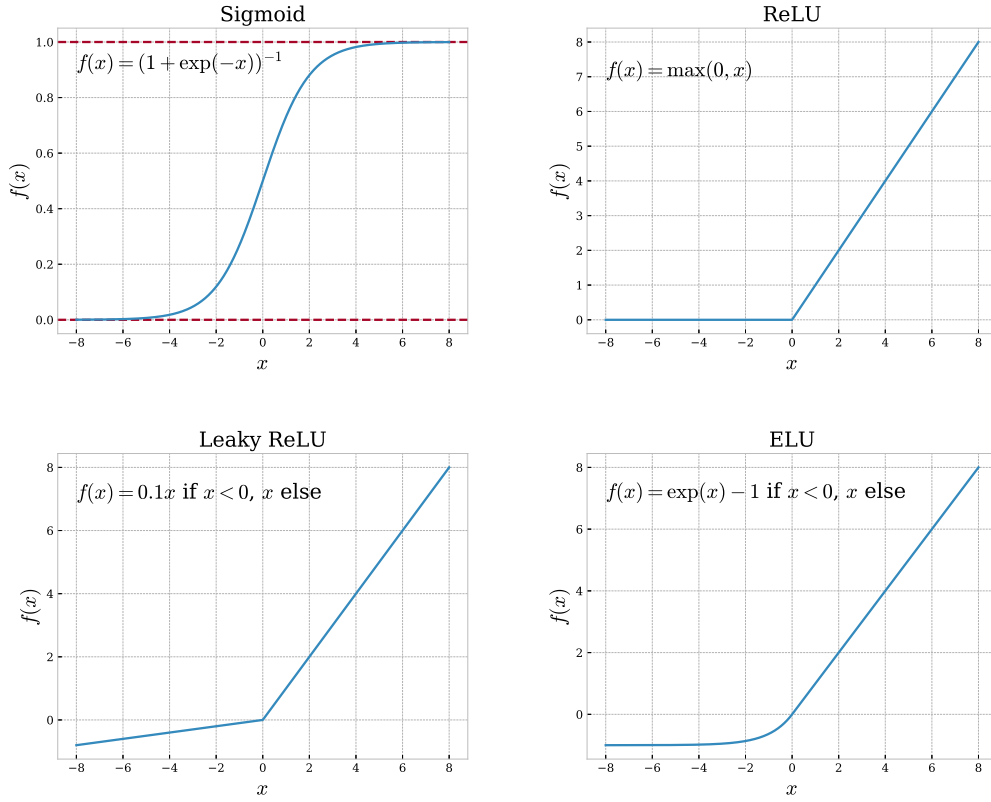


**Figure 5.6:** Some well-known activation functions. The sigmoid function stands out from the others since it maps between 0 and 1, and it is not linear for positive numbers.

Henceforth, we have only discussed the sigmoid activation function. However, there are plenty of other activation functions available and the sigmoid function has in fact lost its popularity. Most notably, functions based on *rectified linear units* (ReLU) have increased in popularity and have become the most popular among activation functions. Some popular variations are the *leaky* ReLU and *exponential linear units* (ELU), which are linear for positive numbers, where all have trivial derivatives. The pure linear activation function is still widely used, especially on the output layer. In figure (5.6), standard RELU, leaky RELU and ELU are plotted along with the sigmoid.

### 5.5.3 Backward propagation

Backward propagation is the basic algorithm for updating the weights in a neural network and is similar to the weight update presented for linear and logistic regression. The algorithm for this was presented by Rumelhart *et al.*<sup>76</sup> in 1986, and enabled deep neural networks to solve relatively complicated problems for the first time. The weights are updated layer-wise based on the outputs until we get to the inputs, hence the backward propagation name.

As observed above, a unit depends on all the units in the previous layers. This means that the units depend on a large number of parameters, resulting in a complex training scheme. Nevertheless, it is possible to generalize this to express the updating formulas on a relatively simple form, similar to the forward phase. From the linear and logistic regression, we know that we need the derivative of the cost function in order to implement the weight update. Again, we

define the cost function as the mean square error,

$$\mathcal{C}(\mathbf{w}) = \frac{1}{2} \sum_{i=1}^{N_{L+1}} (y_i - a_i^{(L+1)})^2, \quad (5.42)$$

where we have  $L$  hidden layers ( $L + 1$  is the last layer) and  $N_{L+1}$  output units. The derivative of this with respect to one of the weights between the  $L$ 'th and  $L + 1$ 'th layer can be written as a sum using the chain rule

$$\frac{\partial \mathcal{C}(\mathbf{w})}{\partial w_{jk}^{(L)}} = \frac{\partial \mathcal{C}(\mathbf{w})}{\partial a_j^{(L+1)}} \frac{\partial a_j^{(L+1)}}{\partial z_j^{(L+1)}} \frac{\partial z_j^{(L+1)}}{\partial w_{jk}^{(L)}}, \quad (5.43)$$

where  $z_j^{(L+1)}$  and  $a_j^{(L+1)}$  are found from equations (5.40) and (5.41), respectively. If we start from the first factor, it can be expressed as

$$\frac{\partial \mathcal{C}(\mathbf{w})}{\partial a_j^{(L+1)}} = -(y_j - a_j^{(L+1)}), \quad (5.44)$$

using the definition of the cost function. The second factor is the derivative of the activation function with respect to its argument, and is for the sigmoid function given by

$$\frac{\partial a_j^{(L+1)}}{\partial z_j^{(L+1)}} = a_j^{(L+1)}(1 - a_j^{(L+1)}). \quad (5.45)$$

Finally, the last factor is found from equation (5.40), and we obtain

$$\frac{\partial z_j^{(L+1)}}{\partial w_{jk}^{(L)}} = a_k^{(L)}. \quad (5.46)$$

Collecting all the factors, the update of the last set of weights is written as

$$\frac{\partial \mathcal{C}(\mathbf{w})}{\partial w_{jk}^{(L)}} = - (y_j - a_j^{(L+1)}) a_j^{(L+1)} (1 - a_j^{(L+1)}) a_k^{(L)}, \quad (5.47)$$

when the sigmoid function is used in the activation. In the next step, we can define

$$\delta_j^{(L+1)} = -a_j^{(L+1)}(1 - a_j^{(L+1)})(y_j - a_j^{(L+1)}) = f'(a_j^{(L+1)}) \frac{\partial \mathcal{C}(\mathbf{w})}{\partial a_j^{(L+1)}} = \frac{\partial \mathcal{C}(\mathbf{w})}{\partial z_j^{(L+1)}}, \quad (5.48)$$

such that the weight update can be expressed on a compressed form

$$\frac{\partial \mathcal{C}(\mathbf{w})}{\partial w_{jk}^{(L)}} = \delta_j^{(L+1)} a_k^{(L)}. \quad (5.49)$$

For a general layer  $l$ , the derivative of the cost function with respect to a weight  $w_{jk}^{(l)}$  is similarly derived, and is given by

$$\frac{\partial \mathcal{C}(\mathbf{w})}{\partial w_{jk}^{(l)}} = \delta_j^{(l+1)} a_k^{(l)}. \quad (5.50)$$

Our goal is to find the general relation between layer  $l$  and  $l + 1$ , and therefore we use the chain rule and sum over all the net outputs in layer  $l + 1$ ,

$$\delta_j^{(l)} = \frac{\partial \mathcal{C}(\mathbf{w})}{\partial z_j^{(l)}} = \sum_k \frac{\partial \mathcal{C}(\mathbf{w})}{\partial z_k^{(l+1)}} \frac{\partial z_k^{(l+1)}}{\partial z_j^{(l)}}. \quad (5.51)$$

We now recognize that the first factor in the sum is just  $\delta_k^{(l+1)}$  and the last factor can be found from equation (5.40). We obtain the final expression,

$$\delta_j^{(l)} = \sum_k \delta_k^{(l+1)} w_{kj}^{(l)} f'(z_j^{(l)}), \quad (5.52)$$

where we use the expression of  $\delta_j^{(L)}$  as our initial condition. As for several of the methods discussed above, a solution of the weight update does not exist in closed form and we need to rely on iterative optimization methods. Using gradient descent, a new set of weights,  $\mathbf{w}_t$ , is computed using the update rule

$$\mathbf{w}_t = \mathbf{w}_{t-1} - \eta \frac{\partial \mathcal{C}(\mathbf{w}_{t-1})}{\partial \mathbf{w}_{t-1}}, \quad (5.53)$$

where the multi-dimensional differentiation is done element-wise. Other optimization methods will be discussed in the following section.

## 5.6 Optimization algorithms

In section 5.3.3, we discussed the gradient descent optimization algorithm, which is among the most basic optimization methods available. That method is based on the gradient, which is the slope of the cost function. However, many other methods depend of the second-order partial derivatives which results in the Hessian matrix, defining the curvature of the cost function. We will barely scratch the surface of this field, limiting us to the gradient methods as they are computationally efficient and straightforward to implement.

To have the method fresh in mind, we will start with reintroducing the gradient descent method before we move on to its stochastic brother. We will then take a look at how momentum can be added. Finally, we examine the stochastic and momentum-based ADAM optimizer. Recall that given a cost function,  $\mathcal{C}(\theta)$ , the gradient with respect to a parameter  $\theta$  can be found from

$$\nabla_\theta \mathcal{C}(\theta) \equiv \frac{\partial \mathcal{C}(\theta)}{\partial \theta}, \quad (5.54)$$

where we henceforth use the short-hand notation with  $\nabla_\theta$  representing the multi-dimensional derivative  $\partial/\partial\theta$ . Differentiating with respect to the vector implies that the operation is done element-wise.

### 5.6.1 Gradient descent

Perhaps the simplest and most intuitive method for finding the minimum is the gradient descent method, which is given by

$$\theta_t = \theta_{t-1} - \eta \nabla_\theta \mathcal{C}(\theta_{t-1}), \quad (5.55)$$

where  $\theta_t$  is the parameter vector at time step (iteration)  $t$  and  $\eta$  is the learning rate.  $\nabla_\theta \mathcal{C}(\theta_{t-1})$  is the gradient of the cost function with respect to all the parameters  $\theta$  at time  $t - 1$ .

The idea is to find the direction where the cost function,  $\mathcal{C}(\theta)$ , has the steepest slope, and move in the direction which minimizes the cost function. When the gradient approaches zero, a minimum is found. A possible, but basic, stop criterion is

$$\nabla_{\theta}\mathcal{C}(\theta_t) < \epsilon, \quad (5.56)$$

where  $\epsilon$  is a tolerance. More advanced methods are based on comparing the value of the cost function for several past iterations. In cases where the cost function is not strictly decreasing, we will have both local and global minima. Often, it is hard to say whether we are stuck in a local or global minimum, and this is where the stochasticity enters the game.

### 5.6.2 Stochastic gradient descent

Stochastic gradient descent is closely related to the gradient descent method, but the method uses randomly selected batches to evaluate the gradients. By introducing this randomness, the parameters will not always be updated in order to minimize the energy. This makes the model less likely to be stuck in a local minimum.

The algorithm splits the data set in  $n$  batches, and select one of them to be used in the parameter update. Our hope is that this batch is representative of most of the data set, such that the new parameters provide a lower cost function. If that is the case, we have reduced the cost of an iteration significantly, since we only need to care about a batch. We are not guaranteed that updating the parameters with respect to a batch gives a lower cost function, and when it is not, we need to run more batches in order to minimize the cost function. Since each iteration is faster than for standard gradient descent, this is acceptable. As long as the batch is slightly representative of the entire data set, the cost function will be minimized in the end. After each batch in the data has been selected without replacement, we say that we have gone through an *epoch*. Mathematically, the method can be expressed as

$$\theta_t = \theta_{t-1} - \eta \nabla_{\theta}\mathcal{C}_i(\theta_{t-1}), \quad (5.57)$$

where we use the  $i$ 'th batch in the parameter update. Standard gradient descent is just a special case of this, where we only have one batch ( $i$  includes the whole data set). If we still get stuck in local minima after adding the stochasticity, it might be a good idea to add momentum as well.

### 5.6.3 Adding momentum

Recalling what we learned in an introductory mechanics course, we might remember that momentum is a quantity that maintains the motion of a body. Imagine a ball that rolls down a steep hill, but then there is a local minimum that it needs to escape to keep rolling. If it has enough momentum it will be able to escape.

The same idea lies behind the momentum used in optimization algorithms; the momentum will try to maintain the motion towards the global minimum, which makes the system less likely to be stuck in a local minimum. Momentum can be added to most optimization algorithms, including gradient descent and stochastic gradient descent. In practice, the previous minimum estimate is stored during the iterations, and use it as a contribution to the next gradient update. A typical implementation of the first-order momentum applied to gradient descent looks like

$$\begin{aligned} m_t &= \gamma m_{t-1} + \eta \nabla_{\theta}\mathcal{C}_i(\theta_{t-1}), \\ \theta_t &= \theta_{t-1} - m_t, \end{aligned} \quad (5.58)$$

where  $\gamma$  is the momentum parameter, which is just another hyper-parameter usually initialized to a small number.  $\mathbf{m}_t$  is the momentum vector and is usually the zero vector, corresponding to no initial momentum.

The optimization algorithm can be modified further in unlimited ways. A common improvement is to add higher-order momentum; another is to make the learning-rate adaptive. We have implemented the most basic version of this, with monotonic adaptivity. We will end this section by setting up the algorithm of a stochastic gradient descent optimization with momentum and monotonic adaptivity. The algorithm is found in algorithm 1.

---

**Algorithm 1:** Adaptive stochastic gradient descent with momentum. See sections (5.6.2-5.6.3) for details. Appropriate default settings for the hyper-parameters are  $\eta = 0.001$ ,  $\gamma = 0.01$  and  $\lambda = 0.1$ . All the operations are element-wise.

---

**Parameter:**  $\eta$ : Learning rate  
**Parameter:**  $\gamma$ : Momentum parameter  
**Parameter:**  $\lambda$ : Monotonic decay rate  
**Require :**  $\mathcal{C}(\theta)$ : Cost function  
**Data :**  $\theta_0$ : Initial parameters

- 1  $\mathbf{m}_0 \leftarrow 0$  (Initialize momentum vector);
- 2  $t \leftarrow 0$  (Initialize time step);
- 3 **while**  $\theta_t$  not converged **do**
- 4      $t \leftarrow t + 1$  (Increase time for each iteration);
- 5      $\mathbf{g}_t \leftarrow \nabla_{\theta} \mathcal{C}_t(\theta_{t-1})$  (Get gradients from a given batch at time  $t$ );
- 6      $\mathbf{m}_t \leftarrow \gamma \mathbf{m}_{t-1} + \eta \cdot \mathbf{g}_t$  (Update first momentum estimate);
- 7      $\theta_t = \theta_{t-1} - \mathbf{m}_t / \lambda^t$  (Update parameters with monotonic, adaptive step);
- 8 **end**

**Result:** Converged parameters  $\theta_t$ .

---

#### 5.6.4 ADAM

ADAM is a first-order stochastic optimization method and is widely used in machine learning. It was first described by Kingma & Ba<sup>77</sup>, and published in 2014. It has experienced an immense popularity, and with its 30,000 citations it is among the most cited articles in the machine learning community. The main reason why it is widely used, is obviously that it provides good performance. The fact that it only requires the gradient makes it efficient, and the way the momentum is implemented still makes it capable of handling a large number of variational parameters. The optimization algorithm can be expressed as a set of equations

$$\begin{aligned}
 \mathbf{g}_t &= \nabla_{\theta} \mathcal{C}_t(\theta_{t-1}), \\
 \mathbf{m}_t &= \gamma_1 \mathbf{m}_{t-1} + (1 - \gamma_1) \mathbf{g}_t, \\
 \mathbf{v}_t &= \gamma_2 \mathbf{v}_{t-1} + (1 - \gamma_2) \mathbf{g}_t^2, \\
 \hat{\mathbf{m}}_t &= \mathbf{m}_t / (1 - \gamma_1^t), \\
 \hat{\mathbf{v}}_t &= \mathbf{v}_t / (1 - \gamma_2^t), \\
 \theta_t &= \theta_{t-1} - \eta \hat{\mathbf{m}}_t / (\sqrt{\hat{\mathbf{v}}_t} + \epsilon),
 \end{aligned} \tag{5.59}$$

where  $\mathbf{m}_t$  is the biased first momentum estimate of the parameter vector  $\theta$  and  $\mathbf{v}_t$  is the biased second raw moment estimate. The momentum parameters need to be in the range  $\gamma_1, \gamma_2 \in [0, 1]$ , and are often set to values close to 1. This makes the optimization adaptive, as the time goes

the factors  $1 - \gamma_1^t$  and  $1 - \gamma_2^t$  approach 1 from below.  $\eta$  is the learning rate, and should be a small number. Finally, the parameters  $\varepsilon$  are added to avoid division by zero. We can set up the algorithm in a way similar to the adaptive stochastic gradient descent algorithm presented above, giving algorithm 2.

---

**Algorithm 2:** ADAM optimizer. Appropriate default settings for the hyper-parameters are  $\eta = 0.001$ ,  $\gamma_1 = 0.99$  and  $\gamma_2 = 0.999$ . All the operations are element-wise, and for in-depth information see the original paper by Kingma & Ba<sup>77</sup>.

---

**Parameter:**  $\eta$ : Learning rate

**Parameter:**  $\gamma_1, \gamma_2 \in [0, 1]$ : Momentum parameters

**Parameter:**  $\varepsilon$ : Division parameter

**Require :**  $\mathcal{C}(\theta)$ : Cost function

**Data** :  $\theta_0$ : Initial parameters

```

1  $m_0 \leftarrow 0$  (Initialize 1st momentum vector);
2  $v_0 \leftarrow 0$  (Initialize 2nd momentum vector);
3  $t \leftarrow 0$  (Initialize time step);
4 while  $\theta_t$  not converged do
5    $t \leftarrow t + 1$  (Increase time for each iteration);
6    $g_t \leftarrow \nabla_{\theta} \mathcal{C}_t(\theta_{t-1})$  (Get gradients from a given batch at time  $t$ );
7    $m_t \leftarrow \gamma_1 m_{t-1} + (1 - \gamma_1) \cdot g_t$  (Update first momentum estimate);
8    $v_t \leftarrow \gamma_2 v_{t-1} + (1 - \gamma_2) \cdot g_t^2$  (Update second raw momentum estimate);
9    $\hat{m}_t \leftarrow m_t / (1 - \gamma_1^t)$  (Bias-corrected first momentum estimate);
10   $\hat{v}_t \leftarrow v_t / (1 - \gamma_2^t)$  (Bias-corrected second momentum estimate) ;
11   $\theta_t \leftarrow \theta_{t-1} - \eta \cdot \hat{m}_t / (\sqrt{\hat{v}_t} + \varepsilon)$  (Update parameters) ;
12 end
```

**Result:** Converged parameters  $\theta_t$ .

---

## CHAPTER 6

# Boltzmann Machines

Available energy is the main object at stake in the struggle for existence and the evolution of the world.

---

Ludwig Boltzmann,<sup>78</sup>

Boltzmann machines are generative, energy-based neural network models that fall under the category unsupervised learning. In unsupervised learning, unlike supervised learning which we discussed in chapter 5, the network is fed with an input data set only. In other words, we do not have labeled data for supervising the network during the training. The task is then to find structures in the data, comparing data sets to each other and categorize the data sets concerning their similarities and differences (clustering).

The Boltzmann machines were invented by Ackley & Hinton<sup>\*80</sup> in 1985, and are based on the Boltzmann distribution, hence the name. Boltzmann machines with constrained connectivity, known as restricted Boltzmann machines (RBM), have found applications in classification<sup>81</sup>, feature learning<sup>82</sup> and many-body quantum mechanics in the form of the Ising model<sup>24</sup>. The RBM is well-suited for simulating the Ising model for two reasons: The model takes binary spins and the system energy of a Boltzmann machine takes the same form as the Ising energy. On the other hand, electronic structure problems require wave functions that obey Fermi-Dirac statistics, which is a challenging task for machine learning. Our approach is to let the statistics be controlled by a Slater determinant, like in traditional variational Monte Carlo (VMC) simulations, and then let the single-particle functions be determined by Boltzmann machines. This is similar to the approach of Pfau *et al.*<sup>25</sup>, who invented a so-called fermionic neural network consisting of a Slater determinant with the multi-electron functions controlled by a deep neural network.

In this chapter, we will focus exclusively on the Boltzmann machines, and move the detailed description of how they actually are used in our work to section 7.2. In chapter 5, we saw how the weights in supervised learning can be adjusted using the backward propagation algorithm, but it does not work when we do not have labeled data. Instead, a set of probabilities controls the weights, and we let the log-likelihood function define the cost function. This is known as Bayesian statistics which is presented in the next section.

---

<sup>\*</sup>Hinton is often referred to as "The Godfather of Deep Learning", and his contribution to machine learning can hardly be overstated. He was co-author of the paper popularizing the backpropagation algorithm<sup>76</sup>, supervisor of Krizhevsky who designed AlexNet<sup>17</sup> and the main author of the paper introducing the regularization technique dropout<sup>79</sup>.

## 6.1 Statistical foundation

In this section, we will use Bayesian statistics to exploit the link between some data  $x$ , called the *hypothesis*, and some other data  $y$  called the *evidence*. We will first do it in a general way before we link it to machine learning in the next section. Bayesian statistics appear in many fields of science, as it is a basic and often useful probability theory. It is based on Bayes' theorem, which gives rise to some marginal and conditional distributions. The expressions can either be set up in the continuous space or the discrete space, but here we will stick to the latter as we in practice will deal with discrete data.

We start expressing the joint probability distribution of measuring both  $x$  and  $y$  using the general relation,

$$P(x, y) = P(x|y)P(y) = P(y|x)P(x), \quad (6.1)$$

which basically states that the probability of observing  $x$  and  $y$  is just the probability of observing  $x$  multiplied with the probability of observing  $y$  given  $x$ .  $P(x|y)$  is the conditional distribution of  $x$  and gives the probability of  $x$  given that  $y$  is true. The opposite applies for  $P(y|x)$ .  $P(x)$  and  $P(y)$  are called the marginal probabilities of  $x$  and  $y$ , respectively. By reordering equation (6.1), we obtain Bayes' theorem

$$P(x|y) = \frac{P(y|x)P(x)}{P(y)}. \quad (6.2)$$

The marginal probability of  $y$ ,  $P(y)$ , is given by the sum over all the possible joint probabilities when  $y$  is fixed,

$$P(y) = \sum_i P(x_i, y) = \sum_i P(y|x_i)P(x_i), \quad (6.3)$$

and from this we observe that Bayes' theorem provides the *posterior* probability ( $P(x|y)$ ) given the *prior* probability ( $P(x)$ ) and the *likelihood*, ( $P(y|x)$ ), seen from

$$P(x|y) = \frac{P(y|x)P(x)}{\sum_i P(y|x_i)P(x_i)}. \quad (6.4)$$

However, the summation gets extremely expensive quickly, and is intractable even for small systems. This was a big problem for a long time, but with the advent of powerful computers, algorithms like Markov chain Monte-Carlo can be used to estimate the posterior without knowing the *normalization constant*,  $P(y)$ . More about this in chapter 7.

In the previous chapter, the cost function was an important concept, and so is the case in unsupervised learning. However, how do we define a cost function when we do not have any targets? We find the answer by revealing the similarities between logistic regression and Bayesian statistics. In logistic regression, we find the probability that a system is in a particular state and define the cost function as the log-likelihood. We can do the same in unsupervised learning, and define the cost function as

$$\mathcal{C}(y) = \ln \prod_{i=1}^l P(x_i|y) = \sum_{i=1}^l \ln P(x_i|y), \quad (6.5)$$

which is the log-likelihood. Maximizing the likelihood is the same as maximizing the log-likelihood, which again corresponds to minimizing the distance between the unknown distribution  $Q$  underlying  $x$  and the distribution  $P$  of the Markov random field  $y$ . This distance is expressed in terms of the Kullback-Leibler divergence (KL divergence), which for a finite state space  $\Omega$  is given by

$$\text{KL}(Q||P) = \sum_{x \in \Omega} Q(x) \frac{Q(x)}{P(x)}. \quad (6.6)$$

The KL divergence is a measure of the difference between two *probability density functions* (PDFs), and is zero for two identical PDFs. The divergence is often called a distance, but that is an unsatisfying description as it is non-symmetric ( $\text{KL}(Q||P) \neq \text{KL}(P||Q)$ ) in general.

To proceed further, we will introduce latent variables in form of hidden units. Suppose we want to model an  $m$ -dimensional unknown probability distribution  $Q$ . Typically, not all the variables  $s$  are observed components, they can also be latent variables. If we split  $s$  into *visible* variables  $x$  and hidden variables  $h$ , and under the assumption that  $x$  and  $h$  are variables in an energy function  $E(x, h)$ , we can express the joint probability as the Boltzmann distribution

$$P(x, h) = \frac{\exp(-E(x, h))}{Z}, \quad (6.7)$$

where  $Z$  is the partition function, which is the sum of the probability of all possible states, which was already introduced in equation (5.30). We have ignored the factor  $k_B T$  by setting it to 1. Where the visible units correspond to components of an observation, the hidden units introduce the system to more degrees of freedom. This allows us to describe complex distributions over the visible variables by means of simple conditional distributions<sup>83</sup>. These conditional distributions will be described later, but let us first take a look at the marginal distributions.

### 6.1.1 Marginal distributions

We have already used the term marginal distribution, which means that we get rid of a set of variables by integrating the joint probability over all of them. The marginal probability of  $x$  is given by

$$P(x) = \sum_{h'} P(x, h') = \frac{1}{Z} \sum_{h'} \exp(-E(x, h')). \quad (6.8)$$

The sum over the  $h'$  vector is just a short-hand notation where we sum over all the hidden units. Further, the marginal probability of  $h$  is expressed similarly, with

$$P(h) = \sum_{x'} P(x', h) = \frac{1}{Z} \sum_{x'} \exp(-E(x', h)). \quad (6.9)$$

$P(x)$  is important as it gives the probability of a particular set of visible units  $x$ , while  $P(h)$  will not be used in the same scope throughout this work.

### 6.1.2 Conditional distributions

The conditional distributions can be found from Bayes' theorem, and read

$$P(h|x) = \frac{P(x, h)}{P(x)} = \frac{\exp(-E(x, h))}{\sum_{h'} \exp(-E(x, h'))}, \quad (6.10)$$

and

$$P(x|h) = \frac{P(x, h)}{P(h)} = \frac{\exp(-E(x, h))}{\sum_{x'} \exp(-E(x', h))}. \quad (6.11)$$

The conditional probabilities are especially important in Gibbs sampling, where we want to update the visible units,  $x$ , given the hidden units,  $h$ , and *vice versa*.

### 6.1.3 Maximum log-likelihood estimate

Now, suppose that the energy function also is a function of some parameters  $\theta$ . We have already expressed the log-likelihood function,

$$\ln P(\mathbf{x}|\theta) = \ln \left[ \frac{1}{Z} \sum_{\mathbf{h}'} \exp(-E(\mathbf{x}, \mathbf{h}')) \right] = \ln \left[ \sum_{\mathbf{h}'} \exp(-E(\mathbf{x}, \mathbf{h}')) \right] - \ln \left[ \sum_{\mathbf{x}', \mathbf{h}'} \exp(-E(\mathbf{x}', \mathbf{h}')) \right], \quad (6.12)$$

and by maximizing this we find the maximum log-likelihood estimate. This estimate is important in neural networks since we always seek to maximize the likelihood in the training process. The function is maximized when

$$\begin{aligned} \frac{\partial \ln P(\mathbf{x}|\theta)}{\partial \theta} &= \frac{\partial}{\partial \theta} \left( \ln \sum_{\mathbf{h}'} \exp(-E(\mathbf{x}, \mathbf{h}')) \right) - \frac{\partial}{\partial \theta} \left( \ln \sum_{\mathbf{x}', \mathbf{h}'} \exp(-E(\mathbf{x}', \mathbf{h}')) \right), \\ &= - \sum_{\mathbf{h}'} P(\mathbf{h}'|\mathbf{x}) \frac{\partial E(\mathbf{x}, \mathbf{h}')}{\partial \theta} + \sum_{\mathbf{x}', \mathbf{h}'} P(\mathbf{x}', \mathbf{h}') \frac{\partial E(\mathbf{x}', \mathbf{h}')}{\partial \theta} = 0. \end{aligned} \quad (6.13)$$

Similarly to the neural networks presented in chapter 5, we cannot find a closed-form expression for this, and we need to solve it iteratively.

## 6.2 Unrestricted Boltzmann machines

Unrestricted Boltzmann machines, or merely Boltzmann machines, are energy-based, generative neural networks based on the more primitive Hopfield network. They consist of a set of units, and similarly to the feed-forward neural networks presented in section 5.5, a weight matrix is connecting the units. However, in a standard unrestricted Boltzmann machine, we only have one layer where all the units connect to all other units, and a bias unit is commonly added to work as a constant term. In figure (6.1), we illustrate a plain Boltzmann machine consisting of  $N = 6$  units and one bias unit.

We multiply each unit with all the other units and the weight connecting them, and obtain the system energy. This should not be confused with the physical energy of a quantum state. For the simplest case, the energy reads

$$E(\mathbf{s}) = - \sum_{i=1}^N s_i b_i - \sum_{i=1}^N \sum_{j=i}^N s_i w_{ij} s_j, \quad (6.14)$$

where  $\mathbf{s}$  are the units and  $w_{ij}$  is the weight connecting the units  $s_i$  and  $s_j$ . The bias unit is fixed to 1, as always, and the weight between the bias unit and the unit  $s_i$  is denoted by  $b_i$ . In its most simple form, the units can only take binary values, and we, therefore, call it a binary-unit Boltzmann machine. The energy formula is then identical to the system energy of Hopfield networks, but what distinguishes a Boltzmann machine from a Hopfield network is that the units are *stochastic*. By stochastic, we mean that their values are randomly determined, introducing some randomness to the system. Also, the energy of an Ising model takes the same form as equation (6.14)<sup>24</sup>. Other architectures are also available, and for the restricted Boltzmann machine we will look at the Gaussian-binary unit model.

The reader has probably already foreseen the next step, which is to use the Boltzmann distribution to define the probability of finding the system in a particular state,  $E(\mathbf{s}; \mathbf{w}, \mathbf{b})$ , as discussed in the previous section. The probability distribution function (PDF) is then given by

$$P(\mathbf{s}) = \frac{1}{Z} \exp(-E(\mathbf{s})), \quad (6.15)$$

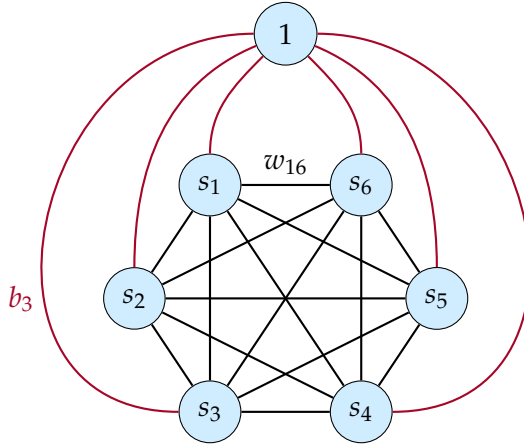


**Figure 6.1:** Unrestricted Boltzmann machine. Connections between units  $s_j$  are represented by the black lines, where, for instance, the line connecting  $s_1$  to  $s_6$  represents the weight  $w_{16}$ . The red lines represent the bias weights, where the line going from the bias unit to the unit  $s_3$  represents the bias weight  $b_3$ .

where  $Z$  again is the partition function. The PDF contains weights, which can be adjusted to change the distribution. In a supervised scheme, one can update the parameters in order to minimize the Kullback-Leibler divergence to a prior known distribution and in that manner reproduce the known distribution. In unsupervised learning, we cannot do this, but hopefully, we can obtain a reasonable distribution by minimizing the system energy.

A Boltzmann machine is also a Markov random field, as the stochastic processes satisfy the Markov property<sup>83</sup>. Loosely speaking, this means that all the probabilities of going from one state to another are known, making it possible to predict the future of the process based solely on its present state. The property is also determined by "memorylessness", meaning that the next state of the system depends only on the current state and not on the sequence of events that preceded it. The Markov chain is an essential part of the sampling methods that will be discussed in chapter 7.

### 6.3 Restricted Boltzmann machines

In the previous section we described the unrestricted Boltzmann machines, and here we will consider the restricted ones. What the term restricted means in this context, is that we ignore all the connections between units in the same layer, and keep only the inter-layer ones. In a restricted Boltzmann machine (RBM), only the units in the first layer are the observable, while the units in the next layer are latent or hidden. In the same manner as in equation (6.14), we can look at the linear case and multiply each unit with the corresponding weight, but now we need to distinguish between a visible unit,  $x_i$ , and a hidden unit,  $h_j$ . For the same reason, we divide all the bias weights into a group connected to the visible units,  $a_i$ , and a group connected to the hidden units,  $b_j$ . The system energy then reads

$$E(\mathbf{x}, \mathbf{h}) = - \sum_{i=1}^F x_i a_i - \sum_{j=1}^H h_j b_j - \sum_{i=1}^F \sum_{j=i}^H x_i w_{ij} h_j, \quad (6.16)$$

which is called a binary-binary unit or Bernoulli-Bernoulli unit RBM.  $H$  is the number of hidden units, and  $F$  is the number of visible units, later known as the degrees of freedom. In figure (6.2), a restricted Boltzmann machine with three visible units and three hidden units is illustrated.

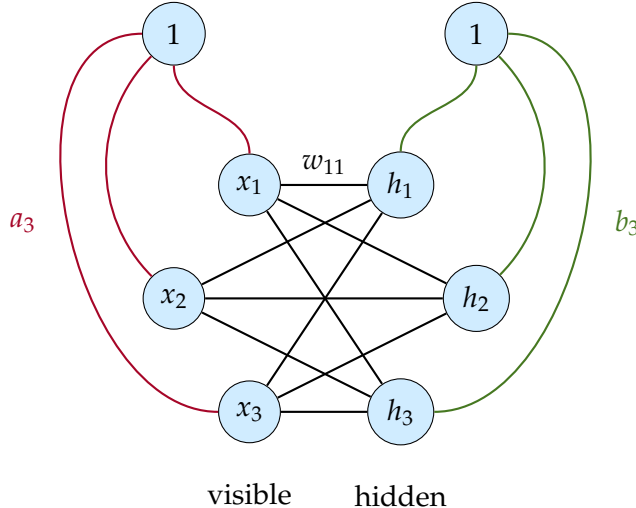


**Figure 6.2:** Restricted Boltzmann machine. Inter-layer connections between the visible and the hidden layer are represented by the black lines, where, for instance, the line connecting  $x_1$  to  $h_1$  represents the weight  $w_{11}$ . The red lines represent the visible bias weights, where the line going from the bias unit to the visible unit  $x_3$  represents the bias weight  $a_3$ . The green lines represent the hidden bias weights, where the line going from the bias unit to the hidden unit  $h_3$  represents the bias weight  $b_3$ .

### 6.3.1 Gaussian-binary units

So far, we have discussed the linear models only, but as for feed-forward neural networks, we need non-linear models to solve non-linear problems. A natural next step is the model with Gaussian-binary units, which has a Gaussian mapping between the visible unit bias and the visible units and possibly also between the two layers. The energy expression of an architecture with Gaussian mapping between the visible units and the bias only, takes the form

$$E(\mathbf{x}, \mathbf{h}) = \sum_{i=1}^F \frac{(x_i - a_i)^2}{2\sigma_i^2} - \sum_{j=1}^H h_j b_j - \sum_{i=1}^F \sum_{j=i}^H \frac{x_i w_{ij} h_j}{\sigma_i^2}, \quad (6.17)$$

where the  $\sigma_i$ 's are the width of the Gaussian distributions, which can take arbitrary numbers. Inserting the energy expression into equation (6.15), we obtain the Gaussian-binary joint probability distribution,

$$P(\mathbf{x}, \mathbf{h}) = \frac{1}{Z} \exp \left( - \sum_{i=1}^F \frac{(x_i - a_i)^2}{2\sigma_i^2} \right) \prod_{j=1}^H \exp \left( h_j b_j + \sum_{i=1}^F \frac{x_i w_{ij} h_j}{\sigma_i^2} \right), \quad (6.18)$$

where the first factor (the exponential function) is actually the definition of a Gaussian function and the product has a complexity proportional to the number of hidden nodes. Generative sampling algorithms, as Gibbs sampling, use this distribution directly, while other sampling tools, like Metropolis sampling, need the marginal distribution. To find the marginal distribution of the visible units, we just need to take the sum over the values  $h = 0$  and  $h = 1$  as the hidden units are binary. The final expression is given by

$$P(\mathbf{x}) = \frac{1}{Z} \exp \left( - \sum_{i=1}^F \frac{(x_i - a_i)^2}{2\sigma_i^2} \right) \prod_{j=1}^H \left[ 1 + \exp \left( b_j + \sum_{i=1}^F \frac{x_i w_{ij}}{\sigma_i^2} \right) \right], \quad (6.19)$$

were the transition from equation (6.17) is shown thoroughly in appendix B. Since the visible units take continuous values, we need to integrate to find the marginal distribution of the hidden units. The derivation is shown in appendix B, and the final expression result reads

$$P(\mathbf{h}) = \frac{1}{Z} \exp\left(\sum_{j=1}^H h_j b_j\right) \prod_{i=1}^F \sqrt{2\pi\sigma_i^2} \exp\left(a_i \sum_{j=1}^H \frac{w_{ij}h_j}{\sigma_i^2} + \left(\sum_{j=1}^H \frac{w_{ij}h_j}{2\sigma_i^2}\right)^2\right), \quad (6.20)$$

which can be used to find the conditional distribution of the hidden units, but other than that it will not be further used. The conditional distributions are important in Gibbs sampling as they are used to determine the value of the hidden and visible nodes and update the weights. The conditional distribution of the visible units is used to update the hidden units and reads

$$P(\mathbf{h}|\mathbf{x}) = \frac{P(\mathbf{x}, \mathbf{h})}{P(\mathbf{x})} = \prod_{j=1}^H \frac{\exp(h_j b_j + \sum_{i=1}^F x_i w_{ij} h_j / \sigma_i^2)}{1 + \exp(b_j + \sum_{i=1}^F x_i w_{ij} / \sigma_i^2)}. \quad (6.21)$$

Similarly, the conditional distribution of the hidden units is used to update the visible units and turns out to be just the normal distribution,

$$P(\mathbf{x}|\mathbf{h}) = \prod_{i=1}^F \mathcal{N}(x_i; a_i + w_{ij}h_j, \sigma_i^2), \quad (6.22)$$

with the width of the Gaussian distribution determining the variance. Note that the mean is  $\mu = \mathbf{a} + \mathbf{w}^T \mathbf{h}$ , which is the vector obtained when going backwards in the restricted Boltzmann machine (multiplying the hidden units with the weights). Both these expressions are derived in appendix B.

In Metropolis sampling, we only use the marginal distribution of the visible units. For completeness reasons, we will discuss the Gibbs sampling, but we will in practice stick to the Metropolis sampling. More about the different sampling tools can be found in chapter 7. We also need the gradient of the log-likelihood function in order to train the network. The likelihood function is defined as the probability of  $\mathbf{x}$  given a set of parameters  $\boldsymbol{\theta}$ , which relate to our problem as  $P(\mathbf{x}|\mathbf{a}, \mathbf{b}, \mathbf{w})$ . We therefore get three maximum log-likelihood estimates,

$$\begin{aligned} \frac{\partial \ln P(\mathbf{x}|\mathbf{a}, \mathbf{b}, \mathbf{w})}{\partial \mathbf{a}} &= \frac{\mathbf{x} - \mathbf{a}}{\sigma^2}, \\ \frac{\partial \ln P(\mathbf{x}|\mathbf{a}, \mathbf{b}, \mathbf{w})}{\partial \mathbf{b}} &= \mathbf{n}, \\ \frac{\partial \ln P(\mathbf{x}|\mathbf{a}, \mathbf{b}, \mathbf{w})}{\partial \mathbf{w}} &= \frac{\mathbf{x}\mathbf{n}^T}{\sigma^2}, \end{aligned} \quad (6.23)$$

where we have defined a vector  $\mathbf{n}$  as the (element-wise) sigmoid

$$\mathbf{n}(\mathbf{v}) \equiv \frac{1}{1 + \exp(-\mathbf{v})}, \quad (6.24)$$

with  $\mathbf{v}$  as the vector containing all the elements in the last exponent in equation (6.19),

$$\mathbf{v} \equiv \mathbf{b} + \frac{\mathbf{w}^T \mathbf{x}}{\sigma^2}. \quad (6.25)$$

We decided to set up the vectorized expressions as that is what we will use in practice. In addition to  $\mathbf{n}$ , we will later introduce its counterpart,  $\mathbf{p}(\mathbf{v}) = \mathbf{n}(-\mathbf{v})$ , and the names make sense as  $\mathbf{n}$  has a negative expression in the exponent, while  $\mathbf{p}$  has a positive expression in the exponent. The expressions in equation (6.23) will later be used to maximize the likelihood with respect to the respective set of parameters.

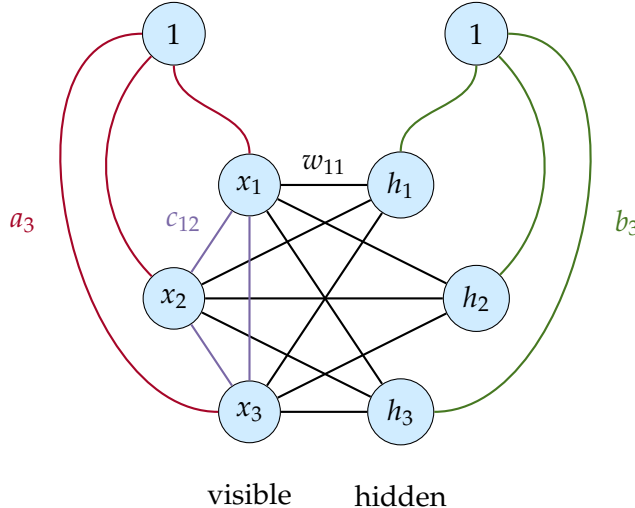


**Figure 6.3:** Partly restricted Boltzmann machine. Inter-layer connections between the visible and the hidden layer are represented by the black lines, where, for instance, the line connecting  $x_1$  to  $h_1$  represents the weight  $w_{11}$ . The red lines represent the visible bias weights, where the line going from the bias unit to the visible unit  $x_3$  represents the bias weight  $a_3$ . The green lines represent the hidden bias weights, where the line going from the bias unit to the hidden unit  $h_3$  represents the bias weight  $b_3$ . Finally, the purple lines represent the intra-layer weights, where, for instance,  $c_{12}$  represents the weight connecting  $x_1$  and  $x_2$ .

## 6.4 Partly restricted Boltzmann machines

One can also imagine a partly restricted architecture, where we have internal connections between the visible units, but not the hidden units. This is what we have decided to call a partly restricted Boltzmann machine, and is very similar to a restricted Boltzmann machine, but with another level of flexibility. Such a neural network with three visible units and three hidden units is illustrated in figure (6.3). Compared to a standard restricted Boltzmann machine, we get an extra term in the energy expression where the visible units are connected. It is easy to see that the expression should be

$$E(\mathbf{x}, \mathbf{h}) = \sum_{i=1}^F \frac{(x_i - a_i)^2}{2\sigma_i^2} - \sum_{i=1}^F \sum_{j>i}^F x_i c_{ij} x_j - \sum_{j=1}^H h_j b_j - \sum_{i=1}^F \sum_{j=i}^H \frac{x_i w_{ij} h_j}{\sigma_i^2}, \quad (6.26)$$

with  $c_{ij}$  as the weights between the visible units. In the rest of this project, we are interested in the marginal distribution of the visible units only, which becomes

$$P(\mathbf{x}) = \frac{1}{Z} \exp \left( - \sum_{i=1}^F \frac{(x_i - a_i)^2}{2\sigma_i^2} + \sum_{i=1}^F \sum_{j>i}^F x_i c_{ij} x_j \right) \prod_{j=1}^H \left[ 1 + \exp \left( b_j + \sum_{i=1}^F \frac{w_{ij} x_i}{\sigma_i^2} \right) \right], \quad (6.27)$$

by again using the approach detailed in appendix B. In chapter 10, we utilize that this marginal distribution can be split in a Gaussian part, a *partly restricted* part and a product part. Then we see that the expression of the gradient of the log-likelihood function becomes the same with respect to  $\mathbf{a}$ ,  $\mathbf{b}$  and  $\mathbf{w}$  compared to the restricted Boltzmann machine, which means that we only need to calculate the expression of the gradient of the log-likelihood with respect to  $\mathbf{c}$ . This is given by the outer product

$$\frac{\partial \ln P(\mathbf{x} | \mathbf{a}, \mathbf{b}, \mathbf{c}, \mathbf{w})}{\partial \mathbf{c}} = \mathbf{x} \mathbf{x}^T, \quad (6.28)$$

which also is written on a vectorized form.

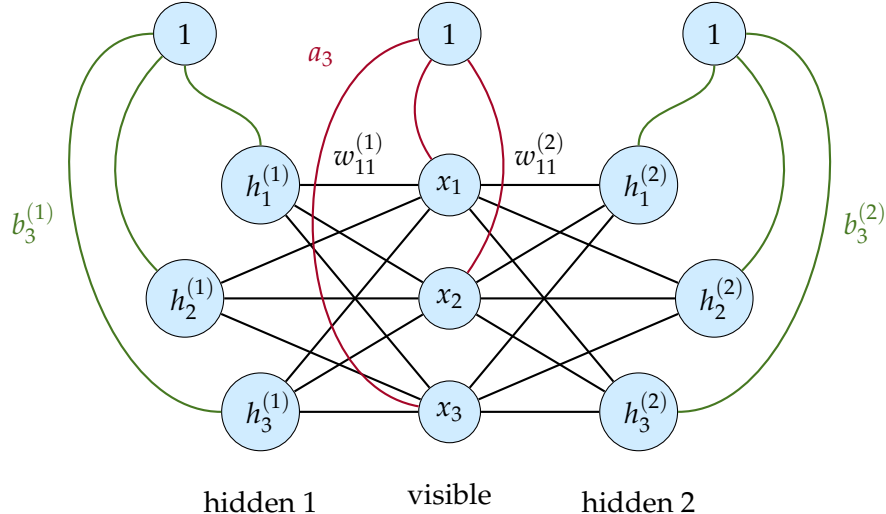


**Figure 6.4:** Deep restricted Boltzmann machine with two hidden layers. Inter-layer connections between the visible and the hidden layer are represented by the black lines, where, for instance, the line connecting  $x_1$  to  $h_1^{(l)}$  represents the weight  $w_{11}^{(l)}$  for  $l \in \{1, 2\}$ . The red lines represent the visible bias weights, where the line going from the bias unit to the visible unit  $x_3$  represents the bias weight  $a_3$ . The green lines represent the hidden bias weights, where the line going from the bias unit to the hidden unit  $h_3^{(l)}$  represents the bias weight  $b_3^{(l)}$  for  $l \in \{1, 2\}$ .

## 6.5 Deep Boltzmann machines

We can also construct deep Boltzmann machines, also known as deep belief networks<sup>84</sup>, where we stack single-layer Boltzmann machines. There are many ways to construct these networks, where the number of layers, unit types, number of units, and the degree of restriction can be chosen by the implementer. The number of combinations is endless, but in order to make use of the depth, all the layers should have different configurations. Otherwise, the deep network can be reduced to a shallower network. In figure (6.4), a restricted Boltzmann machine of two hidden layers is illustrated. We have chosen three hidden units in each layer and three visible units. It should be trivial to imagine how the network can be expanded to more layers. As the main focus so far has been on restricted Boltzmann machines, also the deep networks will be assumed to be restricted, although both partly restricted and unrestricted can be constructed. The system energy of a deep restricted Boltzmann machine of  $L$  layers can be expressed as

$$E(\mathbf{x}, \mathbf{h}) = \sum_{i=1}^F \frac{(x_i - a_i)^2}{2\sigma_i^2} - \sum_{l=1}^L \sum_{j=1}^{H_L} h_j^{(l)} b_j^{(l)} - \sum_{l=1}^L \sum_{i=1}^F \sum_{j=i}^{H_L} \frac{x_i w_{ij}^{(l)} h_j^{(l)}}{\sigma_i^2}, \quad (6.29)$$

where  $H_L$  is the number of hidden units in layer  $L$ . The marginal probability distribution of the visible units read

$$P(\mathbf{x}) = \frac{1}{Z} \exp \left( - \sum_{i=1}^F \frac{(x_i - a_i)^2}{2\sigma^2} \right) \prod_{l=1}^L \prod_{j=1}^{H_L} \left[ 1 + \exp \left( b_j^{(l)} + \sum_{i=1}^F \frac{w_{ij}^{(l)} x_i}{\sigma^2} \right) \right], \quad (6.30)$$

which again can be obtained from the general expressions in appendix B.



## **Part III**

# **Methods**



CHAPTER 7

## Quantum Monte Carlo Methods

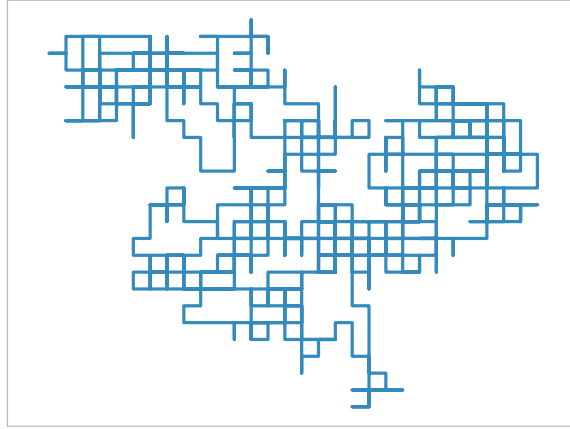


**Figure 7.1:** Random walker on a two-dimensional grid, 1000 moves.

Quantum Monte Carlo methods (QMC) represent a variety *ab initio* methods that attempt to solve the Schrödinger equation using stochastic Monte Carlo integration. *Ab initio* reads "from first principles", which implies that the methods constitute a fundamental approach to the problem. They all seek to evaluate the multi-dimensional integrals that represent various quantum mechanical expectation values. The expression for the energy reads

$$E_0 = \langle \Psi_0 | \hat{\mathcal{H}} | \Psi_0 \rangle = \frac{\int d\mathbf{X} \Psi_0(\mathbf{X})^* \hat{\mathcal{H}} \Psi_0(\mathbf{X})}{\int d\mathbf{X} \Psi_0(\mathbf{X})^* \Psi_0(\mathbf{X})}, \quad (7.1)$$

which provides the ground state energy expectation value for the exact ground state wave function  $\Psi_0(\mathbf{X})$  with  $\mathbf{X} = \{\{r_1, \sigma_1\}, \{r_2, \sigma_2\}, \dots, \{r_N, \sigma_N\}\}$  as the collective coordinates of the  $N$  particles. We use coordinates as a common term for both the spins and the positions. As aforementioned, this integral is analytically infeasible for more or less all interesting systems, evokes the need for numerical methods like QMC. As we will stick to ground state calculations, the wave function  $\Psi(\mathbf{X})$  implies the many-body ground state wave function from this point.

In Monte Carlo integration, we use random numbers to evaluate integrals numerically. Typically, we want to estimate an expectation value  $\langle \hat{O} \rangle$  by approximating the integral with the

sum,

$$\langle \hat{O} \rangle \equiv \int_{-\infty}^{\infty} dx P(x) \hat{O}(x) \approx \frac{1}{M} \sum_{i=1}^M \hat{O}(x_i), \quad (7.2)$$

where  $M$  is the number of *Monte Carlo cycles* and the coordinates  $x_i$  are drawn randomly from the probability density function  $P(x)$ . A great advantage of the QMC methods, is that we obtain approximative ground state wave functions when solving equation (7.1), which by the fourth postulate of quantum mechanics allows estimations of the ground state expectation values associated with other operators as well.

Two widely used QMC methods are the variational Monte Carlo (VMC) method and the diffusion Monte Carlo (DMC) method, where the former is arguably the simplest of all the QMC methods. It attempts to solve the integrals in equation (7.1) directly by varying parameters, with the support of the variational principle presented in section 2.3. This makes VMC a comparably computationally cheap method, but the performance is usually not in the league of the best methods. Diffusion Monte Carlo, on the other hand, is computationally expensive, but is also potentially numerically exact, making it a preferred method when high accuracy is needed. At first glance, it might seem like a tradeoff where VMC is used when computational time is more important than the accuracy and DMC is used when the opposite is true. However, DMC requires a wave function input which is close to the exact wave function, forcing us first to run a VMC calculation to obtain this wave function before the DMC machinery can be started.

As VMC is our main focus in this work, it will be explained thoroughly in this chapter. After that, we will briefly explain the idea behind the DMC method, but since this method is not implemented, it will not be our main priority. To reveal the uncertainty of our results, we will also discuss some methods to estimate the errors, in particular, the blocking method.

## 7.1 Variational Monte Carlo

The variational Monte Carlo method (hereafter the VMC method) is today widely used when it comes to the study of ground state properties of quantum many-body systems. It makes use of Markov chain Monte Carlo methods, often abbreviated MCMC, where the particles are assumed to be moving in Markov chains controlled by Monte Carlo simulations. Going back to the variational principle in equation (2.15), we observe that by choosing an approved wave function, we get an energy larger or equal to the ground state energy.

Before we present the mathematical framework of the method, we will restate the two big challenges in many-body physics, mentioned in the introduction:

1. The correct many-body wave function is generally unavailable.
2. The many-body energy expectation value is analytically infeasible for most systems.

In this section, we will look at how the VMC method tackles these challenges. We start with discussing the trial wave function, and set up our trial wave function ansatz. Then, we define the local energy and explain how it is used to solve the energy integral using Monte Carlo integration. In the end, we will mention some common extensions to the VMC method.

### 7.1.1 The trial wave function

The trial wave function was mentioned in section 3.2.4, but a detailed description of it will first be presented here. In VMC simulations, we start from an initial wave function ansatz, which is our ground state wave function guess. This function is equipped with variational parameters, and in order to estimate the wave function accurately, the trial wave function needs to be able

to approach the correct wave function as we vary the parameters. However, as the many-body wave function is NP-hard to calculate<sup>3</sup>, we will only be able to approximate it and for that reason the wave function is by many considered as the root of all evil in many-body physics. For fermionic systems, the standard trial wave function used in VMC is the Slater-Jastrow wave function. Given a set of variational parameters  $\theta$ , it can be expressed as

$$\Psi_T(\mathbf{X}; \theta) = |\hat{S}(\mathbf{X}; \theta)| J(\mathbf{X}; \theta), \quad (7.3)$$

where  $|\hat{S}(\mathbf{X}; \theta)|$  is a Slater determinant used to bake in the anti-symmetry discussed in section 3.2.1 and  $J(\mathbf{R}; \theta)$  is a Jastrow factor used to model the electron-electron correlations. Recall that the general Slater determinant has the form

$$|\hat{S}(\mathbf{X}; \theta)| = \frac{1}{\sqrt{N!}} \begin{vmatrix} \psi_1(\mathbf{r}_1, \sigma_1; \theta) & \psi_2(\mathbf{r}_1, \sigma_1; \theta) & \dots & \psi_N(\mathbf{r}_1, \sigma_1; \theta) \\ \psi_1(\mathbf{r}_2, \sigma_2; \theta) & \psi_2(\mathbf{r}_2, \sigma_2; \theta) & \dots & \psi_N(\mathbf{r}_2, \sigma_2; \theta) \\ \vdots & \vdots & \ddots & \vdots \\ \psi_1(\mathbf{r}_N, \sigma_N; \theta) & \psi_2(\mathbf{r}_N, \sigma_N; \theta) & \dots & \psi_N(\mathbf{r}_N, \sigma_N; \theta) \end{vmatrix}, \quad (7.4)$$

where the single-particle function  $\psi(\mathbf{r}, \sigma; \theta)$  can be decomposed in a spatial part,  $\phi(\mathbf{r}; \theta)$  and a spin part,  $\xi(\sigma)$ ,

$$\psi(\mathbf{r}, \sigma; \theta) = \phi(\mathbf{r}; \theta) \otimes \xi(\sigma). \quad (7.5)$$

The tensor product is denoted by  $\otimes$ , and the factorization is only possible if the orbital and spin angular momenta of the particle are separable in the Hamiltonian underlying the system's dynamics. We will skip the tensor product notation in the following, but it is implicit that it is there. We also drop the argument  $\theta$  of the single-particle functions. As we in the ground state have double degeneracy, the spatial part will be the same for pairwise spin-up and spin-down particles, and we arrange them as

$$\psi_j(\mathbf{r}_i, \sigma_i) = \begin{cases} \phi_j(\mathbf{r}_i)\xi_{\uparrow}(\sigma_i) & \text{if } j < N_{\uparrow} \\ \phi_j(\mathbf{r}_i)\xi_{\downarrow}(\sigma_i) & \text{if } j \geq N_{\uparrow} \end{cases}. \quad (7.6)$$

Since the first  $N_{\uparrow}$  particles have spin up,  $\sigma_i = \uparrow$ , and the remaining have spin down,  $\sigma_i = \downarrow$ , we can now set up the Slater determinant in equation (7.4) where each single-particle function is split in a spatial part and a spin part,

$$|\hat{S}(\mathbf{X})| = \frac{1}{\sqrt{N!}} \begin{vmatrix} \phi_1(\mathbf{r}_1)\xi_{\uparrow}(\uparrow) & \dots & \phi_{N_{\uparrow}}(\mathbf{r}_1)\xi_{\uparrow}(\uparrow) & \phi_1(\mathbf{r}_1)\xi_{\downarrow}(\uparrow) & \dots & \phi_{N_{\downarrow}}(\mathbf{r}_1)\xi_{\downarrow}(\uparrow) \\ \vdots & & \vdots & \vdots & & \vdots \\ \phi_1(\mathbf{r}_{N_{\uparrow}})\xi_{\uparrow}(\uparrow) & \dots & \phi_{N_{\uparrow}}(\mathbf{r}_{N_{\uparrow}})\xi_{\uparrow}(\uparrow) & \phi_1(\mathbf{r}_{N_{\uparrow}})\xi_{\downarrow}(\uparrow) & \dots & \phi_{N_{\downarrow}}(\mathbf{r}_{N_{\uparrow}})\xi_{\downarrow}(\uparrow) \\ \phi_1(\mathbf{r}_{N_{\uparrow}+1})\xi_{\uparrow}(\downarrow) & \dots & \phi_{N_{\uparrow}}(\mathbf{r}_{N_{\uparrow}+1})\xi_{\uparrow}(\downarrow) & \phi_1(\mathbf{r}_{N_{\uparrow}+1})\xi_{\downarrow}(\downarrow) & \dots & \phi_{N_{\downarrow}}(\mathbf{r}_{N_{\uparrow}+1})\xi_{\downarrow}(\downarrow) \\ \vdots & & \vdots & \vdots & & \vdots \\ \phi_1(\mathbf{r}_N)\xi_{\uparrow}(\downarrow) & \dots & \phi_{N_{\uparrow}}(\mathbf{r}_N)\xi_{\uparrow}(\downarrow) & \phi_1(\mathbf{r}_N)\xi_{\downarrow}(\downarrow) & \dots & \phi_{N_{\downarrow}}(\mathbf{r}_N)\xi_{\downarrow}(\downarrow) \end{vmatrix}.$$

We observe that the the spin-up particles sometimes occupy spin-down states, which they are not allowed to. Therefore, half of the elements become zero and the determinant can be further expressed as

$$|\hat{S}(\mathbf{X})| = \frac{1}{\sqrt{N!}} \begin{vmatrix} \phi_1(\mathbf{r}_1)\xi_{\uparrow}(\uparrow) & \dots & \phi_{N_{\uparrow}}(\mathbf{r}_1)\xi_{\uparrow}(\uparrow) & 0 & \dots & 0 \\ \vdots & & \vdots & \vdots & & \vdots \\ \phi_1(\mathbf{r}_{N_{\uparrow}})\xi_{\uparrow}(\uparrow) & \dots & \phi_{N_{\uparrow}}(\mathbf{r}_{N_{\uparrow}})\xi_{\uparrow}(\uparrow) & 0 & \dots & 0 \\ 0 & \dots & 0 & \phi_1(\mathbf{r}_{N_{\uparrow}+1})\xi_{\downarrow}(\downarrow) & \dots & \phi_{N_{\downarrow}}(\mathbf{r}_{N_{\uparrow}+1})\xi_{\downarrow}(\downarrow) \\ \vdots & & \vdots & \vdots & & \vdots \\ 0 & \dots & 0 & \phi_1(\mathbf{r}_N)\xi_{\downarrow}(\downarrow) & \dots & \phi_{N_{\downarrow}}(\mathbf{r}_N)\xi_{\downarrow}(\downarrow) \end{vmatrix},$$

where the Slater matrix now is block diagonal! For a general block diagonal matrix, the determinant is given by the product of the determinant of each block

$$|\hat{S}(\mathbf{X})| = \frac{1}{\sqrt{N!}} |\hat{S}_\uparrow(\mathbf{X}^\uparrow)| \cdot |\hat{S}_\downarrow(\mathbf{X}^\downarrow)|, \quad (7.7)$$

which can be seen by writing the total matrix as a product over all the block diagonal matrix.  $\hat{S}_\sigma$  is the matrix containing all spin- $\sigma$  states with collective coordinates  $\mathbf{X}^\sigma = \{\{\mathbf{r}_1^\sigma, \xi_\sigma(\sigma)\}, \{\mathbf{r}_2^\sigma, \xi_\sigma(\sigma)\}, \dots, \{\mathbf{r}_N^\sigma, \xi_\sigma(\sigma)\}\}$ . Since all elements in the respective matrices contain the same spin function, it can be factorized out<sup>85</sup>,

$$\begin{aligned} |\hat{S}(\mathbf{X})| &= \frac{1}{\sqrt{N!}} |\hat{D}_\uparrow(\mathbf{r}_1, \mathbf{r}_2, \dots, \mathbf{r}_{N_\uparrow})| \{ \xi_\uparrow(\sigma_1^\uparrow) \xi_\uparrow(\sigma_2^\uparrow) \dots \xi_\uparrow(\sigma_{N_\uparrow}^\uparrow) \}, \\ &\quad \times |\hat{D}_\downarrow(\mathbf{r}_{N_\uparrow+1}, \dots, \mathbf{r}_{N-1}, \mathbf{r}_N)| \{ \xi_\downarrow(\sigma_{N_\uparrow+1}^\downarrow) \dots \xi_\downarrow(\sigma_{N-1}^\downarrow) \xi_\downarrow(\sigma_N^\downarrow) \}, \end{aligned} \quad (7.8)$$

and omitted in the future study. We can then define a set,  $\mathbf{R}^\sigma = \{\mathbf{r}_1^\sigma, \mathbf{r}_2^\sigma, \dots, \mathbf{r}_N^\sigma\}$ , containing the spatial coordinates of the spin- $\sigma$  particles and  $\mathbf{R} = \{\mathbf{r}_1, \mathbf{r}_2, \dots, \mathbf{r}_N\}$  containing the collective spatial coordinates. The Slater determinant we are left with is thus

$$|\hat{S}(\mathbf{R})| = \frac{1}{\sqrt{N!}} |\hat{S}_\uparrow(\mathbf{R}^\uparrow)| \cdot |\hat{S}_\downarrow(\mathbf{R}^\downarrow)|, \quad (7.9)$$

which is independent of spin, i.e. the matrices now consist of the spatial functions  $\phi_j(\mathbf{r}_i)$  as the elements,

$$|\hat{S}_\sigma(\mathbf{R}^\sigma)| = \begin{vmatrix} \phi_1(\mathbf{r}_1^\sigma) & \phi_2(\mathbf{r}_1^\sigma) & \dots & \phi_N(\mathbf{r}_1^\sigma) \\ \phi_1(\mathbf{r}_2^\sigma) & \phi_2(\mathbf{r}_2^\sigma) & \dots & \phi_N(\mathbf{r}_2^\sigma) \\ \vdots & \vdots & & \vdots \\ \phi_1(\mathbf{r}_N^\sigma) & \phi_2(\mathbf{r}_N^\sigma) & \dots & \phi_N(\mathbf{r}_N^\sigma) \end{vmatrix}. \quad (7.10)$$

It is also worth to notice that the number of spin-up particles determines the size of the spin-up matrix, and the number of spin-down particles determines the size of the spin-down matrix. In other words, we can change the ratio between spin-up particles and spin-down particles by adjusting the relative sizes of the determinants. In the implementation, however, we stick to the magic quantum numbers, where  $N_\uparrow = N_\downarrow$ .

## 7.1.2 The Jastrow factor

The second factor in our trial wave function ansatz is the Jastrow factor, which is added in order to account for the electron-electron correlations. As discussed the section 3.2.4, it is crucial to model the so-called cusps correctly, which is the task of the Jastrow factor. We will first discuss a simple Jastrow factor, and then move on the the more complex Padé-Jastrow factor.

### 7.1.2.1 Simple Jastrow

The simple Jastrow factor is just an exponential function with the sum over all particle distances. In addition, each distance  $r_{ij}$  is weighted by a parameter  $\beta_{ij}$ , and the factor becomes

$$J(\mathbf{r}; \boldsymbol{\beta}) = \exp \left( \sum_{i=1}^N \sum_{j>i}^N \beta_{ij} r_{ij} \right). \quad (7.11)$$

All the  $\beta_{ij}$  are free variational parameters, which are expected to be symmetric since the distance matrix is symmetric.

### 7.1.2.2 Padé-Jastrow

The Padé-Jastrow factor is closely related to the simple Jastrow above, but a denominator makes it more complex. It reads

$$J(\mathbf{r}; \beta) = \exp\left(\sum_{i=1}^N \sum_{j>i}^N \frac{a_{ij} r_{ij}}{1 + \beta r_{ij}}\right). \quad (7.12)$$

where  $\beta$  is a variational parameter. In addition, the fractions are multiplied with factors  $a_{ij}$  which depend on the particles  $i$  and  $j$  in the following way:

$$a_{ij} = \begin{cases} 1/(d+1) & \text{if } i, j \text{ are particles of same spin,} \\ 1/(d-1) & \text{if } i, j \text{ are particles of opposite spin,} \end{cases} \quad (7.13)$$

for dimensions  $d \in \{2, 3\}$  where the natural units are used. For two dimensions, this gives  $a_{ij} = 1/3$  (same spin) or  $a_{ij} = 1$  (opposite spin) and for three dimensions  $a_{ij} = 1/4$  (same spin) and  $a_{ij} = 1/2$  (opposite spin)<sup>27,86</sup>. These values are determined by the cusp condition<sup>61</sup>.

### 7.1.3 The local energy

We have now seen how we approximate the wave function by a trial wave function, and in this section we will describe how to find the energy. In chapter 2, we saw that the two-body interaction term makes the integral impossible to solve analytically for many particles, such that we need to rely on numerical methods.

As we have seen, in VMC simulations, we start with a trial wave function guess  $\Psi_T(\mathbf{R}; \theta)$  where the parameters  $\theta$  are varied to minimize the energy. According to the variational principle, the obtained energy will always be higher or equal to the true ground state energy, where the equality is the case if and only if the wave function is the exact ground state wave function. Denoting the exact ground state energy by  $E_0$  and the obtained energy as  $E$ , we can summarize this by the equation

$$E_0 \leq E = \frac{\int d\mathbf{R} \Psi_T(\mathbf{R})^* \hat{\mathcal{H}} \Psi_T(\mathbf{R})}{\int d\mathbf{R} \Psi_T(\mathbf{R})^* \Psi_T(\mathbf{R})}. \quad (7.14)$$

Furthermore, the integral can be written in the form of a general expectation value,

$$E = \int d\mathbf{R} E_L(\mathbf{R}) P(\mathbf{R}), \quad (7.15)$$

defining the local energy as

$$E_L(\mathbf{R}) \equiv \frac{1}{\Psi_T(\mathbf{R})} \hat{\mathcal{H}} \Psi_T(\mathbf{R}). \quad (7.16)$$

$P(\mathbf{R})$  is called the probability density function (PDF) and was first introduced in equation (2.9). In a more general scheme the PDF reads

$$P(\mathbf{R}) = \frac{|\Psi_T(\mathbf{R})|^2}{\int d\mathbf{R} |\Psi_T(\mathbf{R})|^2}, \quad (7.17)$$

where the wave function is not necessarily normalized. Since the energy expectation value now is in the form of a general expectation value, we can use the approximation set up by Monte Carlo integration in equation (7.2), yielding

$$E \approx \frac{1}{M} \sum_{i=1}^M E_L(\mathbf{R}_i), \quad (7.18)$$

where the local energies  $E_L(\mathbf{R}_i)$  are still evaluated with particle coordinates  $\mathbf{R}_i$  drawn from  $P(\mathbf{R})$ . In this manner, the obtained energy is guaranteed to approach the exact energy as the number of Monte Carlo cycles,  $M$ , increases. Actually, the standard error goes as  $\mathcal{O}(1/\sqrt{M})$ , making the method accurate for large  $M$ 's. In the limit  $M \rightarrow \infty$ , the error goes to zero,

$$\langle E_L \rangle = \lim_{M \rightarrow \infty} \frac{1}{M} \sum_{i=1}^M E_L(\mathbf{R}_i), \quad (7.19)$$

indicating the need for a large number of cycles. This is associated with a zero-variance property governing the quantum Monte Carlo methods, stating that the variance in the true ground state should be zero<sup>87,88</sup>. Various sampling regimes are described in section 7.3.

#### 7.1.4 Parameter update

Another important part of the VMC method is the update of parameters, which we need in order to find an approximative wave function. In section 5.6, we discussed various gradient-based optimization algorithms for iterative minimization of the cost function,  $\mathcal{C}(\theta)$ , in machine learning, and the same methods can be used in VMC simulations.

However, we need to define a cost function for VMC which is minimized when the ground state energy is obtained. According to the variational principle, the ground state energy is the lowest energy we can obtain, so an obvious cost function is the energy expectation value. We therefore set

$$\mathcal{C}(\theta) = \langle E_L \rangle, \quad (7.20)$$

since we get the expectation value of the local energy from the Metropolis sampling. Further, we use the definition of the gradient of an expectation value from Umrigar & Filippi<sup>89</sup> and obtain

$$\nabla_{\theta_j} \langle E_L \rangle = 2 \left( \langle E_L \nabla_{\theta_j} \ln \Psi_T \rangle - \langle E_L \rangle \langle \nabla_{\theta_j} \ln \Psi_T \rangle \right), \quad (7.21)$$

which means that we need to calculate the expectation values  $\langle E_L \nabla_{\theta_j} \ln \Psi_T \rangle$  and  $\langle \nabla_{\theta_j} \ln \Psi_T \rangle$  in addition to the expectation value of the local energy. These expectation values are found from the integrals

$$\langle \nabla_{\theta_j} \ln \Psi_T \rangle = \int_{-\infty}^{\infty} d\mathbf{R} \nabla_{\theta_j} \ln \Psi_T(\mathbf{R}) P(\mathbf{R}), \quad (7.22)$$

and

$$\langle E_L \nabla_{\theta_j} \ln \Psi_T \rangle = \int_{-\infty}^{\infty} d\mathbf{R} E_L(\mathbf{R}) \nabla_{\theta_j} \ln \Psi_T(\mathbf{R}) P(\mathbf{R}), \quad (7.23)$$

which can be found by Monte Carlo integration in the same way as the local energy:

$$\langle \nabla_{\theta_j} \ln \Psi_T \rangle \approx \frac{1}{M} \sum_{i=1}^M \nabla_{\theta_j} \ln \Psi_T(\mathbf{R}_i) \quad (7.24)$$

and

$$\langle E_L \nabla_{\theta_j} \ln \Psi_T \rangle \approx \frac{1}{M} \sum_{i=1}^M E_L(\mathbf{R}_i) \nabla_{\theta_j} \ln \Psi_T(\mathbf{R}_i). \quad (7.25)$$

Note that the only closed-form expression needed, in addition to the local energy, is the expression of  $\nabla_{\theta_j} \ln \Psi_T(\mathbf{R}_i)$ . This will later be found for the various wave functions.

We want to stress that the local energy is not the only possible choice of cost function. By taking advantage of the zero-variance property of the expectation value of the local energy in the minimum, one can also minimize the variance. Variance minimization requires the calculation of a few additional expectation values, but it is a fully manageable task to do. See for instance Umrigar & Filippi<sup>89</sup> for more information.

### 7.1.5 The electron density

In section 3.3, we introduced the electron density and defined the  $P$ -body density as an integral over all particles but  $P$ ,

$$\rho_P(\mathbf{r}_1, \dots, \mathbf{r}_P) = N \int_{-\infty}^{\infty} d\mathbf{r}_{P+1} \dots d\mathbf{r}_N |\Psi(\mathbf{r}_1, \dots, \mathbf{r}_N)|^2. \quad (7.26)$$

Not surprising, also this integral will be solved using Monte Carlo integration, but in a slightly different way than the integrals above since this integral returns a distribution rather than an expected value. First, we divide the space into bins of known sizes. After that, we sample the particles and count the number of times a particle occurs in each bin. We want to find the relative number of particles in each bin concerning the size of the bin, so if the bins are of different sizes, we need to standardize them all by dividing by their respective sizes. In the end, we normalize the density such that the sum of all densities becomes equal to  $N$ . This method and the particular implementation is detailed in section 9.8.

### 7.1.6 Common extensions

This finalizes the essential theory behind the VMC method. However, a sampling algorithm is needed to draw samples randomly from  $P(\mathbf{R})$ , and in section 7.3 some popular sampling techniques are described. Before we jump into this field, we will discuss some natural extensions and improvements to the VMC method.

Initially, the particle configuration  $\mathbf{R}$  might not be representative for a configuration in equilibrium, making the first cycles a poor estimate of the expectation value. An easy fix to this problem is to basically ignore the first sampling period, known as the *burn-in period*. With this in mind, we can implement an equilibration fraction describing the fraction of the total number of cycles that are used in the burn-in period. When running multiple parallel processes, the burn-in period should be the same for all the processes.

We also have a technique called *thinning*, which means picking every  $n$ 'th sample in the chain and ignore the rest. This is shown to give a more or less identical expectation value and makes the program less memory-requiring, but due to worse statistics, this should be avoided as long as there is no lack of memory.

## 7.2 Unifying Quantum Mechanics and Machine Learning

Now as we have introduced the necessary theory, both in the form of quantum theory and machine learning theory, in addition to detailing the variational Monte Carlo (VMC) method, we are ready to unify the machine learning and quantum mechanics. As hinted above, the way we do this is to let a restricted Boltzmann machine define our single-particle functions in the trial wave function, and then minimize the energy using a standard VMC framework. This is very similar to the approach of Pfau *et al.*<sup>25</sup>, but an essential difference is that they also used the relative distances between the particles as inputs to the neural network. Further, we investigate how the results change when Jastrow factors with increasing amount of physical intuition are added. As the main goal is to find a method that requires less physical intuition in order to provide accurate results compared to the traditional methods, adding a simple Jastrow factor is also very interesting. We look at three different trial wave function ansätze for the Boltzmann machines: a Slater determinant where the single-particle functions are given by the marginal distribution of the visible units of a Gaussian-binary restricted Boltzmann machine (RBM), an RBM with a simple Jastrow added (RBM+SJ) and an RBM with a Padé-Jastrow factor added (RBM+PJ). They are detailed in respective sections below.

### 7.2.1 Restricted Boltzmann machine without Jastrow factor (RBM)

In section 7.1.1, we saw how the VMC method attempts to solve the time-independent Schrödinger equation directly by varying the parameters in a trial wave function. In order to satisfy the anti-symmetry properties of a fermionic many-body wave function, the trial wave function was composed as a Slater determinant,

$$|\hat{S}(\mathbf{R})| = \frac{1}{\sqrt{N!}} |\hat{S}_\uparrow(\mathbf{R}^\uparrow)| \cdot |\hat{S}_\downarrow(\mathbf{R}^\downarrow)|, \quad (7.27)$$

where

$$|\hat{S}_\sigma(\mathbf{R})| = \begin{vmatrix} \phi_1(\mathbf{r}_1) & \phi_2(\mathbf{r}_1) & \dots & \phi_N(\mathbf{r}_1) \\ \phi_1(\mathbf{r}_2) & \phi_2(\mathbf{r}_2) & \dots & \phi_N(\mathbf{r}_2) \\ \vdots & \vdots & \ddots & \vdots \\ \phi_1(\mathbf{r}_N) & \phi_2(\mathbf{r}_N) & \dots & \phi_N(\mathbf{r}_N) \end{vmatrix}. \quad (7.28)$$

Even though we want a method which requires as little physical intuition as possible, the wave function needs to obey Fermi-Dirac statistics, and we therefore also approximate the trial wave function with the Slater determinant for the machine learning methods. Further, we use the same framework as we did for traditional VMC ansätze, including the Slater determinant, but the single-particle functions (SPFs)  $\phi_j(\mathbf{r}_i)$  are given by the marginal distribution of the visible units from a restricted Boltzmann machine,  $P(\mathbf{r})$ . For quantum dots, we also add the Hermite polynomials,  $H_n(\mathbf{r})$ , to obtain a unique SPF for each state. We then have

$$\phi_j(\mathbf{r}_i) = H_j(\mathbf{r}_i)P(\mathbf{r}_i), \quad (7.29)$$

where the marginal distribution is the distribution obtained in equation (6.19). The RBM ansatz is then simply

$$\Psi_T(\mathbf{R}) = |\hat{S}_\uparrow(\mathbf{R}^\uparrow)| \cdot |\hat{S}_\downarrow(\mathbf{R}^\downarrow)|, \quad (7.30)$$

where we omit the normalization factor,  $Z$ , as it is not required by the method, as we will see in section 7.3.

### 7.2.2 RBM with a simple Jastrow factor (RBM+SJ)

This ansatz, abbreviated RBM+SJ, is just an extension of the RBM ansatz described in the previous section, where we add the simple Jastrow factor described in section 7.1.2 to help modeling the electron-electron cusp. When adding a Jastrow factor we also add some more physical intuition to the trial wave function, but the Jastrow factor used here still contains a minimum of physical intuition. The trial wave function using this method thus takes the form

$$\Psi_T(\mathbf{R}) = |\hat{S}_\uparrow(\mathbf{R}^\uparrow)| \cdot |\hat{S}_\downarrow(\mathbf{R}^\downarrow)| J(\mathbf{R}; \beta), \quad (7.31)$$

where  $\beta$  is a set of variational parameters and where the normalization factor,  $Z$ , again is omitted.

### 7.2.3 RBM with a Padé-Jastrow factor (RBM+PJ)

Lastly, we add the well-known Padé-Jastrow factor to the RBM ansatz, and obtain a new ansatz abbreviated RBM+PJ. As discussed in section 7.1.2, the Padé-Jastrow factor is constructed to satisfy the cusp condition, and it is also interesting to see how an increased amount of physical intuition in the trial wave function affects the results. The RBM+PJ ansatz then reads

$$\Psi_T(\mathbf{R}) = |\hat{S}_\uparrow(\mathbf{R}^\uparrow)| \cdot |\hat{S}_\downarrow(\mathbf{R}^\downarrow)| J(\mathbf{R}; \beta), \quad (7.32)$$

where we recall that the Padé-Jastrow factor contains the variational parameter  $\beta$ .

## 7.3 The Metropolis Algorithm

Metropolis sampling is a Markov chain Monte Carlo method, which generates a Markov chain using a proposal density for new steps, and the method also rejects unsatisfying moves. In its most simple form, a particle is moved in a random direction, which was the original method invented by Metropolis *et al.*<sup>90</sup> back in 1953. Later, the method was improved by Hastings<sup>35</sup>, giving rise to the more general Metropolis-Hastings algorithm. The genius of the Metropolis algorithms is that the acceptance of a move is not based on the probabilities themselves, but rather the ratio between the new and the old probabilities. In that way, we avoid calculating the normalizing factor, which is often computationally intractable.

We will first discuss Markov chains in general, before we connect them to the original Metropolis algorithm, henceforth called *brute-force sampling*, and then the Metropolis-Hastings algorithm, also called *importance sampling*. If we denote the current state by  $\mathbf{R}$ , and the proposed state by  $\mathbf{R}'$ , we have a transition rule  $P(\mathbf{R}'|\mathbf{R})$  for going from  $\mathbf{R}$  to  $\mathbf{R}'$  and a transition rule  $P(\mathbf{R}|\mathbf{R}')$  for going the opposite way. If we then assume that the rules satisfy *ergodicity* and *detailed balance*, we have the following relationship:

$$P(\mathbf{R}'|\mathbf{R})P(\mathbf{R}) = P(\mathbf{R}|\mathbf{R}')P(\mathbf{R}'), \quad (7.33)$$

which is actually a restatement of Bayes' theorem presented in section 6.1. The next step is to rewrite the transition rules in terms of a proposal distribution  $T(\mathbf{R}'|\mathbf{R})$  and an acceptance probability  $A(\mathbf{R}', \mathbf{R})$ ,

$$P(\mathbf{R}'|\mathbf{R}) = T(\mathbf{R}'|\mathbf{R})A(\mathbf{R}', \mathbf{R}). \quad (7.34)$$

In order to satisfy the detailed balance, we need to choose  $A(\mathbf{R}', \mathbf{R})$  such that

$$A(\mathbf{R}', \mathbf{R}) = \min \left[ 1, \frac{T(\mathbf{R}'|\mathbf{R})P(\mathbf{R}')}{T(\mathbf{R}'|\mathbf{R})P(\mathbf{R})} \right], \quad (7.35)$$

where we limit  $A$  to be maximum 1 as the probability should not exceed 1. We want to accept a move with probability  $A(\mathbf{R}', \mathbf{R})$ . One way to do that is to draw a number from a uniform distribution between 0 and 1. If this number is lower than the acceptance, the move should be accepted and if not, the move should be rejected.

### 7.3.1 Brute-force sampling

In its simplest form, the move is proposed randomly both in magnitude and direction. Mathematically, we can write this as

$$\mathbf{R}' = \mathbf{R} + \Delta x d\mathbf{r}, \quad (7.36)$$

where  $\Delta x$  is the step length and  $d\mathbf{r}$  has a random magnitude and direction (typically which particle to move). We obtain the naïve acceptance probability when requiring  $T(\mathbf{R}'|\mathbf{R}) = T(\mathbf{R}|\mathbf{R}')$ , such that it simplifies to

$$A(\mathbf{R}', \mathbf{R}) = \min \left[ 1, \frac{P(\mathbf{R}')}{P(\mathbf{R})} \right]. \quad (7.37)$$

However, with this approach, an unsatisfying number of moves will be rejected as the particles can be moved in all directions, which results in a significant waste of computing power. A better method is **importance sampling**, since the particles are moved according to the so-called quantum force to be defined below.

### 7.3.2 Importance sampling

Importance sampling is a more intelligent sampling method than the brute-force sampling, since the new position is based on an educated guess. To understand how it works, we need to take a quick look at diffusion processes. We start from the Fokker-Planck equation,

$$\frac{\partial P(\mathbf{R}, t)}{\partial t} = D \nabla (\nabla - \mathbf{F}) P(\mathbf{R}, t), \quad (7.38)$$

which describes how a probability distribution  $P(\mathbf{R}, t)$  evolves in appearance of a drift force  $\mathbf{F}$ . In the case  $\mathbf{F} = \mathbf{0}$ , the equation reduces to the diffusion equation with  $D$  as the diffusion constant. This simplifies to  $D = 1/2$  in natural units.

The Langevin equation states that a diffusion particle tends to move parallel to the drift force in the coordinate space, with  $\eta$  introducing some random noise. The equation reads

$$\frac{\partial \mathbf{R}(t)}{\partial t} = D \mathbf{F}(\mathbf{R}(t)) + \eta. \quad (7.39)$$

Given a position  $\mathbf{R}$ , the new position  $\mathbf{R}'$  can be found by applying forward-Euler on the Langevin equation, obtaining

$$\mathbf{R}' = \mathbf{R} + D\Delta t \mathbf{F}(\mathbf{R}) + \xi \sqrt{\Delta t}, \quad (7.40)$$

where  $\Delta t$  is a fictive time step and  $\xi$  is a Gaussian random variable. Further, we want to find an expression of the drift force,  $\mathbf{F}$ , which makes the system converge towards a stationary state. A stationary state is found when the probability density function,  $P(\mathbf{R})$ , is constant in time, i.e. when the left-hand side of the Fokker-Planck equation is zero. In that case, we can rewrite the equation as

$$\nabla^2 P(\mathbf{R}) = P(\mathbf{R}) \nabla \mathbf{F}(\mathbf{R}) + \mathbf{F}(\mathbf{R}) \nabla P(\mathbf{R}), \quad (7.41)$$

where the parenthesis are written out and we have moved the term that is independent of the force  $\mathbf{F}$  to the left-hand side. Moreover, we assume that the drift force takes the form  $\mathbf{F}(\mathbf{R}) = g(\mathbf{R}) \nabla P(\mathbf{R})$  based on the fact that the force should point in the direction of the steepest slope. We can then go ahead and write

$$\nabla^2 P(\mathbf{R}) (1 - P(\mathbf{R})g(\mathbf{R})) = \nabla(g(\mathbf{R})P(\mathbf{R})) \nabla P(\mathbf{R}), \quad (7.42)$$

where the quantity  $\nabla^2 P(\mathbf{R})$  is factorized out from two of the terms. The equation is satisfied when  $g(\mathbf{R}) = 1/P(\mathbf{R})$ , such that the drift force evolves to the well-known form

$$\mathbf{F}(\mathbf{R}) = \frac{\nabla P(\mathbf{R})}{P(\mathbf{R})} = 2 \frac{\nabla \Psi_T(\mathbf{R})}{\Psi_T(\mathbf{R})} = 2 \nabla \ln \Psi_T(\mathbf{R}), \quad (7.43)$$

which is also known as the *quantum force*.

The remaining part concerns the acceptance of the moves. For this, we need to find the sampling distributions  $T(\mathbf{R}'|\mathbf{R})$  from equation (7.35), which are just the solutions of the Fokker-Planck equation. The solutions read

$$G(\mathbf{R}', \mathbf{R}, \Delta t) \frac{1}{(4\pi D \Delta t)^{3N/2}} \exp\left(-(\mathbf{R}' - \mathbf{R} - D\Delta t \mathbf{F}(\mathbf{R}))^2 / 4D\Delta t\right), \quad (7.44)$$

which is categorized as a Green's function. In general, the essential property of any Green's function is that it provides a way to describe the response of an arbitrary differential equation

solution. For our particular case, it correspond to  $\mathcal{N}(\mathbf{R}'|\mathbf{R} + D\Delta t \mathbf{F}(\mathbf{R}), 2D\Delta t)$  which is the normal distribution with mean  $\mu = \mathbf{R} + D\Delta t \mathbf{F}(\mathbf{R})$  and variance  $\sigma^2 = 2D\Delta t$ . By using this, the acceptance probability of the importance sampling can finally be written as

$$A(\mathbf{R}'|\mathbf{R}) = \min \left[ 1, \frac{G(\mathbf{R}, \mathbf{R}', \Delta t) P(\mathbf{R}')}{G(\mathbf{R}', \mathbf{R}, \Delta t) P(\mathbf{R})} \right], \quad (7.45)$$

where the marginal probabilities are still given by equation (7.17).

### 7.3.3 Gibbs sampling

Gibbs sampling has, throughout the years, gained high popularity in the machine learning community when it comes to training Boltzmann machines. There are probably many factors that contribute to this, where the performance is one of them. Another proper motivation is the absence of tuning parameters, which makes the method more comfortable to deal with compared to many of its competitors. The method is an instance of the Metropolis-Hastings algorithm and is therefore classified as another Markov chain Monte Carlo method. It differs from the Metropolis methods discussed above by the fact that all the moves are accepted, such that we do not waste computational time on rejected moves. Nevertheless, we should not use this argument alone to motivate the use of Gibbs sampling, as the algorithm usually and preferably rejects less than 1% of the moves in importance sampling.

We will in the following briefly describe the mathematical foundation of the method, before we, for the sake of clarity, connect it to the restricted Boltzmann machines. The method is built on the concept that, given a multivariate distribution, it is simpler to sample from a conditional distribution than to marginalize by integrating over a joint distribution. This is the reason why we do not need the marginal distributions in Gibbs sampling, but rather the conditional distributions. In the most general case, Gibbs sampling proposes a rule for going from a sample  $\mathbf{x}^{(i)} = \{x_1^{(i)}, x_2^{(i)}, \dots, x_n^{(i)}\}$  to another sample  $\mathbf{x}^{(i+1)} = \{x_1^{(i+1)}, x_2^{(i+1)}, \dots, x_n^{(i+1)}\}$ , similar to the Metropolis algorithm. However, in Gibbs sampling the transition from  $x_j^{(i)}$  to  $x_j^{(i+1)}$  is performed according to the conditional distribution specified by

$$P(x_j^{(i+1)} | x_1^{(i+1)}, \dots, x_{j-1}^{(i+1)}, x_{j+1}^{(i+1)}, \dots, x_n^{(i+1)}). \quad (7.46)$$

The marginal distribution of a subset of variables can then be approximated by simply considering the samples for that subset of variables, ignoring the rest.

For a restricted Boltzmann machine, this becomes a two-step sampling process as we have two layers, such that we use the conditional probabilities  $P(\mathbf{x}|\mathbf{h})$  and  $P(\mathbf{h}|\mathbf{x})$  to update the visible and hidden units respectively. For the restricted Boltzmann machine with Gaussian-binary units presented in section 6.3, the conditional probability of  $h_j = 0$  given a set of visible nodes  $\mathbf{x}$  is

$$P(h_j = 0|\mathbf{x}) = \frac{1}{1 + \exp(+b_j + \sum_{i=1}^N x_i w_{ij} / \sigma_i^2)}, \quad (7.47)$$

and the corresponding conditional probability of  $h_j = 1$  is

$$P(h_j = 1|\mathbf{x}) = \frac{1}{1 + \exp(-b_j - \sum_{i=1}^N x_i w_{ij} / \sigma_i^2)}, \quad (7.48)$$

which is by the way again the sigmoid. Note that  $P(h_j = 0|\mathbf{x}) + P(h_j = 1|\mathbf{x}) = 1$ , indicating that a hidden node,  $h_j$ , can only take the values 0 or 1. When updating the hidden node, we typically

calculate the sigmoid  $P(h_j = 1|x)$  and set  $h_j$  to 1 if this probability is larger than 1/2, and set it to 0 otherwise.

For the update of the visible nodes, we see from equation (6.22) that the visible nodes are chosen after the normal distribution,

$$P(x_i|\mathbf{h}) = \mathcal{N}\left(a_i + \sum_{j=1}^H w_{ij}h_j, \sigma_i^2\right), \quad (7.49)$$

which introduces some stochasticity to the system. By going back and forth in the Boltzmann machine multiple times (a round trip corresponds to an iteration), the hope is that the expectation values can be approximated by averaging over all the iterations.

As pointed out earlier, the Gibbs sampling will not be implemented in this work, but we describe it for completeness purposes. The reason for this is that the method has not shown promising results for our specific problem, and we will instead rely on Metropolis sampling. We have already tested the Gibbs sampling in another similar project on small quantum dots, and so have others like Flugsrud<sup>26</sup>. The results are matching and show poor performance compared to the Metropolis-Hastings algorithm.

However, the Gibbs sampling method should not be underestimated. Carleo & Troyer<sup>24</sup> showed its importance when solving the Ising model using a restricted Boltzmann machine and Gibbs sampling, and in traditional Boltzmann machines, the Gibbs sampling is the preferred tool.

## 7.4 Diffusion Monte Carlo

The second and last quantum Monte Carlo method we will discuss is the diffusion Monte Carlo (DMC) method. DMC belongs to a class of projection and Green's function approaches and provides in principle an exact solution of the Schrödinger equation. However, for fermionic systems, the method is plagued by the occurrence of a sign-problem, known as the fermion sign problem<sup>3</sup>, and we need to use approximations to overcome the problem. The most common fix is the fixed-node approximation, which introduces errors to the computations. The problem is also attempted to solve using shadow wave functions, for instance, by Calcavecchia *et al.*<sup>91</sup>, which have many commonalities with our restricted Boltzmann machine (RBM) approach. The idea is that the RBMs can also contribute to solve the sign problem, but we leave this for later studies.

Since the DMC method is used as a reference for more or less all the produced results, it is natural to give a brief discussion of the idea behind the method. By the fifth postulate of quantum mechanics discussed in section 2.1, the motion of a particle that moves in a potential  $V(\mathbf{R})$  is described by the time-dependent Schrödinger equation,

$$i\frac{\partial\Psi(\mathbf{R},t)}{\partial t} = \hat{\mathcal{H}}\Psi(\mathbf{R},t), \quad (7.50)$$

with  $\Psi(\mathbf{R},t)$  as the many-body wave function,  $t$  as the time and  $i$  as the solution of  $x^2 = -1$ . In natural units, the Hamiltonian is given by

$$\hat{\mathcal{H}} = -\frac{1}{2}\nabla^2 + V(\mathbf{R}). \quad (7.51)$$

Further, we assume that the potential becomes infinite as  $x \rightarrow \pm\infty$ , such that the particle motion is confined to a finite spatial domain. The formal solution of the time-dependent Schrödinger

equation is then given by an expansion of the eigenfunctions of  $\hat{\mathcal{H}}$ ,  $\phi_n(\mathbf{r})$ , given by

$$\Psi(\mathbf{R}, t) = \sum_{n=0}^{\infty} c_n \phi_n(\mathbf{R}) e^{-E_n t / \hbar}. \quad (7.52)$$

$\hbar$  is the reduced Planck's constant and the coefficients can be obtained by integrating up the eigenfunction and the many-body wave function,

$$c_n = \int_{-\infty}^{\infty} d\mathbf{R} \phi_n(\mathbf{R}) \Psi(\mathbf{R}, 0), \quad (7.53)$$

under the assumption that the eigenfunctions are orthonormal and that the energies are sorted in increasing order,  $E_1 < E_2 < E_3 \dots$ . The DMC method is based on the time-imaginary Schrödinger equation, which is obtained by a **shift of energy scale**, setting  $V(\mathbf{R}) \rightarrow V(\mathbf{R}) - E_R$  and  $E_n \rightarrow E_n - E_R$ , which does not change any physical quantity. By further using the **Wick rotation of time** setting  $\tau = it$ , we obtain the time-imaginary Schrödinger equation<sup>92</sup>,

$$-\frac{\partial \Psi(\mathbf{R}, \tau)}{\partial \tau} = -\frac{1}{2} \nabla^2 \Psi(\mathbf{R}, \tau) + [V(\mathbf{r}) - E_R] \Psi(\mathbf{R}, \tau), \quad (7.54)$$

which gives the expansion

$$\Psi(\mathbf{R}, \tau) = \sum_{n=0}^{\infty} c_n \phi_n(\mathbf{R}) e^{-(E_n - E_R)\tau}. \quad (7.55)$$

The time-imaginary Schrödinger equation is similar to the Fokker-Planck equation presented in equation (7.38), which was noticed by Fermi already around 1945<sup>32,33</sup>. Since we have analytical solutions of the Fokker-Planck equation, the idea is to apply the same solutions to equation (7.54). To clarify this, consider the time-imaginary Schrödinger equation for non-interacting particles,

$$\frac{\partial \Psi(\mathbf{R}, \tau)}{\partial \tau} = \frac{1}{2} \nabla^2 \Psi(\mathbf{R}, \tau), \quad (7.56)$$

which is really similar to the diffusion equation,

$$\frac{\partial \phi(\mathbf{R}, t)}{\partial t} = D \nabla^2 \phi(\mathbf{R}, t), \quad (7.57)$$

where  $D$  is the diffusion constant set to 1/2 in our calculations. We end our motivation of the DMC method here, and relegate the reader to Kosztin *et al.*<sup>92</sup> for a thorough and comprehensive explanation of the method. The last section of this chapter is about error estimation, which is very important in experimental physics, including computer experiments.

## 7.5 Error estimation

In experiments, we have two main classes of errors; systematical errors and statistical errors. The former is a result of external factors such as uncertainties in the apparatus. They are often difficult to quantify. Statistical errors, however, can be found by estimating the variance of the sample mean, which we want to find accurately and efficiently. Monte Carlo simulations can be treated as computer experiments, and therefore we can use the same analyzing tools as we do for real experiments.

There are many ways to estimate the variance, where the simplest approach ignores correlation effects between the measurements. More accurate standard error estimations can be performed by resampling methods like blocking<sup>54</sup>, bootstrap<sup>93</sup>, or jackknife<sup>94</sup>. We will cover the blocking method only since we stick to that method in our particular implementations. To save computational time, we resample the final iteration only; for the others, we use the simple estimation method.

### 7.5.1 Central concepts of statistics

Before we go through the blocking method, we will give a brief introduction to some useful statistical quantities. We start with the *moments*, which are given by

$$\langle x^n \rangle = \int dx p(x) x^n, \quad (7.58)$$

where  $p(x)$  is the true probability density function. In order to make physical sense, this function needs to be normalized such that the integral over all possible outcomes gives a total probability of 1. This is associated with the zero'th moment, where we get  $\int dx p(x) = 1$ . The first moment is the *mean* of  $p(x)$ , and is often denoted by the letter  $\mu$ ,

$$\langle x \rangle = \mu = \int dx p(x) x. \quad (7.59)$$

Moreover, we can define the *central moments* given by

$$\langle (x - \langle x \rangle)^n \rangle = \int dx (x - \langle x \rangle)^n p(x), \quad (7.60)$$

which is centered around the mean. With  $n = 0$  and  $n = 1$ , this is easy to find, but what is the central moment with  $n = 2$ ? The central moment with  $n = 2$  is what we call the *variance*, and is often denoted as  $\sigma^2$ . One can show that

$$\sigma^2 = \langle (x - \langle x \rangle)^2 \rangle = \langle x^2 \rangle - \langle x \rangle^2. \quad (7.61)$$

The *standard deviation* is defined as the square-root of the variance,  $\sigma$ , and will be presented as the measure of the uncertainty in the last digit of numerical results. By using the expressions above, we can calculate the mean and the variance of a probability density function  $p(x)$ , but things get harder when  $p(x)$  is unknown. If the probability density function is unavailable, we cannot find the exact sample mean and sample mean variance. However, we can make an estimate, writing

$$\langle X \rangle \approx \frac{1}{n} \sum_{i=1}^n X_i \equiv \bar{X}, \quad (7.62)$$

for the sample mean given a sample  $X$  containing  $n$  points. Assuming that the measurements  $X_i$  are *independent* with identical variance  $\sigma^2$  for each  $i \in \{1, \dots, n\}$ <sup>95</sup>,

$$\text{var}(\bar{X}) = \text{var}\left(\frac{1}{n} \sum_{i=1}^n X_i\right) = \frac{1}{n^2} \sum_{i=1}^n \underbrace{\text{var}(X_i)}_{=\sigma^2} = \frac{1}{n^2} n \sigma^2 = \frac{\sigma^2}{n}. \quad (7.63)$$

Furthermore, in this case, the following is an unbiased estimator of the variance  $\sigma^2$ :

$$S_n^2 = \frac{1}{n-1} \sum_{i=1}^n (X_i - \bar{X})^2. \quad (7.64)$$

The law of large numbers states that the estimated sample mean approaches the true sample mean as  $n$  goes to infinity. This is closely related to the central limit theorem, which states that the probability distribution of  $X$ ,  $p_X(x)$ , can be approximated as a normal distribution  $\mathcal{N}(\mu, \sigma)$  with  $\mu = \bar{X}_n$  and  $\sigma = \text{var}(\bar{X})$  as the number of sampling points,  $n$ , goes to infinity.

On the other hand, if the samples are *correlated*, equation (7.63) becomes an underestimation of the *sample error*  $\text{err}_X^2$ , and is thus more a guideline for the size of the uncertainty, more than an actual estimate of it. In that case, we need to estimate the *covariance* given by

$$\text{cov}(X_i, X_j) = \langle (X_i - \mu)(X_j - \mu) \rangle \quad \forall \quad i, j \in \{1, \dots, n\}. \quad (7.65)$$

Usually, the covariance is not known from the data, and we are advised to use

$$G_{ij} = (X_i - \bar{X})(X_j - \bar{X}), \quad (7.66)$$

in order to obtain an estimate<sup>96</sup>. Note that the variance is just the special case where  $X_i$  and  $X_j$  are independent. We define the sample error as

$$\text{err}_X^2 = \frac{1}{n^2} \sum_{i=1}^n \sum_{j=1}^n \text{cov}(X_i, X_j), \quad (7.67)$$

with an ability to be further expressed as a function of the *autocovariance*, defined as

$$\gamma(h) = \text{cov}(X_i, X_{i+h}), \quad (7.68)$$

and is thus just a measure of the correlation of a section of a time series with another section of the same time series. If  $h = 0$ , this is just the variance  $\gamma(0) = \sigma^2/n$  and the sample error simplifies to

$$\text{err}_X^2 = \frac{\sigma^2}{n} + \frac{2}{n} \sum_{h=1}^{n-1} \left(1 - \frac{h}{n}\right) \gamma(h). \quad (7.69)$$

A problem with this definition of the sampling error is that it turns out to be very expensive to calculate as the number of samples gets large. We require a cheaper method, which is the task of the resampling methods. We will, in the following, discuss the blocking algorithm, which is the resampling method of choice in this work.

### 7.5.2 Blocking

Above, we have described the need for a proper uncertainty estimation in computational simulations, where the covariance was included in the calculation of  $\sigma^2$ . A quick and easy way to get a proper estimate of the uncertainty is by using the blocking method.

When the blocking method was made accessible by Flyvbjerg & Petersen<sup>54</sup> in 1989, the method required hyper-parameters which had to be carefully adjusted for each particular data set. In 2018, Jonsson<sup>97</sup> reinvented the algorithm and made it automated, with no need for external parameters. Despite this, no compromise was made on performance. The method scales as  $12n + \mathcal{O}(\log_2 n)$  for small data sets, but reduces to  $n + \mathcal{O}(1)$  for large data sets, which makes it preferred over bootstrap and jackknife for large data sets. We will now go through the idea behind the blocking method.

Consider a stationary time series  $\{x_1, x_2, \dots, x_n\}$  with  $n = 2^d$  data point for some integer  $d > 1$ . For this series, an autocovariance function  $\gamma(h)$  is guaranteed to exist<sup>97</sup>. We arrange the data in a vector

$$X = (x_1, x_2, \dots, x_n), \quad (7.70)$$

which we assume to be asymptotically uncorrelated. The idea is to take the mean of subsequent pairs of elements from  $X$ , and form a new vector  $X_1$ . We then repeat the operation on  $X_1$  and

form a new vector  $X_2$  and so on. This is the reason why we require  $n = 2^d$  with  $d$  as an integer. If  $k$  denotes an element in vector  $X_i$ , we can write the procedure recursively as

$$\begin{aligned}(X_0)_k &\equiv (X)_k, \\ (X_{i+1})_k &\equiv \frac{1}{2}((X_i)_{2k-1} + (X_i)_{2k}),\end{aligned}\tag{7.71}$$

which are known as the *blocking transformations* where  $1 \leq i \leq d-1$  and  $1 \leq k \leq n/2^i$ . According to equation (7.69), we can express the sample mean variance of  $X_k$  as

$$\text{var}(\bar{X}_k) = \frac{\sigma_k^2}{n_k} + \frac{2}{n_k} \sum_{h=1}^{n_k-1} \left(1 - \frac{h}{n_k}\right) \gamma_k(h),\tag{7.72}$$

where we define the last term as the *truncation error*,  $e_k$ , as it is intractable. It can be shown that the sample variance of all pairs  $(X_i)_k$  and  $(X_j)_k$  after a while will be identical<sup>54</sup>,

$$\text{var}(\bar{X}_i) = \text{var}(\bar{X}_j) \quad \forall i, j \in \{0, 1, \dots, d-1\},\tag{7.73}$$

with the consequence that the sample mean variance of the entire set of samples is also given by

$$\text{var}(\bar{X}) = \frac{\sigma_k^2}{n_k} + e_k \quad \forall k \in \{0, 1, \dots, d-1\}.\tag{7.74}$$

In the original (manual) blocking method, we had to know exactly where to stop the procedure in order to satisfy equation (7.73). If we do not continue long enough, the sample variance has not converged, while if we keep on going for too long, the standard error of  $\text{var}(\hat{\sigma}_k^2/n_k)$  gets very large. If one plots the sample variance as a function of the iterations, one will see that the curve forms a plateau before it gets very noisy, but by using Jonsson's automated method, we do not need to worry about this.

## **Part IV**

# **Implementation**



## CHAPTER 8

# Scientific Programming

Always code as if the guy who ends up maintaining your code will be a violent psychopath who knows where you live.

---

John F. Woods,<sup>98</sup>

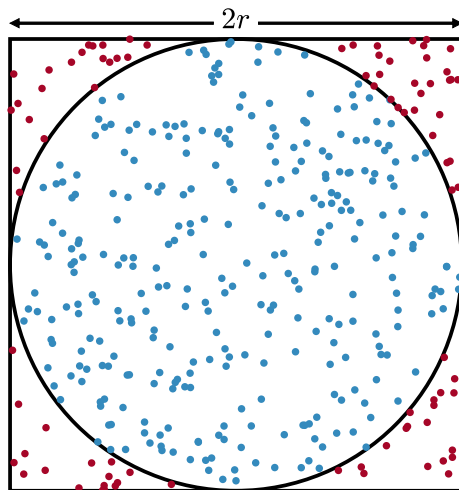


**Figure 8.1:** The value of  $\pi$  can be estimated using Monte Carlo integration. Here we approximate the ratio between the area of a circle of radius  $r$ ,  $A_{\text{circle}}$ , and the area of a square of side lengths  $2r$ ,  $A_{\text{square}}$ , by counting the number of random points occurring inside the circle and inside the square. The estimate of  $\pi$  is found from  $\pi = 4 \cdot A_{\text{circle}} / A_{\text{square}}$ .

Since we base this scientific work on solving equations numerically on the computer, software development is a significant part of the work. We will in this chapter go through the main concepts of scientific programming, and directly relate them to our code in the next chapters on implementation. As a motivation, we will provide a brief recap of some historical milestones in scientific computing.

Computers have long been used for solving complex scientific problems. Actually, for a long time, science was the primary motivation for developing computers. Already in 1929, Egil

Hylleraas used his mechanical desk calculator to calculate the ground state energy of the helium atom, which remains a milestone in computational quantum chemistry as well as quantum chemistry in general<sup>99</sup>. Later, pioneers like Alan Turing and John von Neumann contributed to the invention of the first electronic computer, which made numerical solutions of ordinary differential equations possible<sup>100</sup>.

Also on the software side, big breakthroughs have been made since the advent of the electronic computer. The programming language Fortran was released in 1957, which provided a new basis of scientific programming<sup>101</sup>. Later, Ole Johan Dahl and Kristen Nygaard developed the language SIMULA, which is considered as the first object-oriented language<sup>102</sup>. The language that we mostly will rely on in this work, C++, is an extension of the language C which was developed in the early 1970s and is, together with Fortran, one of few languages that have survived the ravages of time.

The computers used today, including both the hardware and the software, have become possible due to the heroic effort of an array of scientists, engineers, and mechanics over a long period. The computers are stronger than ever, have more memory than ever, are compacter than ever. Last but not least, they are more user-friendly than ever. All this has made heavy computations possible that were unthinkable just decades ago and has contributed to the development of virtually all branches of science. Due to the user-friendliness, advanced simulations have also been available for young and curious students like the author. We should not take this for granted.

The computer's language itself is binary and is the lowest level. To translate commands to this language, we need a "translator", which is a language that fills the gap between the binary language and human commands. We categorize this language in levels based on how similar they are to the binary language. Low-level languages are more similar to the binary language than a high-level language, and the result is that low-level languages, in general, are more demanding to deal with, but they are typically faster than high-level languages. In our work, we use the low-level language C++ for the main code, but for scripting, including plotting and solving less expensive problems, the high-level language Python has been used.

In this chapter, we will explain the essentials behind scientific programming, using examples from both C++ and Python. We will begin from the very basic, so if the reader is an experienced programmer, this chapter will probably be perceived as old news. Programs are often either classified as *procedural programming* or *object-oriented programming*, based on whether the code is written in the same order as the program flow goes (procedural) or is based on objects (object-oriented). We will explain the basics of object-oriented programming in the following.

## 8.1 Object-oriented programming in Python

In everyday life, we are all the time surrounded by objects that we categorize based on properties like their function, behavior, or expression. For instance, a *circle* is an object with properties like area, circumference *et cetera*, and can be categorized as a *shape*. Other members of the shape class might be squares and triangles. In object-oriented programming, we create similar objects, or classes, to make the program flow more intuitive for the reader. The main class is called the parent class, while the sub-classes are called the children. The reason for this analogy is that the sub-classes always inherit from their main class, but not the other way around. The example with the shapes can therefore be implemented with *Shapes* being the parent, and *Circle*, *Square* and *Triangle* being its children. In the high-level language Python, this can be implemented in the following way:

```
import numpy as np
```

```

class Shapes:
    def __init__(self, r):
        self.r = r

    def getArea(self):
        raise NotImplementedError("Class {} has no instance
            ↪ 'getArea'.".format(self.__class__.__name__))

class Circle(Shapes):
    def getArea(self):
        '''Returns the area of the circle.'''
        return np.pi * self.r**2

    def getCircumference(self):
        '''Returns the circumference of the circle.'''
        return 2 * np.pi * self.r

    def contains(self, x, y):
        '''Returns True if the point (x,y) is inside the circle.'''
        if np.linalg.norm([x, y]) < self.r:
            return True
        return False

class Square(Shapes):
    def getArea(self):
        '''Returns the area of the square.'''
        return 4 * self.r**2

    def getCircumference(self):
        '''Returns the circumference of the square.'''
        return 8 * self.r

    def contains(self, x, y):
        '''Returns True if the point (x,y) is inside the square.'''
        if abs(x) < self.r and abs(y) < self.r:
            return True
        return False

class Triangle(Shapes):
    def getCircumference(self):
        '''Returns the circumference of the equilateral triangle.'''
        return 6 * self.r

```

**Listing 8.1:** Geometric shapes implemented in object-oriented Python.

We give the children the properties area, circumference and extent. The length  $r$  means the radius of a circle, half the side length of a square and also half a side length of the equilateral triangle, as illustrated in figure (8.1). We can implement a circle, square and triangle of  $r=1$ , respectively named "circ", "sqr" and "tria" by these three lines

```

circ = Circle(1)
sqr = Square(1)
tria = Triangle(1)

```

Moreover, we can easily get their areas by calling the `getArea()` function,

```

>>> circ.getArea()
3.141592653589793

>>> sqr.getArea()
4

>>> tria.getArea()
NotImplementedError: Class Triangle has no instance 'getArea'.

```

As we can see, the area of the circle and the square were calculated successfully, giving  $\pi r^2$  and  $4r$  respectively. On the other hand, the area of the triangle raised an error, which is because we do not have defined the area of the triangle! This example illustrates that the properties of the children overwrites the properties of the parent, but if a child does not have the called property, it will instead return the parent's property.

### 8.1.1 An example based on Monte Carlo simulations

Up to this point, we have talked a lot about Monte Carlo simulations without giving an illustrating example of what it is. Methods where we draw numbers randomly from a function to reveal properties of a function, are in general classified as Monte Carlo simulations and in that manner, the name might sound more complicated than it is.

Suppose we did not know the value of  $\pi$ , what could we do to approximate its value? There are many ways to do this, where the most intuitive might be to measure the ratio between the diameter and the circumference in a circle. It is not possible to do this very accurate manually. A more accurate solution would be to use Monte Carlo simulations, where we, for instance, can take the starting point on the relation

$$\pi = 4 \frac{A_{\text{circle}}}{A_{\text{square}}}, \quad (8.1)$$

which is derived from the ratio between the area of a circle of radius  $r$  and the area of a square of side lengths  $2r$ . By drawing random numbers from a uniform distribution and count the number of points that are in the square and the circle, we can approximate  $A_{\text{circle}}/A_{\text{square}}$ . We can do this by using the `getExtent()` function of the square class and circle class,

```
for i in range(1,10):
    M = 10**i
    A_square = 0
    A_circle = 0
    for _ in range(int(M)):
        x = np.random.uniform(-1,1)
        y = np.random.uniform(-1,1)
        if circ.contains(x,y):
            A_circle += 1
        if squr.contains(x,y):
            A_square += 1
    print("MC = 10^", i, "Pi: ", 4 * A_circle/A_square)
```

which gives a output similar to

```
MC = 10^1 Pi: 2.4
MC = 10^2 Pi: 3.32
MC = 10^3 Pi: 3.156
MC = 10^4 Pi: 3.1296
MC = 10^5 Pi: 3.14168
MC = 10^6 Pi: 3.140044
MC = 10^7 Pi: 3.1420708
MC = 10^8 Pi: 3.1416844
MC = 10^9 Pi: 3.141615628
```

Note that the value of  $\pi$  was never used in this calculation. Considering the fact that  $\pi = 3.141592653589793\dots$ , the obtained result is quite acceptable. However, to run the program with  $M = 10^9$  Monte Carlo cycles, the program is quite slow. Is it possible to do this faster? The answer is yes, by switching partly or entirely to a low-level language.

## 8.2 Low-level programming with C++

Above, we looked at how inheritance can be implemented in the high-level language Python, and we observed the main weakness of high-level languages: the computational time. In this section, we will repeat the implementation above using C++. Using a low-level language will, hopefully, provide a significant speed-up. A similar C++ class structure as the Python class presented listing 8.1 looks like

```

class Shapes {
public:
    Shapes() {}                                // Constructor
    virtual double getArea() = 0;                // Pure virtual functions
    virtual double getCircumference() = 0;
    virtual bool getExtent(double x, double y) = 0;
    virtual ~Shapes() = 0;                      // Pure virtual destructor
};

class Circle : public Shapes {
public:
    Circle(double r) { m_r = r; }                // Constructor of Circle
    double getArea() { return M_PI * m_r * m_r; }
    double getCircumference() { return 2 * M_PI * m_r; }
    bool getExtent(double x, double y) {
        if (sqrt(x * x + y * y) < m_r) {
            return true;
        }
        return false;
    }
    ~Circle() {}                                // Destructor of Circle
private:
    double m_r = 1;
};

class Square : public Shapes {
public:
    Square(double r) { m_r = r; }                // Constructor of Square
    double getArea() { return 4 * m_r * m_r; }
    double getCircumference() { return 8 * m_r; }
    bool getExtent(double x, double y) {
        if (fabs(x) < m_r && fabs(y) < m_r) {
            return true;
        }
        return false;
    }
    ~Square() {}                                // Destructor of Square
private:
    double m_r = 1;
};

Shapes::~Shapes() {}                          // Destructor of Shapes

```

**Listing 8.2:** Geometric shapes implemented in object-oriented C++.

This looks different from the implementation in Python presented in listing (8.1). We will go thoroughly through the different parts of the code. One of the first thing we observe, is that we here need to *declare* all the variables, meaning that we need to specify the variable type. In the following we will have a look at some standard *data types*.

### 8.2.1 Built-in data types

In low-level languages, we need to specify the data types manually, enhancing the control. The most fundamental data types are `int` representing an integer number, `float` representing a floating number, `bool` representing a Boolean number and `char` representing a character. Often, these

**Table 8.1:** Built-in data types in C++, with their memory occupation and range in a 64-bit processor, taken from Ref. [103]. Extensions in the parenthesis are optional.

Data types	Size [bytes]	Range
(signed) char	1	$-2^7$ to $2^7 - 1$
(signed) short (int)	2	$-2^{15}$ to $2^{15} - 1$
(signed) int / long (int)	4	$-2^{31}$ to $2^{31} - 1$
(signed) long long (int)	8	$-2^{63}$ to $2^{63} - 1$
unsigned char	1	0 to $2^8$
unsigned short (int)	2	0 to $2^{16}$
unsigned int / unsigned long (int)	4	0 to $2^{32}$
unsigned long long (int)	8	0 to $2^{64}$
float	4	$\sim \pm 3.4E38$ ( $\sim 7$ digits)
(long) double	8	$\sim \pm 1.7E308$ ( $\sim 15$ digits)

four data types are not sufficient for the task we want to implement, and we need to introduce more data types. An especially common error is *overflow*, meaning that the number computed is out of the range of our data type. To avoid this, we can switch to data types of longer range, replacing `int` with a `long long int` (or just a `long long`), and replacing `float` with a `double`.

Some languages also deal with `long int` and `long double`, but in C++ an `int` and a `long int` is the same. Additionally, a `long double` is the same as a `double`. As lack of memory is typically not the largest problem when performing simulations, it is common to declare all floating numbers as `doubles`. In table (8.1), the most common data types are listed with their range and memory occupation in C++. For integers, it is also possible to "move" the range from its zero-centered default to only include positive numbers. This is done by declaring an `unsigned` data type. By using `unsigned` data types, the range doubles in the positive direction, but it should not be done if we, by any chance, can get negative numbers, as we then get *underflow*.

## 8.2.2 Access modifiers

Another thing that we observe from the code example in listing (8.2), is that we define the functions as `private` or `public`, which are called access modifiers. The access modifiers specify how much access the environment should have to the function: `private` means that the function can only be called from the particular class, while `public` means that also sub-classes (children) and other classes have access to the function. We also have a third access modifier in C++, called `protected`. `protected` members of a class A are not accessible outside of A's code, but any class that inherits from A has access to the `protected` member.

## 8.2.3 Virtual functions

In the Python example in listing (8.1), we saw how a parent's function was overwritten by a function of the child. This works as long as the child's function has an identical name and identical arguments as the parent's function; otherwise it all will fail. In C++, a safer method exists based on virtual functions, where a child is *forced* to have the same virtual functions as its parent. The virtual functions of the parent therefore serves as a template of its children, such

that all the children have the same features. If the parent function is empty, the function is called pure virtual. This is often very useful, as the children tend to have the same features. Taking it back to the `Shapes` class, all the shapes ought to have features area and circumference, which can be forced by using virtual functions, as done in the example above, where all functions are pure virtual.

### 8.2.4 Constructors and destructors

In the C++ example in (8.2), we observe that the class `Shapes` has a function with the same name, `Shapes` and another virtual function `~Shapes`. The former one is used to create the object and is hence named a *constructor*. This function is called automatically when the object of a class is created. Similarly, the latter one destructs an object when we are done evaluating the object. It is therefore named a *destructor* and is also called automatically when an object is deleted or goes out of scope.

### 8.2.5 Pointers

In the C++ example in (8.2), we have not directly used any pointer. However, pointers are important in low-level languages, and we will here give a very brief introduction to pointers. For a C++ program, the memory of a computer is like a succession of memory cells, each with a unique address and of size one byte. When declaring a variable of size larger than one byte, the object will occupy memory cells that have consecutive addresses. Often, it is useful to know this address, which allows us to change the object directly in the memory. The address of a variable is given by the address-of operator, `&`, working as

```
address=&variable
```

By doing this, we say that we *point to the address*, and a variable that stores the address of another variable is thereby called a pointer. Furthermore, the dereference operator, `*`, gives the value of the address to where a pointer points. Thus, the following is true

```
variable==*address
```

### 8.2.6 Back to the Monte Carlo example

We can now call the class above from the `main` function. We start defining the children `circ` and `sqr`, and use the `contains()` function to approximate the area ratio between them. The code looks like

```
int main() {
    class Shapes *circ = new Circle(1.0);
    class Shapes *sqr = new Square(1.0);

    for(int i=1; i<10; i++) {
        int M = int(pow(10,i));
        long long A_square = 0;
        long long A_circle = 0;
        for(int m=0; m<M; m++) {
            double x = uniform(gen);
            double y = uniform(gen);
            if(circ->contains(x, y)) {
                A_circle++;
            }
            if(sqr->contains(x, y)) {
```

```
        A_square++;
    }
}
std::cout << std::fixed;
std::cout << std::setprecision(10);
std::cout << "MC = 10^" << i << "Pi: " << 4 * double(A_circle)/A_square <<
    std::endl;
}
return 0;
}
```

This gives a similar output as the Python script, but is much faster.

## CHAPTER 9

# Implementation: Variational Monte Carlo

There are only two hard things in Computer Science: cache invalidation and naming things.

---

Phil Karlton,<sup>104</sup>

In this chapter, we will describe the implemented variational Monte Carlo (VMC) code, which was developed from scratch in C++. As the implementation itself is around 7000 significant\* lines of code, we will go through selected and often not obvious parts. As often said, *good planning is half the battle*, which largely relates to writing VMC code. The code was rewritten and restructured several times before we ended on the final version. As a starting point, we used the VMC framework implemented by Ledum<sup>38</sup>. The entire source code can be found on the author's GitHub account, <http://www.github.com/evenmn/VMC>.

We developed the code with focus on three main aims: it should be fast, flexible and readable. It needs to be flexible in order to support the Boltzmann machines as our trial wave function guess, and since we will try out various Jastrow factors, the wave function elements should be easy to add and remove. As quantum mechanical simulations, in general, are very expensive, it is crucial to develop efficient code to be able to study sufficiently large systems. Lastly, we aim to write readable code such that others can reuse the code partly or in its entirety later. How we work to achieve the goals will be illustrated by code mainly picked from the `WaveFunction` class, which is the heart of the code.

For all matrix operations, we use the open-source template library for linear algebra Eigen throughout the code. Eigen provides an elegant interface, with support for all the needed matrix and vector operations. Additionally, Eigen is built on the standard software libraries for numerical linear algebra, BLAS, and LAPACK, which are incredibly fast. These contribute significantly to the performance of the code.

## 9.1 Flexibility and readability

We have done several things in order to keep the code as readable as possible. Firstly, the code is fully object-oriented. This makes it more intuitive to read, as discussed in chapter 8. The Hamiltonians, optimizers, wave functions, sampling methods, and even the random number generator were treated as objects, making the code more or less fully object-oriented. An object-oriented code also makes it straightforward to define a system since we can specify the preferred

---

\*Significant lines of code in this sense means lines that are not blank or commented. Counted by the `cloc` program<sup>105</sup>.

object. Below, we define a two-dimensional quantum dot system of  $N = 6$  electrons with frequency  $\omega = 1.0$ , learning rate  $\eta = 0.1$ , number of Metropolis cycles  $M = 2^{20} = 1,048,576$  and max number of iterations set to 1000.

```
System *QD = new System();

QD->setNumberOfDimensions(2);
QD->setNumberofsingle-single-particles(6);
QD->setNumberOfMetropolisSteps(int(pow(2, 20)));
QD->setFrequency(1.0);
QD->setLearningRate(0.1);

QD->setBasis(new Hermite(QD));
QD->setHamiltonian(new HarmonicOscillator(QD));

QD->setWaveFunctionElement(new Gaussian(QD));
QD->setWaveFunctionElement(new SlaterDeterminant(QD));
QD->setWaveFunctionElement(new PadeJastrow(QD));

QD->setNumberOfIterations(1000);
QD->runSimulation();
```

**Listing 9.1:** Example on how a quantum dot system can be initialized.

We observe that one first needs to define an object to represent the system, and then the other settings are connected to the system in the form of subclasses. The reader might notice that we use the **lowerCamelCase** naming convention for function and variable names, which means that each word begins with a capital letter except the first word. For classes, we use the **UpperCamelCase** to distinguish from function names. Using the camel case is known to make the code readable, and apart from, for example, the popular **snake\_case**, we do not need delimiters between the words, which saves some space. After the naming convention is decided, we are still responsible for giving reasonable names, which is not always an easy task, as Karlton points out<sup>104</sup>. When one sees the variable name, one should know exactly what the variable/-function/class is or does. Besides, as a code format, we use the ClangFormat, which provides a consequent way of formatting the code.

The snippet above also demonstrates how the code was made flexible when it comes to the wave function. One can construct a wave function consisting of various elements by simply calling the `setWaveFunctionElement` multiple times. This creates a wave function vector, `m_waveFunctionVector`, in the background containing all the elements, which makes it easy to compose the wave function in whatever preferred way. All the elements can be combined. The reader might stub on the use of the element `Gaussian`, is not the standard trial wave function defined by the Slater-Jastrow wave function? It is, but as we will see later in section 9.3.1, the Gaussian part can be factorized out from the Slater determinant when using a Hermite basis. However, we will now start from the fundamental assumption that the trial wave function ansatz is the Slater-Jastrow wave function, and take it from there.

## 9.2 Decomposing the trial wave function

In our VMC implementation, the trial wave function,  $\Psi_T(\mathbf{R})$ , is assumed to be the Slater-Jastrow wave function. In section 7.1.1, we saw that the electronic Slater determinant can be split up in a spin-up part and a spin-down part, giving the trial wave function

$$\Psi_T(\mathbf{R}) = |\hat{S}_\uparrow(\mathbf{R})| \cdot |\hat{S}_\downarrow(\mathbf{R})| J(\mathbf{R}) \quad (9.1)$$

where  $\mathbf{R} = \{\mathbf{r}_1, \mathbf{r}_2, \dots, \mathbf{r}_N\}$  is the collective coordinates of all the electrons, where we exclude the spin as it is assumed to not affect the energy.  $J(\mathbf{R})$  is an arbitrary Jastrow factor, while the Slater

determinant is the determinant of the matrix  $\hat{S}(\mathbf{R})$ , henceforth the Slater matrix. To convince the reader that the Slater determinant and the Jastrow factor can be treated separately, we will consider a general trial wave function consisting of  $p$  wave function elements  $\{\Psi_1, \Psi_2 \cdots \Psi_p\}$ ,

$$\Psi_T(\mathbf{R}) = \prod_{i=1}^p \Psi_i(\mathbf{R}), \quad (9.2)$$

where  $\Psi_i(\mathbf{R})$  in principle can be any function of the coordinates  $\mathbf{R}$ . However, we will later see that the parameter update simplifies if we restrict each variational parameter  $\theta_j$  to appear in an element only. Before that, we will look at how the kinetic energy can be expressed in terms of independent factors.

### 9.2.1 Local energy computations

The local energy computation is the heart of the VMC code, and the aim for an efficient and flexible code starts from here. It was first defined in equation (7.16), and by inserting a general Hamiltonian,  $\hat{\mathcal{H}} = -1/2\nabla^2 + V$ , with  $V$  covering all the potential energy, we obtain

$$E_L = \sum_{k=1}^F \left[ -\frac{1}{2} \left( \frac{1}{\Psi_T(\mathbf{R})} \nabla_k^2 \Psi_T(\mathbf{R}) \right) + V_k \right]. \quad (9.3)$$

$F = Nd$  is degrees of freedom, with  $N$  as the number of electrons and  $d$  as the number of dimensions. The first term, which is the kinetic energy term, is the only wave function-dependent one, and we will in this section decompose it with respect to the elements in equation (9.2). The potential energy term,  $V$ , is not directly dependent on the wave function and will therefore not be further touched here.

From the definition of the derivative of a logarithm, we have that

$$\frac{1}{\Psi_T(\mathbf{R})} \nabla_k \Psi_T(\mathbf{R}) = \nabla_k \ln \Psi_T(\mathbf{R}), \quad (9.4)$$

which can be used to prove the following relation

$$\frac{1}{\Psi_T(\mathbf{R})} \nabla_k^2 \Psi_T(\mathbf{R}) = \nabla_k^2 \ln \Psi_T(\mathbf{R}) + (\nabla_k \ln \Psi_T(\mathbf{R}))^2. \quad (9.5)$$

Expressing the kinetic energy in terms of this relation is useful because most of the elements can be easily treated in the log-space as many of them are exponential functions. By using the fact that the trial wave function is a product of the elements, the term above is calculated by

$$\frac{1}{\Psi_T(\mathbf{R})} \nabla_k^2 \Psi_T(\mathbf{R}) = \sum_{i=1}^p \nabla_k^2 \ln \Psi_i(\mathbf{R}) + \left( \sum_{i=1}^p \nabla_k \ln \Psi_i(\mathbf{R}) \right)^2, \quad (9.6)$$

such that the local energy is given by

$$E_L = -\frac{1}{2} \left[ \sum_{i=1}^p \nabla^2 \ln \Psi_i(\mathbf{R}) + \sum_{k=1}^F \left( \sum_{i=1}^p \nabla_k \ln \Psi_i(\mathbf{R}) \right)^2 \right] + V. \quad (9.7)$$

This can be found when all local derivatives  $\nabla^2 \ln \Psi_i(\mathbf{R})$  and  $\nabla_k \ln \Psi_i(\mathbf{R})$  are given. By assuming that the former is returned by a function `computeLaplacian()` and the latter is returned by a function `computeGradient(k)`, we compute the kinetic energy using the following function

```

double System::getKineticEnergy()
{
    double kineticEnergy = 0;
    for (auto &i : m_waveFunctionElements) {
        kineticEnergy += i->computeLaplacian();
    }
    for (int k = 0; k < m_degreesOfFreedom; k++) {
        double nablaLnPsi = 0;
        for (auto &i : m_waveFunctionElements) {
            nablaLnPsi += i->computeGradient(k);
        }
        kineticEnergy += nablaLnPsi * nablaLnPsi;
    }
    return -0.5 * kineticEnergy;
}

```

Note that some of the variables are declared globally, here the vector `m_waveFunctionElements` and the integer `m_degreesOfFreedom` are denoted by an `m_` to distinguish them from the variables declared locally.

### 9.2.2 Parameter gradients

In section 7.1.4, we presented how the parameters can be updated by minimizing the energy expectation value. We recall that the only closed-form expression needed, in addition to the local energy, is  $\nabla_{\theta_j} \ln \Psi_T(\mathbf{R})$ , which needs to be found. By applying equation (9.2), we find that

$$\nabla_{\theta_j} \ln \Psi_T(\mathbf{R}) = \sum_{i=1}^p \nabla_{\theta_j} \ln \Psi_i(\mathbf{R}) = \nabla_{\theta_j} \ln \Psi_{\theta_j}(\mathbf{R}), \quad (9.8)$$

where  $\Psi_{\theta_j}(\mathbf{R})$  is the only element which contains the parameter  $\theta_j$ . With this in mind, we need to find closed-form expressions of  $\nabla_{\theta_j} \ln \Psi_{\theta_j}(\mathbf{R})$  for all wave function elements  $\Psi_{\theta_j}(\mathbf{R})$  that are associated with a variational parameter  $\theta_j$ .

In the code, we store all the parameters in a *parameter matrix* where each element has its own row of parameters. Similarly, we create a *gradient matrix* of the same dimensions to store the gradients  $\nabla_{\theta_j} \ln \Psi_{\theta_j}(\mathbf{R})$  for each variational parameter. The function that collects all the gradients is implemented straightforward, and is given by

```

Eigen::MatrixXd System::getAllParameterGradients()
{
    for (int i = 0; i < m_numberOfElements; i++) {
        m_gradients.row(i) = m_waveFunctionElements[i]->computeParameterGradient();
    }
    return m_gradients;
}

```

where `m_gradients` has the same number of rows as the number of elements and the same number of columns as the maximum number of parameters in an element  $i$ . The function `computeParameterGradient()` returns a vector with all the gradients  $\nabla_{\theta_j} \ln \Psi_i(\mathbf{R})$  of the respective element. Even though the gradients are used to update the parameters, we will postpone the discussion of the parameter update to section 9.6.

### 9.2.3 Probability ratio

In the two previous sections, we have seen how the derivatives of the wave function elements can be used in order to obtain the local energy and the parameter update. However, we also

need the evaluation of the wave function elements themselves to decide whether or not a move should be accepted. If we go back to equation (7.35), we see that what is actually needed is the ratio between the present and the previous probability,  $P(\mathbf{R}_{\text{new}})/P(\mathbf{R}_{\text{old}})$ . Further, we can write this as the product of the probability ratios of all the wave function elements,

$$\frac{P(\mathbf{R}_{\text{new}})}{P(\mathbf{R}_{\text{old}})} = \frac{|\Psi_T(\mathbf{R}_{\text{new}})|^2}{|\Psi_T(\mathbf{R}_{\text{old}})|^2} = \prod_{i=1}^p \frac{|\Psi_i(\mathbf{R}_{\text{new}})|^2}{|\Psi_i(\mathbf{R}_{\text{old}})|^2}, \quad (9.9)$$

again utilizing equation (9.2). Finding closed-form expressions for these ratios is not only beneficial because it is needed in the actual implementation, as we work in the log-space these ratios often take simple forms which are cheap to evaluate. Below, we will calculate these ratios for all the elements since we are going to use that directly in the sampling. We name the function returning the ratio of a particular element `evaluateRatio()`, and we obtain the total probability ratio in the following way

```
double System::evaluateProbabilityRatio()
{
    double ratio = 1;
    for (auto &i : m_waveFunctionElements) {
        ratio *= i->evaluateRatio();
    }
    return ratio;
}
```

With this, we have introduced the four central functions of the wave function elements: `computeLaplacian()`, `computeGradient(k)`, `computeParameterGradient()` and `evaluateRatio()`. In the following, we will evaluate the Slater determinant and see how it can be decomposed further into more elements.

## 9.3 Slater determinant

As we have seen above, the Slater determinant is the fundamental part of the standard electronic structure trial wave function, together with the Jastrow factor. The main problem with the Slater determinant is that it is costly to deal with as the number of electrons increases. To find the gradient of the Slater determinant, as requested by equation (9.7), we need to compute the inverse of the Slater matrix, which by standard LU decomposition scales as  $\sim M^3$  for an  $M \times M$  matrix<sup>106</sup>. Fortunately, there exist algorithms that let us obtain the inverse of the matrix by recursive relations, scaling as  $\sim M^2$ . This will be detailed in section 9.3.4.

Additionally, in section 7.1.1, we showed that the Slater determinant can be split in a spin-up part and a spin-down part with the assumption that the Hamiltonian is spin-independent. This reduces the dimensionality of the Slater matrix from  $N \times N$  to two  $N/2 \times N/2$  matrices, with  $N$  as the number of electrons. Also, factorizing out common factors from the Slater determinant will give some speed-up. In this section, we will mostly discuss the various methods to make the update of the Slater matrix more efficient. We will start from the simplified expression of the Slater determinant derived in section 7.1.1,

$$\Psi_{\text{sd}}(\mathbf{R}) = \frac{1}{\sqrt{N!}} |\hat{S}_\uparrow(\mathbf{R}^\uparrow)| \cdot |\hat{S}_\downarrow(\mathbf{R}^\downarrow)|, \quad (9.10)$$

where  $\hat{S}_\sigma(\mathbf{R}^\sigma)$  is the Slater matrix of spin- $\sigma$  states with collective spatial coordinates  $\mathbf{R}^\sigma = \{\mathbf{r}_1^\sigma, \mathbf{r}_2^\sigma, \dots, \mathbf{r}_{N_\sigma}^\sigma\}$  for  $\sigma \in \{\uparrow, \downarrow\}$ . The determinant of the spin-up state is treated in the same

way as the determinant of the spin-down state, so will from now on consider a general spin- $\sigma$  state,

$$|\hat{S}_\sigma(\mathbf{R})| = \begin{vmatrix} \phi_1(\mathbf{r}_1) & \phi_2(\mathbf{r}_1) & \cdots & \phi_N(\mathbf{r}_1) \\ \phi_1(\mathbf{r}_2) & \phi_2(\mathbf{r}_2) & \cdots & \phi_N(\mathbf{r}_2) \\ \vdots & \vdots & & \vdots \\ \phi_1(\mathbf{r}_N) & \phi_2(\mathbf{r}_N) & \cdots & \phi_N(\mathbf{r}_N) \end{vmatrix}, \quad (9.11)$$

where  $\phi_j(\mathbf{r}_i)$  is the single-particle function occupying the matrix element  $\hat{D}_{ij}$ .

### 9.3.1 Factorizing out elements

We have now seen how the Slater determinant can be split up in a spin-up part and a spin-down part. Before we evaluate these determinants, we should try to make the elements of the Slater matrices as simple as possible to save computational time. If all the elements have the same factor, the computations will get much cheaper if the factor is factorized out of the determinant. How this is possible can easiest be seen if we express the Slater determinant as

$$|\hat{S}_\sigma(\mathbf{R})| = \sum_q (-1)^q \hat{P} \phi_1(\mathbf{r}_1) \phi_2(\mathbf{r}_2) \cdots \phi_N(\mathbf{r}_N), \quad (9.12)$$

where the sum runs over all the possible permutations and  $\hat{P}$  is the permutation operator, permuting coordinates pairwise. If all the (spatial) single-particle functions  $\phi_j(\mathbf{r}_i)$  can be split in two functions  $f_j(\mathbf{r}_i)$  and  $g(\mathbf{r}_i)$  where the latter is common for all the single-particle functions,

$$\phi_j(\mathbf{r}_i) = f_j(\mathbf{r}_i) g(\mathbf{r}_i), \quad (9.13)$$

the determinant can be rewritten as

$$\begin{aligned} |\hat{S}_\sigma(\mathbf{R})| &= \sum_p (-1)^p \hat{P} f_1(\mathbf{r}_1) g(\mathbf{r}_1) f_2(\mathbf{r}_2) g(\mathbf{r}_2) \cdots f_N(\mathbf{r}_N) g(\mathbf{r}_N), \\ &= g(\mathbf{r}_1) g(\mathbf{r}_2) \cdots g(\mathbf{r}_N) \sum_p (-1)^p \hat{P} f_1(\mathbf{r}_1) f_2(\mathbf{r}_2) \cdots f_N(\mathbf{r}_N), \\ &= \underbrace{\prod_{i=1}^N g(\mathbf{r}_i)}_{G(\mathbf{R})} \underbrace{\begin{vmatrix} f_1(\mathbf{r}_1) & f_2(\mathbf{r}_1) & \cdots & f_N(\mathbf{r}_1) \\ f_1(\mathbf{r}_2) & f_2(\mathbf{r}_2) & \cdots & f_N(\mathbf{r}_2) \\ \vdots & \vdots & \ddots & \vdots \\ f_1(\mathbf{r}_N) & f_2(\mathbf{r}_N) & \cdots & f_N(\mathbf{r}_N) \end{vmatrix}}_{|\hat{D}(\mathbf{R})|}. \end{aligned} \quad (9.14)$$

The Slater determinant can then be expressed as

$$\Psi_{\text{sd}}(\mathbf{R}) = \frac{1}{\sqrt{N!}} \Psi_{\text{factor}}(\mathbf{R}) \cdot \Psi_{\text{det}}(\mathbf{R}), \quad (9.15)$$

where we have introduced  $\Psi_{\text{det}}(\mathbf{R}) \equiv |\hat{D}_\uparrow(\mathbf{R}^\uparrow)| \cdot |\hat{D}_\downarrow(\mathbf{R}^\downarrow)|$  to distinguish the reduced determinants from the total Slater determinant,  $\Psi_{\text{sd}}(\mathbf{R})$ , and  $\Psi_{\text{factor}}(\mathbf{R}) \equiv G_\uparrow(\mathbf{R}^\uparrow) \cdot G_\downarrow(\mathbf{R}^\downarrow)$  occurring from the Slater determinant. This is very useful when dealing with some common basis sets. For instance, the Hermite basis is given by

$$\phi_j(\mathbf{r}_i) = \left( \frac{\omega}{4\pi} \right)^{1/4} H_j(\sqrt{\omega} \mathbf{r}_i) \exp\left(-\frac{1}{2}\omega |\mathbf{r}_i|^2\right), \quad (9.16)$$

where  $H_j(\sqrt{\omega} \mathbf{r}_i)$  are the Hermite polynomials and the Gaussian part fulfills the requirement of  $g(\mathbf{r}_i)$ . Therefore, we can construct a Slater determinant containing the Hermite polynomials only,

treating the Gaussian as an independent element. This is not only preferable from an efficiency point of view, by doing this the variational parameter in the Gaussian is also removed from the determinant, which means that we can implement the determinant without worrying about the variational parameters. With this in mind, we will first treat the Gaussian element, obtaining its derivative and optimization schemes. Moreover, in section 9.3.3, we will discuss how the determinant can be treated efficiently.

### 9.3.2 The Gaussian

When factorizing out the Gaussian part from the Slater determinant, we obtain the factor

$$\Psi_{\text{sg}}(\mathbf{R}; \alpha) = \prod_{j=1}^N g(\mathbf{r}_j) = \exp\left(-\frac{1}{2}\omega\alpha \sum_{j=1}^N r_j^2\right) = \exp\left(-\frac{1}{2}\omega\alpha \sum_{j=1}^F x_j^2\right), \quad (9.17)$$

which we will implement as a wave function element with  $\omega$  as the oscillator strength and  $\alpha$  as a variational parameter, which for quantum dots with non-interacting electrons is 1. Because of the presence of  $r_i^2$ , the function can easily be treated both in Cartesian and spherical coordinates, but in this thesis we will focus on the former. We now use  $j$  as our summation index, and reserve  $i$  for the moved electron and  $k$  as our the differentiating index. When changing a coordinate  $x_i$  from  $x_i^{\text{old}}$  to  $x_i^{\text{new}}$ , the probability ratio between the new and the old state can easily be found to be

$$\frac{|\Psi_{\text{sg}}(\mathbf{R}_{\text{new}})|^2}{|\Psi_{\text{sg}}(\mathbf{R}_{\text{old}})|^2} = \exp\left(\omega\alpha((x_i^{\text{old}})^2 - (x_i^{\text{new}})^2)\right), \quad (9.18)$$

which is pretty cheap to evaluate. The gradient of  $\ln \Psi_{\text{sg}}$  with respect to the coordinate  $x_k$  is

$$\nabla_k \ln \Psi_{\text{sg}} = -\omega\alpha x_k, \quad (9.19)$$

and the corresponding Laplacian is

$$\nabla^2 \ln \Psi_{\text{sg}} = -\omega\alpha F. \quad (9.20)$$

We observe that the factor  $\omega\alpha$  is found in all the expressions above and only needs to be calculated again when the parameter  $\alpha$  is updated, which is updated according to

$$\nabla_\alpha \ln \Psi_{\text{sg}} = -\frac{1}{2}\omega \sum_{j=1}^F x_j^2. \quad (9.21)$$

The implementation is very straightforward, and looks like

```
double Gaussian::evaluateRatio()
{
    return m_probabilityRatio;
}

double Gaussian::computeGradient(const int k)
{
    return -m_omegalpha * m_positions(k);
}

double Gaussian::computeLaplacian()
{
```

```

    return -m_omegalpha * m_degreesOfFreedom;
}

Eigen::VectorXd Gaussian::computeParameterGradient()
{
    m_gradients(0) = -0.5 * m_omega * m_positions.cwiseAbs2().sum();
    return m_gradients;
}

```

where `m_omegalpha` is  $\omega\alpha$ . The probability ratio is calculated using

```

double void Gaussian::updateProbabilityRatio(int changedCoord)
{
    m_probabilityRatio = exp(m_omegalpha * (m_positionsOld(changedCoord) *
        ↪ m_positionsOld(changedCoord) - m_positions(changedCoord) *
        ↪ m_positions(changedCoord)));
}

```

We see that matrix-vector operations are used whenever it is possible, which makes the computations very fast.

### 9.3.3 The determinant

As discussed in section 7.1.1, the Slater determinant can be split in a spin-up part and a spin-down part, and further the common functions can be factorized out as shown in section 9.3.1. In this section, we will treat the reduced determinant, i.e., with common factors factorized out. This determinant is a product of the spin-up determinant and the spin-down determinant,

$$\Psi_{\text{det}}(\mathbf{R}) \equiv |\hat{D}_{\uparrow}(\mathbf{R}^{\uparrow})| \cdot |\hat{D}_{\downarrow}(\mathbf{R}^{\downarrow})|, \quad (9.22)$$

where  $\mathbf{R}_{\uparrow}$  are the coordinates of electrons with spin up (defined as the first  $N_{\uparrow}$  coordinates) and  $\mathbf{R}_{\downarrow}$  are the coordinates of electrons with spin down (defined as the last  $N_{\downarrow}$  coordinates).

We can now exploit the logarithmic scale, by using that the logarithm of a product corresponds to sums of the logarithm of each factor,

$$\ln \Psi_{\text{det}}(\mathbf{R}) = \ln |\hat{D}_{\uparrow}(\mathbf{R}^{\uparrow})| + \ln |\hat{D}_{\downarrow}(\mathbf{R}^{\downarrow})|. \quad (9.23)$$

We only need to care about one of the determinants when differentiating, dependent on whether the coordinate we differentiate with respect to is among the spin-up or the spin-down coordinates,

$$\nabla_k \ln \Psi_{\text{det}}(\mathbf{R}) = \begin{cases} \nabla_k \ln |\hat{D}_{\uparrow}(\mathbf{R}^{\uparrow})| & \text{if } k < N_{\uparrow} \\ \nabla_k \ln |\hat{D}_{\downarrow}(\mathbf{R}^{\downarrow})| & \text{if } k \geq N_{\uparrow} \end{cases}. \quad (9.24)$$

Before we continue, we introduce a more general notation which covers both spin cases:

$$\hat{D}(\mathbf{R}) \equiv \hat{D}_{\sigma}(\mathbf{R}^{\sigma}), \quad (9.25)$$

where  $\sigma$  is the spin projection. When summing, the sum is always over all relevant coordinates. Furthermore, we have that

$$\nabla_k \ln |\hat{D}(\mathbf{R})| = \frac{\nabla_k |\hat{D}(\mathbf{R})|}{|\hat{D}(\mathbf{R})|}, \quad (9.26)$$

and

$$\nabla_k^2 \ln |\hat{D}(\mathbf{R})| = \frac{\nabla_k^2 |\hat{D}(\mathbf{R})|}{|\hat{D}(\mathbf{R})|} - \left( \frac{\nabla_k |\hat{D}(\mathbf{R})|}{|\hat{D}(\mathbf{R})|} \right)^2, \quad (9.27)$$

which are consistent with the equations (9.4) and (9.5). At this point, there are (at least) two possible paths to the final expressions. We can keep on using matrix operations and find the expressions of  $\nabla_k |\hat{D}(\mathbf{R})| / |\hat{D}(\mathbf{R})|$  and  $\nabla_k^2 |\hat{D}(\mathbf{R})| / |\hat{D}(\mathbf{R})|$  using Jacobi's formula, or we can switch to element representations of the matrices. We choose the latter, because we believe that is the path of least resistance.

The determinant of an arbitrary matrix  $\hat{A}$  can be expressed by its comatrix  $\hat{C}$  in the following way,

$$|\hat{A}| = \sum_{ij} a_{ij} c_{ji}, \quad (9.28)$$

where  $a_{ij}$  are the matrix elements of  $\hat{A}$  and  $c_{ij}$  are the elements of the comatrix. Going further, an element  $c_{ij}$  can be expressed in terms of an element from the inverse of  $\hat{A}$ ,  $a_{ij}^{-1}$ ,

$$c_{ij} = a_{ij}^{-1} |\hat{A}|. \quad (9.29)$$

Relating this to our particular problem, we can express

$$\begin{aligned} \frac{\nabla_k |\hat{D}(\mathbf{R})|}{|\hat{D}(\mathbf{R})|} &= \frac{\nabla_k \sum_{ij} d_{ij} c_{ji}}{\sum_{ij} d_{ij} c_{ji}} = \frac{\sum_j \nabla_k d_{kj} c_{jk}}{\sum_{ij} d_{ij} c_{ji}}, \\ &= \frac{\sum_j \nabla_k d_{kj} d_{jk}^{-1} |\hat{D}|}{\sum_{ij} d_{ij} d_{ji}^{-1} |\hat{D}|} = \sum_j \nabla_k d_{kj} d_{jk}^{-1}, \end{aligned} \quad (9.30)$$

where  $d_{ij}$  are elements of  $\hat{D}$  and we have used the fact that the elements  $\nabla_k d_{ij}$  contribute to the sum if and only if  $i = k$ , such that the sum over  $i$  collapses. Moreover, we use that multiplying a matrix with its inverse is identity, i.e.  $\sum_{ij} d_{ij} d_{ji}^{-1} = 1$  and the determinants cancel. Similarly, we get

$$\frac{\nabla_k^2 |\hat{D}(\mathbf{R})|}{|\hat{D}(\mathbf{R})|} = \sum_j \nabla_k^2 d_{kj} d_{jk}^{-1}, \quad (9.31)$$

for the Laplacian. We are then ready to write up the final expressions for the gradient and Laplacian of the logarithm of the Slater determinant,

$$\begin{aligned} \nabla_k \ln |\hat{D}(\mathbf{R})| &= \sum_j d_{jk}^{-1} \nabla_k \phi_j(\mathbf{r}_k), \\ \nabla_k^2 \ln |\hat{D}(\mathbf{R})| &= \sum_j d_{jk}^{-1}(\mathbf{R}) \nabla_k^2 \phi_j(\mathbf{r}_k) - \left( \sum_j d_{jk}^{-1} \nabla_k \phi_j(\mathbf{r}_k) \right)^2, \end{aligned} \quad (9.32)$$

where we have used that  $d_{ij} = \phi_j(\mathbf{r}_i)$  with  $\phi_j(\mathbf{r}_i)$  as the spatial functions found in the determinant.

### 9.3.4 Efficient calculation of the determinant

As aforementioned, dealing with the Slater determinant is very computational expensive, mainly because of the requirement of the inverse Slater matrix. However, by revealing that only one row in the Slater matrix is updated for each iteration step, we can update the inverse recursively. We use the same element representation as above, and express the ratio between the new and the old determinant as

$$R \equiv \frac{|\hat{D}(\mathbf{R}_{\text{new}})|}{|\hat{D}(\mathbf{R}_{\text{old}})|} = \frac{\sum_j d_{ij}(\mathbf{R}_{\text{new}}) c_{ij}(\mathbf{R}_{\text{new}})}{\sum_j d_{ij}(\mathbf{R}_{\text{old}}) c_{ij}(\mathbf{R}_{\text{old}})} = \sum_j d_{ij}(\mathbf{R}_{\text{new}}) d_{ji}^{-1}(\mathbf{R}_{\text{old}}), \quad (9.33)$$

which is very similar to the calculation given in equation (9.30). To calculate the inverse matrix  $\hat{D}^{-1}$  efficiently, we need to calculate

$$S_j = \sum_{l=1}^N d_{il}(\mathbf{R}_{\text{new}}) d_{lj}^{-1}(\mathbf{R}_{\text{old}}) \quad (9.34)$$

for all columns but the one associated with the moved electron,  $i$ . For all columns where  $j \neq i$ , we then find the new elements using

$$d_{kj}^{-1}(\mathbf{R}_{\text{new}}) = d_{kj}^{-1}(\mathbf{R}_{\text{old}}) - \frac{S_j}{R} d_{ki}^{-1}(\mathbf{R}_{\text{old}}), \quad (9.35)$$

while the remaining column,  $i$ , is updated using the simple formula<sup>107</sup>

$$d_{ki}^{-1}(\mathbf{R}_{\text{new}}) = \frac{1}{R} d_{ki}^{-1}(\mathbf{R}_{\text{old}}). \quad (9.36)$$

The inverting of the matrix now scales as  $\sim M^2$ , compared to  $\sim M^3$  when applying LU decomposition. This is largely beneficial for complex systems.

Henceforth we assume that we do not have any variational parameter in the determinant. For that reason, we only need the expressions for the probability ratio, gradient and Laplacian. The probability ratio and gradient can be calculated for either the spin-up matrix or the spin-down matrix, depending on the spin of the moved particle. The two expressions for  $k < N_{\uparrow}$  are given by

$$\begin{aligned} \frac{|\Psi_{\text{sd}}(\mathbf{R}_{\text{new}})|^2}{|\Psi_{\text{sd}}(\mathbf{R}_{\text{old}})|^2} &= \frac{|\hat{D}_{\uparrow}(\mathbf{R}_{\uparrow}^{\text{new}})|^2}{|\hat{D}_{\uparrow}(\mathbf{R}_{\uparrow}^{\text{old}})|^2}, \\ \nabla_k \ln |\hat{D}_{\uparrow}(\mathbf{R}_{\uparrow})| &= \sum_{j=1}^{N_{\uparrow}} \nabla_k d_{jk}(\mathbf{R}_{\uparrow}) d_{kj}^{-1}(\mathbf{R}_{\uparrow}), \end{aligned} \quad (9.37)$$

while for  $k \geq N_{\uparrow}$  we have

$$\begin{aligned} \frac{|\Psi_{\text{sd}}(\mathbf{R}_{\text{new}})|^2}{|\Psi_{\text{sd}}(\mathbf{R}_{\text{old}})|^2} &= \frac{|\hat{D}_{\downarrow}(\mathbf{R}_{\downarrow}^{\text{new}})|^2}{|\hat{D}_{\downarrow}(\mathbf{R}_{\downarrow}^{\text{old}})|^2}, \\ \nabla_k \ln |\hat{D}_{\downarrow}(\mathbf{R}_{\downarrow})| &= \sum_{j=N_{\uparrow}}^F \nabla_k d_{jk}(\mathbf{R}_{\downarrow}) d_{kj}^{-1}(\mathbf{R}_{\downarrow}). \end{aligned} \quad (9.38)$$

On the other hand, the local energy in equation (9.7) only requires the sum of all Laplacians, and we obtain an expression that is independent of which particle we have moved,

$$\nabla^2 \ln |\hat{D}(\mathbf{R})| = \sum_{k=1}^F \left[ \sum_{j=1}^F \nabla_k^2 d_{jk}(\mathbf{R}) d_{kj}^{-1}(\mathbf{R}) - \left( \sum_{j=1}^F \nabla_k d_{jk}(\mathbf{R}) d_{kj}^{-1}(\mathbf{R}) \right)^2 \right], \quad (9.39)$$

where we have  $F = Nd$  degrees of freedom.

We have now presented the theory behind finding the ratio between the new and the old probability and the gradients of the determinant (equations (9.37-9.39)), and we have described how we efficiently can find the inverse of the Slater matrix (equations (9.33-9.36)). In order to clarify, we will outline some selected parts of the Slater determinant implementation.

In the code, we create a Slater matrix, `m_slaterMatrix` where all the elements are stored. This matrix contains both  $\hat{D}_\uparrow$  and  $\hat{D}_\downarrow$ , and has therefore dimensions  $N \times N/2$ . Furthermore, we store the gradient of the elements concerning all the  $F$  elements in a matrix `m_slaterMatrixDer`, which naturally gets the dimensions  $F \times N/2$ . We also create a matrix `m_slaterMatrixSecDer` to store all the Laplacians of the elements, which also has the dimensions  $F \times N/2$ . In all of them, we only need to update a row when a electron is moved, resulting in an acceptable computational cost. The `m_slaterMatrixDer` is updated according to

```
void SlaterDeterminant::updateSlaterMatrixDerRow(const int row)
{
    int electron = int(row / m_numberOfDimensions);
    int dimension = row % m_numberOfDimensions;
    for (int col = 0; col < m_numberOfElectronsHalf; col++) {
        m_slaterMatrixDer(row, col) = m_basis->basisElementDer(col, dimension,
            ↪ m_positions.col(electron));
    }
}
```

where each element is taken from the `basisElementDer` function in the `Basis` class. This function returns just the derivative of the single-particle function called for the chosen basis set. Note also that only the coordinates of the moved electron, stored in a column of the `m_positions` matrix, is needed for the update. The update of `m_slaterMatrix` and `m_slaterMatrixSecDer` are very straightforward and similar to the example above, so we will not discuss them further.

What might be less intuitive is how to update the inverse of the Slater matrix. We also store this in a dedicated matrix `m_slaterMatrixInverse`, and we use LU decomposition to initialize it. After that, we use equations (9.33-9.36) to update the inverse. We implement it as

```
void SlaterDeterminant::updateRatio()
{
    m_ratio = m_slaterMatrix.row(m_particle) * m_slaterMatrixInverse.col(m_particle);
}

void SlaterDeterminant::updateSlaterMatrixInverse(int start, int end)
{
    updateRatio();
    for (int j = start; j < m_particle; j++) {
        double S = m_slaterMatrix.row(m_particle) * m_slaterMatrixInverse.col(j);
        m_slaterMatrixInverse.col(j) -= S * m_slaterMatrixInverse.col(m_particle) /
            ↪ m_ratio;
    }
    for (int j = m_electron+1; j < end; j++) {
        double S = m_slaterMatrix.row(m_particle) * m_slaterMatrixInverse.col(j);
        m_slaterMatrixInverse.col(j) -= S * m_slaterMatrixInverse.col(m_particle) /
            ↪ m_ratio;
    }
    m_slaterMatrixInverse.col(m_particle) /= m_ratio;
}
```

where `m_ratio` represents the ratio between the new and the old determinant. Note that the loops never affect the  $i$ 'th columns, where electron  $i$  is moved (in the code denoted by the global variable `m_particle`). The arguments of the function `updateSlaterMatrixInverse` specify which part of the matrix that should be updated, based on whether the moved electron has spin-up or spin-down. We will end our discussions of the Slater determinant by presenting the implementation of the gradient and the Laplacian of the logarithm of the determinant. These were decided stored in the vectors `m_determinantDer` and `m_determinantSecDer` for  $\nabla_k |\hat{D}(\mathbf{R})|/|\hat{D}(\mathbf{R})|$  and  $\nabla_k^2 |\hat{D}(\mathbf{R})|/|\hat{D}(\mathbf{R})|$ , respectively. These vectors are updated using vector operations in the following fashion

```
void SlaterDeterminant::updateSlaterDeterminantDerivatives(int start, int end)
```

```

{
    for (int i = start * m_numberOfDimensions; i < end * m_numberOfDimensions; i++) {
        int electron = int(i / m_numberOfDimensions);
        m_determinantDer(i) = m_slaterMatrixDer.row(i) *
            ↳ m_slaterMatrixInverse.col(electron);
        m_determinantSecDer(i) = m_slaterMatrixSecDer.row(i) *
            ↳ m_slaterMatrixInverse.col(electron);
    }
}

```

We avoid a double loop by taking an inner product instead. However, we are left with one loop which can also be avoided using smart matrix operations.

## 9.4 Jastrow factor

The second part of a Slater-Jastrow wave function is the Jastrow factor, which is meant to take care of the electron-electron correlations. The optimization scheme for this element is not as complex as the determinant, and this section will, therefore, be notably shorter than the previous. We will first discuss the two Jastrow factors given in section 7.1.2: the simple Jastrow and the Padé-Jastrow factor, and then we look at how the distance matrix can be updated efficiently.

### 9.4.1 The Simple Jastrow factor

Recall the simple Jastrow factor from (7.11),

$$\Psi_{sj}(\mathbf{R}; \boldsymbol{\beta}) = \exp \left( \sum_{i=1}^N \sum_{j>i}^N \beta_{ij} r_{ij} \right), \quad (9.40)$$

with  $N$  as the number of electrons,  $r_{ij}$  as the distance between electron  $i$  and  $j$ , and  $\beta_{ij}$  as variational parameters. Albeit this element is simple, challenge are encountered as we operate in Cartesian coordinates, while the expressed Jastrow factor obviously is easier to deal with in polar coordinates. Since we need to differentiate this with respect to all degrees of freedom, we need to be attentive not confusing the electron indices with the coordinate indices. Let us reserve  $j'$  as the coordinate index and  $j$  as the index of the corresponding electron. The relationship between  $j'$  and  $j$  is then *always*  $j = j' \backslash d$  with  $d$  as the number of dimensions and where the backslash denotes integer division. The other way around, we have  $j' = j \cdot d + D$  where  $D$  is the respective dimension of the coordinate  $j'$ . With that notation, the probability ratio is given by

$$\frac{|\Psi_{sj}(\mathbf{R}_{\text{new}})|^2}{|\Psi_{sj}(\mathbf{R}_{\text{old}})|^2} = \exp \left( 2 \sum_{j=1}^N \beta_{ij} (r_{ij}^{\text{new}} - r_{ij}^{\text{old}}) \right), \quad (9.41)$$

where  $i$  again is the moved electron. The gradient is straightforward to find, and reads

$$\nabla_{k'} \ln \Psi_{sj} = \sum_{j=1}^N \beta_{kj} \frac{x_{k'} - x_{j'}}{r_{kj}}, \quad (9.42)$$

where  $j'$  is related to the same dimension as  $k'$ . Here we use  $x_{j'}$  as a general coordinate, irrespective whether it is associated with the  $x$ -direction or not. This also applies to the Laplacian,

$$\nabla^2 \ln \Psi_{sj} = \sum_{k'=1}^F \sum_{j=1}^N \frac{\beta_{kj}}{r_{kj}} \left[ 1 - \left( \frac{x_{k'} - x_{j'}}{r_{kj}} \right)^2 \right], \quad (9.43)$$

with  $F = Nd$  again as the degrees of freedom. Finally, the parameter update is given by

$$\nabla_{\beta_{ml}} \ln \Psi_{sj} = r_{ml}. \quad (9.44)$$

For this element, the most important thing we can do to keep the computational cost low is to reveal that only a row and a column of the distance matrix is changed as we move a particle. Updating the entire distance matrix means updating  $N^2$  elements, while updating a row and a column means updating  $2N$  elements, which is an important difference for large systems. This is detailed in section 9.4.3.

We also observe that the factor  $(x_{k'} - x_j)/r_{kj}$  is found in both the gradient and the Laplacian, so by storing this matrix, we can speed-up the computations. Most naturally, the matrix has dimensions  $F \times F$ , but using that we only are interested in the elements where  $x_{k'}$  and  $x_j$  are associated with the same dimension and where the diagonal is zero, only  $F$  of the elements need to be found. Further, the matrix is obviously anti-symmetric, so we only need to calculate  $F/2$  of the elements. When an electron is moved, only the elements related to the moved electron need to be updated. In total, we therefore have to update  $2(N - 1)$  elements. Again, we utilize that the matrix is anti-symmetric and get the following efficient update scheme

```
void SimpleJastrow::updatePrincipalDistance(int i)
{
    int i_d = i % m_numberOfDimensions;
    for (int j_p = 0; j_p < i_p; j_p++) {
        int j = i_d + j_p * m_numberOfDimensions;
        m_principalDistance(i, j) = (m_positions(i) - m_positions(j)) /
            ↪ m_distanceMatrix(i_p, j_p);
        m_principalDistance(j, i) = -m_principalDistance(i, j);
    }
    for (int j_p = i_p + 1; j_p < m_numberOfElectrons; j_p++) {
        int j = i_d + j_p * m_numberOfDimensions;
        m_principalDistance(i, j) = (m_positions(i) - m_positions(j)) /
            ↪ m_distanceMatrix(i_p, j_p);
        m_principalDistance(j, i) = -m_principalDistance(i, j);
    }
}
```

with  $i_p$  as the moved electron,  $i_d$  as the direction the electron is moved in and  $i$  as the coordinate index. Similarly, the loop goes over the electrons  $j_p$  with the associated coordinate  $j$ . Note that we split the loop in two parts to avoid calculating the distance from an electron to itself. This trick is also done in many of the other functions in the simple Jastrow and Padé-Jastrow classes.

### 9.4.2 The Padé-Jastrow factor

The Padé-Jastrow factor is a more complicated Jastrow factor, and was specified in equation (7.12),

$$\Psi_{pj}(R; \beta) = \exp \left( \sum_{i=1}^N \sum_{j>i}^N \frac{a_{ij} r_{ij}}{1 + \beta r_{ij}} \right), \quad (9.45)$$

where  $\beta$  is a variational parameter and the  $a_{ij}$  is **not** a variational parameter, but rather constants dependent on the spin of electrons  $i$  and  $j$ . Similar to the simple Jastrow, we also here need to distinguish between electron indices and coordinate indices because of the radial distances  $r_{ij}$ . We do the same trick with denoting the coordinate index by  $j'$  and the electron index by  $j$ . Then gradient is then obtained as

$$\nabla_{k'} \ln \Psi_{pj} = \sum_{j \neq k=1}^N \frac{a_{kj}}{(1 + \beta r_{kj})^2} \frac{x_{k'} - x_{j'}}{r_{kj}}, \quad (9.46)$$

with respect to the coordinate  $x_{k'}$ . By again differentiating this with respect to  $x_{k'}$ , we obtain the Laplacian. We again only need the sum of all the Laplacians, which is given by

$$\nabla^2 \ln \Psi_{\text{pj}} = \sum_{k'=1}^F \sum_{j \neq k=1}^N \frac{a_{kj}}{(1 + \beta r_{kj})^2} \left[ 1 - \left( 1 + 2 \frac{\beta r_{kj}}{1 + \beta r_{kj}} \right) \left( \frac{x_{k'} - x_{j'}}{r_{kj}} \right)^2 \right] \frac{1}{r_{kj}}. \quad (9.47)$$

Similar to the simple Jastrow factor, we again observe that the factor  $(x_{k'} - x_{j'})/r_{kj}$  appears in both the gradient and the Laplacian, which can be stored as a matrix and updated in the same way as described for the simple Jastrow factor. The last expression we need is the one used to update the variational parameter  $\beta$ , which is found to be

$$\nabla_\beta \ln \Psi_{\text{pj}} = - \sum_{i=1}^N \sum_{j>i}^N \frac{a_{ij} r_{ij}^2}{(1 + \beta r_{ij})^2}. \quad (9.48)$$

In addition to the factor  $g_{i'j'} \equiv (x_{k'} - x_{j'})/r_{kj}$ , there are multiple factors that we can store to make the computations cheaper. The factor  $f_{ij} \equiv a_{ij}/(1 + \beta r_{ij})^2$  is found both in the gradient, Laplacian and parameter gradient, and storing it will save a significant amount of computational time. Lastly, the factor  $h_{ij} \equiv r_{ij}/(1 + \beta r_{ij})$  is found in several places and will be stored as well. As a summary, we use

$$f_{ij} = \frac{a_{ij}}{(1 + \beta r_{ij})^2} \quad \wedge \quad g_{i'j'} = \frac{x_{i'} - x_{j'}}{r_{ij}} \quad \wedge \quad h_{ij} = \frac{r_{ij}}{1 + \beta r_{ij}}. \quad (9.49)$$

and obtain the simplified expressions

$$\begin{aligned} \frac{|\Psi_{\text{pj}}(\mathbf{R}_{\text{new}})|^2}{|\Psi_{\text{pj}}(\mathbf{R}_{\text{old}})|^2} &= \exp \left( 2 \sum_{j=1}^N a_{ij} (h_{ij}^{\text{new}} - h_{ij}^{\text{old}}) \right), \\ \nabla_{k'} \ln \Psi_{\text{pj}} &= \sum_{j \neq k=1}^N f_{kj} \cdot g_{k'j'}, \\ \nabla^2 \ln \Psi_{\text{pj}} &= \sum_{k'=1}^F \sum_{j \neq k=1}^N \frac{f_{kj}}{r_{kj}} \left[ 1 - (1 + 2\beta h_{kj}) g_{k'j'}^2 \right], \\ \nabla_\beta \ln \Psi_{\text{pj}} &= - \sum_{l=1}^N \sum_{j>l}^N a_{lj} h_{lj}^2 = - \sum_{l=1}^N \sum_{j>l}^N f_{lj} r_{lj}^2, \end{aligned} \quad (9.50)$$

with unmarked indices ( $j$ ) as the electron related ones and the marked ( $j'$ ) as the coordinate related ones.  $i$  is the moved electron. We now proceed further to the update of the distance matrix, which is where we can find the remaining optimization possibilities.

### 9.4.3 Updating the distance matrix

The distance matrix, used in the Jastrow factors, gives an illustrating example on how we can avoid repeating calculations. The matrix, henceforth named  $M$ , contains the relative distances between all the electrons, for three electrons given by

$$M = \begin{pmatrix} r_{11} & r_{12} & r_{13} \\ r_{21} & r_{22} & r_{23} \\ r_{31} & r_{32} & r_{33} \end{pmatrix} = \begin{pmatrix} 0 & r_{12} & r_{13} \\ r_{12} & 0 & r_{23} \\ r_{13} & r_{23} & 0 \end{pmatrix}, \quad (9.51)$$

where  $r_{ij}$  means the distance between electrons  $i$  and  $j$ . Since  $r_{ij} = r_{ji}$  and  $r_{ii} = 0$ , the matrix becomes symmetric with zeros on the diagonal, which means that we only need to calculate  $N(N - 1)/2$  elements instead of  $N^2$ . Further, we can utilize that only an electron is moved at a time, which means that only a row and a column are changed when an electron is moved. For instance, if electron 1 is moved, the upper row and the left-hand side column in matrix  $M$  need to be updated. In our program, we have implemented this in the following way

```
double Metropolis::calculateDistanceMatrixElement(const int i, const int j)
{
    double dist = 0;
    int parti = m_numberOfDimensions*i;
    int partj = m_numberOfDimensions*j;
    for(int d=0; d<m_numberOfDimensions; d++) {
        double diff = m_positions(parti+d)-m_positions(partj+d);
        dist += diff*diff;
    }
    return sqrt(dist);
}

void Metropolis::calculateDistanceMatrixCross(const int electron) {
    for(int i=0; i<m_numberOfElectrons; i++) {
        m_distanceMatrix(electron, i) = calculateDistanceMatrixElement(electron, i);
        m_distanceMatrix(i, electron) = m_distanceMatrix(electron, i);
    }
}
```

where the function `calculateDistanceMatrixElement(i,j)` returns element  $i,j$  of the matrix, which is called from the function `calculateDistanceMatrixCross(electron)`. The latter takes the moved electron index as input, and updates the necessary row and column of the matrix.

For systems of non-interacting electrons, the distance matrix is redundant, and should therefore not be calculated. We have solved this by giving all the wave function elements and the Hamiltonians a number which indicated whether they require the distance matrix or not. If no part of the code needs the distance matrix, it is never calculated. We also calculate the radial position globally when any part of the code requires it. The components are stored in a vector named `radialVector`, applying the same optimization ideas as the distance matrix.

## 9.5 Sampling

Also, when it comes to the sampling itself, there exist optimization schemes to speed-up the process. Remember that the sampling algorithm often is repeated millions of times for each iteration, so even a small change in the code may give a massive impact on the computational cost. We will initially present the brute force sampling implementation in its entirety before we move on to the importance of sampling implementation. For the latter, we will discuss the optimization possibilities and connect them to the actual implementation.

### 9.5.1 Brute force sampling

The brute force sampling was introduced in section 7.3.1, and is the most basic sampling method implemented. The sampling function `BruteForce::acceptMove`, which returns true if the move is accepted, is implemented as

```
bool BruteForce::acceptMove()
{
    int i = m_RNG->nextInt(m_degreesOfFreedom);

    m_positionsOld = m_positions;
```

```

m_radialVectorOld = m_radialVector;
m_distanceMatrixOld = m_distanceMatrix;

m_positions(i) += (m_rng->nextDouble() - 0.5) * m_stepLength;
if (m_calculateDistanceMatrix) {
    Metropolis::calculateDistanceMatrixCross(int(i / m_numberOfDimensions));
}
if (m_calculateRadialVector) {
    Metropolis::calculateRadialVectorElement(int(i / m_numberOfDimensions));
}
m_system->updateAllArrays(m_positions, m_radialVector, m_distanceMatrix, i);

double p = m_system->evaluateProbabilityRatio();
if (p < m_rng->nextDouble()) {
    m_positions = m_positionsOld;
    m_distanceMatrix = m_distanceMatrixOld;
    m_radialVector = m_radialVectorOld;
    m_system->resetAllArrays();
    return false;
}
return true;
}

```

where  $i$  is the changed coordinate drawn from the random number generator `m.RNG`. Initially the old positions, radial vector and distance matrix are stored, in case the move is rejected, and then a new move is proposed in positive or negative direction. If the radial vector or distance matrix (or both) are needed somewhere in the code, they are updated in this function, using the ideas and implementation presented in section 9.4.3. They are distributed to the wave function elements using the function `updateAllArrays`.

In the end, the probability ratio is evaluated using the function `evaluateProbabilityRatio` presented in section 9.2.3. If this ratio is larger than a random number between 0 and 1, the move is accepted, and otherwise, we set all the arrays back to the old ones (also the ones in the wave function elements).

### 9.5.2 Importance sampling

The importance sampling implementation is very similar to the brute force sampling implementation, and we will, therefore, not repeat it. However, we need to calculate the quantum force and the ratio between the new and the old Green's function, which can be calculated in clever ways to keep the code efficient.

We have already seen that the quantum force takes the same form as the gradient of the trial wave function,  $F(\mathbf{R}) = 2(\nabla\Psi_T(\mathbf{R}))/\Psi_T(\mathbf{R})$ , and we can therefore simply reuse the function `computeGradient`, which is a part of the local energy computations from section 9.2.1. We call this from the function `ImportanceSampling::QuantumForce`, which contains the few lines of code

```

double ImportanceSampling::QuantumForce(const int i)
{
    double QF = 0;
    for (auto &j : m_waveFunctionVector) {
        QF += j->computeGradient(i);
    }
    return 2 * QF;
}

```

where the force in dimension  $i$  is returned. The Green's function was first presented in section 7.3.2, and at first glance it might look computational expensive to evaluate. Fortunately, we only need the ratio between the old and the new function which can be found in a quite simple fashion. Actually, both the diffusion constant  $D$  and the time step  $\Delta t$  cancel in the exponent, and

the ratio can be expressed in the elegant form

$$g(\mathbf{R}', \mathbf{R}, \Delta t) \equiv \frac{G(\mathbf{R}', \mathbf{R}, \Delta t)}{G(\mathbf{R}, \mathbf{R}', \Delta t)} = \exp(-( \mathbf{R}' - \mathbf{R}) \cdot (\mathbf{F}(\mathbf{R}') - \mathbf{F}(\mathbf{R})) / 2), \quad (9.52)$$

where  $\mathbf{R}$  and  $\mathbf{R}'$  differ by one element and so does  $\mathbf{F}(\mathbf{R})$  and  $\mathbf{F}(\mathbf{R}')$ . It can therefore be evaluated in a very efficient scheme

```
double ImportanceSampling::GreenRatio(const int i)
{
    double dQF = m_quantumForceOld(i) - m_quantumForceNew(i);
    return exp(0.5 * dQF * m_dx) + 1;
}
```

where  $dQF$  is the difference between the new and the old force and  $m_dx$  is the distance electron  $i$  is moved. The contribution 1 appears from the term where  $m_dx$  is zero, such that we get zero in the exponent.

## 9.6 Update of parameters

The parameter update is a central part of a VMC implementation, and a good VMC implementation requires a good optimization algorithm. Since the optimization functions are called outside the sampling, they are just called a fraction of times, compared to the function called from the sampling. Therefore, we will not put too much effort into making them efficient, but they should still be thought-through. We will here discuss the gradient descent method with momentum and monotonic decaying step and the ADAM optimizer. The Optimizer class contains a pure virtual function `updateParameters`, which is thus forced to be included in the optimizer subclasses. This function returns the update of the new parameters and is the function we will discuss in this section.

### 9.6.1 Gradient descent

Gradient descent is a simple optimization algorithm, and so is the implementation. Based on the theory presented in section 5.6.1, the implementation is really straightforward and reads

```
Eigen::MatrixXd GradientDescent::updateParameters()
{
    m_step += 1;
    double monotonic = 1 / pow(m_step, m_monotonicExp);
    m_v = m_gamma * m_v + m_eta * Optimization::getEnergyGradient() * monotonic;
    return m_v;
}
```

where  $m_v$  is the momentum vector and  $m_{monotonicExp}$  describes how fast the rate should decrease. Further,  $m_\gamma$  is the momentum parameter defining the relative size of the momentum. The function `Optimization::getEnergyGradient` returns a matrix with the gradients of the energy expectation value with respect to all the parameters, given in equation (7.21).

### 9.6.2 ADAM optimizer

The ADAM optimizer implementation also is very straightforward based on the algorithm given in section 5.6.4. The momentum vectors were implemented as matrices to match the dimensions of the parameter matrix. By matrix operations, we could also have made the function efficient,

but since that is not the aim here, we decided to keep the loops in order to make the code readable. The implementation looks like

```
Eigen::MatrixXd ADAM::updateParameters()
{
    m_step += 1;
    m_g = Optimization::getEnergyGradient();
    m_m = m_beta1 * m_m + (1 - m_beta1) * m_g;
    m_v = m_beta2 * m_v + (1 - m_beta2) * m_g.cwiseAbs2();
    m_mHat = m_m / (1 - pow(m_beta1, m_step));
    m_vHat = m_v / (1 - pow(m_beta2, m_step));
    for (int i = 0; i < m.numberOfElements(); i++) {
        for (int j = 0; j < m_maxParameters; j++) {
            m_theta(i, j) = m_eta * m_mHat(i, j) / (sqrt(m_vHat(i, j) + m_epsilon));
        }
    }
    return m_theta;
}
```

where effort was made naming variables consistently with what we did in section 5.6.4. The parameter matrix, named `m_parameters`, can then easily be updated by the code

```
if (m_rank == 0) {
    m_sampler->computeAverages();
    m_parameters -= m_optimization->updateParameters();
}
```

where `m_optimization` is the specified optimizer and `m_myrank` is the *rank* of the process. Parallel processing is not discussed yet, but we will describe it briefly in the following section.

## 9.7 Parallel processing

The code was parallelized using MPI to make studies of large systems possible. This means that the code can run multiple parallel threads and in that manner, utilize all the processors. Most notably, this allows us to run on computer clusters which typically reduce the running time with a factor 10-100. We will not explain how MPI works in detail, nor will we detail the implementation of MPI since the commands are distributed over the entire code. The thing we present is a sketch of the idea behind the parallelization used for our particular code.

One thing that makes VMC preferred over other many-body methods is that the algorithm easily can be split into independent parts, which encourages parallelization. The entire sampling can be split into as many parallel processes as needed, such that the code can be run on an arbitrary number of CPUs. We typically distinguish between wall clock time,  $t_{clock}$  and CPU time  $t_{cpu}$  where the former is the time measured by a clock, and the latter is the total computation time from all the CPUs. The speed-up will in general not be 100%, i.e.  $t_{clock} \neq t_{cpu}/n$  with  $n$  as the number of processes, mainly because the code that is not part of the sampling cannot be parallelized and needs to be run on one CPU. The process that takes care of this part is the primary process with rank 0.

In algorithm 3, we have sketched very roughly how the parallelization goes. We first run the entire sampling individually for all the  $n$  processes, and if something goes wrong, we call the `MPI_Abort` function. To align the processes before we collect all the cumulative values, we use the function `MPI_Barrier` and we use `MPI_Reduce` for the actual summation. After that, the average energies are calculated by the primary process *only*, and in the end, the updated parameters are broadcast to all the other processes. Note that this is just a sketch where we avoid the arguments and the actual implementation of the MPI functions. This is of course found in the code.

**Algorithm 3:** Sketch of the parallelization.

---

```

1 MPI_Init() (Initialize MPI);
2 while not converged do
3    $E_L = 0;$ 
4   gradient = 0;
5   Egradient = 0;
6   for  $i \leftarrow 1$  to  $M$  do
7      $E_L += (\hat{\mathcal{H}}\Psi)/\Psi;$ 
8     gradient +=  $\nabla_\theta \ln \Psi;$ 
9     Egradient +=  $(\hat{\mathcal{H}}\Psi)/\Psi * \nabla_\theta \ln \Psi;$ 
10  end
11  if something goes wrong then
12    | MPI_Abort() (Terminate all processes);
13  end
14  MPI_Barrier() (Align processes);
15  MPI_Reduce( $E_L$ , gradients, Egradients) (Collect cumulative values);
16  if myrank == 0 then
17    |  $\bar{E}_L = E_L / M;$ 
18    | gradient = gradient /  $M;$ 
19    | Egradient = Egradient /  $M;$ 
20    |  $G = 2 * (\text{Egradient} - \bar{E}_L * \bar{\text{Egradient}});$ 
21    |  $\theta -= \eta G;$ 
22  end
23  MPI_Bcast( $\theta$ ) (Broadcast parameters);
24 end
25 MPI_Finalize() (Finalize MPI);
Result: Optimal variational parameters  $\theta$ .

```

---

## 9.8 Electron density

We presented the theory behind the electron density in section 3.3, where we saw that the  $P$ -body density is given by an integral over all probability density functions,  $|\Psi(\mathbf{R}_1, \dots, \mathbf{R}_N)|^2$ , but  $P$  of them. Usually, we look at the one-body density or the two-body density, leaving out one or two electrons from the integration. Further in section 7.1.5, we gave a brief explanation of how the one-body density can be found using Monte Carlo integration in a VMC scheme. In this section, we will discuss the technique in more detail, and of course, give the actual implementation.

In our particular implementation, we have technically calculated the one-body density in two different ways; by dividing the space into annuluses<sup>†</sup> to calculate the radial electron distribution and by dividing the space into a grid to calculate the spatial electron distribution. The former is convenient when we want to present the density in a two-dimensional plot, making a comparison between multiple methods easy. Often, the one-body density is only dependent on the radial distance from the center, and then it is sufficient to look at the radial density profile. On the other hand, the spatial density profile contains more information between the position of the electrons, which is interesting when the density is also dependent on the angle.

For the radial density profile, we in practice deal with bins formed by annuluses of equal width  $\Delta r$ , the two-dimensional case is illustrated in figure (9.1). This means that the bins do not

---

<sup>†</sup>An annulus is a ring-shaped object with a region bounded by two concentric circles.

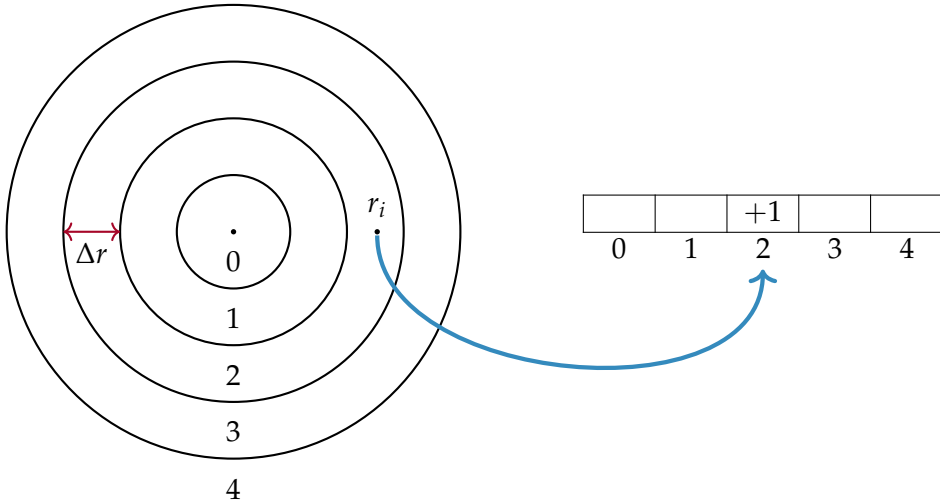


**Figure 9.1:** This figure is meant to illustrate how the radial one-body density is calculated using Monte Carlo integration. The space is divided into  $n$  bins (here  $n = 5$ ), and the number of times the electrons appear in each bin is counted throughout the sampling. Afterward, the bins need to be standardized.

have an equal extent, and we need to compensate for this by dividing by the respective volume. In two dimensions, a bin  $i$  has the area

$$A_i = (2i + 1)\pi\Delta r^2, \quad (9.53)$$

and in three dimensions the volume of bin  $i$  is

$$V_i = 4(i(i + 1) + 1/3)\pi\Delta r^3. \quad (9.54)$$

The most intuitive way of finding the correct bin of an electron, is to loop through all the bins and check if the electrons belong to the particular bin. However, this is a rather inefficient method of doing it, and it can be done much smarter revealing that an electron at radius  $r$  belong to the bin of index

$$i = r \backslash \Delta r + 1, \quad (9.55)$$

where  $\backslash$  indicates integer division.

By defining a vector `m_electronsPerBin` with the length number of bins, we can find the number of electrons in each bin by a simple loop over all electrons,

```
void Sampler::computeOneBodyDensity(const Eigen::VectorXd& radialVector)
{
    for (int i_p = 0; i_p < m_numberOfElectrons; i_p++) {
        int bin = int(radialVector(i_p) / m_radialStep) + 1;
        m_electronsPerBin(bin)++;
    }
}
```

where `m_radialStep` is the width of each annulus, above denoted by  $\Delta r$ . In the end, `m_electronsPerBin` is printed to file, and we do the normalization when a script reads this file. For the case where we look at the spatial density distribution, all the bins have equal size, and the approach is therefore straight-forward. Also, for the two-body density, we can choose to either calculate the radial or the spatial density distribution, but as the spatial distribution becomes higher-dimensional, we stick to the radial distribution for this quantity. This distribution is calculated in a similar way as the one-body density, and it will not be further detailed.

## 9.9 Random number generator

Monte Carlo integration rely on random numbers that are received from a random number generator (RNG). The RNG should have two main properties: It should give many independent, uncorrelated random numbers and it should be fast. The former depends on the *period* of the RNG, where a long period gives many independent numbers.

In this work, we have used the Mersenne Twister random number generator, as it has a period of  $2^{19937} - 1$  which is known as the Mersenne prime. This is an incredibly large number and should be more than sufficient for our purpose. We use the built-in package in C++, `std::mt19937`, which is also very efficient.

It is important to be aware that the way we use the RNG is not optimized for parallel processing. The reason for this, is that we do not necessarily have different seeds for different processes. However, since the communication between the various processes is limited, this will not affect our results.



## CHAPTER 10

# Implementation: Restricted Boltzmann Machines

The restricted Boltzmann machines where detailed in chapter 6 from a machine learning point of view. In section 7.2, we described briefly how the Boltzmann machines can be used as the trial wave function ansatz in a variational Monte Carlo framework. The implementation of this framework was described in the previous chapter, with examples taken from the code. The remaining part is to detail the implementation of ansätze based on the restricted Boltzmann machine.

This work aims to reduce the physical intuition needed when performing electron structure calculations. However, as argued before, we do not expect a restricted Boltzmann machine to understand the complex Fermi-Dirac statistics. Therefore, a Slater determinant is implemented in the trial wave function ansatz in order to enforce anti-symmetry. In section 7.1.1, we decomposed the Slater determinant in a spin-up part and a spin-down part with the assumption that the Hamiltonian is spin-independent. Therefore, we can express the determinant as

$$|\hat{S}(\mathbf{R})| = \frac{1}{\sqrt{N!}} |\hat{S}_\uparrow(\mathbf{R}^\uparrow)| \cdot |\hat{S}_\downarrow(\mathbf{R}^\downarrow)|, \quad (10.1)$$

with  $N$  as the number of electrons and  $\mathbf{R} = \{\mathbf{r}_1, \mathbf{r}_2, \dots, \mathbf{r}_N\}$  as the collective spatial coordinates.  $\mathbf{R}^\sigma = \{\mathbf{r}_1^\sigma, \mathbf{r}_2^\sigma, \dots, \mathbf{r}_{N_\sigma}^\sigma\}$  are the spin- $\sigma$  spatial coordinates for  $\sigma \in \{\uparrow, \downarrow\}$ . For quantum dot systems, the spin- $\sigma$  determinant can be split in a factor  $G(\mathbf{R})$  and a determinant containing the Hermite polynomials,

$$|\hat{S}_\sigma(\mathbf{R})| = G(\mathbf{R}) \underbrace{\begin{vmatrix} H_1(\mathbf{r}_1) & H_2(\mathbf{r}_1) & \cdots & H_N(\mathbf{r}_1) \\ H_1(\mathbf{r}_2) & H_2(\mathbf{r}_2) & \cdots & H_N(\mathbf{r}_2) \\ \vdots & \vdots & \ddots & \vdots \\ H_1(\mathbf{r}_N) & H_2(\mathbf{r}_N) & \cdots & H_N(\mathbf{r}_N) \end{vmatrix}}_{|\hat{D}(\mathbf{R})|}, \quad (10.2)$$

as seen in section 9.3.1. For the standard single-particle functions for quantum dots, the factor  $G(\mathbf{R})$  is just the Gaussian function,  $G(\mathbf{R}) = \exp\left(-\frac{1}{2}\alpha\omega\sum_{i=1}^F x_i^2\right)$ , but as suggested by Carleo & Troyer<sup>24</sup>, this can be replaced by the marginal distribution of the visible units of a Gaussian-binary restricted Boltzmann machine in order to find a more flexible ansatz. This will be our first machine learning trial wave function ansatz, denoted by the RBM ansatz. We then get the determinant

$$|\hat{S}_\sigma(\mathbf{R})| = P(\mathbf{R}) \underbrace{\begin{vmatrix} H_1(\mathbf{r}_1) & H_2(\mathbf{r}_1) & \cdots & H_N(\mathbf{r}_1) \\ H_1(\mathbf{r}_2) & H_2(\mathbf{r}_2) & \cdots & H_N(\mathbf{r}_2) \\ \vdots & \vdots & \ddots & \vdots \\ H_1(\mathbf{r}_N) & H_2(\mathbf{r}_N) & \cdots & H_N(\mathbf{r}_N) \end{vmatrix}}_{|\hat{D}(\mathbf{R})|}, \quad (10.3)$$

with

$$P(\mathbf{R}) = \frac{1}{Z} \exp\left(-\sum_{i=1}^F \frac{(x_i - a_i)^2}{2\sigma_i^2}\right) \prod_{j=1}^H \left[1 + \exp\left(b_j + \sum_{i=1}^F \frac{x_i w_{ij}}{2\sigma_i^2}\right)\right] \quad (10.4)$$

as the marginal distribution, taken from section 6.3.1 where all the symbols are defined. This can be treated as a separate wave function element, as discussed in section 9.3.1, and we can reuse the evaluation of the determinant  $|\hat{D}(\mathbf{R})|$  discussed in section 9.3.3. If we denote this element by "rbm" and omit the normalization factor  $Z$ , the total element is given by

$$\Psi_{\text{rbm}}(\mathbf{x}; \mathbf{a}, \mathbf{b}, \mathbf{w}) = \exp\left(-\sum_{i=1}^F \frac{(x_i - a_i)^2}{2\sigma_i^2}\right) \prod_{j=1}^H \left[1 + \exp\left(b_j + \sum_{i=1}^F \frac{x_i w_{ij}}{\sigma_i^2}\right)\right], \quad (10.5)$$

which can naturally be split further into a Gaussian part and a product part. This splitting is performed in order to simplify the equations needed when computing the kinetic energy. They will also be implemented as separate wave function elements, as this will reduce the complexity of the derivatives associated with each element. The first part will henceforth be denoted by "RBM-Gaussian", while the last part will be denoted by "RBM-product".

## 10.1 RBM-Gaussian

The RBM-Gaussian is the first part of equation (10.5) and reads

$$\Psi_{\text{rg}}(\mathbf{x}; \mathbf{a}) = \exp\left(-\sum_{i=1}^F \frac{(x_i - a_i)^2}{2\sigma_i^2}\right). \quad (10.6)$$

The element is similar to the Gaussian element presented in section 9.3.2, and the derivatives also become similar. For that reason, they will be listed up without further explanation:

$$\begin{aligned} \frac{|\Psi_{\text{rg}}(\mathbf{x}_{\text{new}})|^2}{|\Psi_{\text{rg}}(\mathbf{x}_{\text{old}})|^2} &= \exp\left(\frac{(x_i^{\text{old}} - a_i)^2 - (x_i^{\text{new}} - a_i)^2}{2\sigma_i^2}\right), \\ \nabla_k \ln \Psi_{\text{rg}} &= -\frac{x_k - a_k}{\sigma_i^2}, \\ \nabla_k^2 \ln \Psi_{\text{rg}} &= -\frac{1}{\sigma_i^2}, \\ \nabla_{a_l} \ln \Psi_{\text{rg}} &= \frac{x_l - a_l}{\sigma_i^2}. \end{aligned} \quad (10.7)$$

Further, the frequency of the quantum dots should be inversely proportional to the Gaussian sampling width from the Gaussian-binary RBM,  $\sigma_i^2$ , such that we can set

$$\omega = \frac{1}{\sigma_i^2} \quad \forall \quad i \in \{1, \dots, F\}. \quad (10.8)$$

An obvious optimization concerning this element, is that we can introduce a vector  $\mathbf{x}\mathbf{a} \equiv \mathbf{x} - \mathbf{a}$ , which we deal with instead of the position vector  $\mathbf{x}$  and the parameter vector  $\mathbf{a}$ . We update the arrays using the virtual function `updateArrays`, given by

```
void RBMGaussian::updateArrays(const Eigen::VectorXd& positions,
                                const Eigen::VectorXd& /*radialVector*/,
                                const Eigen::MatrixXd& /*distanceMatrix*/,
```

```

        const int i)
{
    m_positions = positions;
    m_Xa = positions - m_a;
    double sqrdDiff = m_XaOld(i) * m_XaOld(i) - m_Xa(i) * m_Xa(i);
    m_probabilityRatio = exp(sqrdDiff / (2 * m_sigma_iSqr));
}

```

We see that the vector  $m_Xa$ , associated with  $xa$ , is declared globally such that it can be used in the gradients in equation (10.7). The updated coordinate is again denoted by  $i$ .

## 10.2 RBM-product

The RBM product is the last part of (6.19), and is thus given by

$$\Psi_{rp}(x; b, w) = \prod_{j=1}^H \left[ 1 + \exp \left( b_j + \sum_{i=1}^F \frac{x_i w_{ij}}{\sigma_i^2} \right) \right]. \quad (10.9)$$

For a general Gaussian-binary restricted Boltzmann machine product in the form of

$$\Psi(x; \theta) = \prod_{j=1}^H \left[ 1 + \exp(f_j(x; \theta)) \right], \quad (10.10)$$

it can be shown that the gradient and the Laplacian are

$$\nabla_k \ln \Psi_{rp} = \sum_{j=1}^H n_j \nabla_k(f_j), \quad (10.11)$$

and

$$\nabla_k^2 \ln \Psi_{rp} = \sum_{j=1}^H n_j [\nabla_k^2(f_j) + p_j (\nabla_k(f_j))^2], \quad (10.12)$$

respectively.  $p_j$  and  $n_j$  are the sigmoid and its counterpart,

$$n_j \equiv \frac{1}{1 + \exp(-f_j)} \quad \wedge \quad p_j \equiv \frac{1}{1 + \exp(+f_j)}. \quad (10.13)$$

These expressions can be used to directly find the kinetic energy contribution from this element, as the contribution is just the sum over the gradients and Laplacians,  $T = \sum_{k=1}^F [\nabla_k^2 \ln \Psi_{rp} + (\nabla_k \ln \Psi_{rp})^2]$ . An arbitrary parameter  $\theta_i$  can be updated according to the log-likelihood function, which is just the derivative of the log-likelihood function

$$\frac{\partial}{\partial \theta_i} \ln \Psi_{rp} = \sum_{j=1}^H n_j \frac{\partial}{\partial \theta_i}(f_j), \quad (10.14)$$

and the ratio between the new and the old wave function elements can be found by the product

$$\frac{\Psi_{rp}^{\text{new}}}{\Psi_{rp}^{\text{old}}} = \prod_{j=1}^H \frac{p_j^{\text{old}}}{p_j^{\text{new}}}. \quad (10.15)$$

In conclusion, what we actually need for obtaining the local energy and the parameter update, are closed-form expressions of  $\nabla_k(f_j)$ ,  $\nabla_k^2(f_j)$  and  $\partial_{\theta_i}(f_j)$  for all variational parameters  $\theta_i$ . For our particular expression of  $f_j = b_j + \sum_{i=1}^F x_i w_{ij} / \sigma_i^2$ , they can be found to be

$$\begin{aligned}\nabla_k(f_j) &= \frac{w_{kj}}{\sigma_i^2}, \\ \nabla_k^2(f_j) &= 0, \\ \partial_{b_l}(f_j) &= \delta_{lj}, \\ \partial_{w_{ml}}(f_j) &= \frac{x_m}{\sigma_i^2} \delta_{lj},\end{aligned}\tag{10.16}$$

where  $\delta_{lj}$  is the Kronecker delta. Finally, we obtain the required equations

$$\begin{aligned}\frac{|\Psi_{rp}(x_{\text{new}})|^2}{|\Psi_{rp}(x_{\text{old}})|^2} &= \prod_{j=1}^H \frac{p_j(x_{\text{old}})^2}{p_j(x_{\text{new}})^2}, \\ \nabla_k \ln \Psi_{rp} &= \sum_{j=1}^H \frac{w_{kj}}{\sigma_i^2} n_j, \\ \nabla_k^2 \ln \Psi_{rp} &= \sum_{j=1}^H \frac{w_{kj}^2}{\sigma_i^4} p_j n_j, \\ \nabla_{b_l} \ln \Psi_{rp} &= n_l, \\ \nabla_{w_{ml}} \ln \Psi_{rp} &= \frac{x_m n_l}{\sigma_i^2}.\end{aligned}\tag{10.17}$$

This is the same result as obtained for the gradient of the log-likelihood function presented in chapter 5. In this element, there are plenty of optimization possibilities. For the RBM-Gaussian, we saw that the distribution width,  $\sigma_i$ , was set such that  $\omega = 1/\sigma_i^2$ , but for this product the value of  $\sigma_i$  has no impact on the output since it is always multiplied with the weights which are adjusted freely. By further revealing that some sums can be expressed as vector products, we can get a significant speed-up. Firstly, we will define a vector

$$v = b + w^T x,\tag{10.18}$$

which is the transformation for going from the hidden units to the visible units in Gaussian-binary restricted Boltzmann machine, what we above have called  $f(x; \theta)$ . Thereafter, we define the vectors  $n$  and  $p$  as described above. These vectors are declared as `m_v`, `m_n` and `m_p` respectively, and are initialized and updated using the function `updateVectors` in the following way

```
void RBMProduct::updateVectors()
{
    m_v = m_b + m_W.transpose() * m_positions;
    Eigen::VectorXd e = m_v.array().exp();
    m_p = (e + Eigen::VectorXd::Ones(m_numberOfHiddenNodes)).cwiseInverse();
    m_n = e.cwiseProduct(m_p);
}
```

One can see that all the operations are vectorized, which makes the operations affordable.

### 10.3 Partly restricted Boltzmann machine

For the partly restricted Boltzmann machine given in equation (6.27), we observe that the only difference from a standard Boltzmann machine is the factor

$$\Psi_{\text{pr}} = \exp \left( \sum_{i=1}^F \sum_{j=1}^F x_i c_{ij} x_j \right), \quad (10.19)$$

which we also can threat separately. To run a computation with the partly restricted Boltzmann machine, we thus need to add the elements RBMGaussian, RBMProduct and PartlyRestricted in a similar way as in the example 9.1. When differentiating, we end up with the expressions

$$\begin{aligned} \frac{|\Psi_{\text{pr}}(\mathbf{R}_{\text{new}})|^2}{|\Psi_{\text{pr}}(\mathbf{R}_{\text{old}})|^2} &= \exp \left( 2 \sum_{j=1}^F c_{ij} x_j (x_i^{\text{new}} - x_i^{\text{old}}) \right), \\ \nabla_k \ln \Psi_{\text{pr}} &= 2 \sum_{j=1}^F c_{kj} x_j, \\ \nabla_k^2 \ln \Psi_{\text{pr}} &= 2 c_{kk}, \\ \nabla_{c_{ml}} \ln \Psi_{\text{pr}} &= x_m x_l, \end{aligned} \quad (10.20)$$

where  $x_i$  is the changed coordinate. We can use vectorization to speed-up the computations again, most elegantly shown by the `computeParameterGradient`,

```
Eigen::VectorXd PartlyRestricted::computeParameterGradient()
{
    Eigen::MatrixXd out = m_positions * m_positions.transpose();
    m_gradients.head(out.size()) = WaveFunction::flatten(out);
    return m_gradients;
}
```

where we use that the parameter gradient  $\nabla_{c_{ml}} \ln \Psi_{\text{pr}}$  is given by the outer product between the coordinate vectors, as already hinted in equation (6.28).



**Part V**

**Results and Discussion**



## CHAPTER 11

# Selected Results

Results! Why, man, I have gotten a lot of results. I know several thousand things that won't work.

---

Thomas A. Edison,<sup>108</sup>

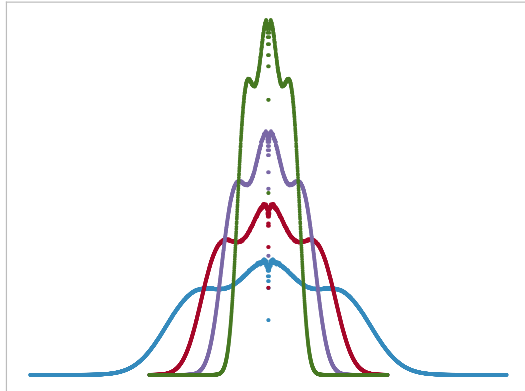


**Figure 11.1:** Radial one-body density profiles for two-dimensional quantum dots with  $N = 12$  electrons, popularly titled an artificial Magnesium atom. The four graphs correspond to four different oscillator frequencies, where the weakest oscillator gives the broadest density distribution.

We are finally ready to discuss the most exciting part of this thesis, namely the results. Since this work is associated with a degree in physics, the physical insights should be our focus and in this chapter we finally get the opportunity to discuss various physical interpretations of the results. Moreover, the various trial wave function ansätze used in variational Monte Carlo simulations (henceforth merely simulations) are discussed and compared. The Slater-Jastrow wave function is the *de facto* standard ansatz used in variational Monte Carlo calculations of electronic structure problems. This ansatz, thoroughly discussed in chapter 7, is used as reference for our machine learning ansätze. Additionally, it is used for simulations of atomic systems, and will hereafter be abbreviated as the VMC ansatz. The most basic machine learning ansatz consists of a Slater determinant where the single-particle functions are determined by the marginal distributions of the visible nodes of a Gaussian-binary restricted Boltzmann machine. This is abbreviated as the RBM ansatz. When adding a simple Jastrow factor to this ansatz, we obtain

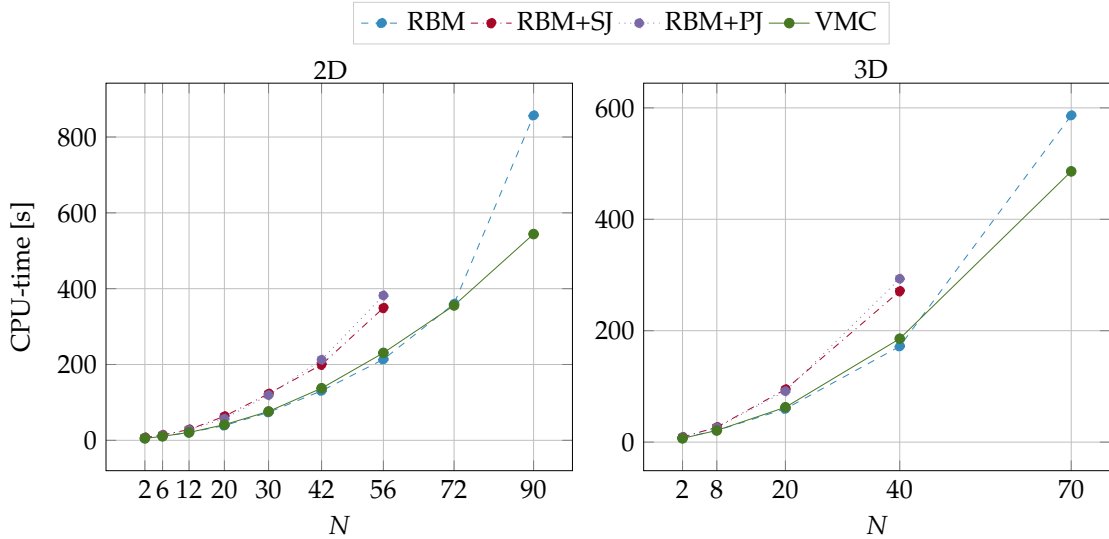


**Figure 11.2:** CPU-time per iteration as a function of the number of electrons,  $N$ , for two-dimensional (2D) and three-dimensional (3D) quantum dots. The number of Monte Carlo cycles per iteration is  $M = 2^{20} = 1,048,576$ . For more details see the text and appendix C.

the RBM+SJ ansatz. The RBM+PJ ansatz means that the Padé-Jastrow factor is added to the RBM ansatz. The respective Jastrow factors were discussed in section 7.1.2.

By using the implemented variational Monte Carlo framework described in chapter 9, we can examine a large number of different systems. For quantum dot systems, the number of electrons, number of dimensions and oscillator frequency can all be varied. In total, we have looked at more than 150 different quantum dot systems using the four wave function ansätze mentioned above, which means that we have generated a large set of results. A selection of these results will be presented and discussed in this chapter, while a more extensive collection of results is presented in appendix C. The results presented below have been selected since they describe physically interesting properties and allow for a comparison of the various ansätze. We will choose systems and configurations that can be compared with existing results. Our primary focus will be on ground state energy and electron density calculations, and we will stick to natural units as discussed in appendix A. A brief recapitulation is that for quantum dots, the energy is given in units of Planck's reduced constant,  $E' = E/\hbar$ , and length is scaled as  $x' = x/\sqrt{\hbar/m}$  with  $m$  as the mass of an electron. This implies that the  $d$ -dimensional density,  $\rho_d(\mathbf{r})$ , is given in units of  $(\hbar/m)^{-d/2}$ . For atoms, we use Hartree atomic units, meaning that the length is given in units of the Bohr radius,  $a_0$ , the  $d$ -dimensional density is given in units of  $a_0^{-d}$  and the energy is scaled as  $E' = E/(\hbar^2/m_e a_0)$ .

Before we move on to the physical results, we will take a quick look at some more technical results. More precisely, we will discuss the computational cost of the various ansätze and the energy convergence using various optimization tools. For validation purposes, we will present a few selected results on the case without repulsive interaction and compare it to analytical results. After that, we study the case with repulsive interaction on a much larger scale, where we first look at quantum dots and then on atoms.

## 11.1 Computational cost

Quantum many-body simulations are frequently ranked among the most computationally intensive fields. A reason for this is the large amount of information stored in the wave function.

**Table 11.1:** The scaling of the computational cost for two-dimensional (2D) and three-dimensional (3D) quantum dots as a function of the number of electrons,  $N$ . The numbers presented in the table are the optimal  $b$ -value found from fitting the power function  $f(N) = 0.5N^b$  to the cost graph. For abbreviations see the text.

	RBM	RBM+SJ	RBM+PJ	VMC
2D	1.498	1.639	1.621	1.515
3D	1.584	1.710	1.729	1.605

Albeit the VMC ansatz is known to have a high performance-to-cost ratio, it is still not cheap. In this section, we will find the average cost of the VMC ansatz and compare it to the cost of the machine learning ansätze described above. In figure (11.2), the CPU-time is plotted as a function of the number of electrons,  $N$ , for two-dimensional (left) and three-dimensional (right) quantum dots. To obtain accurate CPU-times, all the simulations were run on the Abel computer cluster with  $M = 2^{20} = 1,048,576$  Monte Carlo cycles per iteration. The time presented is the average time over at least four independent runs with thousands of iterations each. For more details, see appendix C, section C.1.

Our immediate observation is that the ansätze are pairwise quite similar, with the RBM and VMC as the cheapest ones, and the RBM+SJ and RBM+PJ as the most expensive. This is not surprising, as RBM requires a neural network, VMC requires a Jastrow factor while RBM+SJ and RBM+PJ require both a neural network and a Jastrow factor. For two-dimensional dots, RBM is the cheapest among all the ansätze, but for larger systems ( $N = 42, 56$ ), VMC is cheaper due to an explosion in CPU-time for the RBM ansatz. This explosion can be explained by our choice of the number of hidden nodes,  $H$ , which consequently is set to the number of electrons, i.e.  $H = N$ , which was found to give the lowest energy for small quantum dots<sup>26</sup>. Since the RBM ansatz has  $N \cdot d \cdot (1 + H) + H$  variational parameters with  $d$  as the number of dimensions, the number of variational parameters for a two-dimensional dot with  $N = 90$  electrons is 16,470. On the other hand, the VMC ansatz is equipped with two variational parameters for all system sizes, which obviously makes the parameter update less costly. We also observe that the RBM+PJ ansatz is cheaper than the RBM+SJ ansatz for systems up to  $N = 42$ , but after that, the RBM+SJ ansatz is slightly cheaper. This might be surprising, as the simple Jastrow factor contains  $N^2$  variational parameters, but a possible explanation is that BLAS is optimized for large matrix-vector operations and is thus fully utilized first when the matrices get large. We observe the same behavior for the three-dimensional dots as for the two-dimensional dots, and the discussion above is representative for them as well.

The standard way of estimating the scaling of variational Monte Carlo simulations is to fit the power functions,  $f(x) = ax^b$ , to the cost graphs. As all the simulations were performed with the same hyper-parameters and with equal external factors. We fix the first parameter by setting  $a = 0.5$ , as this was found to be a reasonable average value based on two-parameter fitting. In that manner, we can focus on optimizing  $b$  only, which is the parameter that specifies the scaling, i.e.; we say that the method scales as  $N^b$ . In table (11.1), the optimal  $b$  from linear regression is presented for our four ansätze for two- and three-dimensional quantum dots. We want to emphasize that we only did the regression for CPU-times up to  $N = 56$  in two-dimensional dots and  $N = 40$  in three-dimensional dots, partly because we only have data for all methods in this interval and partly because the CPU-time for the RBM explodes for large dots. We believe that this was the best way to do it in order to make the various methods comparable.

The numbers in the table match our impression from figure (11.2), where RBM and VMC

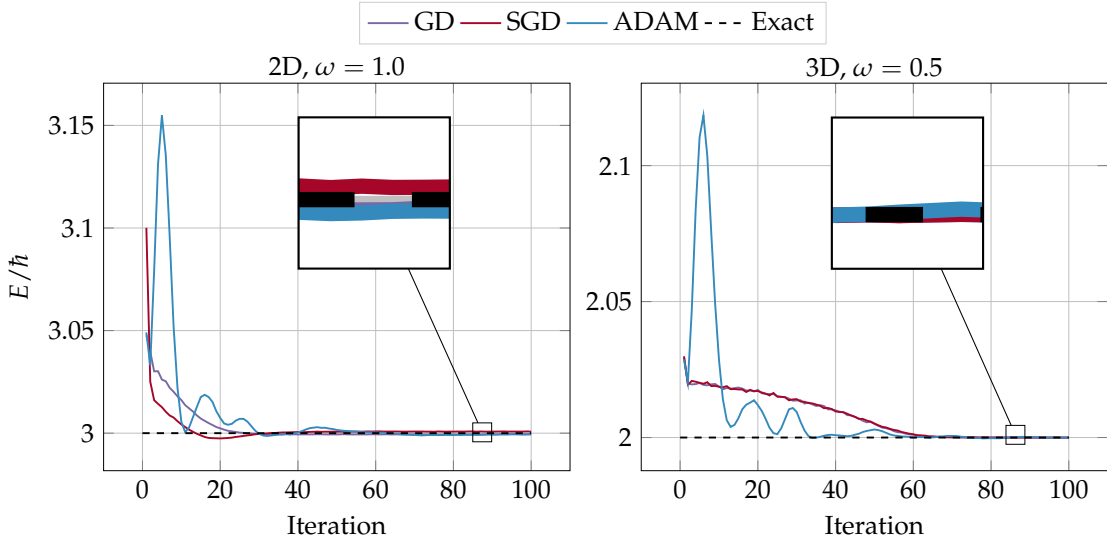


**Figure 11.3:** Convergence of the obtained ground state energy,  $E$ , for quantum dots with  $N = 2$  in two dimensions (2D) with frequency  $\omega = 1.0$  (left) and in three dimensions (3D) with frequency  $\omega = 0.5$  (right). The VMC ansatz was used, described in the text, and the optimization tools gradient descent (GD), stochastic gradient descent with 10 batches (SGD) and the ADAM optimizer are all compared. Semi-analytical energies (Exact) are taken from Taut<sup>50</sup> (2D) and Taut<sup>51</sup> (3D). The learning rate was set to  $\eta = 0.5$  and the number of Metropolis steps was  $M = 2^{24} = 16,777,216$ . All energies are given in units of  $\hbar$  (natural units).

were found to be more expensive than RBM+SJ and RBM+PJ. For all the ansätze, the scaling was found to be between linear and quadratic as a function of the number of electrons, which is surprising as the update of the Slater matrix scales as  $\sim N^2$ .

## 11.2 Energy convergence

We always want our simulations to converge fast and to be stable, which the optimization tool is responsible for. In figure (11.3), we compare standard gradient descent (GD) to stochastic gradient descent (SGD) and ADAM for two- and three-dimensional quantum dots with  $N = 2$  interacting electrons. The optimization algorithms were detailed in section 5.6. The gradient descent methods are plain, meaning it is without momentum and adaptive learning rate, while the ADAM optimizer has momentum and adaptivity by nature. The frequency  $\omega = 1.0$  is used for the two-dimensional case since the analytical energy,  $E = 3.0$ , is available<sup>50</sup>. Similarly, we use the frequency  $\omega = 0.5$  for the three-dimensional case since the exact energy is  $E = 2.0$ <sup>51</sup>.

The first thing we observe is that all three optimization tools manage to converge to a value close to the exact energy (see spy window). The stochastic and non-stochastic gradient descent methods behave similarly, but we observe that the SGD goes below the exact energy before it stabilizes. The ADAM optimizer, fluctuates much more, which can be explained by the momentum, as discussed in section 5.6.3. It is also important to remember that we use the VMC ansatz, which is equipped with two variational parameters only, and thus is easier to control. The ADAM optimizer is known to be good at minimizing functions with many variational parameters, so we will stick to it even though gradient descent seems like a clever choice seen from the figure. Another point is that the quantum dots have neat potentials without local minima. When we move on to more complex systems, ADAM generally works better according to the literature<sup>77</sup>.

Further, we compare the energy convergence of the various trial wave function ansätze in

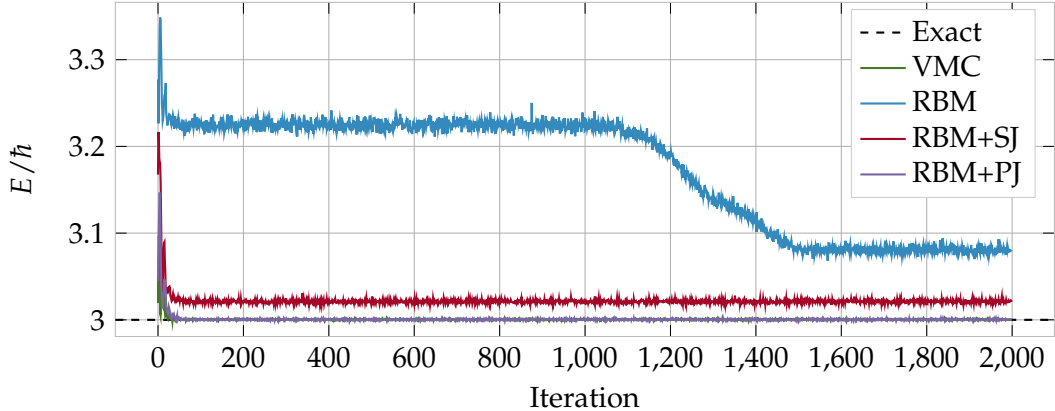


**Figure 11.4:** Convergence of the obtained ground state energy,  $E$ , for a two-dimensional quantum dot with  $N = 2$  and frequency  $\omega = 1.0$ . The energy is obtained using various trial wave function ansätze detailed in the text. The learning rate was set to  $\eta = 0.5$  and the number of Metropolis steps used for each iteration was  $M = 2^{20} = 1,048,576$ . We use the ADAM algorithm for optimization. The semi-analytical energy,  $E = 3.0$ , (Exact) is taken from Taut<sup>50</sup>, and all energies are given in units of  $\hbar$  (natural units).

figure (11.4). VMC and RBM+PJ apparently give the lowest energy, followed by the RBM+SJ and RBM. Also the scale of the fluctuations (noise) seems to be in the same order, agreeing with the zero-variance property<sup>88</sup>. While VMC, RBM+SJ and RBM+PJ all immediately converge and stabilize, the RBM ansatz first converges to a value before it after more than 1000 iterations converges further to a new value. This illustrates that it can be hard to decide whether or not the simulation has converged when using machine learning ansätze, and an intelligent convergence criterion is needed in order to reveal if the simulation can be stopped or not. In practice, we often turn off the convergence check and let the simulation run the maximum number of iterations. We also observe that RBM is harder to train than the other methods, which is a result of the absence of a Jastrow factor.

## 11.3 No repulsive interaction

We start with the non-interacting case in order to validate the implemented code. For this case, we can calculate the energy and the electron density analytically for both quantum dots and atoms. It therefore serves as an excellent benchmark and validation for our code. The physical significance is though limited as non-interacting systems do not appear in the real world.

### 11.3.1 Quantum dots

The quantum dot system is the system we will keep most of the attention on, and for that reason, we will also validate the implemented quantum dot code thoroughly. As we use the harmonic oscillator potential to describe the external potential in the quantum dots, the system has well-known analytical results for the energy and other observables. The quantum dots have analytical expressions for the ground state energy given by equation (4.4). The number of electrons in closed-shell are given by the magic numbers in equation (4.5). In table (11.2), we compare the energies obtained using the VMC and RBM ansätze to the analytical energy. The system we look at is a quantum dots with some selected numbers of electrons and the frequencies  $\omega = 0.5$  and  $\omega = 1.0$ . From the results, it is clear that both the VMC and RBM ansätze reproduce the analytical expression when all the parameters are set to 1 and 0, respectively. This is expected as

**Table 11.2:** The ground state energy of two-dimensional (2D) and three-dimensional (3D) quantum dots with  $N$  non-interacting electrons and frequencies  $\omega = 0.5, 1.0$ . Analytical values (Exact) are obtained by  $E_n = \omega(n + 1/2)$ , and all values are given in units of  $\hbar$  (natural units). The standard error is zero down to machine precision, and for abbreviations see the text.

	$\omega = 0.5$			$\omega = 1.0$			
	$N$	RBM	VMC	Exact	RBM	VMC	Exact
2D	2	1.0	1.0	1	2.0	2.0	2
	12	14.0	14.0	14	28.0	28.0	28
	30	55.0	55.0	55	110.0	110.0	110
3D	2	1.5	1.5	1.5	3.0	3.0	3
	20	30.0	30.0	30	60.0	60.0	60
	70	157.5	157.5	157.5	315.0	315.0	315

the exact wave functions are found when the parameters have these particular values. RBM+SJ and RBM+PJ were not included in the comparison as we expect them to give similar results to RBM and VMC.

Electron density is another observable that we will devote particular attention to in this chapter. Comparing the obtained density to the analytical density gives a good indication of whether the implementation is correct or not. In figure (11.5), the radial one-body density is plotted for two-dimensional (left) and three-dimensional (right) quantum dots with  $N = 2$  non-interacting electrons and frequency  $\omega = 1.0$ . The VMC and RBM ansätze are used, and the density is compared to the exact density profile found from the definition of the one-body density in equation 3.13. The results demonstrate that both ansätze are able to reproduce the exact density profile. This indicates that we have done the implementation correctly. However, the densities get noisy when they approach  $r = 0$ , most notably in three dimensions, which can be explained by the way we calculate the radial one-body density. In section 9.8, we saw that the innermost bins are also the smallest. This means that electrons are less likely to be observed there when the number of Monte Carlo cycles is finite. Apart from this noise, the density plot in two and three dimensions are identical, which can be explained mathematically by the fact that the electron density for non-interacting systems is trivially separable.

Furthermore, we examine the spatial one-body density and radial two-body density. For the same quantum dot system as above, the density profiles are compared to analytical results in figure (11.6). For the one-body density plots, we observe that both the RBM and VMC ansätze provide density profiles similar the exact profile. Also the two-body densities match the analytical density profile for both ansätze, but we observe a suspicious cross on the obtained two-body density profiles. This cross occurs since we in practice calculate the density for positive  $r_i$  and  $r_j$ . We then get the density profile presented in the first quadrant of the plots, and simply rotate the same density around origin ( $r_i = r_j = 0$ ) to get intuitive and illustrative plots. This also explains the negative values of  $r_i$  and  $r_j$ , which otherwise would not make sense.

As discussed in section 3.3, the electron density should be normalized such that the integral over the density function,  $\rho$ , corresponds to the number of electrons. However, there is no standard way of normalizing these densities when they are calculated using bins, as the normalization constant depends on the number of bins. This is not very important either; we are only interested in the relative densities and the shapes of the density plots. We have been consequent when normalizing the density plots, such that the various density magnitudes can be compared

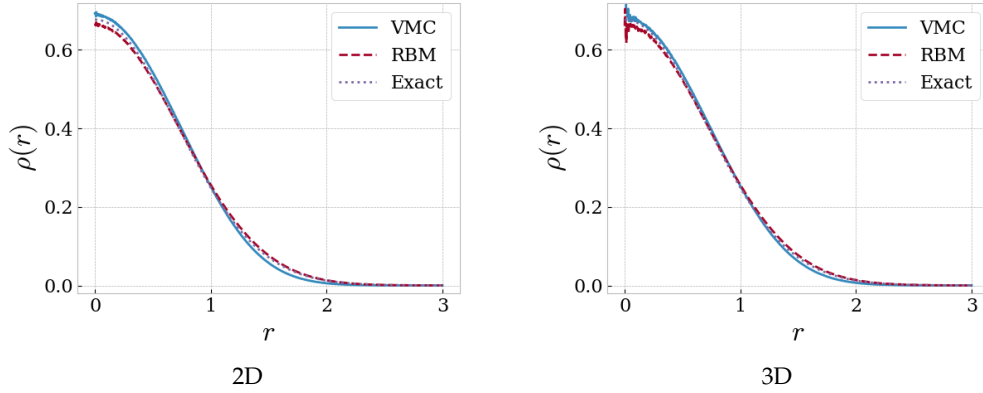


**Figure 11.5:** Plots of the radial one-body density profile for quantum dots with  $N = 2$  non-interacting electrons and frequency  $\omega = 1.0$ . Both two-dimensional (2D) and three-dimensional (3D) dots are simulated using the VMC and RBM ansätze, and they are compared to the analytical case  $\rho(r) \propto \exp(-r^2)$  (Exact). For abbreviations and description of the natural units used, see the text.

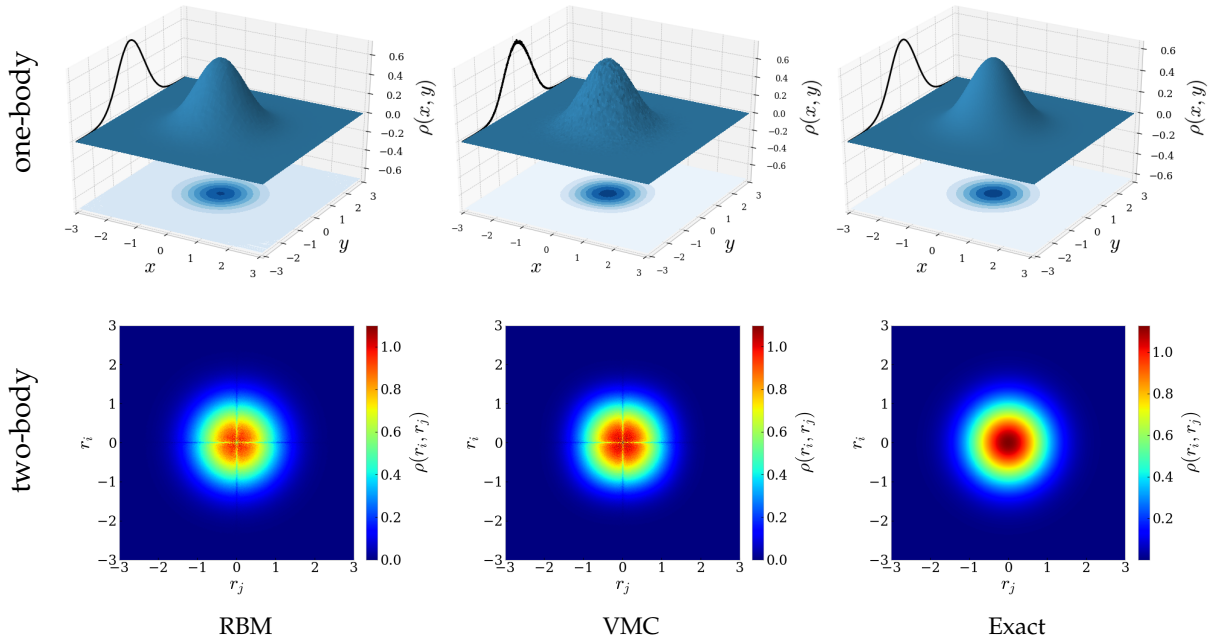


**Figure 11.6:** Plots of the electron density profile,  $\rho$ , of a two-dimensional quantum dot with  $N = 2$  non-interacting electrons and frequency  $\omega = 1.0$ . The upper plots are the (spatial) one-body density distribution (one-body), where the surface plot and the contour plot on the  $xy$ -plane illustrate the density, and the graph on the  $yz$ -plane represents the cross-section through  $x = 0$ . The lower plots are the radial two-body density distributions (two-body). Besides, we compare the results to the analytical densities (Exact), given by  $\rho(x, y) \propto \exp(-x^2 - y^2)$  and  $\rho(r_i, r_j) \propto \exp(-r_i^2 - r_j^2)$ , respectively. For abbreviations and description of the natural units used, see the text.

**Table 11.3:** Ground state energy of neutral atoms with atomic number  $Z$  and non-interacting electrons. A single Slater determinant with hydrogen-like orbitals was used as the trial wave function ansatz. The analytical energy (Exact) is obtained by the Bohr formula,  $E_n = Z^2/2n^2$ . The variance is zero to machine-precision for all listed results. For abbreviations and description of the Hartree atomic units used, see the text.

Atom	Z	VMC	Exact
H	1	-0.5	-0.5
He	2	-4.0	-4
Be	4	-20.0	-20
Ne	10	-200.0	-200

to each other.

### 11.3.2 Atoms

To further verify the implementation, we address atomic systems with non-interacting electrons. For these systems, the variational Monte Carlo simulations are based on a trial wave function ansatz consisting of a single Slater determinant with the hydrogen-like orbitals as the single-particle functions. In table (11.3), the ground state energy of some selected atoms are listed with the exact energies, given by the Bohr formula presented in equation (4.9). Besides, we add calculations of the hydrogen ground state energy as another simple validation of the code. It is apparent that the obtained energies are in line with the exact energies, indicating that the code simulates atomic systems correctly.

For completeness, we present the radial one-body density of the helium atom in figure (11.7). The density is multiplied by  $r^2$  as this allows us to clarify the peaks in the one-body density. We see that the produced density curve is more or less identical to the exact density curve, found from the definition in section 3.13.

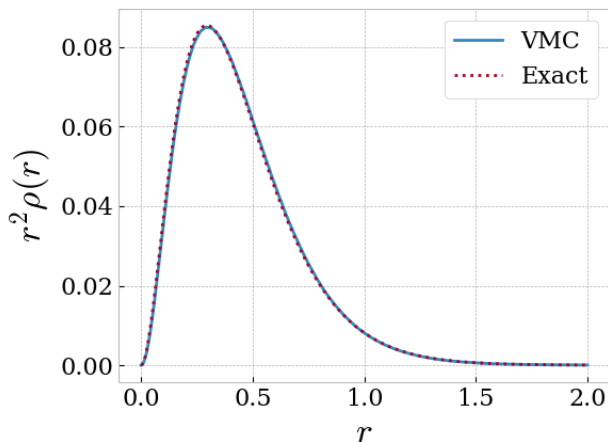


**Figure 11.7:** Plot of the radial one-body density profile for the non-interacting helium atom. A single Slater determinant with hydrogen-like orbitals was used as the trial wave function ansatz. The analytical density (Exact) was obtained by the formula  $\rho(r) \propto \exp(-2r)$ , and the densities were multiplied with the radius squared. For abbreviations and description of the Hartree atomic units used, see the text.

## 11.4 Quantum dots

We now move on to the more interesting case with repulsive interaction between the electrons. Analytical results are in general unavailable for this case, apart from a few semi-analytical energies and wave functions for the two- and three-dimensional quantum dots. We will for this system calculate the ground state energy, the one-body density, and the two-body density.

The simulations depend on an array of hyper-parameters, which need to be reasonable in order to achieve acceptable results. Firstly, the simulations are very sensitive to the learning rate. On one hand, it has to be large enough for the simulation to converge in an adequate number of steps. On the other hand, it needs to be small to avoid the gradients to explode as discussed in chapter 5. Appropriate learning rates were found to be in the range  $\eta \in \{10^{-5}, 10^0\}$ , where large systems and/or systems with low frequency required the lowest learning rates. Also, the step length needs to be set cleverly, as we want to sample over the space where the electrons physically can be located in a reasonable number of cycles. For a narrow oscillator potential (high frequency), the step length is typically smaller than for a wide oscillator (low frequency). The acceptance ratio is directly dependent on the step length, where we want a high acceptance ratio to keep the computational cost low. However, we experienced that a too high acceptance ratio is neither favorable, as it makes the simulation diverge. Keeping an acceptance ratio at around 0.995 was found to be optimal, with a step length in the range  $\Delta x \in \{10^{-2}, 10^0\}$ . The initial electron and parameter configurations are crucial in order to make the simulations converge rapidly. Furthermore, the statistical error depends on the number of Monte Carlo cycles, where a large number of cycles is preferred as discussed in section 7.1.

We have applied an adaptive number of cycles, which means that the number of Monte Carlo cycles per iteration is increased for the last iterations. Firstly, this makes the final energy more accurate due to more statistics. Secondly, we obtain less noisy convergence and density plots with this technique. All results below are produced using  $M = 2^{20} = 1,048,576$  number of cycles per iteration until the energy has converged. Then, we run 10 more iterations with the number of cycles increased to  $M = 2^{24} = 16,777,216$  and for the very last iteration we run  $M = 2^{28} = 268,435,456$  or  $M = 2^{30} = 1,073,741,824$  cycles.

Initially, we look at two-dimensional quantum dots with up to  $N = 56$  electrons and three-dimensional quantum dots with up to  $N = 40$  electrons. The frequencies span from  $\omega = 0.1$  to  $\omega = 1.0$ . For these systems, we will compute the ground state energy, the one-body density, and the two-body density. After that, we move on to some special cases where the dots have low frequency ( $\omega = 0.01$ ) and large dots ( $N > 56$ ) to test how far we can go. We also have a thorough discussion of how the energy is distributed between kinetic and potential energy, and compare the kinetic-potential energy ratio to the virial theorem.

### 11.4.1 Ground state energy

The ground state energy is a natural starting point as the simulations are based on energy minimization. Moreover, the energy can easily be compared to benchmarks. By exploiting the symmetry of quantum dots with  $n = 2$  electrons, Taut was able to obtain semi-analytical energies for quantum dots of certain frequencies  $\omega$ . For two-dimensional dots, he found the energy to be  $E = 3$  for the frequency  $\omega = 1$  and  $E = 2/3$  with  $\omega = 1/6$  as the frequency<sup>50</sup>. Additionally, his studies of three-dimensional dots revealed the energy  $E = 2$  for the frequency  $\omega = 1/2$  and  $E = 1/2$  with  $\omega = 1/10$  as the frequency<sup>51</sup>. For other references we need to rely on earlier research, usually other simulations. Since diffusion Monte Carlo (DMC) simulations are known to give very accurate results, we will mainly compare our results to the DMC computations by Høgberget<sup>27</sup>. These results exist for quantum dots with up to  $N = 56$  electrons in two dimensions and with up to  $N = 20$  electrons in three dimensions. Another important reference is the

**Table 11.4:** The ground state energy of two-dimensional quantum dots with  $N$  electrons and frequency  $\omega$ . The HF results are taken from Mariadason<sup>86</sup>, the DMC results are taken from Høgberget<sup>27</sup> and semi-analytical results (Exact) are taken from Taut<sup>51</sup>. The energy is given in units of  $\hbar$  (natural units), and the numbers in parenthesis are the statistical uncertainties in the last digit. Empty cells in the table imply that the result is not available. For abbreviations see the text. \* For  $N = 2$  and  $\omega = 1/6$ , the HF result was generated using the code developed by Mariadason<sup>109</sup>.

$N$	$\omega$	RBM	RBM+SJ	RBM+PJ	HF (Ref.[86])	VMC	DMC (Ref.[27])	Exact (Ref.[51])
2	0.1	0.4728(1)	0.44856(1)	0.440975(8)	0.525635	0.44129(1)	0.44079(1)	2/3
	1/6	0.7036(1)	0.67684(7)	0.66715(6)	0.768675*	0.66710(1)		
	0.28	1.07050(4)	1.03470(7)	1.021668(7)	1.14171	1.02192(1)	1.02164(1)	
	0.5	1.72293(7)	1.67739(9)	1.659637(6)	1.79974	1.65974(1)	1.65977(1)	
	1.0	3.0803(2)	3.02108(5)	2.999587(5)	3.16190	2.99936(1)	3.00000(1)	3.0
6	0.1	3.697(1)	3.63825(9)	3.5700(2)	3.85238	3.5695(1)	3.55385(5)	2/3
	0.28	7.9273(9)	7.7313(2)	7.6203(2)	8.01957	7.6219(1)	7.60019(6)	
	0.5	12.241(1)	11.9659(5)	11.8074(2)	12.2713	11.8104(2)	11.78484(6)	
	1.0	20.716(1)	20.3393(8)	20.1832(2)	20.7192	20.1918(2)	20.15932(8)	
12	0.1	12.679(1)	12.5964(7)	12.3416(4)	12.9247	12.29962(9)	12.26984(8)	2/3
	0.28	26.389(2)	26.051(1)	25.7331(5)	26.5500	25.7049(4)	25.63577(9)	
	0.5	40.440(3)	39.6340(7)	39.2743(6)	40.2161	39.2421(5)	39.1596(1)	
	1.0	67.632(3)	66.1898(8)	65.7911(7)	66.9113	65.7026(4)	65.7001(1)	

20	0.1	30.824(2)	30.567(3)	30.1553(9)	31.1902	30.0403(2)	29.9779(1)
	0.28	63.788(4)	62.786(3)	62.148(1)	63.5390	62.0755(7)	61.9268(1)
	0.5	96.410(1)	94.920(4)	94.104(1)	95.7328	94.0433(9)	93.8752(1)
	1.0	159.428(3)	156.816(4)	156.104(1)	158.004	155.8900(4)	155.8822(1)
30	0.1	61.829(5)	61.198(2)	60.774(2)		60.585(1)	60.4205(2)
	0.28	126.958(6)	125.413(2)	124.437(2)		124.195(2)	123.9683(2)
	0.5	191.495(7)	188.995(5)	187.488(2)		187.325(3)	187.0426(2)
	1.0	315.364(8)	309.997(6)	308.989(2)		308.576(1)	308.5627(2)
42	0.1	109.892(6)	109.48(2)	108.183(1)		107.928(2)	107.6389(2)
	0.28	224.462(8)	224.184(9)	222.200(5)		220.224(2)	219.8426(2)
	0.5	337.523(8)	333.582(9)	331.410(3)		331.276(3)	330.6306(2)
	1.0	553.40(1)	545.817(9)	543.746(3)		542.977(2)	542.9428(8)
56	0.1	179.789(6)	179.59(1)	178.501(5)		176.774(3)	175.9553(7)
	0.28	364.85(1)	364.165(9)	359.83(2)		359.63(1)	358.145(2)
	0.5	547.46(1)	545.74(1)	538.810(7)		538.686(9)	537.353(2)
	1.0	894.12(2)	882.93(1)	881.010(5)		879.514(3)	879.3986(6)

**Table 11.5:** The ground state energy of three-dimensional quantum dots with  $N$  electrons and frequency  $\omega$ . The HF results are taken from Mariadason<sup>86</sup>, the DMC results are taken from Høgberget<sup>27</sup> and semi-analytical results (Exact) are taken from Taut<sup>50</sup>. The energy is given in units of  $\hbar$  (natural units), and the numbers in parenthesis are the statistical uncertainties in the last digit. Empty cells in the table imply that the result is not available. For abbreviations see the text.

$N$	$\omega$	RBM	RBM+SJ	RBM+PJ	HF (Ref.[86])	VMC	DMC (Ref.[27])	Exact (Ref.[50])
2	0.1	0.5177(1)	0.50214(3)	0.500080(6)	0.529065	0.500083(7)	0.499997(3)	0.5
	0.28	1.2261(1)	1.20475(4)	1.201710(6)	1.23722	1.201752(6)	1.201725(2)	
	0.5	2.0269(1)	2.00371(4)	1.999912(5)	2.03851	1.999977(5)	2.000000(2)	2.0
	1.0	3.7574(1)	3.73543(4)	3.729827(5)	3.77157	3.730030(5)	3.730123(3)	
8	0.1	5.8910(6)	5.7498(4)	5.718(4)	5.86255	5.7126(1)	5.7028(1)	
	0.28	12.650(1)	12.2492(4)	12.2056(2)	12.3987	12.2050(2)	12.1927(1)	
	0.5	19.487(2)	19.0241(4)	18.9747(2)	19.1916	18.9759(1)	18.9611(1)	
	1.0	33.302(1)	32.7159(6)	32.6820(2)	32.9246	32.6863(2)	32.6680(1)	
20	0.1	27.813(2)	27.470(1)	27.3382(8)		27.3144(5)	27.2717(2)	
	0.28	57.700(4)	56.600(1)	56.4477(6)		56.4297(5)	56.3868(2)	
	0.5	87.840(4)	85.893(1)	85.7153(6)		85.7161(5)	85.6555(2)	
	1.0	146.292(4)	143.209(2)	142.9409(6)		142.9560(7)	142.8875(2)	
40	0.1	89.45(8)	89.618(4)	88.596(4)		88.182(1)		
	0.28	182.714(6)	181.877(4)	179.630(1)		179.567(1)		
	0.5	275.262(7)	271.030(4)	269.782(2)		269.746(1)		
	1.0	452.732(8)	442.874(4)	442.630(1)		442.602(2)		

Hartree-Fock (HF) limit, as the HF method approximates the electron-electron correlations by a mean-field. This is a particular interesting reference for simulations with the RBM ansatz, as both the methods approximate the many-body wave function with a single Slater determinant only. Practically, RBM should give a lower energy than the HF limit as the latter is known to be computationally cheap. We use the HF computations from Mariadason<sup>86</sup> for two-dimensional quantum dots with up to  $N = 20$  electrons and three-dimensional quantum dots with up to  $N = 8$  electrons. For the two-dimensional quantum dot with  $N = 2$  and frequency  $\omega = 1/6$ , we obtained the HF energy using the code developed by Mariadason<sup>109</sup>.

Ground state energy computations of two- and three dimensional quantum dots are found in tables (11.4) and (11.5), respectively. They are computed using the RBM, RBM+SJ, RBM+PJ and VMC ansätze, and the HF limit and DMC are present for reference purposes. The analytical values are found in the last column. We observe that the ansatz that requires least physical intuition is used, RBM, is the one that gives the highest energies among the ansätze. This is expected as no Jastrow factor is added to account for the correlations.

For small quantum dots ( $N < 8$ ), the RBM ansatz provides a lower energy than the HF limit, and for low frequencies ( $\omega < 0.5$ ) the obtained energy is generally also lower. This indicates that simulations with the RBM ansatz is better at modeling the correlations compared to the HF method. Nevertheless, for higher frequencies and larger dots, the HF limit is lower than the energy obtained using the RBM ansatz. When we add more intuition to the trial wave function ansatz in the form of a simple Jastrow factor (RBM+SJ), the energy drops significantly, especially for high frequencies. It is, therefore, lower than the HF limit for all simulations, and surprisingly close to the reference considering the simple form of the Jastrow factor. The statistical errors of RBM+SJ is in general smaller than for RBM, which is a good indication that the method provides a better ground state estimate as the actual ground state obeys a zero-variance property<sup>88</sup>.

Furthermore, we add a more complex Jastrow factor in the form of a Padé-Jastrow factor to the RBM ansatz, and we observe that the energy drops further. The RBM+PJ ansatz provides energies entirely on par with VMC, in many cases even lower. Notably, RBM+PJ provides the lowest energies among our implemented methods for dots with  $N = 2$  electrons, and the statistical errors are also the lowest. This hints that RBM+PJ can obtain a better ground state estimate than VMC for the smallest dots. However, for large dots, RBM+PJ provides slightly higher energies than VMC. We speculate that this might be due to the large number of variational parameters residing in the trial wave function, resulting in a too complex model for the problem. If we recall that the number of hidden units is set to the number of electrons, the number of variational parameters increases rapidly as the number of electrons increases.

A further novel finding is that all the methods and ansätze provide energies closer to the reference energy in three dimensions compared to two dimensions. For three-dimensional dots, we have a phase space of higher dimensionality than for two-dimensional dots, allowing a larger set of particle configurations. Obtaining an adequate estimate of the ground state energy is therefore more accessible in three dimensions compared to two dimensions.

### 11.4.2 One-body density

Another quantity of particular interest is the one-body density. For all the systems presented in tables (11.4) and (11.5) we have also calculated the one-body density. However, since this results in a large number of plots, the total collection is moved to appendix C. Instead, we present the (arguably) most interesting plots of the one-body density here.

We have computed the one-body density in two different ways: The radial one-body density profile is obtained by dividing the space into plural annuluses, as discussed in section 9.8. The spatial one-body density profile is obtained by dividing the space into a grid of equally sized bins and counting the number of times an electrons occurs in each bin. The radial density is

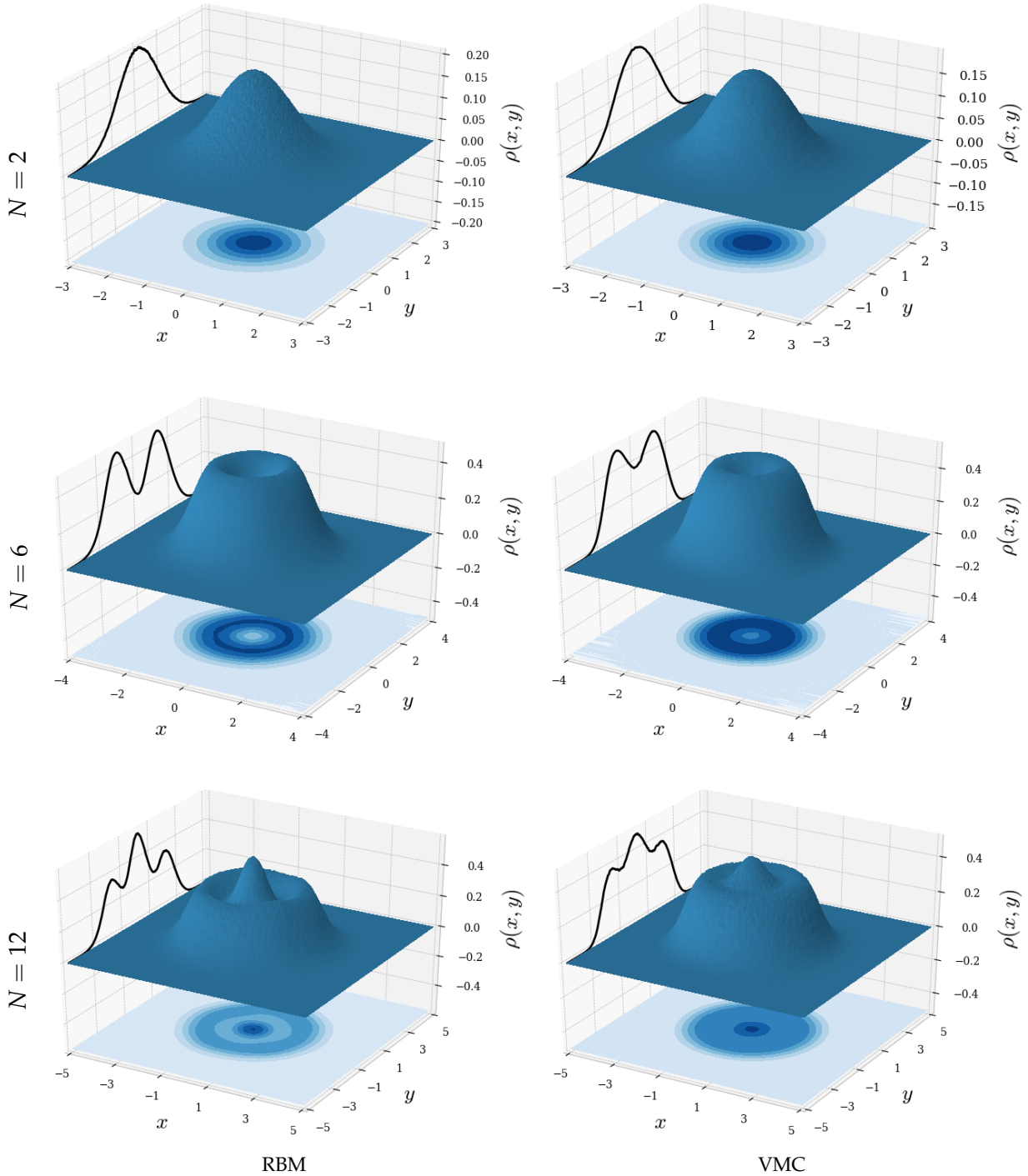


**Figure 11.8:** Plots of the one-body density profiles,  $\rho(x, y)$ , for two-dimensional quantum dots with frequency  $\omega = 1.0$  and  $N = 2, 6$  and 12 electrons seen from the top. The surface plot and the contour plot on the  $xy$ -plane illustrate the density, and the graph on the  $yz$ -plane represents the cross-section through  $x = 0$ . They were obtained using RBM (left column) and VMC (right column), with the ADAM optimizer and  $M = 2^{30} = 1,073,741,824$  Monte Carlo cycles after convergence. The plots are noise-reduced using a Savitzky-Golay filter. For abbreviations and description of the natural units used, see the text.

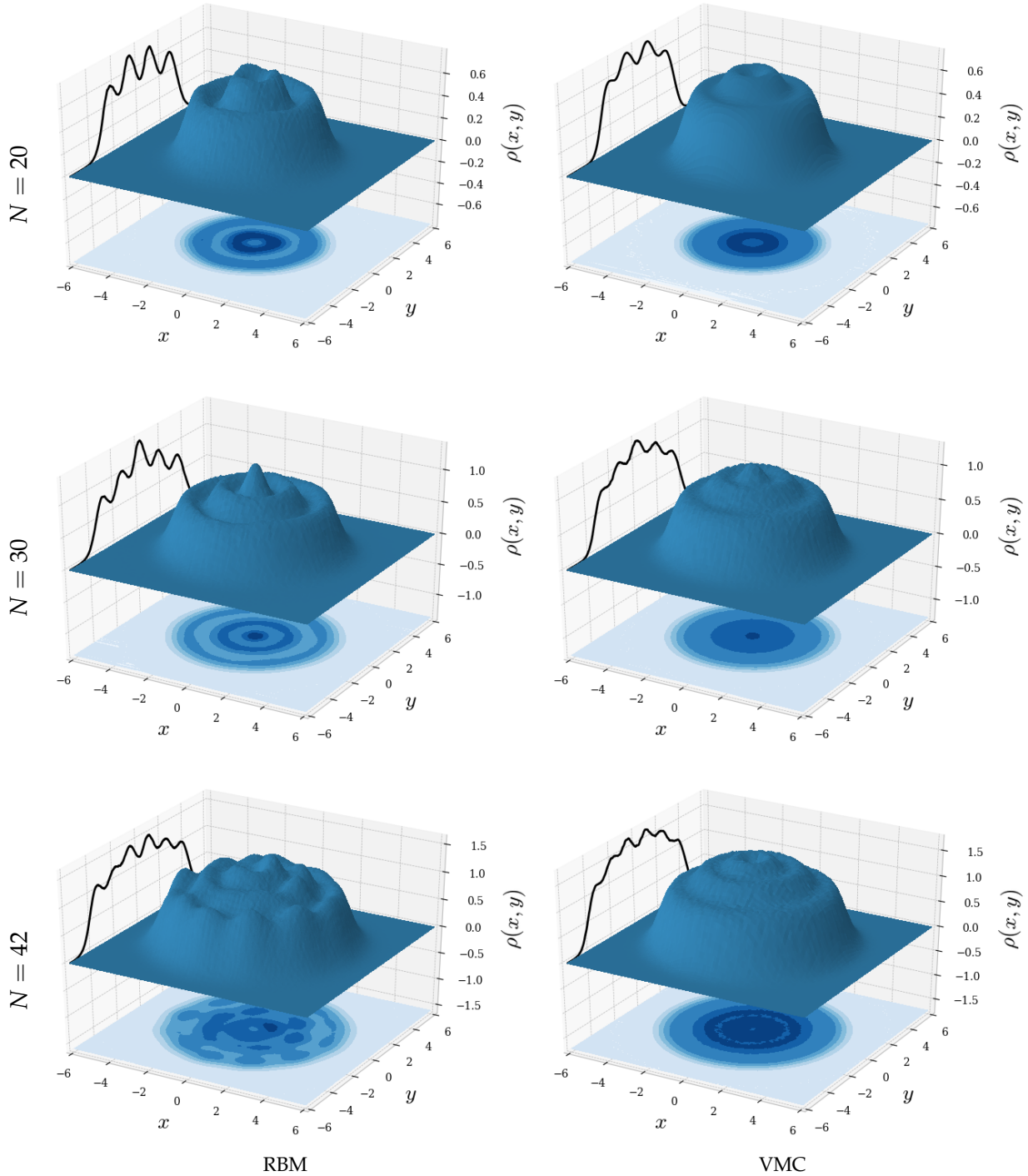


**Figure 11.9:** Plots of the one-body density profiles,  $\rho(x, y)$ , for two-dimensional quantum dots with frequency  $\omega = 1.0$  and  $N = 20, 30$  and  $42$  electrons seen from the top. The surface plot and the contour plot on the  $xy$ -plane illustrate the density, and the graph on the  $yz$ -plane represents the cross-section through  $x = 0$ . They were obtained using RBM (left column) and VMC (right column), with the ADAM optimizer and  $M = 2^{30} = 1,073,741,824$  Monte Carlo cycles after convergence. The plots are noise-reduced using a Savitzky-Golay filter. For abbreviations and description of the natural units used, see the text.

computationally beneficial as the density typically is stored in  $n$  bins compared to  $n^2$  bins for the second method, while the spatial density profile can clearly store more information. The spatial profile thereby gives more informative plots, but a radial profile is more convenient when we want to compare multiple ansätze. In other words, there are advantages and disadvantages associated with both methods, and we will, therefore, present both to give an as comprehensive description of the results as possible.

Initially, we will present the spatial density profiles of two-dimensional quantum dots with frequency  $\omega = 1.0$ . In figure (11.8) and (11.9), the evolution of the one-body density for dots of sizes  $N = 2, 6, 12, 20, 30$  and  $42$  are presented, produced using the RBM and VMC trial wave function ansätze. To maximize the amount of information in the plots, we have included a graph presenting the cross-section through  $x = 0$  on the  $yz$ -plane and a contour plot of the density on the  $xy$ -plane, in addition to a 3D surface plot of the density. We observe that the density profile is smooth, with more peaks as the number of electrons increases, representing high densities. For an odd number of shells ( $N = 2, 12$  and  $30$ ) the density has its maximum at the center of the dot, resulting in equal shapes where for example the shape of  $N = 12$  is seen as the top of  $N = 30$ . On the other hand, for an even number of shells ( $N = 6, 20$  and  $42$ ) the highest density is found at a ridge that encircles the center. Also here the shape of for example  $N = 20$  is seen as the top of  $N = 42$ . It is apparent that these are the configurations that minimize the energy, with a structure following directly from the Pauli principle, as the electrons are forced to distribute over multiple shells. We have seen that even when we remove the electron-electron interaction, we get the same characteristic wave shape, though narrower. The RBM ansatz provides sharper and more distinct peaks than the VMC ansatz, but the extrema seem to be located at the same radii. These differences may be caused by the way the ansätze model the correlations, where VMC employs the Padé-Jastrow factor and RBM needs to find the best way to account for the correlations itself.

To connect the observations to something everyone is familiar with, we can draw parallels between the density plots and water ripples. Högberget<sup>27</sup> discusses this in his work, and his plots of the one-body density are consistent with what we have obtained. However, for  $N = 42$  the RBM ansatz provides a density profile that has ripples in both radial and angular direction, indicating that the simulation has not fully converged to the minimum. This may be an effect of the large number of variational parameters in the trial wave function. Plots of the one-body density profile for the same systems using RBM+SJ and RBM+PJ were generated, but in order to limit us to a few plots we decided move the others in appendix C.

In figure (11.10), we stick to the frequency  $\omega = 1.0$  for small two- and three-dimensional quantum dots and compare the results obtained by the VMC, RBM, RBM+SJ, and RBM+PJ ansätze. We investigate dots with  $N = 2, 6$  and  $12$  in two dimensions and  $N = 2, 8$  and  $20$  in three dimensions. This corresponds to one shell ( $S = 1$ ), two shells ( $S = 2$ ) and three shells ( $S = 3$ ), respectively. For all the numbers of shells, we immediately see that the density plots are similar for two- and three-dimensional dots. The same phenomenon was observed for quantum dots with non-interacting electrons in figure (11.5), where we argued that the wave function is trivially separable. However, this is not the situation when we look at the interacting case, and it was therefore not obvious to us that the same phenomenon would occur here. Physically, this means that the electrons configure in the same way in three dimensions as in two dimensions, where the average distance from a shell to the center of the dot is dimensionless. Besides the physics, we are also interested in analyzing the performance of the various ansätze. We observe that they all give similar radial density profiles, but the RBM ansatz stands out. Apparently, RBM tends to exaggerate the peaks discussed above and gives a more wavy density plot,

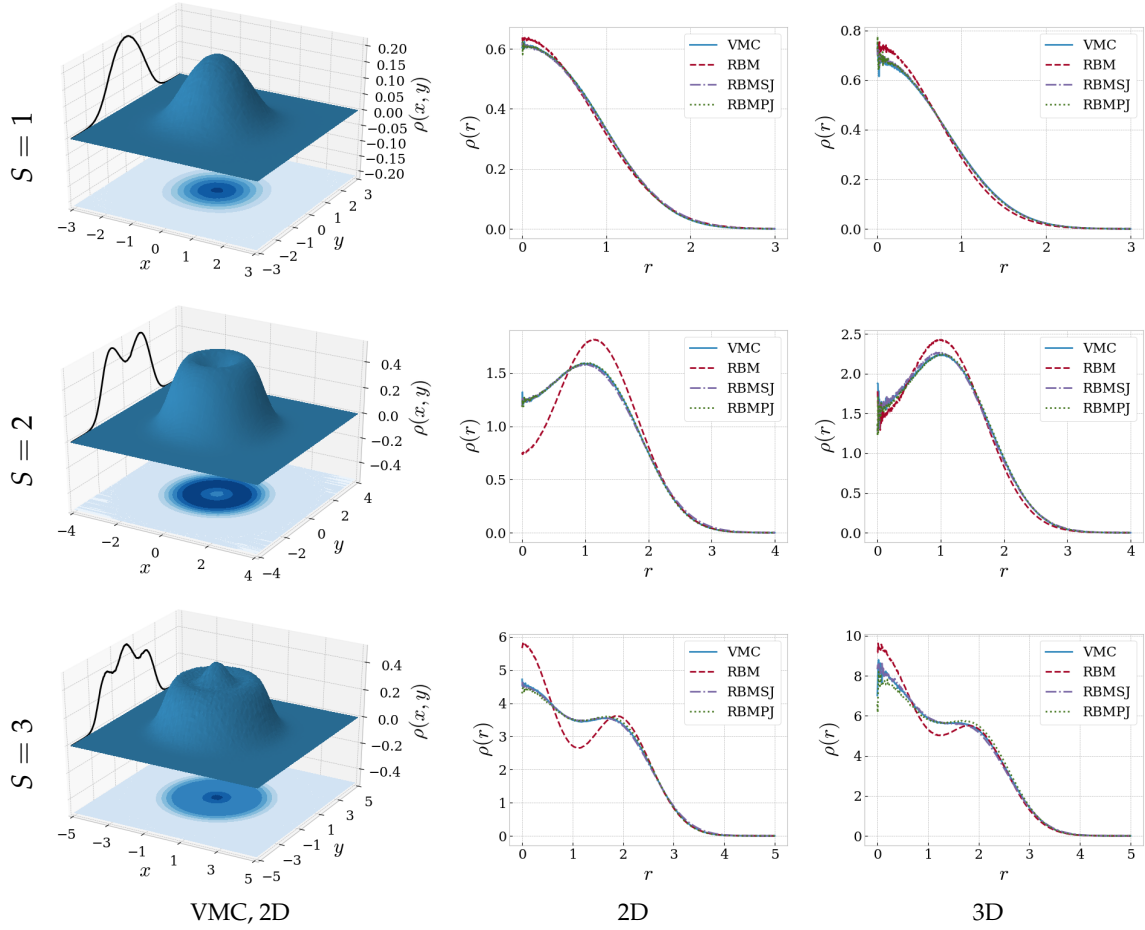


**Figure 11.10:** Plots of the one-body density profile,  $\rho$ , for small quantum dots with frequency  $\omega = 1.0$ . We look at the three lowest shells  $S = 1, 2$  and  $3$  seen from the top, corresponding to  $N = 2, 6$ , and  $12$  electrons in two dimensions (2D) and  $N = 2, 8$  and  $20$  electrons in three dimensions (3D). In the first column, the surface plot and the contour plot on the  $xy$ -plane illustrate the density and the graph on the  $yz$ -plane represents the cross-section through  $x = 0$ . In the middle column, the corresponding radial density profiles are obtained using RBM, RBM+SJ, RBM+PJ and VMC. In the last column, the radial density profiles for the three-dimensional dots are given using the same methods. ADAM optimizer was used, and after convergence, the number of Monte Carlo cycles was  $M = 2^{30} = 1,073,741,824$ . The surface plots are noise-reduced using a Savitzky-Golay filter. For abbreviations and description of the natural units used, see the text.

as also observed in figures (11.8) and (11.9). Further, RBM+SJ provides results similar to VMC and RBM+PJ. This is consistent with the energy analysis in section 11.4.1, where we found VMC and RBM+PJ to be the most accurate ansätze, followed by RBM+SJ and RBM in that order. We also observe some noise close to  $r = 0$ , which is caused by the fact that the number of Monte Carlo cycles is finite and we in practice have bins of different sizes.

We now move on to larger two-dimensional dots and frequencies lower than  $\omega = 1.0$  to see if the observed behavior is conserved also when the correlations get stronger. In figure (11.11), we plot the radial density profile for two-dimensional quantum dots with  $N = 20$  and  $42$ , and frequencies  $\omega = 0.1, 0.5$  and  $1.0$ . The results demonstrate that the peaks discussed above are conserved for lower frequencies, and their shapes change slightly as the frequency drops. Also, the density distribution is spatially expanded as the frequency drops, since the

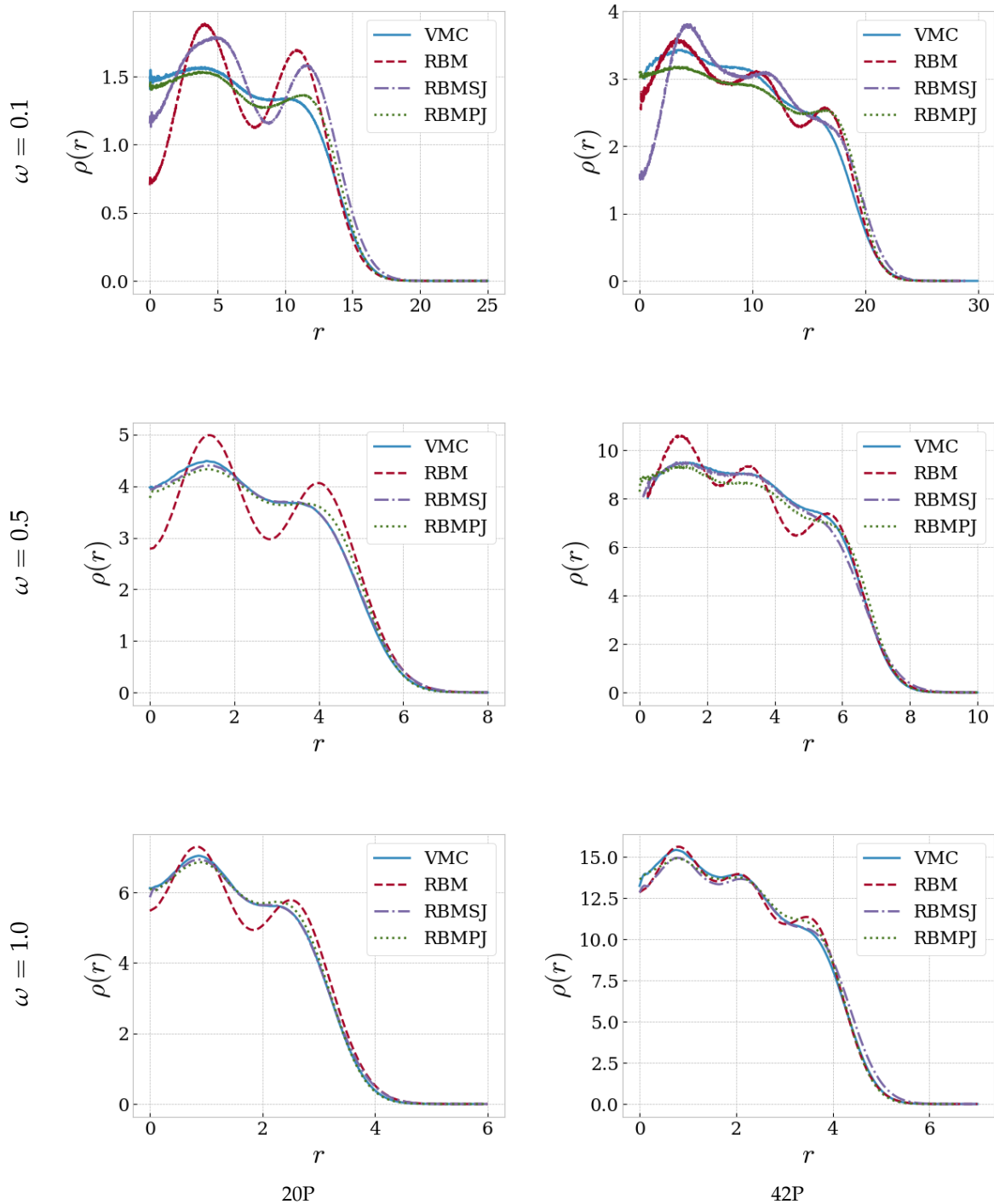


**Figure 11.11:** Plots of the one-body density profiles,  $\rho(r)$ , for two-dimensional quantum dots with  $N = 20$  (left column) and  $N = 42$  (right column) and oscillator frequencies  $\omega = 0.1, 0.5$  and  $1.0$  seen from the top. The ADAM optimizer was used, and after convergence the number of Monte Carlo cycles was  $M = 2^{28} = 268,435,456$ . For abbreviations and description of the natural units used, see the text.

force pushing the electrons towards the center of the dot gets weaker. For high frequencies, the VMC, RBM+PJ, and RBM+SJ ansätze appear to give similar density plots. When lowering the frequency, the difference gets gradually more visible. In particular, the peaks for frequency  $\omega = 0.1$  do no longer match for the various ansätze. Especially, RBM and RBM+SJ differ from VMC and RBM+PJ, indicating that the final results are heavily dependent on the way the ansatz account for the correlations. RBM+SJ tends to slightly exaggerate the peaks in the density plots, and RBM takes the exaggeration to the next level. This trend was also observed in the plots in figures (11.8, 11.9, 11.10), and technically speaking, this means that the RBM ansatz determines the most likely places to find the electrons, but fails to determine the actual density there. We have also seen that the one-body density is shape-invariant for the frequencies  $\omega = 0.5$  and  $1.0$  except for their radial extent. For that reason, it is not very exciting to further study these high frequencies, and in section 11.4.5 we move on to low-frequency dots. Before that, we will look at the two-body density.

### 11.4.3 Two-body density

Electron density has been discussed on several occasions in this thesis, and also the two-body density has been mentioned. The two-body density gives the probability of finding an electron at a certain position, given the position of another electron. Unlike the one-body density, this density gives, for example, information about how the electrons distribute pairwise, and how they correlate. This may lead to a better understanding of electron-electron correlations. Similar to the one-body density, we can plot both the radial two-body density profile and the spatial two-body density distribution. However, since the latter results in a higher-dimensional object, we stick to the radial density profile in this work. The radial density is obtained as a function of the distance from particles  $i$  and  $j$  to the center of the dots,  $r_i$  and  $r_j$  respectively. The plots are created in the same way as for the non-interacting case discussed in section 11.3.1. By means of this we rotate the density profile around origin ( $r_i = r_j = 0$ ) to make the plots more informative. Unlike the results presented above, we do not have any reference for our plots of the two-body density. We will focus on the two-dimensional systems, as the three-dimensional systems have similar two-body density profiles. This was also seen for the one-body density.

In figure (11.12), we plot the two-body density for a two-dimensional quantum dot with  $N = 2$  and frequencies  $\omega = 0.1, 0.5$  and  $1.0$ . For the frequency  $\omega = 1.0$ , the density profiles are similar for the four trial wave function ansätze covered in this work, but RBM gives a higher two-body density in the middle of the quantum dot, compared to the other ansätze. The higher density can be seen from the magnitude of the density at the center, but also the density itself is narrower than for its fellow methods, making it more compact. Also, the RBM+SJ ansatz gives a slightly narrower distribution than the RBM+PJ and VMC ansätze, hinting that the Padé-Jastrow factor results in a stronger repulsive force between the electrons. The same indication can be seen from the density at the origin, which is low for RBM+PJ and VMC, but high for RBM and RBM+SJ. Furthermore, we know that the potential, and thus the interaction energy, gets more dominating as the frequency drops. For VMC and RBM+PJ, this can be observed by a circle of significantly higher density at a certain distance from the origin, most notably for  $\omega = 0.1$ , meaning that both electrons are less likely to be found at the center of the dot at the same time. If an electron is close to the center, the other electron is likely to be far from the center and *vice versa*. For the RBM+SJ ansatz, this behavior can only be observed for  $\omega = 0.1$ , while the RBM ansatz is not able to reproduce this phenomenon at all. This indicates that RBM does not model the correlations correctly, and it needs a Jastrow factor to account for them. The resolutions of the plots get lower when we decrease the frequency, as the electrons spread over a larger area and therefore more bins.

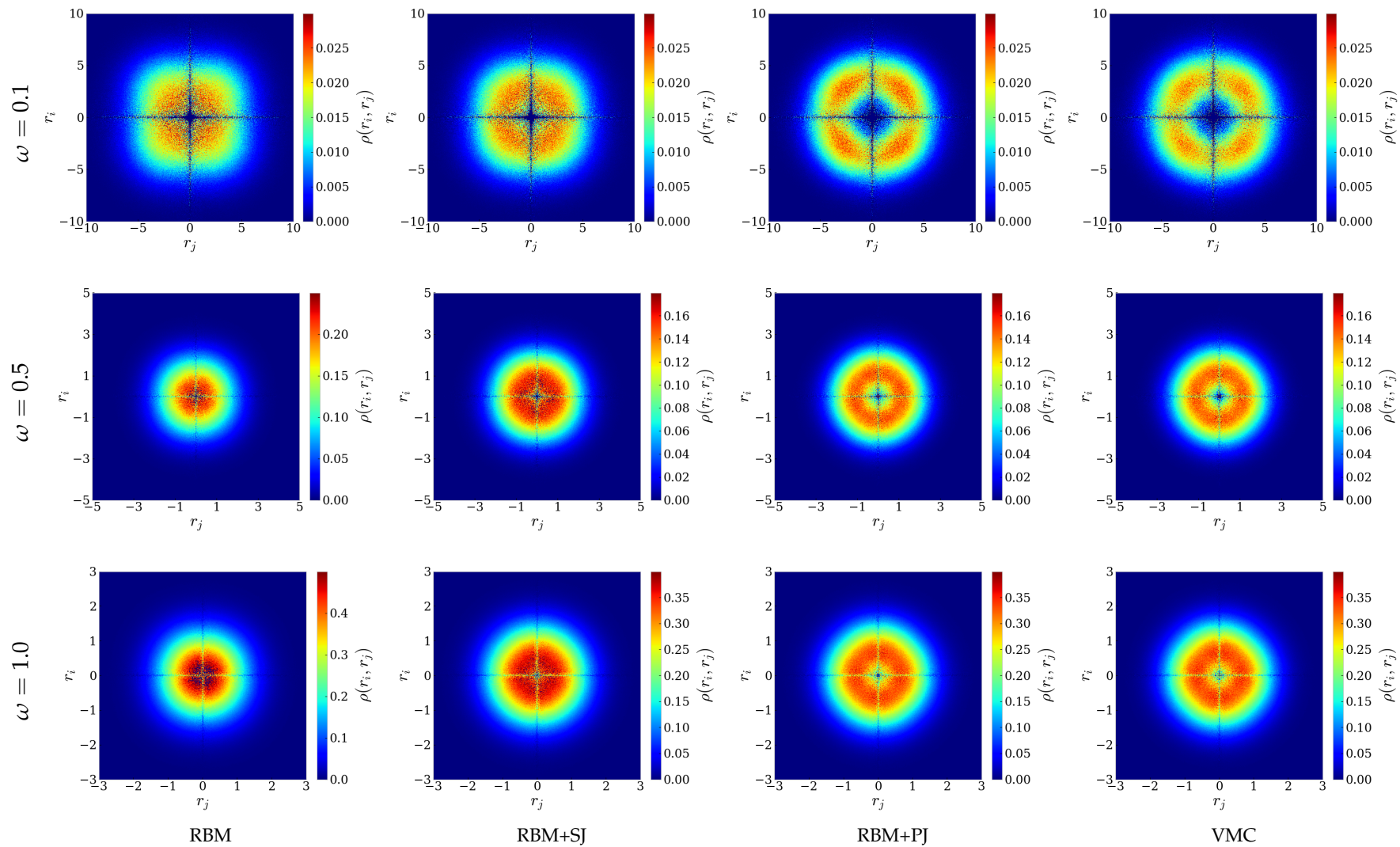


**Figure 11.12:** Plots of the radial two-body density profiles,  $\rho(r_i, r_j)$ , for two-dimensional quantum dots with  $N = 2$  electrons and oscillator frequencies  $\omega = 0.1, 0.5$  and  $1.0$  seen from the top. The RBM, RBM+SJ, RBM+PJ and VMC ansätze (from the left) were used, with the ADAM optimizer and  $M = 2^{28} = 268,435,456$  Monte Carlo cycles after convergence. For abbreviations and description of the natural units used, see the text.

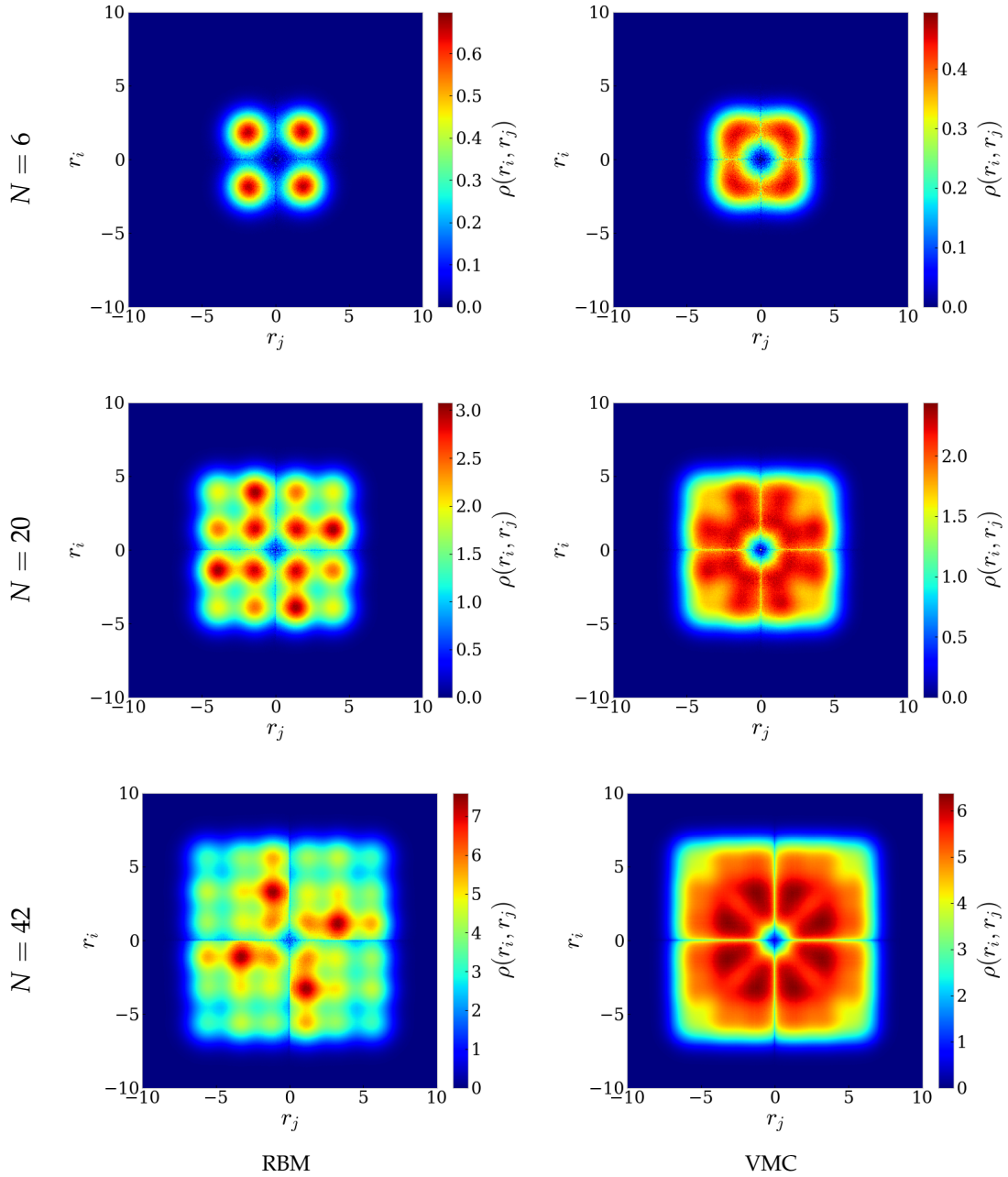


**Figure 11.13:** Plots of the two-body density profiles,  $\rho(r_i, r_j)$ , for two-dimensional quantum dots with an even number of closed shells ( $N = 6, 20$  and  $42$  electrons from the top) and oscillator frequency  $\omega = 0.5$ . The RBM (left column) and VMC (right column) ansätze were used, with the ADAM optimizer and  $M = 2^{28} = 268,435,456$  Monte Carlo cycles after convergence. For abbreviations and description of the natural units used, see the text.

We also present plots of the two-body density of two-dimensional quantum dots with frequency  $\omega = 0.5$  and an even number of closed shells ( $N = 6, 20$  and  $42$ ). For the simulations, we use the RBM and VMC ansätze, and the plots are found in figure (11.13). The first thing we observe is that RBM manages to obtain the same peaks as VMC, but all the peaks are circular, unlike VMC. The peaks are also more distinct and higher than for VMC. This is the same effect we saw from the one-body density plots, where we argued the the effect was caused by the different ways of modeling the correlations. If we now keep our attention on plots produced by

the VMC ansatz, it is apparent that two electrons will not be observed in the center of the dot at the same time, as the density there is almost absent. For  $N = 6$ , an electron pair is most likely to be found at the same radius around  $r = 2$ , which matches the one-body density plot. When we move on to  $N = 20$ , the most probable location is not ambiguous anymore, but an electron pair is likely to be found at the same radius at around  $r = 1$ , which matches the highest peak in the one-body density plot. However, the density is also high along both axes, which means that if one of the electrons moves towards the center of the dot, the other will also move towards the center. This is probably a consequence of the repulsive interactions. For  $N = 42$ , finding two electrons at the same radius is not the most likely case anymore. This is because the electrons now spread over a large area. The density plot clearly has some distinct peaks around  $r_i \sim 2.5$  and  $r_j \sim 1$ , matching the peaks found in the one-body density plots. For dots with an odd number of closed shells, the same tendency was found, but the peaks were found at the intersection between the quadrants, again matching the one-body density.

#### 11.4.4 Energy distribution

If we now recall the general Hamiltonian presented in chapter 3, the total energy is just the sum of the kinetic energy, harmonic oscillator potential energy and interaction energy. As the variational Monte Carlo method attempts to solve the Schrödinger equation directly, it is trivial to find the distribution between the various energy sources. Finding this is in general interesting when we want to exploit the most important contributions to the energy. Additionally, we can use these results to check the virial theorem presented in section 2.5. It is also interesting to see if the different ansätze give different energy distributions. We will denote the kinetic energy by  $\langle \hat{T} \rangle$ . The harmonic oscillator potential energy is associated with the more general term external potential energy, and is denoted by  $\langle \hat{V}_{\text{ext}} \rangle$ . The electron-electron interaction potential energy, or just the interaction energy, is denoted by  $\langle \hat{V}_{\text{int}} \rangle$ . In figure (11.14), we plot the ratio between the kinetic energy and total potential energy ( $\langle \hat{V} \rangle = \langle \hat{V}_{\text{ext}} \rangle + \langle \hat{V}_{\text{int}} \rangle$ ) as a function of the oscillator frequency. The systems considered are two-dimensional quantum dots with up to  $N = 20$  electrons. We base the plots on the numbers in the tables (C.3-C.6) in appendix C.

Firstly, the graphs are very similar for all the ansätze, which means that they all give the same distribution between kinetic energy and total potential energy, although they do not provide the same total energy. This is an interesting observation and indicates that both the obtained kinetic energy, external potential energy and interaction energy differ for the various ansätze when the total energy is different. Physically, this means that the electron configurations are fundamentally different for the different ansätze, as the electron configuration is the only factor that alters the potential energy. This was already observed in the one-body density plots. Further, we see a significant trend where the ratio drops as the frequency is decreased, implying that the total potential energy dominates over the kinetic energy at low frequencies. This is a known phenomenon already mentioned several times throughout this thesis. The ratio is consequently lower for larger dots. This is a result of gradually more interaction energy as we increase the number of electrons.

If we further recall the virial theorem presented in section 2.5, it states that the kinetic energy is related to the potential energies in a certain way. We have tested the virial theorem for non-interacting quantum dots and verified the a modified virial theorem,  $\langle \hat{T} \rangle = \langle \hat{V}_{\text{ext}} \rangle$ , deduced from equation (2.17). When we do the same calculation for the correlated quantum dots, we find the relation to not be satisfied. This can be seen from table (11.6), where we present the energy distribution for two-dimensional quantum dots with  $N = 12$  and selected frequencies. Especially for low frequency dots, the kinetic energy is dominated by the interaction energy. When the frequency is increased, the interacting energy contributes less. The kinetic and total potential energy then approach the same energy. This can also be seen from figure (11.14), as the

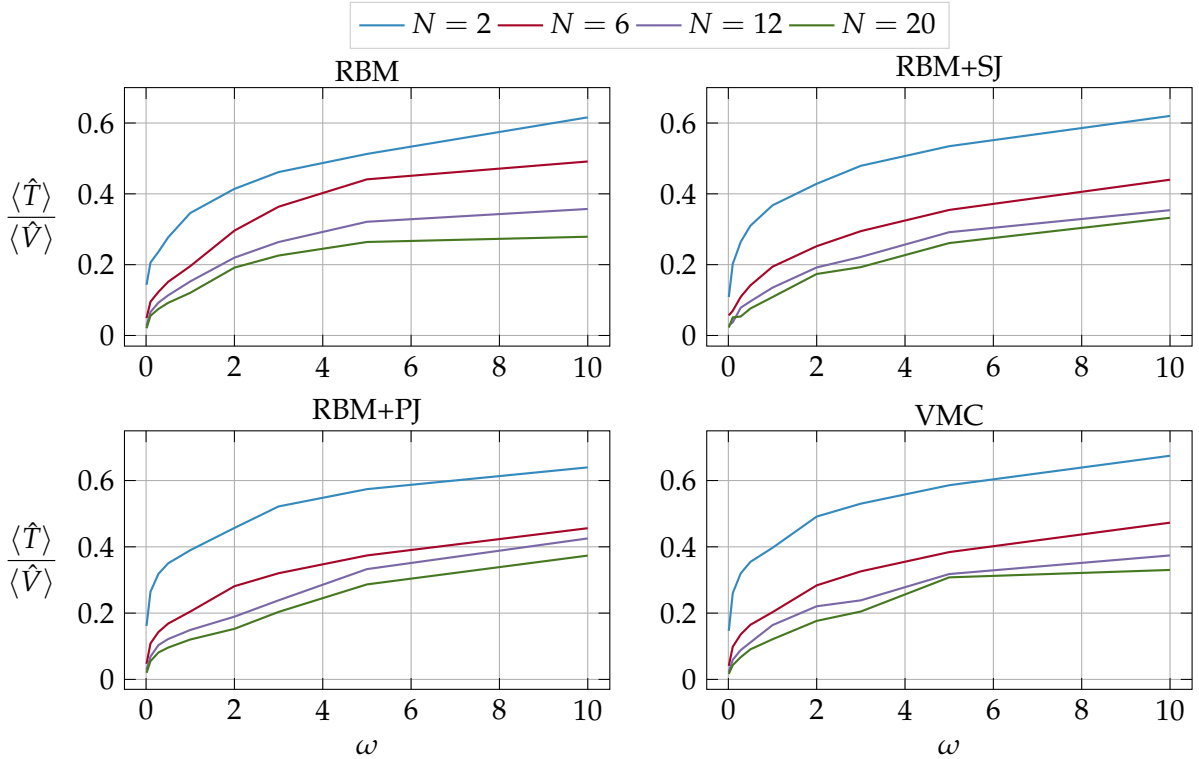


**Figure 11.14:** The kinetic-potential energy ratio,  $\langle \hat{T} \rangle / \langle \hat{V} \rangle$ , plotted as a function of the oscillator frequency for two-dimensional quantum dots with  $N = 2, 6, 12$  and  $20$  electrons. Simulations with frequencies  $\omega = 0.01, 0.1, 0.28, 0.5, 1.0, 2.0, 3.0, 5.0, 10.0$  were performed, see appendix C for exact energies. For abbreviations and description of the natural units used, see the text.

graphs flatten out as the frequency increases. Based on this, we believe that  $\langle \hat{T} \rangle \simeq \langle \hat{V}_{\text{ext}} \rangle$  when  $\omega \rightarrow \infty$ . This finding highlights that the behavior of the interacting system approaches the non-interacting behavior as the frequency increases, indicating that the one-body contributions dominate. The interaction contribution is apparently less important for high-frequency dots, paradoxically as the average electron-electron distance is small. Contrarily, the interactions are important for low-frequency dots. This is because the range of the Coulomb interactions is infinite, making the electrons affect each other even at long distances. To reduce the range of the Coulomb potential, we may introduce Coulomb screening potential,

$$\hat{V}_{\text{int}} = \begin{cases} \frac{1}{r_{ij}} & \text{if } r_{ij} < \lambda, \\ \frac{\exp(-r_{ij}/\mu)}{r_{ij}} & \text{if } r_{ij} > \lambda, \end{cases} \quad (11.1)$$

where  $\lambda$  is the screening length and  $\mu$  is the screening strength. The screening potential makes the interactions go rapidly to zero when the electron-electron distance is larger than the screening length. This can, for instance, be representative for a quantum dot in-medium. We have simulated low-frequency quantum dots using the Coulomb screening potential, and observed that the kinetic energy and the external potential energy are more or less identical for appropriate values of  $\mu$  and  $\lambda$ . The findings are directly in line with previous findings.

Another interesting aspect is how the energy is distributed for the various ansätze. Most notably, we see that VMC and RBM+PJ provide different kinetic and total potential energy distributions, albeit the total energy is more or less identical. Physically, this means that RBM+PJ finds another electron configuration than VMC to minimize the energy, which is exciting as the

**Table 11.6:** The ground state energy,  $E$ , of two-dimensional quantum dots with  $N = 12$  electrons and frequency  $\omega$ . In the following columns, the distribution between kinetic,  $\langle \hat{T} \rangle$ , external potential,  $\langle \hat{V}_{\text{ext}} \rangle$ , and interaction,  $\langle \hat{V}_{\text{int}} \rangle$ , energy are presented. The energy is given in units of  $\hbar$  (natural units), and the numbers in parenthesis are the statistical uncertainties in the last digit. For abbreviations see the text.

	$\omega$	$E$	$\langle \hat{T} \rangle$	$\langle \hat{V}_{\text{ext}} \rangle$	$\langle \hat{V}_{\text{int}} \rangle$
RBM	0.01	6.217(2)	0.1236(4)	2.244(2)	3.849(2)
	2.0	269.086(8)	43.262(8)	95.17(2)	130.65(1)
	10.0	961.03(4)	260.2(1)	364.8(1)	336.06(7)
RBM+SJ	0.01	6.239(2)	0.1372(6)	2.184(2)	3.919(3)
	2.0	265.66(9)	39.31(8)	95.78(1)	130.57(2)
	10.0	952.71(2)	237.65(4)	392.06(7)	323.00(3)
RBM+PJ	0.01	6.210(1)	0.1208(5)	2.189(2)	3.900(2)
	2.0	262.598(1)	34.758(6)	108.546(9)	119.293(7)
	10.0	947.33(2)	257.67(5)	348.35(6)	341.31(3)
VMC	0.01	6.2097(8)	0.1005(4)	2.270(3)	3.839(3)
	2.0	262.5339(9)	38.402(3)	95.681(7)	128.451(5)
	10.0	945.596(8)	231.56(4)	389.26(7)	324.77(3)

former ansatz is supposed to be more flexible than the latter. For more frequencies and system sizes, see appendix C.

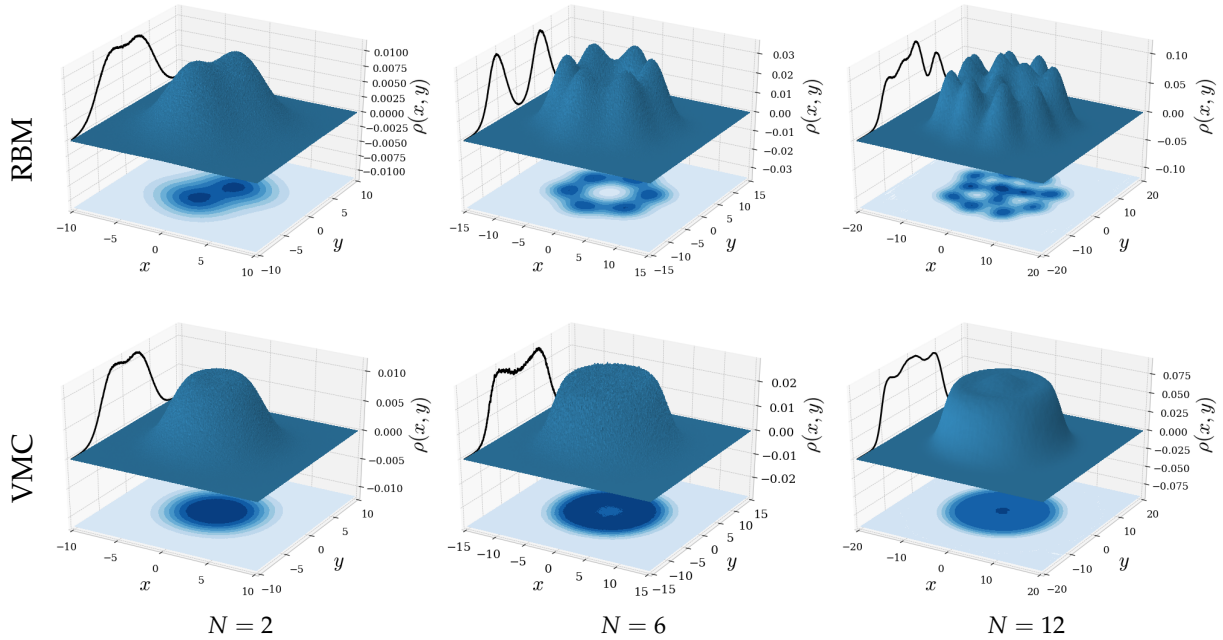


**Figure 11.15:** Plots of the one-body density profile,  $\rho(x,y)$ , of two-dimensional quantum dots with frequency  $\omega = 0.1$  and  $N = 2, 6$  and  $12$  electrons seen from left to right. The ansätze used are RBM (upper plots) and VMC (lower plots). The surface plot and the contour plot on the  $xy$ -plane illustrate the density, and the graph on the  $yz$ -plane represents the cross-section through  $x = 0$ . The surface plots are noise-reduced using a Savitzky-Golay filter. For abbreviations and description of the natural units used, see the text.

### 11.4.5 Low frequency dots

In section 11.4.2, we found the one-body density to be shape-invariant for high-frequency dots with  $\omega \geq 0.28$ . However, when we further decreased the frequency down to  $\omega = 0.1$ , the density profiles changed significantly, and we got other extrema. This section aims to investigate the transitions between the various shapes with frequencies down to  $\omega = 0.01$ . At this points, it is important to recall that our choice of the trial wave function is a single Slater determinant. This is not necessarily a good approximation for these low-frequency dots, as the gaps between the excited states around the Fermi level is small.

We start by looking at quantum dots with frequency  $\omega = 0.1$ , and in figure (11.15) we compare the spatial density profiles for  $N = 2, 6$  and  $12$  produced using RBM and VMC. The density profiles appear to be completely different. While VMC provides a single peak with some bumps on the top, RBM gives more distinct peaks. The numbers of peaks for the RBM ansatz is equal to the number of electrons, which indicates that the RBM finds the electrons to be localized at some fixed spots. The two ansätze model the correlations in completely different ways, and as the correlations become more important for low frequencies, it was expected that the results would also be different. However, the ground state energies obtained by the two ansätze do not differ this much for the same systems. This indicates that the electron density plots are better to reveal differences between the ansätze than the energy itself.

Furthermore, in figure (11.16) we fix the number of electrons to be  $N = 2$ , and vary the frequency from  $\omega = 0.28$  down to  $\omega = 0.01$  with density profiles produced by VMC and RBM+PJ. These ansätze were selected as they hitherto have provided the lowest ground state energies and we want to see if RBM+PJ can reveal effects that VMC is not able to capture. We see that the two ansätze obtain very similar density plots, where they agree that a ridge around the center of the

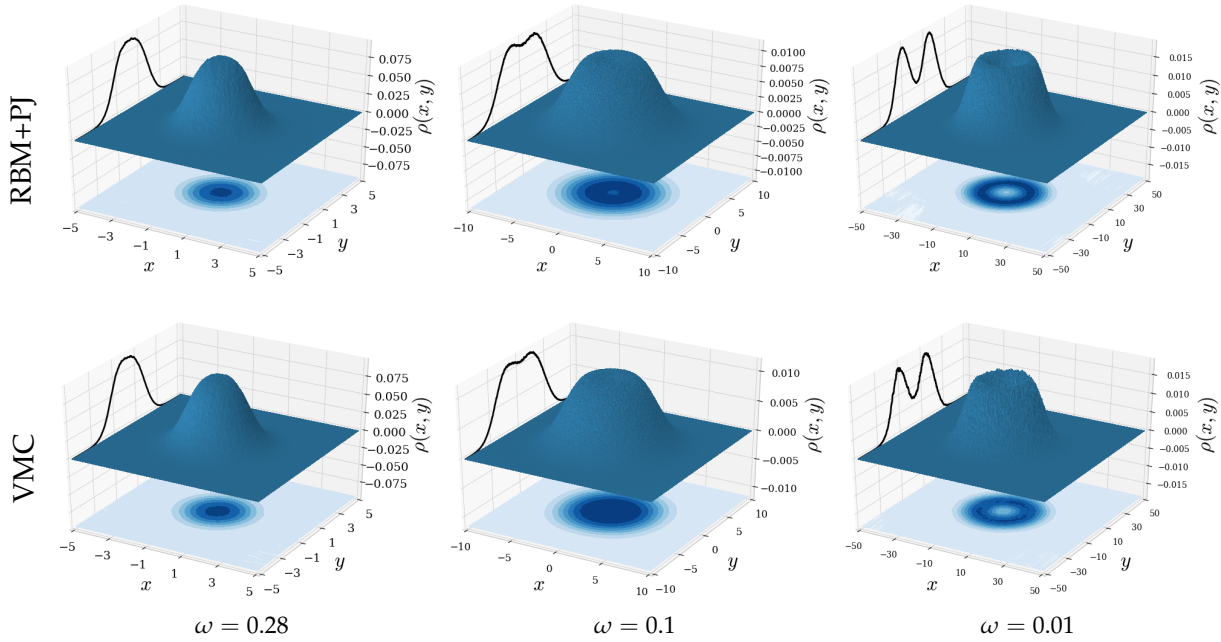


**Figure 11.16:** Plots of the one-body density profile,  $\rho(x, y)$ , of two-dimensional quantum dots with  $N = 2$  electrons and frequencies  $\omega = 0.28, 0.1$  and  $0.01$  from left to right. The ansätze used are RBM+PJ (upper plots) and VMC (lower plots). The surface plot and the contour plot on the  $xy$ -plane illustrate the density, and the graph on the  $yz$ -plane represents the cross-section through  $x = 0$ . The surface plots are noise-reduced using a Savitzky-Golay filter. For abbreviations and description of the natural units used, see the text.

dot should be more distinct as the frequency drops. If we go back to figure (11.14), we saw that the kinetic energy was negligible for the lowest energies, and the effect is therefore an indication of the Wigner localization effect discussed in section 3.3.1. As in the classical limit, the two electrons will repel each other and seldom be located at the same place when their kinetic energy is low. RBM+PJ possibly provides a sharper ridge for  $\omega = 0.01$ , which is closer to the DMC results found in Høgberget<sup>27</sup> and thus perhaps more correct. However, the energy provided by RBM+PJ and VMC are more or less identical ( $E = 0.074107$  and  $E = 0.074070$ , respectively), which means that the difference in one-body density does not affect energy.

We repeat the exercise for quantum dots with  $N = 6$  electrons, and obtain the plots in figure (11.17). With VMC, we observe the same tendency as for the dots with  $N = 2$  electrons, where we get an additional peak in the density plot as the frequency decreases. However, for RBM+PJ we do not get this peak in the center, but rather a significant density drop. This is contrary to the DMC one-body density plots obtained by Høgberget<sup>27</sup>, where there is a sharp peak in the center. The density plot for quantum dots is also to approach the classical limit as the frequency is decreased<sup>5</sup>, where the potential energy is minimized when we have one electron in the center and five electrons surrounding it.

In order to give a more qualitative comparison of the various ansätze, we also present the radial one-body density profiles. In figure (11.18), the one-body density of quantum dots with frequency  $\omega = 0.01$  and  $N = 2, 6$  electrons is presented. We see that the ansätze agree on the density shape for  $N = 2$ , where RBM+PJ gives the most distinct peak, followed by VMC, RBM+SJ and RBM, in that order. For  $N = 6$ , the various ansätze give completely different density profiles. The variation might again be explained by different approaches to model the correlations, but future investigations on this is needed.

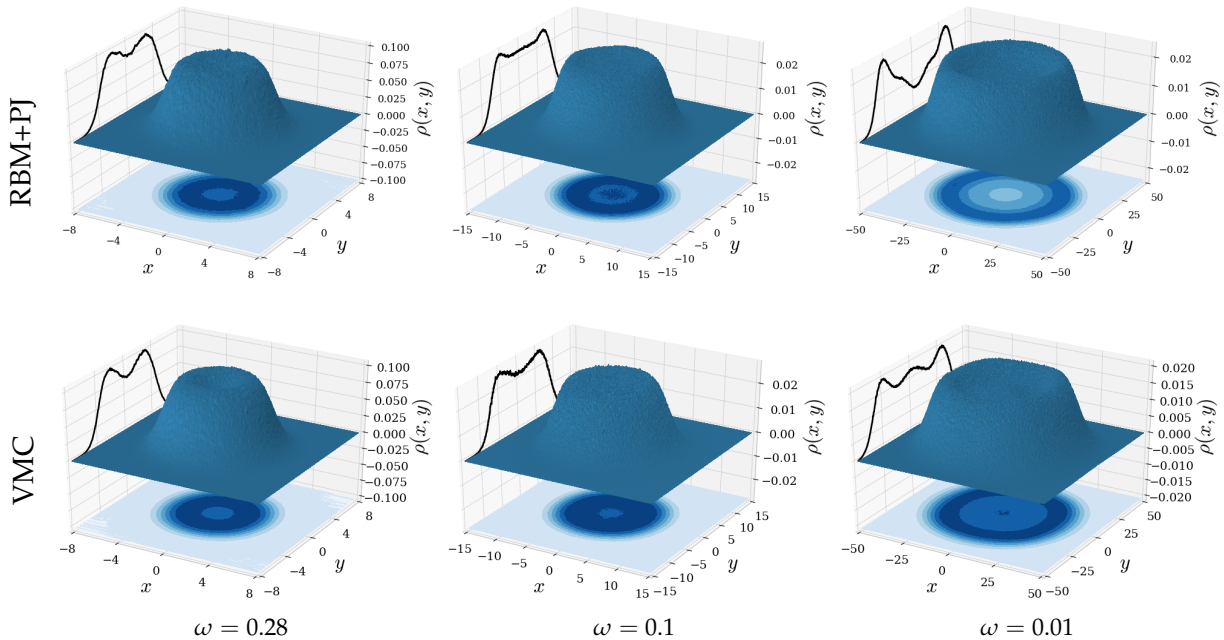


**Figure 11.17:** Plots of the one-body density profile,  $\rho(x, y)$ , of two-dimensional quantum dots with  $N = 6$  electrons and frequencies  $\omega = 0.28, 0.1$  and  $0.01$  seen from left to right. The ansätze used are RBM+PJ (upper plots) and VMC (lower plots). The surface plot and the contour plot on the  $xy$ -plane illustrate the density, and the graph on the  $yz$ -plane represents the cross-section through  $x = 0$ . The surface plots are noise-reduced using a Savitzky-Golay filter. For abbreviations and description of the natural units used, see the text.

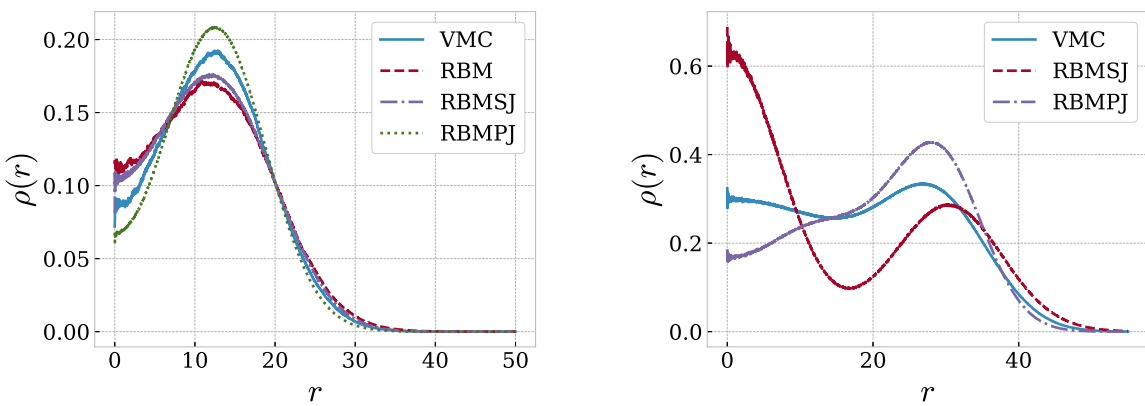


**Figure 11.18:** Plots of the one-body density profile,  $\rho(r)$ , of two-dimensional quantum dots of frequency  $\omega = 0.01$  and  $N = 72, 90$ . The ADAM optimizer was used, and after convergence the number of Monte Carlo cycles was  $M = 2^{28} = 268,435,456$ . For abbreviations and description of the natural units used, see the text.

**Table 11.7:** Ground state energy of large quantum dots with frequency  $\omega = 1.0$  and  $N = 72$  and 90 electrons in two dimensions (2D) and  $N = 70$  electrons in three dimensions (3D). All energies are given in units of  $\hbar$  (natural units), and the numbers in parenthesis are the statistical uncertainties in the last digit. For abbreviations see the text.

	$N$	RBM	VMC
2D	72	1355.37(2)	1340.520(7)
	90	2194.12(9)	1990.89(2)
3D	70	1129.40(2)	1108.950(4)

### 11.4.6 Large dots

In order to test the code, we also decided to run for systems with  $N > 56$ . We do this for the sake of completeness and to test how far a VMC code can go. One thing is that the computations get extremely expensive as the number of electrons increases, but we have also seen that the statistical error increases as the system size increases. This means that we cannot just crack up the wall clock time and wait when studying large systems; at some point, the standard error gets too large and we need to increase the number of Monte Carlo cycles further. The learning rate also needs to be decreased as the system size increases, which requires more iterations. In table (11.7), the ground state energy of two-dimensional quantum dots with frequency  $\omega = 1.0$ , and  $N = 72, 90$  electrons and three-dimensional quantum dots with  $N = 70$  electrons is listed. We observe that the difference between the VMC ansatz and the RBM ansatz is significant, notably for  $N = 90$  electrons in two dimensions. We suspect that this simulation simply has not converged.

In figure (11.19), the radial one-body density profile is plotted for two-dimensional quantum dots with frequency  $\omega = 1.0$  and  $N = 72, 90$  electrons. Again, we observe the same peaks as we observed in section 11.4.2, and the number of peaks substantiates that we get an additional peak every time we add a closed-shell. However, for  $N = 90$ , the peaks are not as significant as before, most notably for the RBM, which might be another indication that the simulation has not converged.

## 11.5 Atoms

The last systems we will address are the real atoms, which have been investigated by physicists since the childhood of quantum mechanics. This section is added to show the flexibility of the implemented code, which can easily be expanded to new systems. The simple hydrogen-like orbitals, detailed in section 4.3, are used. We investigate four selected atoms: Helium, beryllium, neon and magnesium. These atoms were not selected arbitrary; helium and neon are the two smallest noble gases and are thus closed-shell systems. Beryllium and magnesium are, on the other hand, not closed-shell systems, but since the valence electrons might occupy the  $s$ -shell in the ground state, a single Slater determinant as the trial wave function guess might be a reasonable guess. In table (11.8), the obtained ground state energy is obtained, including an overview of how the energy is distributed. Also, the ratio between the kinetic energy ( $\langle \hat{T} \rangle$ ) and total potential energy ( $\langle \hat{V} \rangle = \langle \hat{V}_{\text{ext}} \rangle + \langle \hat{V}_{\text{int}} \rangle$ ) is presented, and we compare the obtained results to experimental values.

We observe that the total energy is similar, but slightly higher than our reference. This is as expected considering the simple basis used. Magnesium is the atom where we get largest

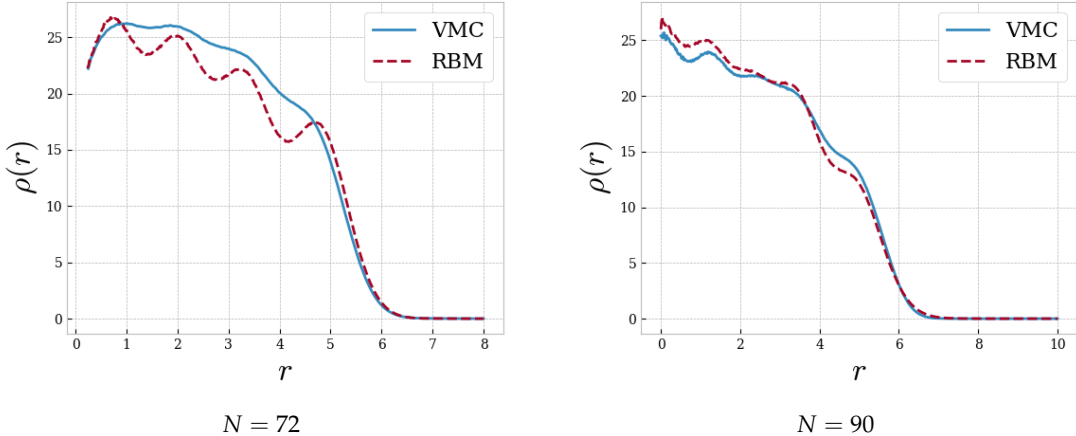


**Figure 11.19:** Plots of the radial one-body density profile,  $\rho(r)$ , of large quantum dots with  $N = 72$  (left) and  $90$  (right), and frequency  $\omega = 1.0$  produced with RBM and VMC. For abbreviations and description of the natural units used, see the text.

**Table 11.8:** Ground state energy,  $E$ , of neutral atoms with atomic number,  $Z$ , produced by the VMC method. In the following columns, the distribution between kinetic,  $\langle \hat{T} \rangle$ , external potential,  $\langle \hat{V}_{\text{ext}} \rangle$ , and interaction,  $\langle \hat{V}_{\text{int}} \rangle$ , energy are presented, as well as the kinetic-potential energy ratio,  $\langle \hat{T} \rangle / \langle \hat{V} \rangle$ . The experimental energies (Expr.) are taken from Degroote<sup>110</sup>, table 4.4. The energy is given in Hartree atomic units, and the numbers in parenthesis is the statistical error. For abbreviations and description of the units, see the text.

Atom	$Z$	Expr. (Ref.[110])	$E$	$\langle \hat{T} \rangle$	$\langle \hat{V}_{\text{ext}} \rangle$	$\langle \hat{V}_{\text{int}} \rangle$	$\langle \hat{T} \rangle / \langle \hat{V} \rangle$
He	2	-2.9037	-2.8719(3)	2.813(3)	-6.696(4)	1.010(7)	-0.495
Be	4	-14.6674	-14.4992(5)	15.465(6)	-34.987(7)	5.023(1)	-0.516
Ne	10	-128.9383	-128.09(1)	133.4(2)	-318.4(2)	56.94(5)	-0.510
Mg	12	-200.054	-196.81(4)	251.9(2)	-557.0(2)	108.23(6)	-0.379

deviation between the obtained and the experimental energy, which indicates that the single Slater determinant is not a sufficient trial wave function ansatz for this system.

If we once again recall the virial theorem, first introduced in section 2.5, it reads

$$2\langle \hat{T} \rangle = -\langle \hat{V}_{\text{ext}} \rangle \quad (11.2)$$

for non-interacting atoms, for which the equation has been verified. For interacting atoms, equation (11.2) is not valid, but based on table (11.8) it is closer than what we observed for the two-dimensional quantum dots in section 11.4.4. As the quantum dots got weaker interactions, the modified virial theorem got more correct. Moreover, in section 11.4.1 we observed that a two-dimensional system is more sensitive on the wave function guess than a three-dimensional system. As atoms are three-dimensional, we expected the virial theorem to be more correct than for two-dimensional systems.

Furthermore, we look at the radial one-body density profiles, which are presented in figure (11.20) for our four selected atoms. To reveal peaks in the plots of the one-body density,

they are multiplied with  $r^2$ , similar to previous studies<sup>27</sup>. Again comparing Högberget<sup>27</sup> to, we observe that the densities agree with the diffusion Monte Carlo results, which again substantiates that our framework and electron density computations work as they should. However, for magnesium, the density plot is slightly different, which again indicates that the single Slater determinant is not a sufficient trial wave function ansatz for this system.

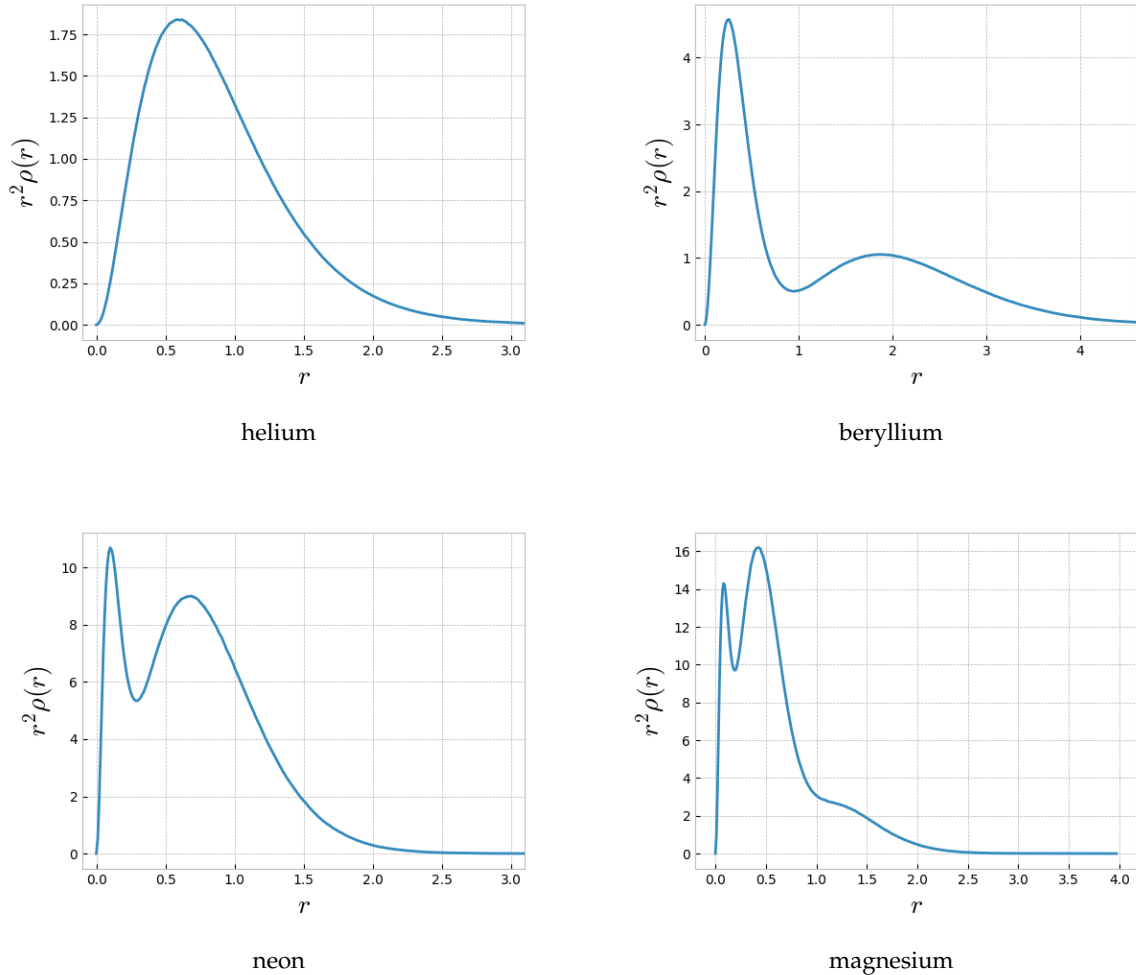


**Figure 11.20:** Plots of the radial one-body density profiles,  $\rho(r)$ , as a function of the radial distance from the nucleus, multiplied with the radius squared. We look at the helium atom (upper left), the beryllium atom (upper right), the neon atom (lower left) and the magnesium atom (lower right). VMC was used, which is detailed in the text. The number of Monte Carlo cycles used was  $M = 2^{28} = 268,435,456$  and the ADAM optimizer was used. Hartree atomic units were used, see the text.



## **Part VI**

# **Conclusion**



## CHAPTER 12

# Conclusions and Future Work

In this chapter, we attempt to compress the relatively comprehensive discussion in the previous chapter down to a more tangible conclusion. Thereafter, we address some possible extensions of our work and how our work can contribute to solving the quantum many-body puzzle.

All the results presented in this work are obtained using a variational Monte Carlo framework with various trial wave function ansätze. The ansatz where the standard Slater-Jastrow wave function is used as the trial wave function guess is abbreviated as VMC. We also apply the marginal distributions of a Gaussian-binary restricted Boltzmann machine as the single-particle functions in a Slater determinant, and get another ansatz denoted by RBM. This ansatz produces reasonable ground state energy estimates compared to the diffusion Monte Carlo (DMC) and VMC energy. When more physical intuition in the form of Jastrow factors is added, the energy drops further towards the DMC energy. Most notably, the RBM ansatz with the Padé-Jastrow factor added (abbreviated RBM+PJ) provides lower ground state energy and statistical error than the VMC ansatz for the smallest dots. This indicates that the RBM+PJ ansatz can provide a wave function closer to the exact one than the VMC ansatz. However, for larger quantum dots, RBM+PJ gives a slightly higher energy than VMC. As we consequently set the number of hidden units,  $H$ , equal to the number of electrons,  $N$ , this may be a consequence of the large number of variational parameters residing in the ansatz. In machine learning terms, we use a too complex model for our problem. We decided to do this because  $H = N$  was found to be optimal for small quantum dots<sup>26</sup>, but it could be different for larger dots. Carleo & Troyer<sup>24</sup> operate with a hidden variable density  $\alpha = H/F$  with  $F$  as the degrees of freedom (number of visible units). They fix  $\alpha$  to an integer and thus end up with more variational parameters than we do. A conclusion is that the number of hidden units might not be optimal, and need future investigation. We also observe that all the ansätze give more or less the same ratio between kinetic and total potential energy for all system sizes and all frequencies, indicating that the electron configuration is fundamentally different for the different ansätze.

Throughout the results, the electron density was thoroughly studied the various ansätze. The studies revealed some significant differences between the ansätze that cannot be seen just from the ground state energy. The most notable difference is found for the one-body density produced using VMC and RBM, where RBM tends to exaggerate the fluctuations compared to VMC. As discussed, this difference is probably caused by how the two ansätze model the electron-electron correlations. The same effect was found in the two-body density plots, where the difference between the various correlation models is even more significant. In general, RBM+PJ and VMC give more significant electron-electron repulsion than the fellow ansätze, RBM and RBM with a simple Jastrow factor (abbreviated RBM+SJ). This allows the conclusion that the energy estimates are not necessarily the best way to compare various trial wave function ansätze, other observable are potentially more crucial. The RBM+SJ ansatz is an excellent example of this, as it provides energy estimates similar to VMC, but the two-body density plots exploit that the correlations were somewhat weaker. In general, we believe that the Padé-Jastrow factor works

better than the simple Jastrow factor as it provides a lower energy and is constructed to satisfy the cusp condition. As the simple Jastrow factor is more or less as computationally expensive as the Padé-Jastrow factor, we conclude that the RBM+PJ ansatz is a better choice than the RBM+SJ ansatz for quantum dots.

Based on the discussions above, the RBM ansatz provides exciting results, but at its current version it is not able to compete with the existing many-body methods when it comes to the performance. However, we see the outcome of this work as a step in the right direction, and with some more investigation we believe that the RBM ansatz can be an alternative to traditional ansätze. More precisely, RBM has some properties that makes it able to estimate the ground state energy at a lower cost than the VMC ansatz. Other RBM ansätze, for instance based on spherical coordinates, might enhance the performance at the same cost. We also see a bright future for the RBM+PJ ansatz, which for some systems gives a lower energy than the VMC ansatz.

The overall goal of this work was to develop and investigate a method that required less physical intuition. To achieve this, we had to develop a flexible VMC framework from scratch and implement the restricted Boltzmann machines (RBMs) as a trial wave function ansatz. Throughout the results in the previous chapter, we have carefully validated the framework, which seems to give consistent results with references. It is hard to validate the trial wave functions based on RBMs as no previous research has done anything comparable. However, when comparing to the results obtained using other methods, we are confident that also this implementation is correct. Furthermore, we managed to produce a large number of ground state results of the quantum dots using various trial wave function ansätze with and without adding a Jastrow factor. These results were compared extensively, resulting in a thorough evaluation of the trial wave functions. Selected atoms were studied using the hydrogen-like orbitals in the trial wave function, but we did not have time or manage to study them using the RBMs. We put some effort in trying to model the atoms using the same RBMs as for the quantum dots, but even with a large number of hidden units, these Gaussian-binary unit RBMs were not flexible enough to capture the properties of the atoms. Other possible attempts include expanding a Hartree-Fock basis in a set of RBMs, or simply choose another RBM structure which is not based on the Gaussian mapping. This is something that can and should be tried, and is one among many things that are desirable for future work.

## Future work

The use of machine learning for solving the many-body problem is just in the starting block, and there are millions of features to be investigated. Using the same approach as we did, there are plenty of network architectures, hyper-parameter setting and initial conditions that we did not have time to explore. The RBM ansatz with a smaller number of hidden units is something that requires future investigations. Also, writing an RBM code in spherical coordinates, instead of Cartesian coordinates, could be interesting as it might be easier to model the correlations in that coordinate system.

Pfau *et al.*<sup>25</sup> created a trial wave function ansatz based on Slater determinants, where the single-particle functions were determined by neural networks. Both the relative distances between all the particles and the collective positions where passed into the neural network. Using a standard VMC framework, they obtained lower ground state energies of atoms than provided by traditional methods. In future studies, these calculations could be repeated using RBMs as the single-particle functions.

Initially, the idea behind the use of a restricted Boltzmann machine as the trial wave function ansatz, was that it can be used to investigate systems with unavailable wave functions. Future studies should therefore consider more complicated systems. In the first place, multi-quantum

dots (multiple quantum dots with intern connections) are good candidates as there exist comparable experiments<sup>30,31</sup>. As the RBM ansatz is able to model two-body correlations, it is also imaginable that it can model three-body correlations and therefore be used to simulate nuclear systems where the three-body component in the wave function is not properly understood<sup>73</sup>.

In section 7.4, we discussed the sign-problem plaguing the diffusion Monte Carlo method, and that shadow wave functions can be used to overcome this problem. There are many similarities between the shadow wave functions and wave functions based on restricted Boltzmann machines. Future studies could fruitfully explore this link further.

As the quantum simulations are costly, one should always try to find the bottleneck and optimize that part of the code in order to simulate larger systems. For the RBM ansatz, the bottleneck might be the neural networks, which can be evaluated extremely fast on a GPU. However, the remaining framework is probably faster to evaluate on CPUs, so a hybrid of GPU and CPU would might be optimal and can be investigated in future studies.



## APPENDIX A

# Natural Units

In everyday life, we usually stick to the standard SI units when measuring or expressing quantities like distance, energy, mass and time. A standardized unit system is important because it is common for people around the world and simplifies communication across borders. Moreover, we gradually develop intuitions about units when they are used frequently. We then immediately observe if a number makes sense or not when it is expressed in the preferred units. As a European, I use the metric system. When a person is 1.90 meters tall, I can easily imagine their height. On the other hand, when Americans tell their height, I do not have an intuition for how tall 6 feet 3 inches is.

In science, the SI units are often not the preferred ones, especially not on very large or small scales. For instance, measuring cosmological distances in meters is very unpractical, as the distance to the Sun is  $\sim 1.5 \cdot 10^{11}$  meters and the distance to our closest neighbor galaxy, Andromeda, is  $\sim 2.4 \cdot 10^{22}$  meters. Instead, we use units like the astronomical unit [a.u.] (should not be confused with atomic units) and light-years.

For small scales, the situation is similar. For instance, the most probable distance between the nucleus and the electron in the hydrogen atom is the Bohr radius, which is  $a_0 \approx 5.3 \cdot 10^{-11}$  meters. These scales are unpractical to work with in SI units. Instead, we define so-called natural units, which is a common term for units based on universal physical constants. The hydrogen atom is usually treated in a variant of atomic units with  $a_0 = 1$ , and in section A.2 we will discuss the Hartree atomic units. The quantum dots will be scaled differently, with units named just natural units.

## A.1 Quantum dots

For quantum dots, the one-dimensional Hamiltonian in SI units reads

$$\hat{\mathcal{H}} = -\frac{\hbar^2}{2m} \frac{\partial^2}{\partial x^2} + \frac{1}{2} m \omega^2 x^2, \quad (\text{A.1})$$

with  $\hbar$  as the reduced Planck's constant,  $m$  as the electron mass and  $\omega$  as the oscillator frequency. The corresponding wave functions read

$$\phi_n(x) = \frac{1}{\sqrt{2^n n!}} \cdot \left( \frac{m\omega}{\pi\hbar} \right)^{1/4} \exp\left(-\frac{m\omega}{2\hbar}x^2\right) H_n\left(\sqrt{\frac{m\omega}{\hbar}}x\right), \quad (\text{A.2})$$

where  $H_n(x)$  are the Hermite polynomials. We want to get rid of  $\hbar$  and  $m$  in equation (A.1) to make it dimensionless. This can be accomplished by scaling  $\hat{\mathcal{H}}' = \hat{\mathcal{H}}/\hbar$ , such that the Hamiltonian reduces to

$$\hat{\mathcal{H}}' = -\frac{\hbar}{2m} \frac{\partial^2}{\partial x^2} + \frac{1}{2} \frac{m\omega^2}{\hbar} x^2. \quad (\text{A.3})$$

We now observe that the fraction  $\hbar/m$  appears in both terms, so we can avoid the constants by introducing a characteristic length,  $x' = x/\sqrt{\hbar/m}$ . This results in the Hamiltonian

$$\hat{\mathcal{H}} = \frac{1}{2} \frac{\partial^2}{\partial x^2} + \frac{1}{2} \omega^2 x^2, \quad (\text{A.4})$$

which corresponds to setting  $\hbar = m = 1$ . In natural units, one often sets  $\omega = 1$  as well by scaling  $\hat{\mathcal{H}}' = \hat{\mathcal{H}}/\hbar\omega$ , but since we want to keep the  $\omega$ -dependency, we do it slightly different. This means that the exact wave functions for the one-particle one-dimensional case is given by

$$\phi_n(x) = \frac{1}{\sqrt{2^n n!}} \cdot \left(\frac{\omega}{\pi}\right)^{1/4} \exp\left(-\frac{\omega}{2}x^2\right) H_n(\sqrt{\omega}x) \quad (\text{A.5})$$

in natural units.

## A.2 Atoms

The atomic Hamiltonian for an electron in subshell  $l$  affected by a nucleus with atomic number  $Z$  reads

$$\hat{\mathcal{H}} = -\frac{\hbar^2}{2m_e} \nabla^2 - \frac{1}{4\pi\epsilon_0} \frac{Ze^2}{r} + \frac{\hbar^2 l(l+1)}{2m_e r^2} \quad (\text{A.6})$$

in SI units, where  $e$  is the elementary charge and  $k_e = 1/4\pi\epsilon_0$  is Coulomb's constant. Again we want to get rid of the reduced Planck's constant,  $\hbar$ , and the electron mass,  $m_e$ , in order to make the Hamiltonian dimensionless. We can do this by multiplying all terms by  $(4\pi\epsilon_0)^2 \hbar^2 / m_e e^4 Z^2$ ,

$$\hat{\mathcal{H}} \cdot \frac{(4\pi\epsilon_0)^2 \hbar^2}{m_e e^4 Z^2} = -\frac{(4\pi\epsilon_0)^2 \hbar^4}{2m_e^2 e^4 Z^2} \nabla^2 + \frac{4\pi\epsilon_0 \hbar^2}{m_e e^2 Z r} - \frac{(4\pi\epsilon_0)^2 \hbar^4}{m_e^2 e^4 Z^2} \frac{l(l+1)}{r^2}. \quad (\text{A.7})$$

This might look very chaotic, but by exploiting that the Bohr radius,

$$a_0 \equiv \frac{4\pi\epsilon_0 \hbar^2}{m_e e^2 Z}, \quad (\text{A.8})$$

is found in all the right-hand side terms, the Hamiltonian reduces to

$$\hat{\mathcal{H}} \cdot \frac{(4\pi\epsilon_0)^2 \hbar^2}{m_e e^4 Z^2} = -\frac{a_0^2}{2} \nabla^2 + a_0 \frac{Z}{r} - a_0^2 \frac{l(l+1)}{2r^2}. \quad (\text{A.9})$$

We obtain the dimensionless Hamiltonian in Hartree atomic units by introduce the length scaling  $r' = r/a_0$  and the energy scaling  $\hat{\mathcal{H}}' = \hat{\mathcal{H}}/(m_e e^4 Z^2 / (4\pi\epsilon_0)^2 \hbar^2)$ ,

$$\hat{\mathcal{H}} = -\frac{1}{2} \nabla^2 - \frac{Z}{r} + \frac{l(l+1)}{2r^2}. \quad (\text{A.10})$$

Similar to the natural units discussed for the quantum dots, this corresponds to setting  $\hbar = m_e = k_e = e = 1$ .

## APPENDIX B

# Distributions of Gaussian-binary restricted Boltzmann machines

In this appendix, we will derive the marginal and conditional distributions of a Gaussian-binary restricted Boltzmann machine with the system energy

$$E(\mathbf{x}, \mathbf{h}) = \sum_{i=1}^F \frac{(x_i - a_i)^2}{2\sigma_i^2} - \sum_{j=1}^H b_j h_j - \sum_{i=1}^F \sum_{j=1}^H \frac{x_i w_{ij} h_j}{\sigma_i^2}. \quad (\text{B.1})$$

There are  $F$  visible units  $x_i$  with related bias weights  $a_i$  and  $H$  hidden units  $h_j$  with related bias weights  $b_j$ .  $w_{ij}$  are the weights connecting the visible units to the hidden units. The joint probability distribution is given by the Boltzmann distribution

$$P(\mathbf{x}, \mathbf{h}) = \frac{1}{Z} \exp(-\beta E(\mathbf{x}, \mathbf{h})), \quad (\text{B.2})$$

where  $Z$  is the partition function,

$$Z = \iint d\mathbf{x} d\mathbf{h} P(\mathbf{x}, \mathbf{h}), \quad (\text{B.3})$$

and  $\beta = 1/k_B T$  is a factor which will be fixed to 1. As the marginal and conditional distributions are closely related both for the visible and hidden layer, we present the distributions in sections respective for the two layers.

## B.1 Distributions of visible units

The distributions of the visible units are used to find properties related to the visible units. If we recall a restricted Boltzmann machine, the transformation between the visible units and the hidden units is  $f_j(\mathbf{x}; \boldsymbol{\theta}) = b_j + \sum_{i=1}^F w_{ij} x_i / \sigma_i^2$ . By this expression, we can express the joint probability distribution as

$$\begin{aligned} P(\mathbf{x}, \mathbf{h}) &= \frac{1}{Z} \exp \left( - \sum_{i=1}^F \frac{(x_i - a_i)^2}{2\sigma_i^2} + \sum_{j=1}^H b_j h_j + \sum_{i=1}^F \sum_{j=1}^H \frac{x_i w_{ij} h_j}{\sigma_i^2} \right), \\ &= \frac{1}{Z} \exp \left( - \sum_{i=1}^F \frac{(x_i - a_i)^2}{2\sigma^2} + \sum_{j=1}^H \left[ b_j h_j + \frac{\sum_{i=1}^F h_j w_{ij} x_i}{\sigma_i^2} \right] \right), \\ &= \frac{1}{Z} \exp \left( - \sum_{i=1}^F \frac{(x_i - a_i)^2}{2\sigma^2} + \sum_{j=1}^H h_j f_j(\mathbf{x}; \boldsymbol{\theta}) \right), \end{aligned} \quad (\text{B.4})$$

which will be the base of the other distributions of the visible units.

### B.1.1 Marginal distribution

The marginal distribution of the visible units is given by the sum

$$P(\mathbf{h}) = \sum_{\{\mathbf{h}\}} P(\mathbf{x}, \mathbf{h}), \quad (\text{B.5})$$

as the hidden units can take binary values only. By inserting the expression of the joint probability distribution from equation (B.4), we obtain

$$\begin{aligned} P(\mathbf{x}) &= \frac{1}{Z} \sum_{\{\mathbf{h}\}} \exp \left( \sum_{i=1}^F \frac{(x_i - a_i)^2}{2\sigma^2} + \sum_{j=1}^H h_j f_j(\mathbf{x}; \boldsymbol{\theta}) \right), \\ &= \frac{1}{Z} \exp \left( - \sum_{i=1}^F \frac{(x_i - a_i)^2}{2\sigma^2} \right) \sum_{\{\mathbf{h}\}} \prod_{j=1}^H \exp(h_j f_j), \\ &= \frac{1}{Z} \exp \left( - \sum_{i=1}^F \frac{(x_i - a_i)^2}{2\sigma^2} \right) \sum_{h_1=0}^1 \sum_{h_2=0}^1 \dots \sum_{h_H=0}^1 \exp(h_1 f_1) \exp(h_2 f_2) \dots \exp(h_H f_H), \quad (\text{B.6}) \\ &= \frac{1}{Z} \exp \left( - \sum_{i=1}^F \frac{(x_i - a_i)^2}{2\sigma^2} \right) \prod_{j=1}^H \sum_{h_j=0}^1 \exp(h_j f_j), \\ &= \frac{1}{Z} \exp \left( - \sum_{i=1}^F \frac{(x_i - a_i)^2}{2\sigma^2} \right) \prod_{j=1}^H [1 + \exp(f_j(\mathbf{x}; \boldsymbol{\theta}))]. \end{aligned}$$

This is what we will use as the marginal distribution of the visible units.

### B.1.2 Conditional distribution

The conditional distribution of the visible units is given by

$$P(\mathbf{h}|\mathbf{x}) = \frac{P(\mathbf{x}, \mathbf{h})}{P(\mathbf{x})}, \quad (\text{B.7})$$

where the numerator is the joint probability distribution given in equation (B.4) and the denominator is the marginal distribution of the visible units given in equation (B.6). This gives the conditional probability

$$\begin{aligned} P(\mathbf{h}|\mathbf{x}) &= \frac{\frac{1}{Z} \exp \left( - \sum_{i=1}^F \frac{(x_i - a_i)^2}{2\sigma^2} + \sum_{j=1}^H h_j f_j(\mathbf{x}; \boldsymbol{\theta}) \right)}{\frac{1}{Z} \exp \left( - \sum_{i=1}^F \frac{(x_i - a_i)^2}{2\sigma^2} \right) \prod_{j=1}^H [1 + \exp(f_j(\mathbf{x}; \boldsymbol{\theta}))]}, \\ &= \prod_{j=1}^H \frac{\exp(h_j f_j(\mathbf{x}; \boldsymbol{\theta}))}{1 + \exp(f_j(\mathbf{x}; \boldsymbol{\theta}))}, \quad (\text{B.8}) \end{aligned}$$

where we recall that  $f_j(\mathbf{x}; \boldsymbol{\theta}) = b_j + \sum_{i=1}^F w_{ij} x_i / \sigma_i^2$  are just the transition going from the visible units to the hidden units.

## B.2 Distributions of hidden units

The distributions of the hidden units are used to find properties related to the hidden units. If we recall a restricted Boltzmann machine, the transformation between the hidden units and

the visible units is  $g_i(\mathbf{h}; \boldsymbol{\theta}) = a_i + \sum_{j=1}^H h_j w_{ij}$ . By using that expression, we can express the joint probability distribution as

$$\begin{aligned} P(\mathbf{x}, \mathbf{h}) &= \frac{1}{Z} \exp \left( -\sum_{i=1}^F \frac{(x_i - a_i)^2}{2\sigma_i^2} + \sum_{j=1}^H b_j h_j + \sum_{i=1}^F \sum_{j=1}^H \frac{x_i w_{ij} h_j}{\sigma_i^2} \right), \\ &= \frac{1}{Z} \exp \left( \sum_{j=1}^H b_j h_j - \sum_{i=1}^F \frac{x_i^2 + a_i^2 - 2a_i x_i - 2x_i \sum_{j=1}^H h_j w_{ij}}{2\sigma_i^2} \right), \\ &= \frac{1}{Z} \exp \left( \sum_{j=1}^H b_j h_j - \sum_{i=1}^F \frac{x_i^2 + a_i^2 - 2x_i g_i(\mathbf{h}; \boldsymbol{\theta})}{2\sigma_i^2} \right), \end{aligned} \quad (\text{B.9})$$

which will be the base of the other distributions of the hidden units.

### B.2.1 Marginal distribution

The marginal distribution of the hidden units is given by the integral

$$P(\mathbf{h}) = \int d\mathbf{x} P(\mathbf{x}, \mathbf{h}), \quad (\text{B.10})$$

as the visible units can take continuous values. By inserting the expression of the joint probability distribution from equation (B.9), we obtain

$$\begin{aligned} P(\mathbf{h}) &= \frac{1}{Z} \int d\mathbf{x} \exp \left( \sum_{j=1}^H b_j h_j - \sum_{i=1}^F \frac{x_i^2 + a_i^2 - 2x_i g_i(\mathbf{h}; \boldsymbol{\theta})}{2\sigma_i^2} \right), \\ &= \frac{1}{Z} \exp \left( \sum_{j=1}^H b_j h_j \right) \prod_{i=1}^F \int dx_i \exp \left( \frac{x_i^2 + a_i^2 - 2x_i g_i(\mathbf{h}; \boldsymbol{\theta})}{2\sigma_i^2} \right), \\ &= \frac{1}{Z} \exp \left( \sum_{j=1}^H b_j h_j \right) \prod_{i=1}^F \int dx_i \exp \left( \frac{x_i^2 + a_i^2 - 2x_i g_i(\mathbf{h}; \boldsymbol{\theta}) + g_i(\mathbf{h}; \boldsymbol{\theta})^2 - g_i(\mathbf{h}; \boldsymbol{\theta})^2}{2\sigma_i^2} \right), \\ &= \frac{1}{Z} \exp \left( \sum_{j=1}^H b_j h_j \right) \prod_{i=1}^F \int dx_i \exp \left( \frac{(x_i - g_i(\mathbf{h}; \boldsymbol{\theta}))^2 + a_i^2 - g_i(\mathbf{h}; \boldsymbol{\theta})^2}{2\sigma_i^2} \right), \\ &= \frac{1}{Z} \exp \left( \sum_{j=1}^H b_j h_j \right) \prod_{i=1}^F \underbrace{\exp \left( \frac{-a_i^2 + g_i(\mathbf{h}; \boldsymbol{\theta})}{2\sigma_i^2} \right)}_{\sqrt{2\pi\sigma_i^2}} \underbrace{\int dx_i \exp \left( \frac{(x_i - g_i(\mathbf{h}; \boldsymbol{\theta}))^2}{2\sigma_i^2} \right)}_{\sqrt{2\pi\sigma_i^2}}, \\ &= \frac{1}{Z} \exp \left( \sum_{j=1}^H b_j h_j \right) \prod_{i=1}^F \sqrt{2\pi\sigma_i^2} \exp \left( \frac{-a_i^2 + g_i(\mathbf{h}; \boldsymbol{\theta})}{2\sigma_i^2} \right). \end{aligned} \quad (\text{B.11})$$

This is what we have used as the marginal distribution of the hidden units.

### B.2.2 Conditional distribution

The conditional distribution of the hidden units is given by

$$P(\mathbf{x}|\mathbf{h}) = \frac{P(\mathbf{x}, \mathbf{h})}{P(\mathbf{h})}, \quad (\text{B.12})$$

where the numerator is the joint probability distribution given in equation (B.9) and the denominator is the marginal distribution of the hidden units given in equation (B.11). This gives the conditional probability

$$\begin{aligned}
 P(\mathbf{x}|\mathbf{h}) &= \frac{\frac{1}{Z} \exp\left(\sum_{j=1}^H b_j h_j - \sum_{i=1}^F \frac{x_i^2 + a_i^2 - 2x_i g_i(\mathbf{h}; \boldsymbol{\theta})}{2\sigma_i^2}\right)}{\frac{1}{Z} \exp\left(\sum_{j=1}^H b_j h_j\right) \prod_{i=1}^F \sqrt{2\pi\sigma_i^2} \exp\left(\frac{-a_i^2 + g_i(\mathbf{h}; \boldsymbol{\theta})}{2\sigma_i^2}\right)}, \\
 &= \prod_{i=1}^F \frac{1}{\sqrt{2\pi\sigma_i^2}} \exp\left(-\frac{x_i^2 + a_i^2 - 2s_i g_i(\mathbf{h}; \boldsymbol{\theta}) - a_i^2 + g_i(\mathbf{h}; \boldsymbol{\theta})}{2\sigma_i^2}\right), \\
 &= \prod_{i=1}^F \frac{1}{\sqrt{2\pi\sigma_i^2}} \exp\left(-\frac{(x_i - g_i(\mathbf{h}; \boldsymbol{\theta}))^2}{2\sigma_i^2}\right), \\
 &= \prod_{i=1}^F \mathcal{N}(x_i; g_i(\mathbf{h}; \boldsymbol{\theta})),
 \end{aligned} \tag{B.13}$$

which is just the joint normal distribution centered around  $g_i(\mathbf{h}; \boldsymbol{\theta}) = a_i + \sum_{j=1}^H b_j h_j$  with  $\sigma_i^2$  as the variance.

## APPENDIX C

# Collection of Results

In this appendix, we present a more or less complete collection of the quantum dot results obtained through our work, including ground state energy and one-body and two-body density profiles. It is meant as a complementary part to substitute the selected results in chapter 11, where the (arguably) most important results are presented and discussed. For that reason, the discussion above covers most of the results also in this appendix, and they will not be discussed further. The raw files, containing energies and standard errors directly from the Abel computer cluster, can be found in Ref. [40]. A complete collection of the plots in this appendix can be found at <https://github.com/evenmn/Master-thesis/plots/>.

We look at four different trial wave function ansätze, included three versions based on the restricted Boltzmann machine. A Slater determinant with the Boltzmann machines as the single-particle functions will be denoted by the RBM ansatz. When adding a simple Jastrow factor to the RBM ansatz, we obtain the RBM+SJ ansatz. We can also add the more complicated Padé-Jastrow factor to the RBM ansatz, obtaining the RBM+PJ ansatz. We have also implemented the *de facto* standard trial wave function ansatz used in electronic structure calculation, the Slater-Jastrow ansatz. This will simply be denoted by the VMC ansatz. We will stick to natural units as discussed in appendix A. A brief recap is that for quantum dots, the energy is given in units of Planck's reduced constant,  $E' = E/\hbar$ , length is scaled as  $x' = x/\sqrt{\hbar/m}$  where  $m$  is the mass of a particle, which implies that the  $d$ -dimensional density,  $\rho_d(\mathbf{r})$ , is given in units of  $(\hbar/m)^{-d/2}$ .

First, the computational time for two- and three-dimensional quantum dots will be listed, which is just the information plotted in figure (11.2). After that, we list the ground state energies obtained for two- and three-dimensional quantum dots with up to  $N = 20$  electrons. This includes the distribution between kinetic energy, harmonic oscillator energy and electron-electron interaction energy. Lastly, we present a complete set of plots of the radial and spatial one-body density and the radial two-body density.

## C.1 CPU time

The CPU-time per iteration was calculated for all the quantum dot systems we have been looking at, i.e. two-dimensional dots containing up to  $N = 90$  electrons and three-dimensional quantum dots containing up to  $N = 70$  electrons. We assume that the CPU-time per iteration is independent of the frequency, such that the times are obtained using a variety of different oscillator frequencies. To make precise estimations of the CPU-time per iteration, all simulations were run with  $M = 2^{20} = 1,048,576$  cycles per iteration on the computer cluster Abel. As not the entire code can be parallelized, and as the processes need to communicate, the parallelism is not 100% efficient and we also need the same number of cores for all the simulations in order to get comparable times. We decided to use 8 nodes à 16 cores, giving 128 parallel processes in total. In order to obtain precise estimates, we performed at least four independent runs for each

system, where the average time over thousands of iterations was calculated automatically by the program. The results can be found in the tables (C.1) and (C.2) for two- and three-dimensional quantum dots, respectively. As we only consider closed-shell dots, the  $N$  in the tables do only include the magic numbers.

**Table C.1:** The CPU time (in seconds) per iteration when simulating two-dimensional quantum dots with  $N = 2, 6, 12, 20, 30, 42, 56, 72$  and  $90$  electrons. The time was clocked for  $M = 2^{20} = 1,048,576$  Monte Carlo cycles, and to get accurate times we took the average over at least four independent runs with thousands of iterations. For more information, see the text.

$N \rightarrow$	2	6	12	20	30	42	56	72	90
RBM	6.05	11.25	20.53	38.99	73.72	130.49	213.47	360.22	856.84
RBM+SJ	7.12	14.07	28.42	63.27	122.93	199.60	349.22	-	-
RBM+PJ	7.26	13.50	27.68	57.09	119.17	212.53	382.13	-	-
VMC	5.11	10.51	20.85	41.20	76.26	137.39	230.63	355.81	544.03

**Table C.2:** The CPU time (in seconds) per iteration when simulating three-dimensional quantum dots with  $N = 2, 8, 20, 40$  and  $70$  electrons. The time was clocked for  $M = 2^{20} = 1,048,576$  Monte Carlo cycles, and to get accurate times we took the average over at least four independent runs with thousands of iterations. For more information, see the text.

$N \rightarrow$	2	8	20	40	70
RBM	7.69	20.92	59.67	171.84	586.39
RBM+SJ	8.95	26.86	94.64	270.92	-
RBM+PJ	8.87	26.36	91.40	293.25	-
VMC	6.70	20.99	62.54	185.65	486.02

## C.2 Ground state energy

In this section, we present the ground state energy for two- and three-dimensional quantum dots with up to  $N = 20$  electrons with frequencies spanning from  $\omega = 0.01$  to  $\omega = 10$ . We also list the distribution between the kinetic energy, harmonic oscillator potential energy and electron-electron interaction potential energy. This serves as another dimension of comparison for the various methods, at the same time as we can check the virial theorem, described in section 2.5. In addition, one can also compare the energy of dots with the same number of electrons, but in different dimensions (for  $N = 2$  and  $N = 20$ ). The kinetic energy will be denoted by  $\langle \hat{T} \rangle$ . For the harmonic oscillator potential, we will use the more general term external potential, and denote it by  $\langle \hat{V}_{\text{ext}} \rangle$ . The electron-electron interaction potential energy, or just the interaction energy, is denoted by  $\langle \hat{V}_{\text{int}} \rangle$ . The total energy is the sum of the kinetic energy, external potential energy and interaction energy,  $E = \langle \hat{T} \rangle + \langle \hat{V}_{\text{ext}} \rangle + \langle \hat{V}_{\text{int}} \rangle$ .

We have created respective tables for each of our four ansätze, which were described in the introduction to this appendix. As we will look at two- and three-dimensional dots, this results in eight tables in total. The first four tables (C.3-C.6) present the energy of the two-dimensional dots, starting from the RBM ansatz and then RBM+SJ, RBM+PJ and VMC. Then we address the three-dimensional dots in the same order in tables (C.7-C.10).

### C.2.1 Two dimensions

**Table C.3:** The ground state energy,  $E$ , of two-dimensional quantum dots with  $N$  electrons and frequency  $\omega$  obtained by the RBM ansatz. In the following columns, the distribution between kinetic,  $\langle \hat{T} \rangle$ , external potential,  $\langle \hat{V}_{\text{ext}} \rangle$ , and interaction,  $\langle \hat{V}_{\text{int}} \rangle$ , energy are presented. The energy is given in units of  $\hbar$  (natural units), and the numbers in parenthesis are the statistical uncertainties in the last digit. For abbreviations see the text.

$N$	$\omega$	$E$	$\langle \hat{T} \rangle$	$\langle \hat{V}_{\text{ext}} \rangle$	$\langle \hat{V}_{\text{int}} \rangle$
2	0.01	0.078643(5)	0.009835(3)	0.031930(8)	0.03688(1)
	0.1	0.4743(1)	0.08102(8)	0.2082(2)	0.1851(2)
	0.28	1.07050(4)	0.20869(2)	0.47103(7)	0.39078(7)
	0.5	1.72293(7)	0.38006(6)	0.75598(1)	0.5869(1)
	1.0	3.0803(2)	0.7919(2)	1.3657(4)	0.9227(3)
	2.0	5.5936(3)	1.6377(4)	2.5507(5)	1.4051(4)
	3.0	7.9859(2)	2.5215(3)	3.6733(4)	1.7910(2)
	5.0	12.6141(2)	4.2752(4)	5.9493(6)	2.3896(3)
	10.0	23.7748(7)	9.063(3)	11.132(4)	3.580(1)
6	0.01	0.7072(5)	0.033(2)	0.2660(4)	0.4080(6)
	0.1	3.7337(5)	0.3251(3)	1.4070(9)	2.002(1)
	0.28	7.9273(9)	0.8684(6)	3.009(1)	4.050(2)
	0.5	12.241(1)	1.611(1)	4.709(2)	5.921(2)
	1.0	20.716(1)	3.391(1)	7.914(3)	9.411(2)
	2.0	36.383(5)	8.311(7)	13.705(8)	14.367(6)
	3.0	49.415(1)	10.309(3)	21.456(4)	17.649(2)
	5.0	76.801(6)	23.50(1)	27.33(1)	25.967(7)
	10.0	137.338(4)	45.25(1)	55.75(1)	36.336(6)
12	0.01	2.5106(8)	0.0682(2)	0.893(1)	1.549(1)
	0.1	12.679(2)	0.8141(7)	4.692(1)	7.173(2)
	0.28	26.564(3)	2.254(2)	9.635(3)	14.675(4)
	0.5	40.442(3)	4.116(2)	14.868(4)	21.458(4)
	1.0	67.614(3)	8.953(3)	25.207(6)	33.455(5)
	2.0	115.214(5)	20.760(6)	43.69(1)	50.764(7)
	3.0	158.145(6)	33.020(8)	59.72(1)	65.407(9)
	5.0	239.527(8)	58.22(1)	93.92(2)	87.39(1)
	10.0	435.36(2)	114.61(2)	200.13(4)	120.62(1)
20	0.01	6.217(2)	0.1236(4)	2.244(2)	3.849(2)
	0.1	32.308(5)	1.708(2)	7.680(4)	22.919(7)
	0.28	63.788(4)	4.443(3)	22.707(6)	36.638(7)
	0.5	96.491(4)	8.144(3)	34.953(8)	53.394(8)
	1.0	159.645(5)	17.12(5)	58.74(5)	83.397(9)
	2.0	269.086(8)	43.262(8)	95.17(2)	130.65(1)
	3.0	362.52(1)	57.005(9)	148.08(2)	157.43(1)
	5.0	551.21(2)	115.12(2)	219.12(4)	216.97(2)
	10.0	961.03(4)	260.2(1)	364.8(1)	336.06(7)

**Table C.4:** The ground state energy,  $E$ , of two-dimensional quantum dots with  $N$  electrons and frequency  $\omega$  obtained by the RBM+SJ ansatz. In the following columns, the distribution between kinetic,  $\langle \hat{T} \rangle$ , external potential,  $\langle \hat{V}_{\text{ext}} \rangle$ , and interaction,  $\langle \hat{V}_{\text{int}} \rangle$ , energy are presented. The energy is given in units of  $\hbar$  (natural units), and the numbers in parenthesis are the statistical uncertainties in the last digit. For abbreviations see the text.

$N$	$\omega$	$E$	$\langle \hat{T} \rangle$	$\langle \hat{V}_{\text{ext}} \rangle$	$\langle \hat{V}_{\text{int}} \rangle$
2	0.01	0.074940(4)	0.007688(2)	0.029945(7)	0.037307(8)
	0.1	0.44856(1)	0.07620(2)	0.19318(4)	0.17918(4)
	0.28	1.03470(7)	0.2163(1)	0.4547(2)	0.3637(2)
	0.5	1.67636(8)	0.3967(2)	0.7366(3)	0.5430(2)
	1.0	3.02108(5)	0.8139(1)	1.3548(2)	0.8524(1)
	2.0	5.5254(1)	1.6572(3)	2.5447(5)	1.3234(3)
	3.0	7.9103(2)	2.5627(7)	3.664(1)	1.6840(5)
	5.0	12.5322(2)	4.369(1)	5.890(2)	2.2838(7)
	10.0	23.6773(3)	9.062(3)	11.208(3)	3.408(1)
6	0.01	0.7006(3)	0.0376(2)	0.2467(4)	0.4163(4)
	0.1	3.63825(9)	0.23798(6)	1.3992(2)	1.3992(2)
	0.28	7.7313(2)	0.7703(1)	2.9608(4)	4.0002(4)
	0.5	11.9392(5)	1.4801(5)	4.678(1)	5.781(1)
	1.0	20.3393(8)	3.308(1)	7.983(2)	9.048(2)
	2.0	35.2446(8)	7.098(2)	14.587(3)	13.560(2)
	3.0	49.050(1)	11.164(3)	20.6469(5)	17.240(3)
	5.0	75.116(1)	19.661(5)	32.283(7)	23.172(3)
	10.0	136.331(2)	41.65(1)	60.53(1)	34.152(5)
12	0.01	2.4950(5)	0.07(2)	0.845(4)	1.58(2)
	0.1	12.5964(7)	0.4520(4)	4.644(1)	7.500(1)
	0.28	26.051(1)	1.7307(6)	9.668(2)	14.652(2)
	0.5	39.6340(7)	3.4852(5)	14.948(2)	21.201(2)
	1.0	66.1898(8)	7.8777(8)	25.822(2)	32.490(2)
	2.0	112.502(2)	18.118(4)	44.118(4)	50.201(6)
	3.0	154.521(3)	28.050(5)	63.84(1)	62.634(6)
	5.0	234.110(6)	52.86(1)	94.50(2)	86.75(1)
	10.0	415.384(7)	108.57(2)	181.90(3)	124.92(1)
20	0.01	6.239(2)	0.1372(6)	2.184(2)	3.919(3)
	0.1	30.624(3)	1.487(2)	10.893(5)	18.243(5)
	0.28	62.786(3)	3.190(2)	22.782(7)	36.814(6)
	0.5	94.755(3)	6.709(2)	34.845(7)	53.200(6)
	1.0	156.816(4)	15.340(3)	59.931(9)	81.545(7)
	2.0	265.66(9)	39.31(8)	95.78(1)	130.57(2)
	3.0	360.630(6)	58.36(1)	141.54(2)	160.72(2)
	5.0	543.06(1)	112.38(2)	210.52(4)	220.15(2)
	10.0	952.71(2)	237.65(4)	392.06(7)	323.00(3)

**Table C.5:** The ground state energy,  $E$ , of two-dimensional quantum dots with  $N$  electrons and frequency  $\omega$  obtained by the RBM+PJ ansatz. In the following columns, the distribution between kinetic,  $\langle \hat{T} \rangle$ , external potential,  $\langle \hat{V}_{\text{ext}} \rangle$ , and interaction,  $\langle \hat{V}_{\text{int}} \rangle$ , energy are presented. The energy is given in units of  $\hbar$  (natural units), and the numbers in parenthesis are the statistical uncertainties in the last digit. For abbreviations see the text.

$N$	$\omega$	$E$	$\langle \hat{T} \rangle$	$\langle \hat{V}_{\text{ext}} \rangle$	$\langle \hat{V}_{\text{int}} \rangle$
2	0.01	0.074107(8)	0.01031(3)	0.02703(4)	0.03677(3)
	0.1	0.440975(8)	0.09223(9)	0.1757(1)	0.17304(9)
	0.28	1.021668(7)	0.2468(1)	0.4258(2)	0.3490(1)
	0.5	1.659637(6)	0.4305(2)	0.7112(2)	0.5179(2)
	1.0	2.999587(5)	0.8440(3)	1.3418(3)	0.8238(2)
	2.0	5.49475(1)	1.7234(4)	2.4657(4)	1.3057(3)
	3.0	7.87961(1)	2.3144(5)	3.9349(6)	1.6413(3)
	5.0	12.49832(1)	3.9569(7)	6.3068(8)	2.2347(4)
	10.0	23.65275(7)	9.228(3)	11.059(3)	3.366(1)
6	0.01	0.6932(5)	0.031(2)	0.260(2)	0.401(1)
	0.1	3.5700(2)	0.3494(3)	1.2805(9)	1.9401(8)
	0.28	7.6203(2)	0.9519(6)	2.82(1)	3.84(1)
	0.5	11.8074(2)	1.7018(7)	4.513(1)	5.5927(9)
	1.0	20.1832(1)	3.428(1)	8.068(1)	8.687(1)
	2.0	35.0872(3)	7.670(2)	14.139(3)	13.279(2)
	3.0	48.9157(8)	10.789(5)	20.383(5)	17.743(2)
	5.0	74.9545(5)	20.402(5)	31.744(7)	22.809(3)
	10.0	136.1738(8)	42.66(1)	59.71(1)	33.799(5)
12	0.01	2.5019(4)	0.0699(2)	0.893(1)	1.539(1)
	0.1	12.361(1)	0.797(1)	4.394(3)	7.169(3)
	0.28	25.7461(6)	2.415(1)	9.050(2)	14.281(2)
	0.5	39.2661(6)	4.262(2)	14.277(2)	20.728(2)
	1.0	65.7911(5)	8.537(3)	25.197(4)	32.067(3)
	2.0	111.9426(5)	17.817(3)	46.532(4)	47.593(3)
	3.0	154.206(1)	29.701(6)	60.74(1)	63.763(7)
	5.0	233.633(4)	58.33(1)	84.76(1)	90.537(9)
	10.0	415.943(9)	124.13(2)	157.92(3)	133.89(1)
20	0.01	6.210(1)	0.1208(5)	2.189(2)	3.900(2)
	0.1	30.156(1)	1.574(1)	10.473(3)	18.109(3)
	0.28	62.210(1)	4.657(2)	21.227(4)	36.106(4)
	0.5	94.127(1)	8.249(3)	33.543(5)	52.335(4)
	1.0	156.099(1)	16.768(6)	58.513(8)	80.818(6)
	2.0	262.598(1)	34.758(6)	108.546(9)	119.293(7)
	3.0	359.072(4)	60.75(2)	140.51(4)	157.82(2)
	5.0	539.13(1)	120.09(2)	188.45(2)	230.58(1)
	10.0	947.33(2)	257.67(5)	348.35(6)	341.31(3)

**Table C.6:** The ground state energy,  $E$ , of two-dimensional quantum dots with  $N$  electrons and frequency  $\omega$  obtained by the VMC ansatz. In the following columns, the distribution between kinetic,  $\langle \hat{T} \rangle$ , external potential,  $\langle \hat{V}_{\text{ext}} \rangle$ , and interaction,  $\langle \hat{V}_{\text{int}} \rangle$ , energy are presented. The energy is given in units of  $\hbar$  (natural units), and the numbers in parenthesis are the statistical uncertainties in the last digit. For abbreviations see the text.

$N$	$\omega$	$E$	$\langle \hat{T} \rangle$	$\langle \hat{V}_{\text{ext}} \rangle$	$\langle \hat{V}_{\text{int}} \rangle$
2	0.01	0.074070(8)	0.00947(3)	0.02732(5)	0.03728(4)
	0.1	0.44129(1)	0.09117(9)	0.1789(1)	0.17119(9)
	0.28	1.02192(1)	0.2477(1)	0.4256(2)	0.3487(1)
	0.5	1.65974(1)	0.4346(2)	0.7057(2)	0.5195(2)
	1.0	2.99936(1)	0.8523(3)	1.3149(3)	0.8321(2)
	2.0	5.49689(4)	1.811(2)	2.403(2)	1.283(1)
	3.0	7.88401(4)	2.732(2)	3.500(3)	1.652(1)
	5.0	12.50405(5)	4.619(4)	5.629(4)	2.255(2)
	10.0	23.65035(1)	9.529(1)	10.538(1)	3.583(1)
6	0.01	0.69647(2)	0.02886(1)	0.23363(5)	0.43398(5)
	0.1	3.5695(1)	0.3201(3)	1.2934(6)	1.9560(5)
	0.28	7.6219(1)	0.9105(4)	2.8821(9)	3.8292(7)
	0.5	11.8104(2)	1.6710(7)	4.535(1)	5.6045(9)
	1.0	20.1918(2)	3.405(1)	8.046(1)	8.741(1)
	2.0	35.0734(3)	7.751(2)	13.846(3)	13.476(2)
	3.0	48.8728(4)	12.016(2)	19.682(4)	17.175(2)
	5.0	74.9356(5)	20.796(4)	31.043(6)	23.097(3)
	10.0	136.1522(7)	43.712(9)	58.20(1)	34.240(5)
12	0.01	2.4972(3)	0.05506(2)	0.858(1)	1.584(1)
	0.1	12.29962(9)	0.7524(2)	4.2159(4)	7.3312(4)
	0.28	25.7049(4)	2.090(1)	9.355(2)	14.260(2)
	0.5	39.2421(5)	3.939(2)	14.564(3)	20.739(3)
	1.0	65.7026(4)	9.246(2)	23.079(3)	33.378(3)
	2.0	111.8377(3)	19.678(2)	41.349(3)	50.811(2)
	3.0	154.206(1)	29.701(6)	60.74(1)	63.763(7)
	5.0	232.818(2)	56.157(9)	88.18(1)	88.478(9)
	10.0	415.056(4)	112.99(2)	173.91(3)	128.15(1)
20	0.01	6.2097(8)	0.1005(4)	2.270(3)	3.839(3)
	0.1	30.0403(2)	1.3743(3)	10.206(1)	18.4604(9)
	0.28	62.0755(7)	3.902(2)	22.228(5)	35.946(4)
	0.5	94.0433(9)	7.823(3)	33.938(6)	52.282(5)
	1.0	155.8900(4)	17.921(2)	54.076(3)	83.893(3)
	2.0	262.5339(9)	38.402(3)	95.681(7)	128.451(5)
	3.0	358.927(1)	61.017(5)	133.99(1)	163.924(7)
	5.0	542.680(7)	127.77(2)	177.89(2)	237.12(2)
	10.0	945.596(8)	231.56(4)	389.26(7)	324.77(3)

### C.2.2 Three dimensions

**Table C.7:** The ground state energy,  $E$ , of three-dimensional quantum dots with  $N$  electrons and frequency  $\omega$  obtained by the RBM ansatz. In the following columns, the distribution between kinetic,  $\langle \hat{T} \rangle$ , external potential,  $\langle \hat{V}_{\text{ext}} \rangle$ , and interaction,  $\langle \hat{V}_{\text{int}} \rangle$ , energy are presented. The energy is given in units of  $\hbar$  (natural units), and the numbers in parenthesis are the statistical uncertainties in the last digit. For abbreviations see the text.

$N$	$\omega$	$E$	$\langle \hat{T} \rangle$	$\langle \hat{V}_{\text{ext}} \rangle$	$\langle \hat{V}_{\text{int}} \rangle$
2	0.01	0.85193(5)	0.014853(4)	0.03141(9)	0.03893(1)
	0.1	0.5177(1)	0.1249(1)	0.2065(2)	0.1863(2)
	0.28	1.22565(3)	0.36111(4)	0.51675(7)	0.34779(4)
	0.5	2.0269(1)	0.6595(3)	0.8778(4)	0.4896(2)
	1.0	3.7574(1)	1.3224(5)	1.7215(5)	0.7136(2)
	2.0	7.0870(1)	2.7338(6)	3.3183(7)	1.0350(2)
	3.0	10.2981(2)	3.7507(8)	5.2896(9)	1.2578(2)
	5.0	16.7018(1)	6.211(1)	8.890(1)	1.6012(2)
	10.0	32.2186(2)	7.879(3)	22.306(3)	2.0343(2)
8	0.01	1.1350(1)	0.0626(2)	0.3951(7)	0.6774(7)
	0.1	5.8910(6)	0.6480(6)	2.075(2)	3.168(2)
	0.28	12.650(1)	1.931(1)	4.641(2)	6.078(2)
	0.5	19.680(2)	3.601(2)	7.289(4)	8.786(3)
	1.0	33.305(1)	7.032(2)	12.267(3)	14.006(2)
	2.0	58.889(3)	16.976(4)	19.717(5)	22.195(3)
	3.0	81.648(3)	23.987(6)	31.157(8)	26.504(4)
	5.0	126.03(9)	42.68(6)	47.58(5)	35.77(2)
	10.0	231.410(6)	85.62(2)	95.00(2)	50.789(7)
20	0.01	5.6448(4)	0.1624(4)	1.955(2)	3.527(2)
	0.1	27.9277(5)	1.7925(5)	9.676(2)	16.459(2)
	0.28	57.822(1)	5.240(1)	20.384(4)	32.198(3)
	0.5	87.798(5)	9.635(5)	32.12(1)	46.047(9)
	1.0	147.407(3)	22.085(5)	52.32(1)	73.003(8)
	2.0	250.159(7)	49.76(1)	83.69(2)	116.71(1)
	3.0	335.440(5)	64.59(1)	130.27(2)	140.578(9)
	5.0	524.94(2)	121.39(3)	225.61(5)	177.94(2)
	10.0	1005.24(6)	225.76(5)	552.3(1)	227.20(2)

**Table C.8:** The ground state energy,  $E$ , of three-dimensional quantum dots with  $N$  electrons and frequency  $\omega$  obtained by the RBM+SJ ansatz. In the following columns, the distribution between kinetic,  $\langle \hat{T} \rangle$ , external potential,  $\langle \hat{V}_{\text{ext}} \rangle$ , and interaction,  $\langle \hat{V}_{\text{int}} \rangle$ , energy are presented. The energy is given in units of  $\hbar$  (natural units), and the numbers in parenthesis are the statistical uncertainties in the last digit. For abbreviations see the text.

$N$	$\omega$	$E$	$\langle \hat{T} \rangle$	$\langle \hat{V}_{\text{ext}} \rangle$	$\langle \hat{V}_{\text{int}} \rangle$
2	0.01	0.07994(2)	0.01069(3)	0.03190(8)	0.03735(8)
	0.1	0.50214(3)	0.1178(1)	0.2177(2)	0.1666(1)
	0.28	1.20475(4)	0.3497(2)	0.5326(3)	0.3225(1)
	0.5	2.00371(4)	0.6340(3)	0.9201(4)	0.4496(2)
	1.0	3.73543(4)	1.2801(4)	1.7871(5)	0.6683(2)
	2.0	7.06343(7)	2.7117(7)	3.3574(9)	0.9944(2)
	3.0	10.32289(5)	3.5281(8)	5.6147(9)	1.1801(2)
	5.0	16.7155(1)	7.035(2)	8.035(2)	1.6462(4)
	10.0	32.6045(9)	14.568(4)	15.613(5)	2.4238(6)
8	0.01	1.1371(5)	0.02(1)	0.388(6)	0.73(2)
	0.1	5.7498(4)	0.4107(3)	2.113(1)	3.226(1)
	0.28	12.2492(4)	1.3909(6)	4.756(2)	6.101(1)
	0.5	19.0241(4)	2.7417(9)	7.579(2)	8.704(2)
	1.0	32.7159(6)	6.137(1)	13.440(3)	13.139(2)
	2.0	57.4473(8)	13.451(3)	24.361(5)	19.636(2)
	3.0	80.6370(9)	21.039(5)	34.888(8)	24.710(3)
	5.0	124.955(1)	37.126(9)	54.81(1)	33.020(5)
	10.0	230.149(2)	76.75(2)	105.83(2)	47.560(6)
20	0.01	5.6448(4)	0.1624(4)	1.955(2)	3.527(2)
	0.1	27.470(1)	0.9593(9)	9.711(6)	16.800(5)
	0.28	56.600(1)	3.515(1)	20.616(7)	32.469(6)
	0.5	85.893(1)	7.212(2)	31.722(8)	46.958(7)
	1.0	143.209(2)	16.531(7)	54.86(1)	71.819(7)
	2.0	242.195(2)	37.591(8)	96.36(2)	108.24(1)
	3.0	333.07(6)	53.2(5)	138.0(5)	141.835(9)
	5.0	507.35(1)	119.91(2)	196.89(4)	190.55(2)
	10.0	903.79(2)	253.59(5)	372.83(7)	277.37(3)

**Table C.9:** The ground state energy,  $E$ , of three-dimensional quantum dots with  $N$  electrons and frequency  $\omega$  obtained by the RBM+PJ ansatz. In the following columns, the distribution between kinetic,  $\langle \hat{T} \rangle$ , external potential,  $\langle \hat{V}_{\text{ext}} \rangle$ , and interaction,  $\langle \hat{V}_{\text{int}} \rangle$ , energy are presented. The energy is given in units of  $\hbar$  (natural units), and the numbers in parenthesis are the statistical uncertainties in the last digit. For abbreviations see the text.

$N$	$\omega$	$E$	$\langle \hat{T} \rangle$	$\langle \hat{V}_{\text{ext}} \rangle$	$\langle \hat{V}_{\text{int}} \rangle$
2	0.01	0.079312(6)	0.01283(4)	0.02987(6)	0.03661(4)
	0.1	0.500080(6)	0.1271(1)	0.2085(2)	0.1644(1)
	0.28	1.201710(6)	0.3624(2)	0.5253(3)	0.3140(1)
	0.5	1.999912(5)	0.6515(3)	0.9040(3)	0.4444(1)
	1.0	3.729827(5)	1.2995(4)	1.7688(5)	0.6615(2)
	2.0	7.05785(1)	2.7017(6)	3.3705(6)	0.9856(1)
	3.0	10.31271(4)	3.5410(8)	5.5989(9)	1.1728(2)
	5.0	16.7170(1)	7.012(2)	8.072(2)	1.632(4)
	10.0	32.44255(9)	8.054(3)	22.384(3)	2.0042(2)
8	0.01	1.1346(1)	0.0624(2)	0.3910(7)	0.6812(7)
	0.1	5.8562(9)	0.6134(7)	2.088(2)	3.155(2)
	0.28	12.2056(2)	1.5665(7)	4.605(1)	6.034(1)
	0.5	18.9747(2)	2.972(1)	7.344(2)	8.659(1)
	1.0	32.6820(2)	6.266(2)	13.390(3)	13.026(1)
	2.0	57.4148(3)	13.744(3)	24.205(5)	19.466(2)
	3.0	80.6280(3)	18.35(2)	38.64(2)	23.627(2)
	5.0	124.915(1)	37.61(2)	54.44(2)	32.87(8)
	10.0	230.186(1)	78.64(4)	103.59(5)	47.95(1)
20	0.01	5.6328(3)	0.1621(4)	1.923(2)	3.558(2)
	0.1	27.3382(8)	1.336(3)	9.408(4)	16.595(3)
	0.28	56.4477(6)	4.157(2)	20.124(4)	32.167(4)
	0.5	85.7153(6)	8.028(2)	31.333(6)	46.354(4)
	1.0	142.9409(6)	17.603(3)	54.592(7)	70.746(5)
	2.0	242.1168(8)	38.487(5)	96.23(1)	107.403(7)
	3.0	333.027(1)	49.3(3)	152.1(3)	131.618(7)
	5.0	506.58(1)	130.79(3)	172.35(3)	203.45(2)
	10.0	897.68(2)	273.53(5)	328.64(6)	295.52(3)

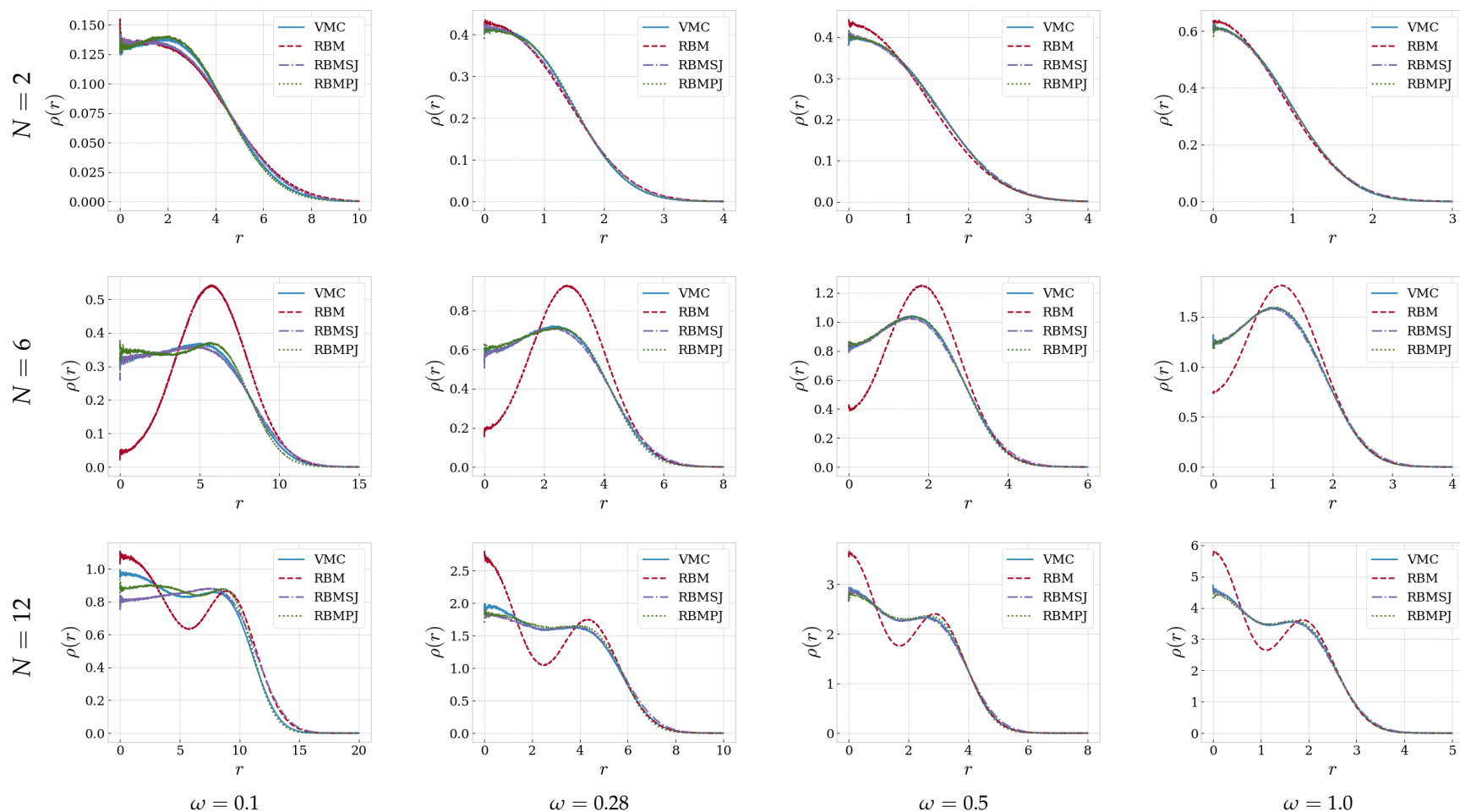
**Table C.10:** The ground state energy,  $E$ , of three-dimensional quantum dots with  $N$  electrons and frequency  $\omega$  obtained by the VMC ansatz. In the following columns, the distribution between kinetic,  $\langle \hat{T} \rangle$ , external potential,  $\langle \hat{V}_{\text{ext}} \rangle$ , and interaction,  $\langle \hat{V}_{\text{int}} \rangle$ , energy are presented. The energy is given in units of  $\hbar$  (natural units), and the numbers in parenthesis are the statistical uncertainties in the last digit. For abbreviations see the text.

$N$	$\omega$	$E$	$\langle \hat{T} \rangle$	$\langle \hat{V}_{\text{ext}} \rangle$	$\langle \hat{V}_{\text{int}} \rangle$
2	0.01	0.079284(6)	0.01221(4)	0.039757(6)	0.036319(4)
	0.1	0.500083(7)	0.1263(1)	0.2082(2)	0.1656(1)
	0.28	1.201752(6)	0.3606(2)	0.5272(3)	0.3140(1)
	0.5	1.999977(5)	0.6517(3)	0.9032(3)	0.4451(1)
	1.0	3.730030(5)	1.3105(4)	1.7551(5)	0.6644(2)
	2.0	7.065911(7)	3.2766(4)	2.6932(5)	1.0961(2)
	3.0	10.31717(1)	3.8365(7)	5.2770(8)	1.2037(2)
	5.0	16.713925(4)	8.1523(8)	6.7797(9)	1.7819(2)
	10.0	32.449053(8)	14.586(2)	15.470(2)	2.3933(2)
8	0.01	1.12283(7)	0.04384(7)	0.3832(2)	0.6958(2)
	0.1	5.7126(1)	0.4930(4)	2.085(1)	3.1342(9)
	0.28	12.2050(2)	1.5332(7)	4.630(2)	6.041(1)
	0.5	18.96747(8)	3.2098(4)	6.7892(8)	8.9647(6)
	1.0	32.6863(2)	6.244(2)	13.378(3)	13.064(1)
	2.0	57.4197(5)	14.344(6)	23.14(1)	19.932(5)
	3.0	80.6193(3)	22.281(5)	33.286(7)	25.052(3)
	5.0	124.9024(4)	38.713(8)	52.89(1)	33.300(4)
	10.0	230.1668(7)	81.03(2)	100.56(2)	48.573(6)
20	0.01	5.6428(3)	0.1621(4)	1.923(2)	3.558(2)
	0.1	27.3152(5)	1.247(1)	9.392(3)	16.676(3)
	0.28	56.4386(5)	3.991(2)	20.125(5)	32.322(4)
	0.5	85.7197(6)	7.868(2)	31.383(6)	46.469(5)
	1.0	142.9561(7)	17.29(2)	54.45(3)	71.218(6)
	2.0	242.0320(6)	42.246(3)	86.317(9)	113.469(6)
	3.0	332.6976(6)	67.976(5)	119.95(1)	144.772(7)
	5.0	509.45(1)	137.93(2)	163.28(3)	208.24(2)
	10.0	902.58(2)	288.99(4)	310.87(5)	302.72(3)

### C.3 One-body density

The one-body density gives the probability of finding a particle at a certain position in the space. We have both calculated the radial one-body density profile and the actual one-body density profile throughout the space. The former contains all the information about the density as long as the distribution is symmetric around the origin, and is a compact and informative way of comparing the various ansätze. However, sometimes the densities are not symmetric around the origin, and then only the spatial profile contains all the information about the density.

The density profiles become identical for two- and three-dimensional quantum dots for the same number of electron shells, and we will for that reason focus on two-dimensional dots. In figure (C.1), we present the plots of radial density profiles of quantum dots with  $N = 2 - 42$  electrons and frequencies  $\omega = 0.1, 0.28, 0.5$  and  $1.0$ . The results were obtained using the ansätze described in the introduction to this appendix. Further, in figures (C.2-C.5), we present the corresponding plots of the spatial density profiles, but the frequency  $\omega = 0.28$  is omitted. Lastly, the plots of the spatial one-body density profile for large quantum dots with frequency  $\omega = 1.0$  and  $N = 30, 42$  and  $56$  electrons is presented in figure (C.6).



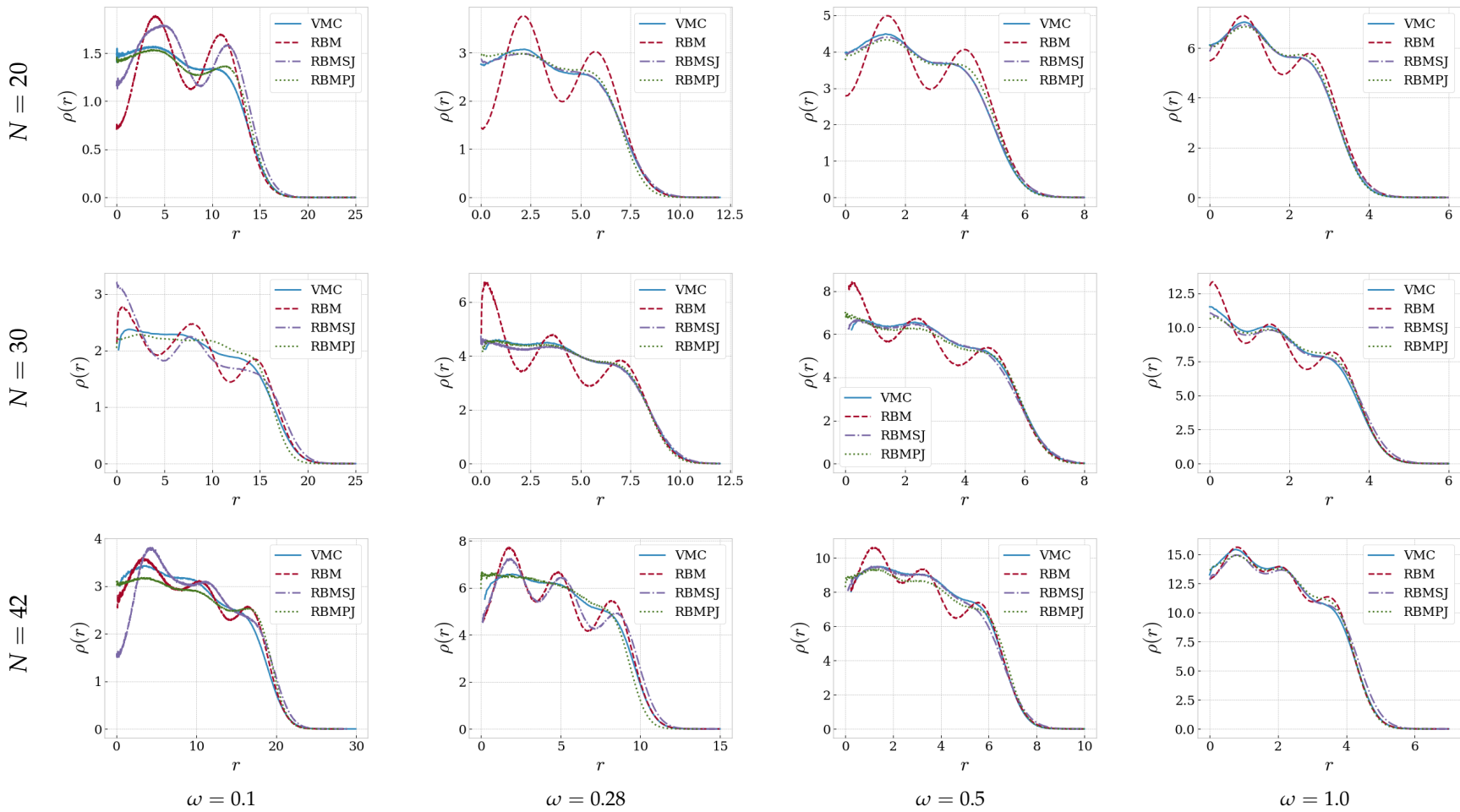


**Figure C.1:** Plots of the one-body density profiles,  $\rho(r)$ , for two-dimensional quantum dots with  $N = 2, 6, 12, 20, 30$  and  $42$  electrons seen from the top and oscillator frequencies  $\omega = 0.1, 0.28, 0.5$  and  $1.0$  from left to right. The ansätze used were RBM, RBM+SJ, RBM+PJ and VMC, the ADAM optimizer was used, and after convergence the number of Monte-Carlo cycles was  $M = 2^{28} = 268,435,456$ . For abbreviations and description of the natural units used, see the text.

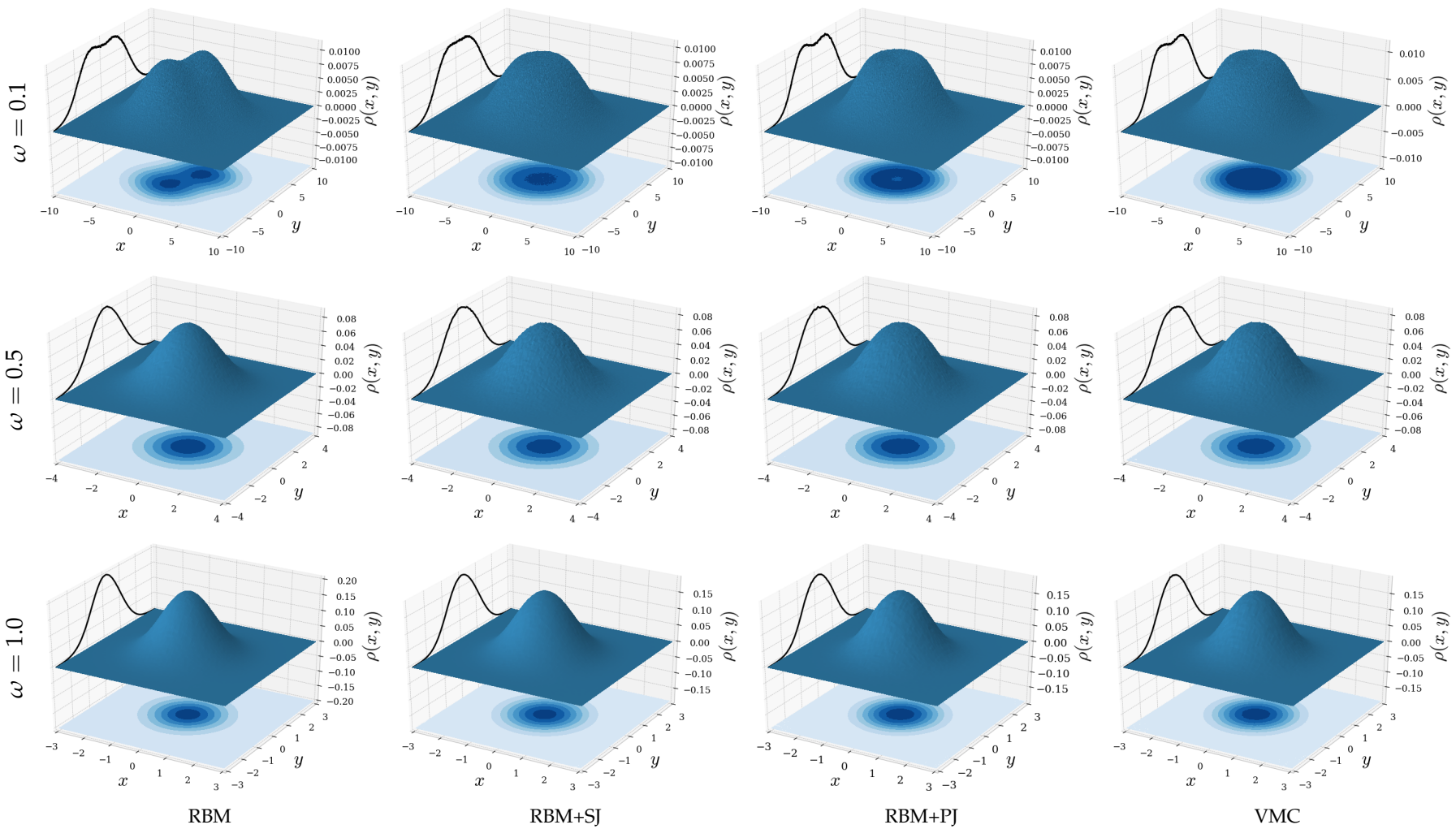


**Figure C.2:** Plots of the one-body density profiles,  $\rho(x, y)$ , for two-dimensional quantum dots with  $N = 2$  electrons and frequencies  $\omega = 0.1, 0.5$  and  $1.0$  seen from the top. The surface plot and the contour plot on the  $xy$ -plane illustrate the density, and the graph on the  $yz$ -plane represents the cross-section through  $x = 0$ . They were obtained using the RBM, RBM+SJ, RBM+PJ and VMC ansätze from left to right, with the ADAM optimizer and  $M = 2^{30} = 1,073,741,824$  Monte Carlo cycles after convergence. The plots are noise-reduced using a Savitzky-Golay filter. For abbreviations and description of the natural units used, see the text.

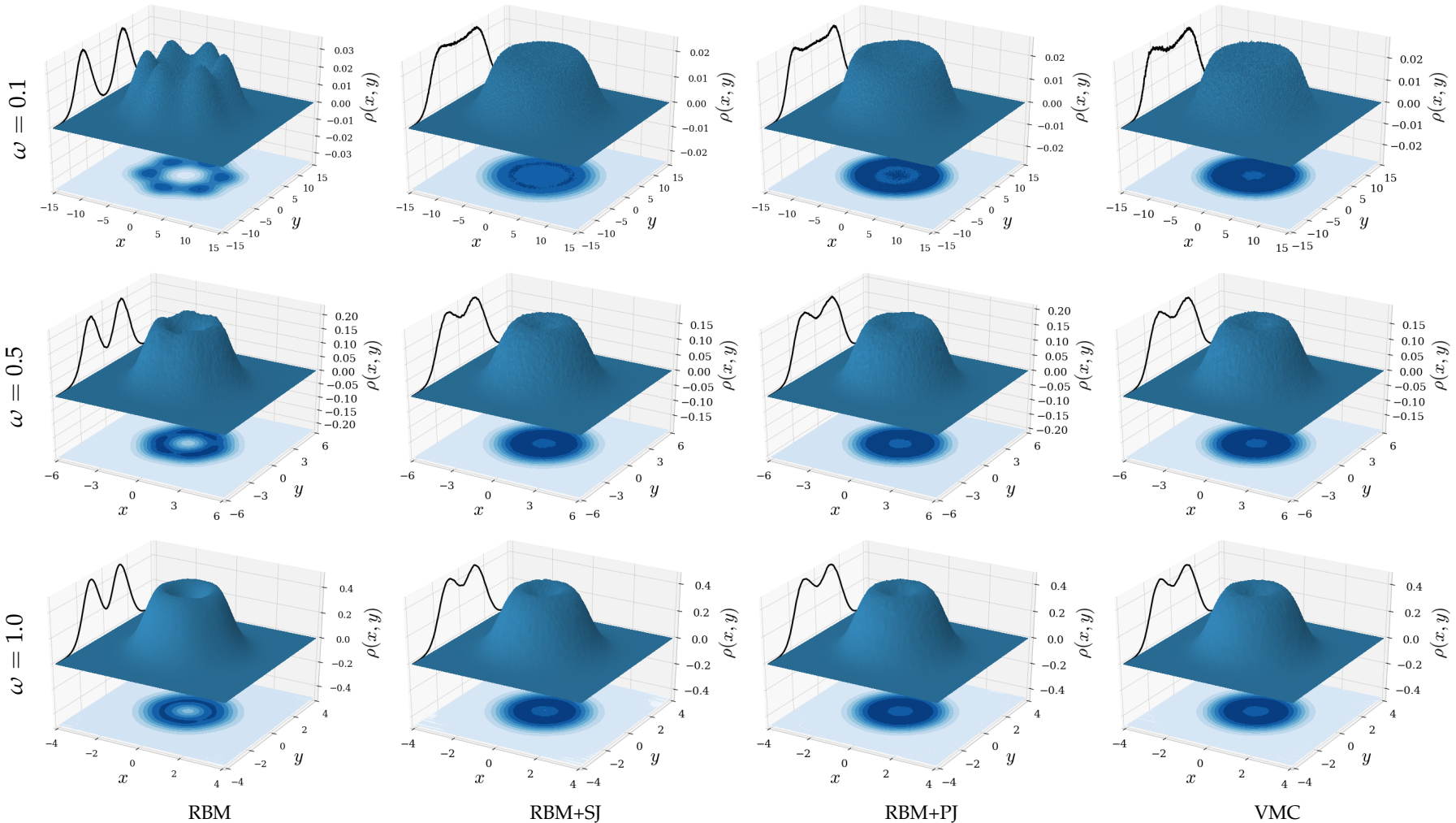


**Figure C.3:** Plots of the one-body density profiles,  $\rho(x, y)$ , for two-dimensional quantum dots with  $N = 6$  electrons and frequencies  $\omega = 0.1, 0.5$  and  $1.0$  seen from the top. The surface plot and the contour plot on the  $xy$ -plane illustrate the density, and the graph on the  $yz$ -plane represents the cross-section through  $x = 0$ . They were obtained using the RBM, RBM+SJ, RBM+PJ and VMC ansätze from left to right, with the ADAM optimizer and  $M = 2^{30} = 1,073,741,824$  Monte Carlo cycles after convergence. The plots are noise-reduced using a Savitzky-Golay filter. For abbreviations and description of the natural units used, see the text.

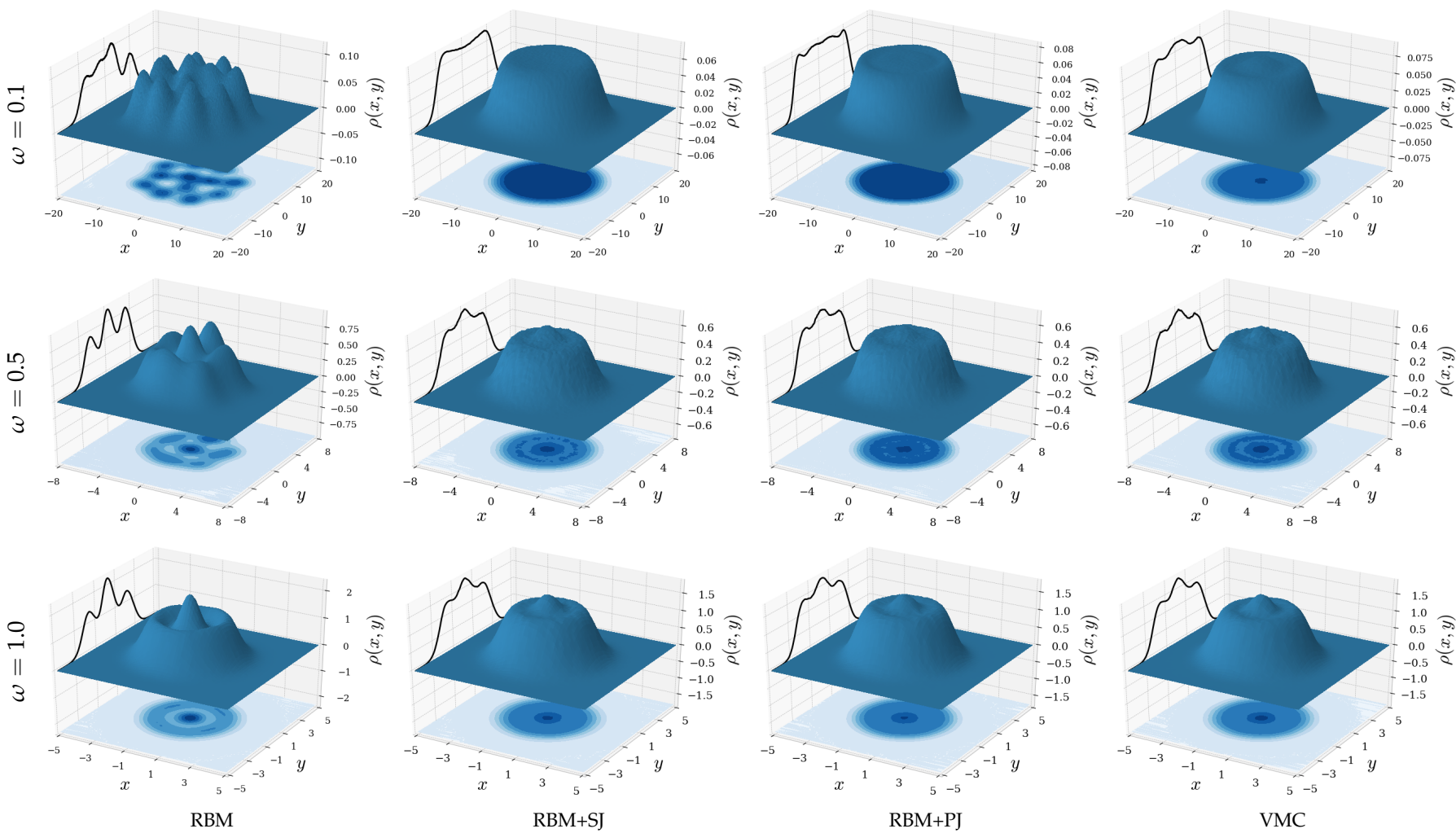


**Figure C.4:** Plots of the one-body density profiles,  $\rho(x,y)$ , for two-dimensional quantum dots with  $N = 12$  electrons and frequencies  $\omega = 0.1, 0.5$  and  $1.0$  seen from the top. The surface plot and the contour plot on the  $xy$ -plane illustrate the density, and the graph on the  $yz$ -plane represents the cross-section through  $x = 0$ . They were obtained using the RBM, RBM+SJ, RBM+PJ and VMC ansätze from left to right, with the ADAM optimizer and  $M = 2^{30} = 1,073,741,824$  Monte Carlo cycles after convergence. The plots are noise-reduced using a Savitzky-Golay filter. For abbreviations and description of the natural units used, see the text.

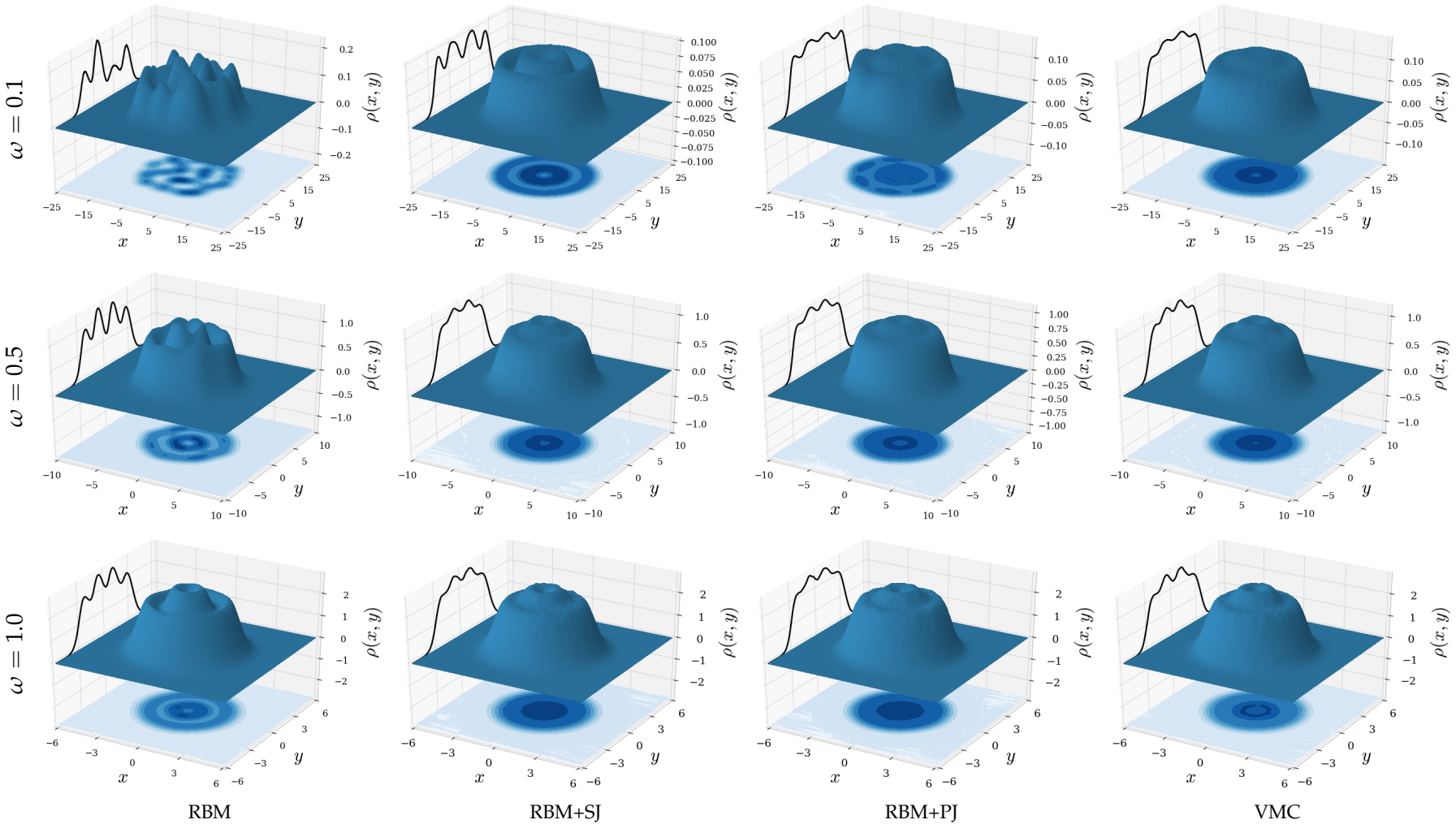


**Figure C.5:** Plots of the one-body density profiles,  $\rho(x,y)$ , for two-dimensional quantum dots with  $N = 20$  electrons and frequencies  $\omega = 0.1, 0.5$  and  $1.0$  seen from the top. The surface plot and the contour plot on the  $xy$ -plane illustrate the density, and the graph on the  $yz$ -plane represents the cross-section through  $x = 0$ . They were obtained using the RBM, RBM+SJ, RBM+PJ and VMC ansätze from left to right, with the ADAM optimizer and  $M = 2^{30} = 1,073,741,824$  Monte Carlo cycles after convergence. The plots are noise-reduced using a Savitzky-Golay filter. For abbreviations and description of the natural units used, see the text.

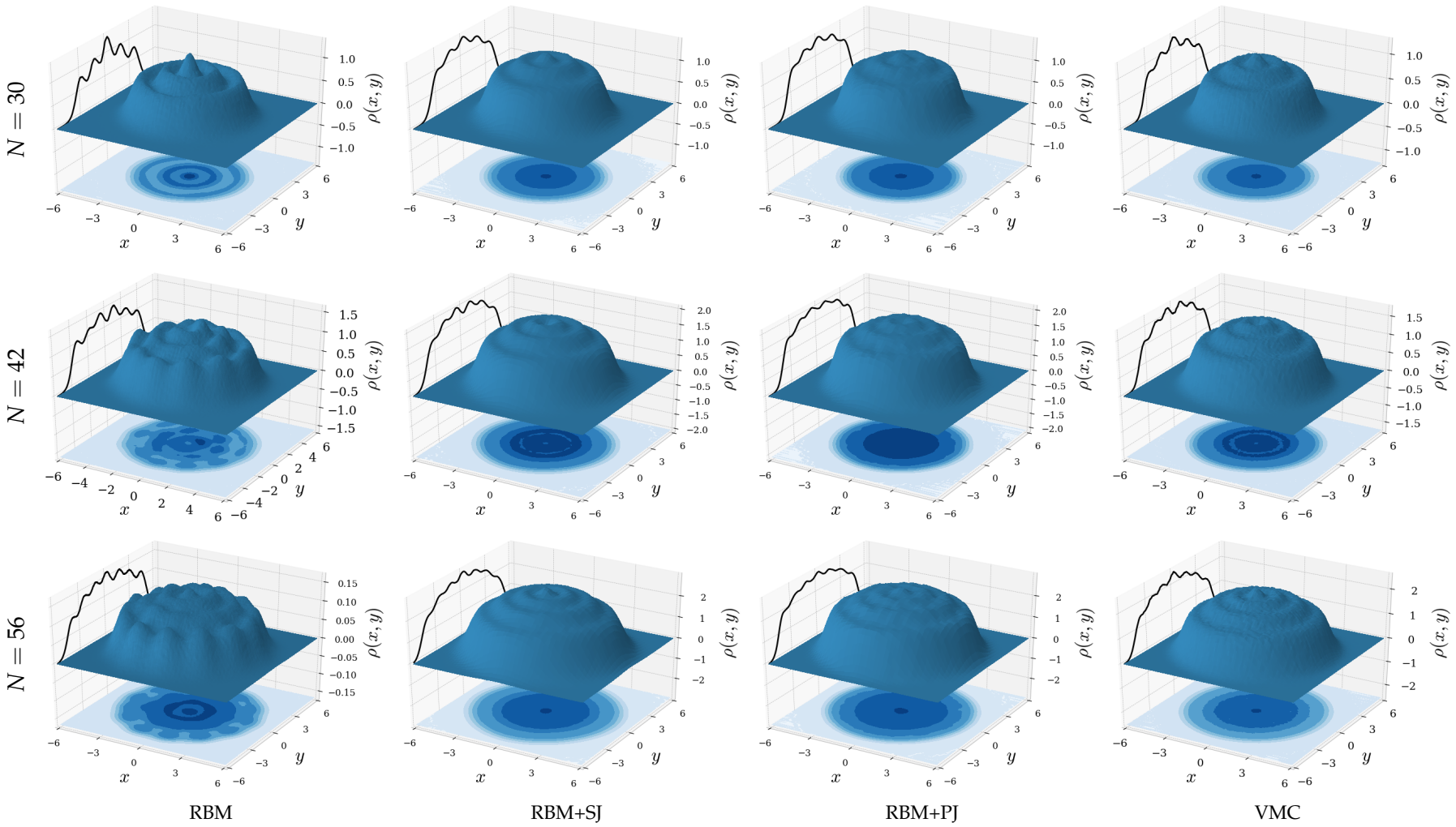
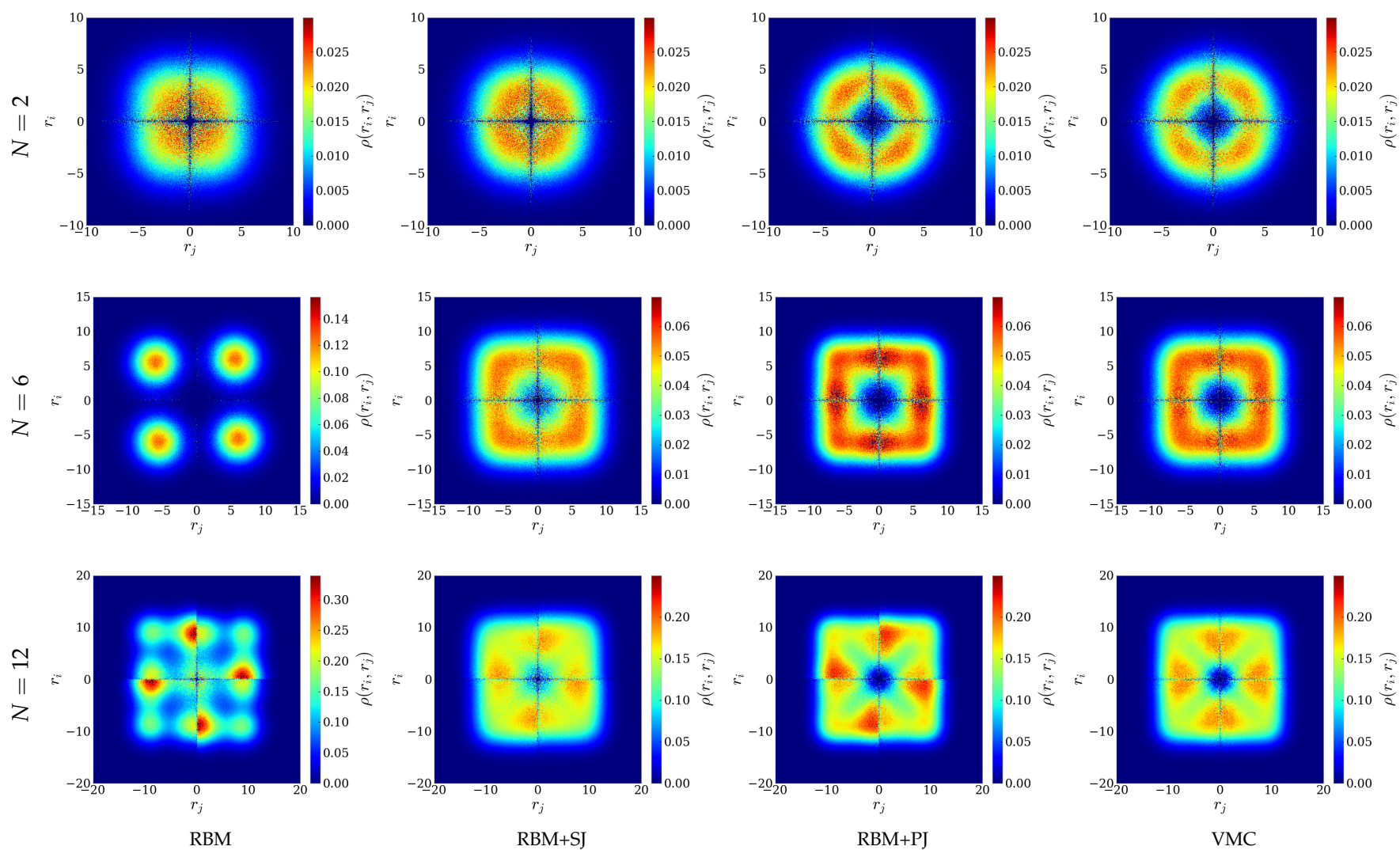


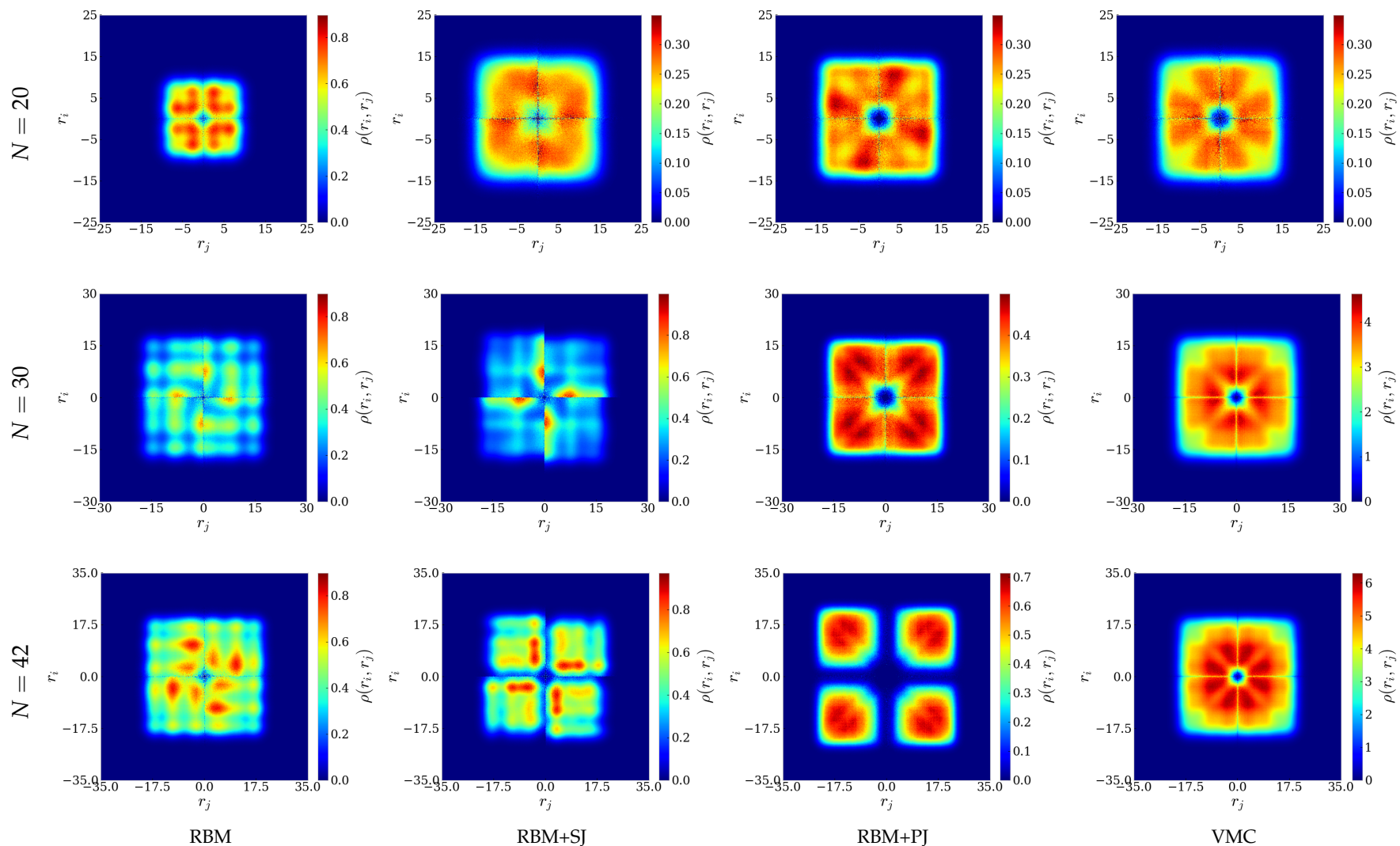
**Figure C.6:** Plots of the one-body density profiles,  $\rho(x, y)$ , for two-dimensional quantum dots with frequency  $\omega = 1.0$  and  $N = 20, 30$  and  $42$  electrons seen from the top. The surface plot and the contour plot on the  $xy$ -plane illustrate the density, and the graph on the  $yz$ -plane represents the cross-section through  $x = 0$ . They were obtained using the RBM, RBM+SJ, RBM+PJ and VMC ansätze from left to right, with the ADAM optimizer and  $M = 2^{30} = 1,073,741,824$  Monte Carlo cycles after convergence. The plots are noise-reduced using a Savitzky-Golay filter. For abbreviations and description of the natural units used, see the text.

## C.4 Two-body density plots

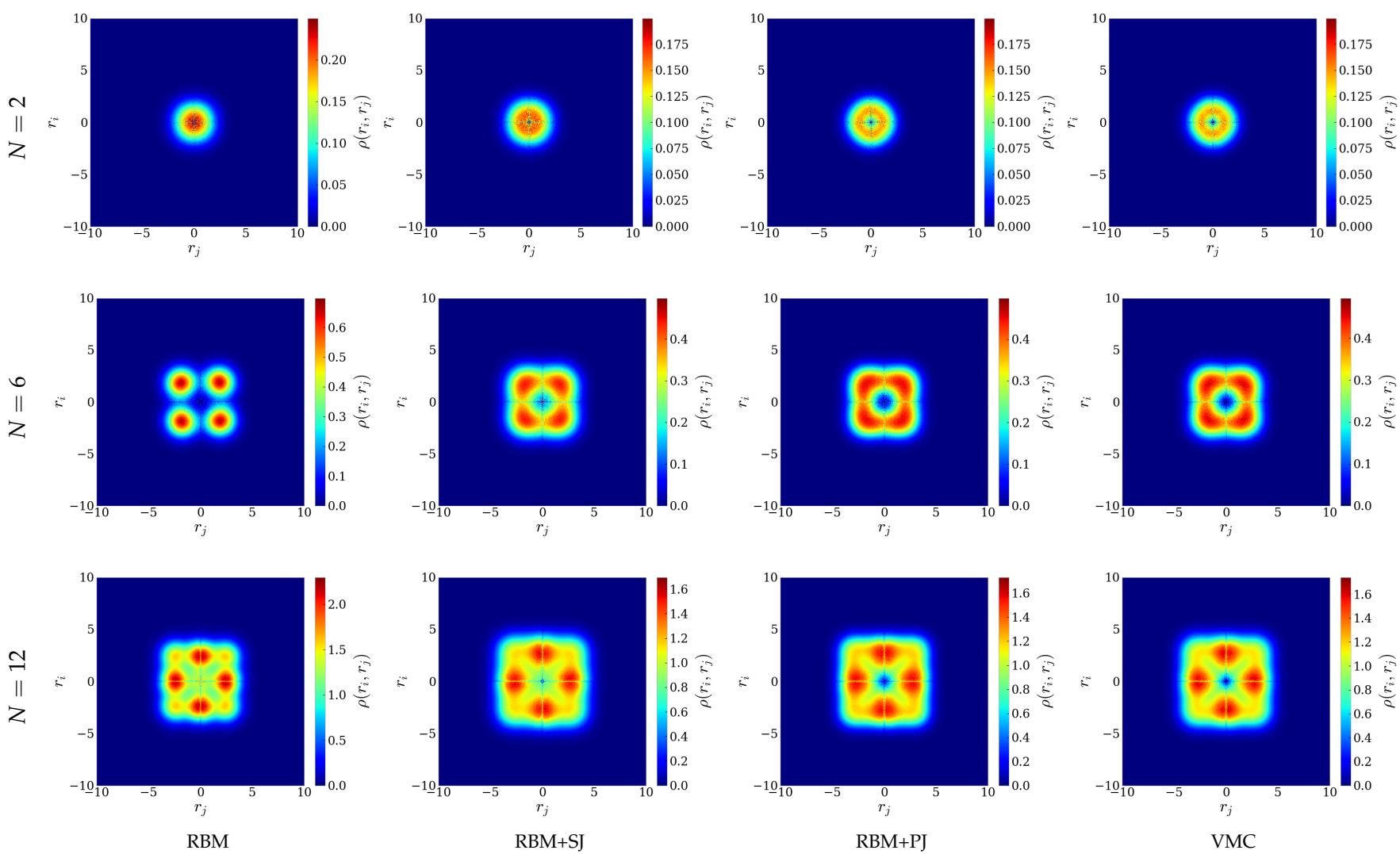
The two-body density gives the probability of finding a particle at a certain position in space, given the position of another particle. Similarly to the one-body density, it is possible to calculate both the radial two-body density profile and the spatial two-body density profile. However, since it is hard to visualize the spatial density, as it turns out to be a higher-dimensional object, we keep our focus on the radial profile. The density becomes identical for two- and three-dimensional quantum dots of same number of electron shells, and we therefore focus on the two-dimensional case.

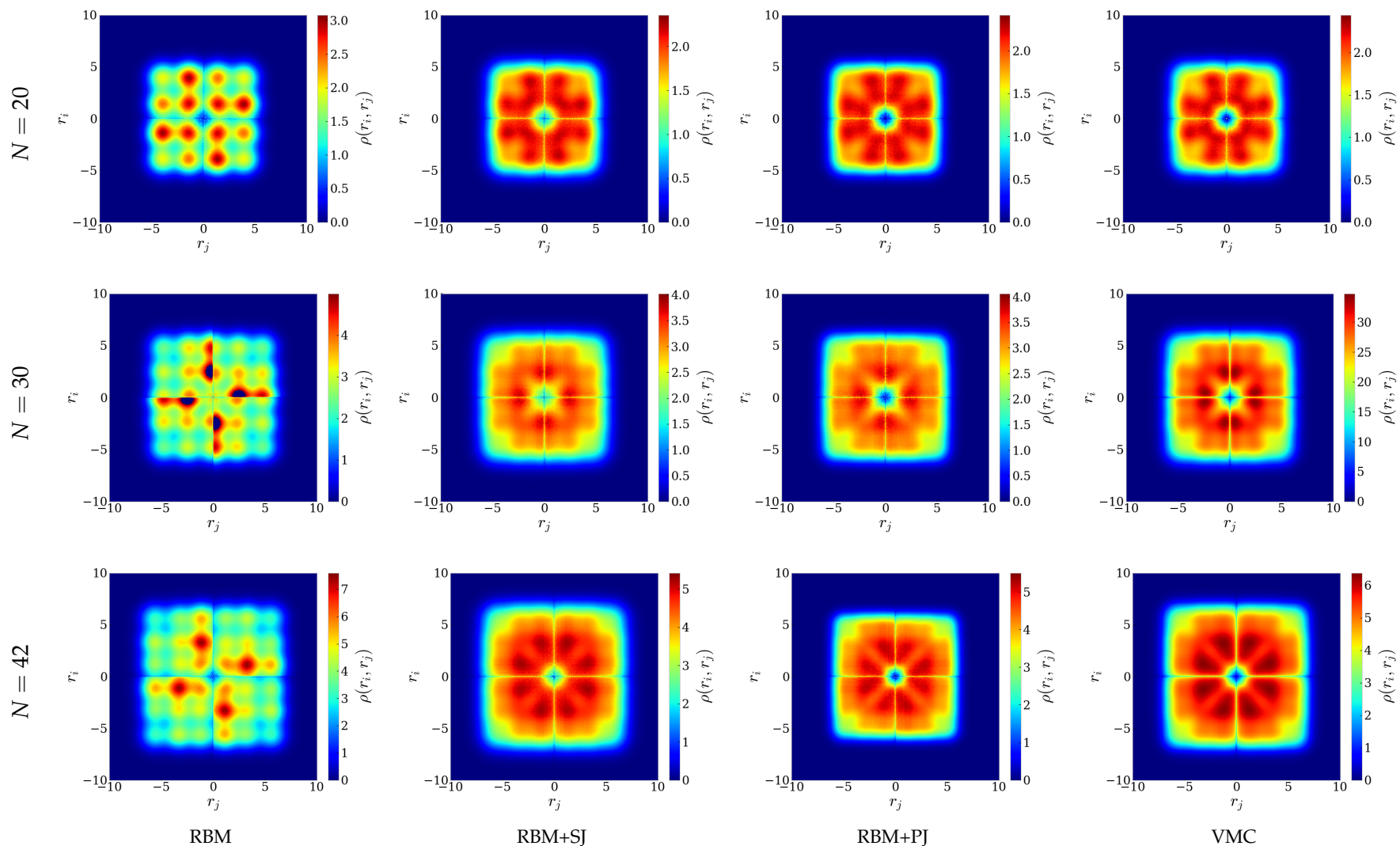
In figures (C.7-C.9), we present the two-body density for quantum dots with  $N = 2, 6, 12, 20, 30$  and  $42$  electrons and the frequencies  $\omega = 0.1, 0.5$  and  $1.0$ , respectively.



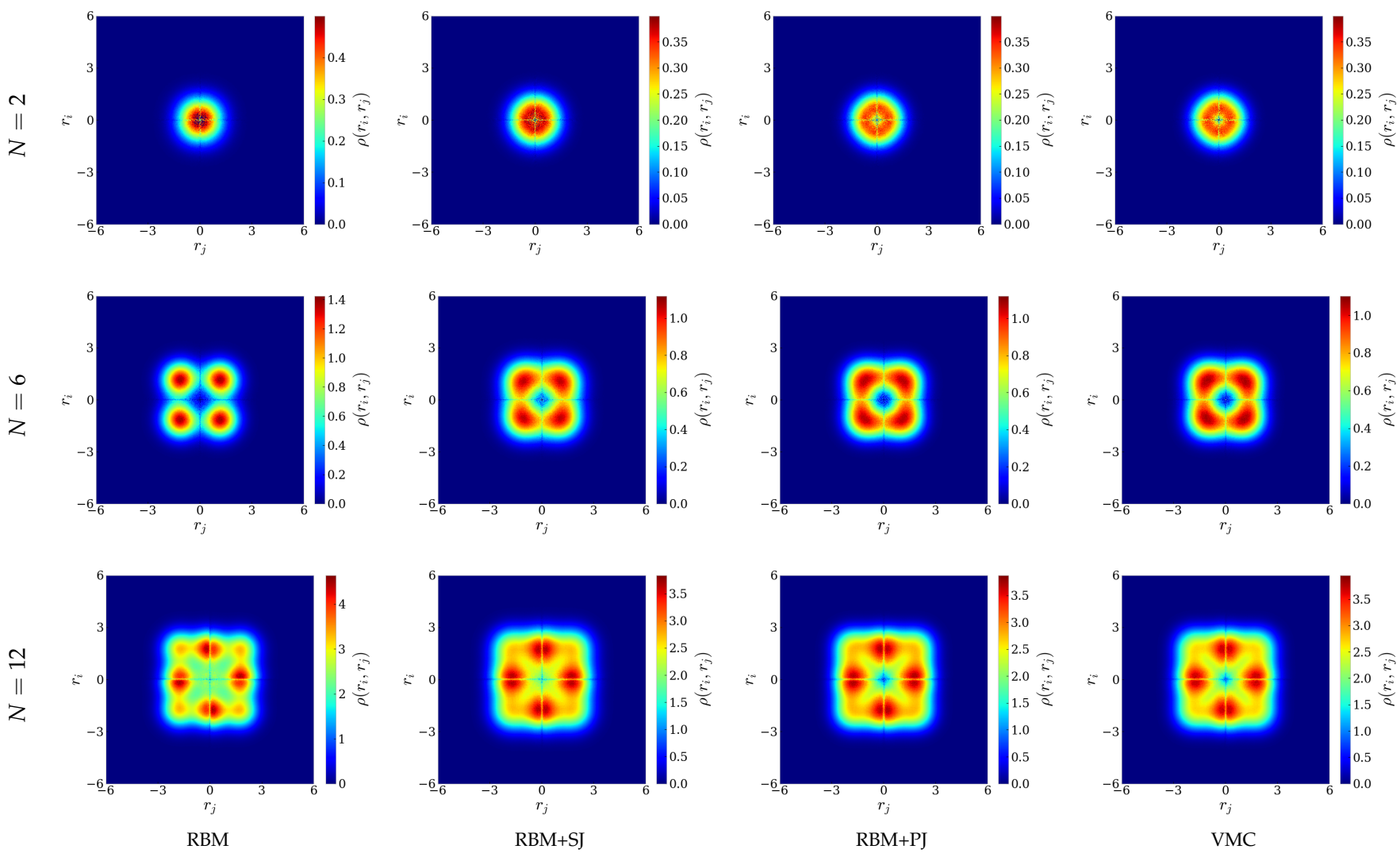


**Figure C.7:** Plots of the radial two-body density profiles,  $\rho(r_i, r_j)$ , for two-dimensional quantum dots with  $N = 2, 6, 12, 20, 30$  and  $42$  electrons seen from the top and oscillator frequency  $\omega = 0.1$ . The RBM, RBM+SJ, RBM+PJ and VMC ansätze (from the left) were used, with the ADAM optimizer and  $M = 2^{28} = 268,435,456$  Monte-Carlo cycles after convergence. For abbreviations and description of the natural units used, see the text.





**Figure C.8:** Plots of the radial two-body density profiles,  $\rho(r_i, r_j)$ , for two-dimensional quantum dots with  $N = 2, 6, 12, 20, 30$  and  $42$  electrons seen from the top and oscillator frequency  $\omega = 0.5$ . The RBM, RBM+SJ, RBM+PJ and VMC ansätze (from the left) were used, with the ADAM optimizer and  $M = 2^{28} = 268,435,456$  Monte-Carlo cycles after convergence. For abbreviations and description of the natural units used, see the text.



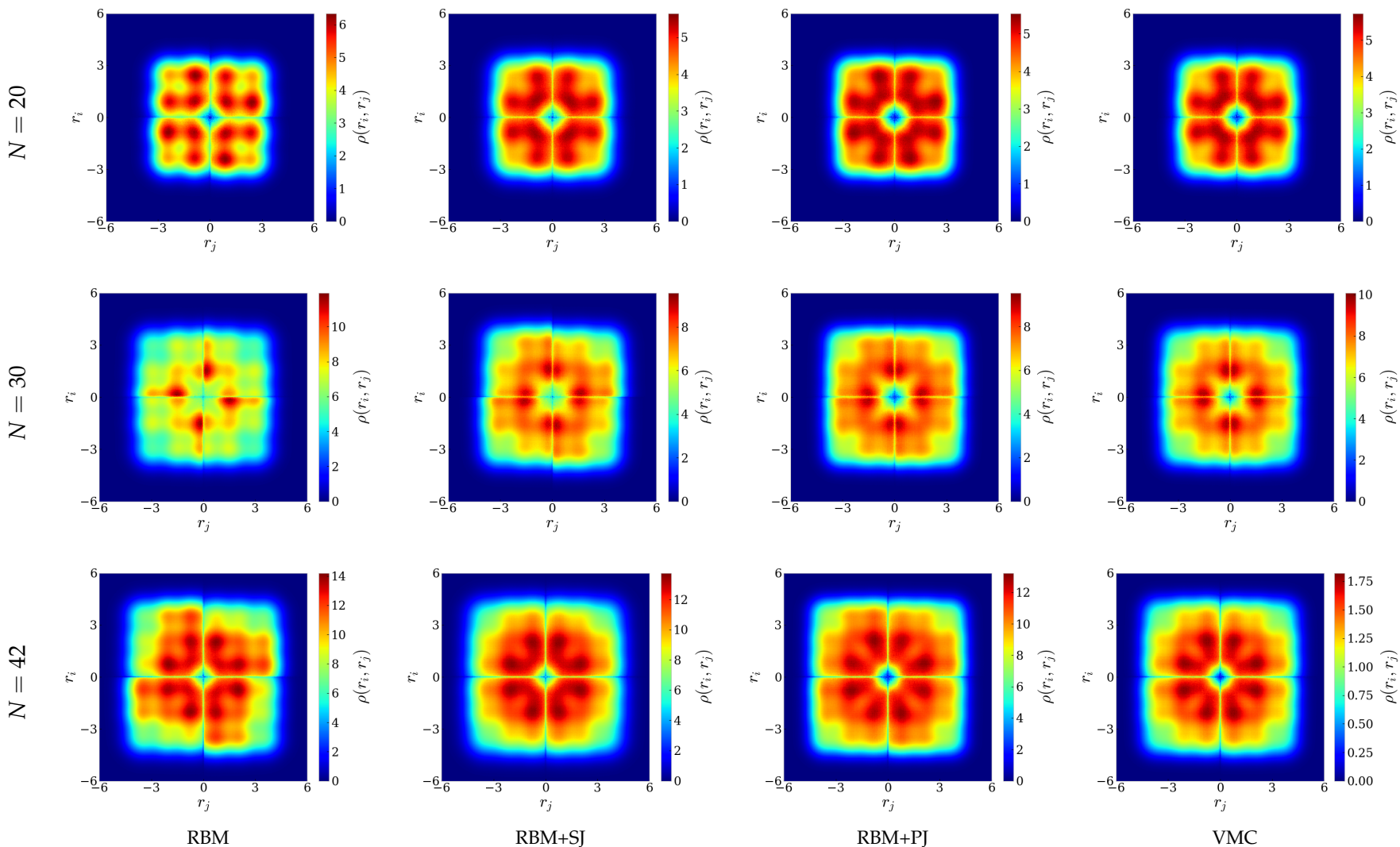


**Figure C.9:** Plots of the radial two-body density profiles,  $\rho(r_i, r_j)$ , for two-dimensional quantum dots with  $N = 2, 6, 12, 20, 30$  and  $42$  electrons seen from the top and oscillator frequency  $\omega = 1.0$ . The RBM, RBM+SJ, RBM+PJ and VMC ansätze (from the left) were used, with the ADAM optimizer and  $M = 2^{28} = 268,435,456$  Monte-Carlo cycles after convergence. For abbreviations and description of the natural units used, see the text.



## Bibliography: Articles

2. Hunter, J. D. Matplotlib: A 2D Graphics Environment. *Computing in Science Engineering* **9**, 90 (2007).
3. Troyer, M. & Wiese, U.-J. Computational Complexity and Fundamental Limitations to Fermionic Quantum Monte Carlo Simulations. *Physical Review Letters* **94**, 170201 (2005).
4. Drummond, N. D., Towler, M. D. & Needs, R. J. Jastrow correlation factor for atoms, molecules, and solids. *Physical Review B* **70**, 235119 (2004).
5. Ghosal, A., Güçlü, A. D., Umrigar, C. J., Ullmo, D. & Baranger, H. U. Incipient Wigner localization in circular quantum dots. *Physical Review B* **76**, 085341 (2007).
6. Reimann, S. M. & Manninen, M. Electronic structure of quantum dots. *Reviews of Modern Physics* **74**, 1283 (2002).
7. Wang, J., Polizzi, E. & Lundstrom, M. A three-dimensional quantum simulation of silicon nanowire transistors with the effective-mass approximation. *Journal of Applied Physics* **96**, 2192 (2004).
8. DuBois, J. L. & Glyde, H. R. Bose-Einstein condensation in trapped bosons: A variational Monte Carlo analysis. *Physical Review A* **63**, 023602 (2001).
9. Odom, B., Hanneke, D., D'Urso, B. & Gabrielse, G. New Measurement of the Electron Magnetic Moment Using a One-Electron Quantum Cyclotron. *Physical Review Letters* **97**, 030801 (2006).
10. Dirac, P. A. M. & Fowler, R. H. Quantum mechanics of many-electron systems. *Proceedings of the Royal Society A* **123**, 714 (1929).
11. Hartree, D. R. The Wave Mechanics of an Atom with a Non-Coulomb Central Field. Part II. Some Results and Discussion. *Mathematical Proceedings of the Cambridge Philosophical Society* **24**, 111 (1928).
12. Fock, V. „Selfconsistent field“ mit Austausch für Natrium. *Zeitschrift für Physik* **62**, 795 (1930).
14. Bajdich, M. & Mitas, L. Electronic structure quantum Monte Carlo. *Acta Physica Slovaca* **59**, 81 (2010).
15. Dubé, J.-P. & Misra, S. Scalable Price Targeting. *National Bureau of Economic Research* (2017).
16. Chernova, S. & Veloso, M. Interactive Policy Learning through Confidence-Based Autonomy. *Journal of Artificial Intelligence Research* **34**, 1 (2009).
17. Krizhevsky, A., Sutskever, I. & Hinton, G. E. ImageNet Classification with Deep Convolutional Neural Networks. *Advances in Neural Information Processing Systems* **25**, 1097 (2012).
18. Alom, Z. *et al.* The History Began from AlexNet: A Comprehensive Survey on Deep Learning Approaches. arXiv: [1803.01164](https://arxiv.org/abs/1803.01164) (2018).

19. Wu, Y. *et al.* Google’s Neural Machine Translation System: Bridging the Gap between Human and Machine Translation. arXiv: [1609.08144](https://arxiv.org/abs/1609.08144) (2016).
22. Silver, D. *et al.* Mastering the game of Go with deep neural networks and tree search. *Nature* **529**, 484 (2016).
23. Silver, D. *et al.* Mastering Chess and Shogi by Self-Play with a General Reinforcement Learning Algorithm. arXiv: [1712.01815](https://arxiv.org/abs/1712.01815) (2017).
24. Carleo, G. & Troyer, M. Solving the Quantum Many-Body Problem with Artificial Neural Networks. *Science* **355**, 602 (2017).
25. Pfau, D., Spencer, J. S., Matthews, A. G. G. & Foulkes, W. M. C. Ab-Initio Solution of the Many-Electron Schrödinger Equation with Deep Neural Networks. arXiv: [1909.02487](https://arxiv.org/abs/1909.02487) (2019).
29. Manders, J. R. *et al.* 8.3: Distinguished Paper: Next-Generation Display Technology: Quantum-Dot LEDs. *SID Symposium Digest of Technical Papers* **46**, 73 (2015).
30. Marzin, J. Y., Gérard, J. M., Izraël, A., Barrier, D. & Bastard, G. Photoluminescence of Single InAs Quantum Dots Obtained by Self-Organized Growth on GaAs. *Physical Review Letters* **73**, 716 (1994).
31. Brunner, K., Abstreiter, G., Böhm, G., Tränkle, G. & Weimann, G. Sharp-Line Photoluminescence and Two-Photon Absorption of Zero-Dimensional Biexcitons in a GaAs/AlGaAs Structure. *Physical Review Letters* **73**, 1138 (1994).
32. Metropolis, N. & Ulam, S. The Monte Carlo Method. *Journal of the American Statistical Association* **44**, 335 (1949).
33. Ceperley, D. & Alder, B. Quantum Monte Carlo. *Science* **231**, 555 (1986).
34. Kalos, M. H. Monte Carlo Calculations of the Ground State of Three- and Four-Body Nuclei. *Physical Review* **128**, 1791 (1962).
35. Hastings, W. K. Monte Carlo sampling methods using Markov chains and their applications. en. *Biometrika* **57**, 97 (1970).
42. Moreau, P. A. *et al.* Imaging Bell-type nonlocal behavior. *Science Advances* **5**, aaw2563 (2019).
43. Schrödinger, E. An Undulatory Theory of the Mechanics of Atoms and Molecules. *Physical Review* **28**, 1049 (1926).
44. Born, M. Zur Quantenmechanik der Stoßvorgänge. *Zeitschrift für Physik* **37**, 863 (1926).
45. Heisenberg, W. Über quantentheoretische Umdeutung kinematischer und mechanischer Beziehungen. *Zeitschrift für Physik* **33**, 879 (1925).
46. Einstein, A., Podolsky, B. & Rosen, N. Can Quantum-Mechanical Description of Physical Reality Be Considered Complete? *Physical Review* **47**, 777 (1935).
49. Ehrenfest, P. Bemerkung über die angenäherte Gültigkeit der klassischen Mechanik innerhalb der Quantenmechanik. *Zeitschrift für Physik* **45**, 455 (1927).
50. Taut, M. Two electrons in an external oscillator potential: Particular analytic solutions of a Coulomb correlation problem. *Physical Review A* **48**, 3561 (1993).
51. Taut, M. Two electrons in a homogeneous magnetic field: particular analytical solutions. *Journal of Physics A* **27**, 1045 (1994).
52. Clausius, R. XVI. On a mechanical theorem applicable to heat. *The London, Edinburgh, and Dublin Philosophical Magazine and Journal of Science* **40**, 122 (1870).

53. Fock, V. Bemerkung zum Virialsatz. *Zeitschrift für Physik* **63**, 855 (1930).
54. Flyvbjerg, H. & Petersen, H. G. Error estimates on averages of correlated data. *The Journal of Chemical Physics* **91**, 461 (1989).
56. Stodolna, A. S. *et al.* Hydrogen Atoms under Magnification: Direct Observation of the Nodal Structure of Stark States. *Physical Review Letters* **110**, 213001 (2013).
57. Leinaas, J. M. & Myrheim, J. On the Theory of Identical Particles. *IL NUOVO CIMENTO* **37**, 1 (1977).
58. Ditchfield, R., Hehre, W. J. & Pople, J. A. Self-Consistent Molecular-Orbital Methods. IX. An Extended Gaussian-Type Basis for Molecular-Orbital Studies of Organic Molecules. *The Journal of Chemical Physics* **54**, 724 (1971).
59. Dunning, T. H. Gaussian basis sets for use in correlated molecular calculations. I. The atoms boron through neon and hydrogen. *The Journal of Chemical Physics* **90**, 1007 (1989).
60. Slater, J. C. Atomic Shielding Constants. *Physical Review* **36**, 57 (1930).
61. A Physical Interpretation of the Cusp Conditions for Molecular Wave Functions. *Theoretica Chimica Acta* **8**, 54 (1967).
64. Cahill, D. G. & Pohl, R. O. Heat Flow and Lattice Vibrations in Glasses. *Solid State Communications* **70**, 927 (1989).
65. Cai, L., Zhang, P., Yang, T. & Pan, X.-Y. Hookes Atom in an Arbitrary External Electric Field: Analytical Solutions of Two-Electron Problem by Path Integral Approach. *Communications in Theoretical Physics* **55**, 565 (2011).
66. Jelic, V. & Marsiglio, F. The double well potential in quantum mechanics: a simple, numerically exact formulation. *European Journal of Physics* **33**, 1651 (2012).
67. Hehre, W. J., Stewart, R. F. & Pople, J. A. Self-Consistent Molecular-Orbital Methods. I. Use of Gaussian Expansions of Slater-Type Atomic Orbitals. *The Journal of Chemical Physics* **51**, 2657 (1969).
69. Legendre, A. M. Nouvelles méthodes pour la détermination des orbites des comètes (1805).
70. Gauss, C. F. *Theoria Motus Corporum Coelestium in Sectionibus Conicis Solem Ambientum* (1809).
72. Holzmann, M. & Castin, Y. Pair correlation function of an inhomogeneous interacting Bose-Einstein condensate. *European Physical Journal D* **7**, 425 (1999).
73. Sauer, P. U. Three-nucleon forces. *International Journal of Modern Physics E* **23**, 1430015 (2014).
74. Mehta, P. *et al.* A high-bias, low-variance introduction to Machine Learning for physicists. *Physics Reports* **810**, 1 (2019).
75. Hornik, K., Stinchcombe, M. & White, H. Multilayer feedforward networks are universal approximators. *Neural Networks* **2**, 359 (1989).
76. Rumelhart, D. E., Hinton, G. E. & Williams, R. J. Learning representations by back-propagating errors. *Nature* **323**, 533 (1986).
77. Kingma, D. P. & Ba, J. Adam: A Method for Stochastic Optimization. *International Conference on Learning Representations*. arXiv: [1412.6980](https://arxiv.org/abs/1412.6980) (2014).
78. Rajasekar, S. & Athavan, N. Ludwig Edward Boltzmann. arXiv: [physics/0609047](https://arxiv.org/abs/physics/0609047) (2006).

79. Hinton, G. E., Srivastava, N., Krizhevsky, A., Sutskever, I. & Salakhutdinov, R. R. Improving neural networks by preventing co-adaptation of feature detectors. arXiv: [1207.0580](https://arxiv.org/abs/1207.0580) (2012).
80. Ackley, D. H., Hinton, G. E. & Sejnowski, T. J. A Learning Algorithm for Boltzmann Machines. *Cognitive Science* **9**, 147 (1985).
82. Coates, A., Ng, A. & Lee, H. An Analysis of Single-Layer Networks in Unsupervised Feature Learning. *15*, 215 (2011).
83. Fischer, A. & Igel, C. Training restricted Boltzmann machines: An introduction. *Pattern Recognition* **47**, 25 (2014).
84. Roux, N. L. & Bengio, Y. Representational Power of Restricted Boltzmann Machines and Deep Belief Networks. *Neural Computation* **20**, 1631 (2008).
87. Deb, S. Variational Monte Carlo technique. *Resonance* **19**, 713 (2014).
88. Assaraf, R. & Caffarel, M. Zero-Variance Zero-Bias Principle for Observables in quantum Monte Carlo: Application to Forces. *The Journal of Chemical Physics* **119** (2003).
89. Umrigar, C. J. & Filippi, C. Energy and Variance Optimization of Many-Body Wave Functions. *Physical Review Letters* **94**, 150201 (2005).
90. Metropolis, N., Rosenbluth, A. W., Rosenbluth, M. N., Teller, A. H. & Teller, E. Equation of State Calculations by Fast Computing Machines. *The Journal of Chemical Physics* **21**, 1087 (1953).
91. Calcavecchia, F., Pederiva, F., Kalos, M. H. & Kühne, T. D. Sign Problem of the Fermionic Shadow Wave Function. *Physical Review E* **90**, 053304 (2014).
92. Kosztin, I., Faber, B. & Schulten, K. Introduction to the Diffusion Monte Carlo Method. *American Journal of Physics* **64**, 633 (1996).
93. Efron, B. Bootstrap Methods: Another Look at the Jackknife. *The Annals of Statistics* **7**, 1 (1979).
94. Quenouille, M. H. Problems in Plane Sampling. *The Annals of Mathematical Statistics* **20**, 355 (1949).
97. Jonsson, M. Standard error estimation by an automated blocking method. *Physical Review E* **98**, 043304 (2018).
99. Helgaker, T. & Klopper, W. Perspective on “Neue Berechnung der Energie des Heliums im Grundzustande, sowie des tiefsten Terms von Ortho-Helium”. *Theoretical Chemistry Accounts* **103**, 180 (2000).
101. Allen, F. E. The History of Language Processor Technology in IBM. *IBM Journal of Research and Development* **25**, 535 (1981).
102. Holmevik, J. R. Compiling SIMULA: a historical study of technological genesis. *IEEE Annals of the History of Computing* **16**, 25 (1994).
110. Degroote, M. Faddeev random phase approximation applied to molecules. *European Physical Journal* **218**, 1 (2013).
111. Pederiva, F., Umrigar, C. J. & Lipparini, E. Diffusion Monte Carlo study of circular quantum dots. *Physics Review B* **62**, 8120 (2000).
112. Dirac, P. A. M. A new notation for quantum mechanics. *Mathematical Proceedings of the Cambridge Philosophical Society* **35**, 416 (1939).

## Bibliography: Books

13. Crawford, D. & Schaefer III, H. *An Introduction to Coupled Cluster Theory for Computational Chemists* 33. ISBN: 978-0-470125-91-5 (Wiley-VCH, 2007).
26. Flugsrud, V. M. *Solving Quantum Mechanical Problems with Machine Learning* MA thesis (2018).
27. Høgberget, J. *Quantum Monte-Carlo Studies of Generalized Many-body Systems* MA thesis (2013).
37. Vance, A. *Elon Musk: Tesla, SpaceX, and the Quest for a Fantastic Future* ISBN: 978-0-062301-25-3 (Ecco, 2015).
47. Griffiths, D. J. *Introduction to Quantum Mechanics* 2nd Edition. ISBN: 978-0-13-191175-9 (Pearson PH, 2005).
55. Heisenberg, W. *Across the frontiers* ISBN: 978-0-918024-80-0 (Ox Bow Press, 1990).
62. Heisenberg, W. *Physics and Beyond: Encounters and Conversations* ISBN: 978-0-049250-08-6 (Allen and Unwin, 1971).
63. Wilson, E. B. j., Decius, J. C. & Cross, P. C. *Molecular Vibrations: The Theory of Infrared and Raman Vibrational Spectra* ISBN: 978-0-486-63941-3 (Dover Books on Chemistry, 1955).
68. Domingos, P. *The Master Algorithm: How the Quest for the Ultimate Learning Machine Will Remake Our World* ISBN: 978-0-241-00455-5 (Penguin UK, 2015).
85. Nissenbaum, D. A. *The Stochastic Gradient Approximation: An Application to Li Nanoclusters* PhD dissertation (2008).
86. Mariadason, A. A. *Quantum Many-Body Simulations of Double Dot System* MA thesis (2018).
95. Devore, J. L. & Berk, K. N. *Modern Mathematical Statistics with Applications* ISBN: 978-1-4614-0391-3 (Springer, 2012).
96. Shumway, R. H. & Stoffer, D. S. *Time Series Analysis and Its Applications* 4th Edition. ISBN: 978-3-319-52452-8 (Springer, 2017).
100. Gustafsson, B. *Scientific Computing: A Historical Perspective* ISBN: 978-3-319-69846-5 (Springer, 2018).
106. Trahan, J., Kaw, A. & Martin, K. *Computational time for finding the inverse of a matrix: LU decomposition vs. naive gaussian elimination* (2006).



# Bibliography: Online

20. Smith, C. *iOS 10: Siri now works in third-party apps, comes with extra AI features* 2016. <https://bgr.com/2016/06/13/ios-10-siri-third-party-apps/>.
21. *Bringing the Magic of Amazon AI and Alexa to Apps on AWS. - All Things Distributed* <https://www.allthingsdistributed.com/2016/11/amazon-ai-and-alexa-for-all-aws-apps.html>.
28. *Samsung QLED TV | The Frame | Premium UHD TV* <http://www.samsung.com/global/tv/blog/why-are-quantum-dot-displays-so-good/>.
36. Cellan-Jones, R. *Hawking: AI could end human race* 2014. <https://www.bbc.com/news/technology-30290540> (2019).
38. Ledum, M. *Simple Variational Monte Carlo solve for FYS4411* 2016. <https://github.com/mortele/variational-monte-carlo-fys4411>.
39. *MIT License* <https://choosealicense.com/licenses/mit/> (2019).
40. Nordhagen, E. M. *Ground state properties of quantum dots provided by VMC and RBM* 2019. doi:[10.5281/zenodo.3477946](https://doi.org/10.5281/zenodo.3477946).
41. *A Quantum Sampler* 2005. <https://www.nytimes.com/2005/12/26/science/a-quantum-sampler.html>.
48. Sherrill, D. *Postulates of Quantum Mechanics* 2003. [http://vergil.chemistry.gatech.edu/notes/intro\\_estruc/node4.html](http://vergil.chemistry.gatech.edu/notes/intro_estruc/node4.html).
71. *Machine Learning - Stanford University* <http://mlclass.stanford.edu/>.
98. Woods, J. F. *Usage of comma operator - Google Groups* <https://groups.google.com/forum/#msg/comp.lang.c++/rYCO5yn4lXw/oITtSkZOtoUJ>.
103. *C++ Data Types* 2017. <https://www.geeksforgeeks.org/c-data-types/>.
104. Fowler, M. *Two Hard Things* <https://martinfowler.com/bliki/TwoHardThings.html>.
105. AlDanial. *cloc counts blank lines, comment lines, and physical lines of source code in many programming languages.*: AlDanial/cloc original-date: 2015-09-07T03:30:43Z. 2019. <https://github.com/AlDanial/cloc>.
107. Hjorth-Jensen, M. *Computational Physics 2: Variational Monte Carlo methods* 2019. <http://compphysics.github.io/ComputationalPhysics2/doc/pub/vmc/html/vmc-reveal.html>.
108. *The Edisonian - Volume 8 The Thomas Edison Papers at Rutgers University* <http://edison.rutgers.edu/newsletter9.html>.
109. Mariadason, A. A. *HartreeFock* 2018. <https://github.com/Oo1Insane1oO/HartreeFock>.